

RENSIT: RadioElectronics. NanoSystems. Information Technologies

Journal "Radioelectronics. Nanosystems. Information Technologies" (abbr. RENSIT) publishes original articles, reviews and brief reports, not previously published, on topical problems in **radioelectronics (including biomedical) and fundamentals of information, nano- and biotechnologies and adjacent areas of physics and mathematics.**

Designed for **researchers, graduate students, physics students of senior courses and teachers.**
It turns out **2 times a year** (that includes 2 issues)

Authors of journal are academicians, corresponding members and foreign members of Russian Academy of Natural Sciences (RANS) and their colleagues, as well as other russian and foreign authors on presentation of their manuscripts by the members of RANS, which can be obtained by authors before sending articles to editors. And also after its receiving - on recommendation of a member of editorial board of journal, or another member of Academy of Natural Sciences, that gave her opinion on article at request of editor. The editors will accept articles in both **Russian and English** languages.

Articles are internally peer reviewed (**double-blind peer review**) by members of the Editorial Board.
Some articles undergo external review, if necessary.

Journal RENSIT is included in the **DB SCOPUS, EBSCO Publishing**, in the international abstracts database - **Ulrich's International Periodicals Directory**,(USA, New York, <http://www.ulrichsweb.com>), in the **AJ and DB VINITI RAS** (<http://wwwviniti.ru>), and DB **Russian Science Citation Index (RSCI)** (http://elibrary.ru/project_risc.asp).

Full-text content is posted in the DB of the **Russian Scientific Electronic Library**

- information resource on the Internet <http://elibrary.ru> and is available for registered users.

And also - in Open Access **CyberLeninka NEB** of Russian Federation <http://cyberleninka.ru>.

On journal's website <http://www.rensit.ru> posted metadata publications

and **RENSIT: Radioelectronics. Nanosystems. Infomation Technologies - english version** (cover-to-cover translation) of journal, which is a party to **CrossRef**.

The founder - the **Russian Academy of Natural Sciences**

Publisher - Publishing Center of the Russian Academy of Natural Sciences

Publisher Address: 119002 Moscow, per. Sivtsev Vrazhek 29/16

CONTENTS

MULTIDIMENSIONAL THEORIES OF PHYSICAL FIELDS

INSTALLATION FOR STUDYING ELECTROMAGNETIC WAVE LOCALIZATION PARAMETERS IN A VARIABLE CROSS-SECTION WAVEGUIDE IN THE 5-D EXTENDED SPACE MODEL PREDICTION'S FRAMEWORK
Dmitry Yu. Tsipenyuk, Sergey I. Derzhavin, Yaroslav V. Kravchenko, Mikhail R. Bogdanov 407

RADIOELECTRONICS

STUDY OF THIN FILMS FOR THE MANUFACTURE OF TUNNEL JUNCTIONS Nb/AlN/NBN

Artem M. Chekushkin, Vadim V. Kashin, Leonid V. Filippenko, Mikhail Yu. Fominsky, Valery P. Koshelets 419

USING ADDITIVE TECHNOLOGIES TO CREATE BROADBAND ANTENNAS WITH FRACTAL GEOMETRY

Andrey V. Smirnov, Alexander S. Fionov, Ilia A. Gorbachev, Elizaveta S. Shamsutdinova, Irina E. Kuznetsova, Vladimir V. Kolesov 427

PASSIVE MEASUREMENTS OF THE REFRACTIVE INDEX OF LIQUID NITROGEN AND FREE-FLOWING SUBSTANCES BY THE PRISM METHOD IN THE MILLIMETER WAVELENGTH RANGE

Valery A. Golunov, Konstantin V. Gordeev, Konstantin N. Rykov 435

MILLIMETER-WAVE BAND SUBSURFACE SOUNDING MODULE

Gennady I. Khokhlov, Roman N. Denisyuk 443

SIMULATION OF THE CHARACTERISTICS OF LOW-VOLTAGE GATES ON COMBINED CYLINDRICAL SURROUNDING GATE FIELD-EFFECT NANOTRANSISTORS

Nikolae V. Masalsky 449

NANOSYSTEMS

STRUCTURE AND ELECTRICAL CONDUCTIVITY OF POLYVINYL ALCOHOL FILMS WITH MULTI-WALLED CARBON NANOTUBES CURED IN A MAGNETIC FIELD

Sergey V. Vasin, Azat M. Nizametdinov, Viacheslav A. Sergeev, Michael S. Efimov 457

INFLUENCE OF DIFFERENT TYPES OF SOLVENTS ON MORPHOLOGY, OPTICAL AND CONDUCTIVE PROPERTIES OF PCBM FILMS

Olga A. Krokhina, Nikita E. Podolsky, Angrey S. Tyutyunik, Vladimir S. Gurchenko 465

NANOSTRUCTURES FOR INFORMATION TECHNOLOGIES

THE MIXED HYDROGEN BONDS NETWORK IN A LIQUID SYSTEM

ETHYLENE GLYCOL-MONOETHANOLAMINE

Karen Y. Constantinian, Gennady A. Ovsyannikov, Anton V. Shadrin, Yuliia V. Kislynski, Andrey M. Petrzlik, Alexei Kalaboukhov 471

SPIN CURRENT AND SPIN MAGNETORESISTANCE OF THE

HETEROSTRUCTURE IRIDATE/MANGANITE INTERFACE

Gennady A. Ovsyannikov, Karen Y. Constantinian, Vladislav A. Shmakov, Anton V. Shadrin, Yuliia V. Kislynski, Nikolay V. Andreev, Filipp O. Milovich, Andrey P. Orlov, Peter V. Lega 479

INFORMATION TECHNOLOGIES

CHARACTERISTIC FORM OF DYNAMICS EQUATIONS OF COSSERAT MEDIUM

George G. Bulychev 487

DEVELOPMENT OF A MATHEMATICAL MODEL OF FUNCTIONING SYSTEM COMMUNICATIONS SPACECRAFT

Mikhail A. Zaytsev, Alexander K. Korovin, Sergey B. Savilkin, Andrey V. Suhov 495

NUCLEAR PHYSICS OF CONDENSED MATTER

JOINT TRANSMUTATION OF STABLE Cs AND Sr ISOTOPES IN

MICROBIOLOGICAL SYSTEMS AND PROSPECTS FOR ACCELERATED

DEACTIVATION OF LIQUID RADIOACTIVE WASTE

Alla A. Kornilova, Vladimir I. Vysotskii, Sergey N. Gaydamaka, Marina A. Gladchenko 501

METHODOLOGY OF SCIENCE

NEW PARADIGM AND PARAMETRY

Gennady V. Mishinsky 509

CHRONICLE

HIGH-TEMPERATURE SINGLE-ELECTRON TRANSISTORS BASED ON MOLECULES AND SMALL NANOPARTICLES

Evgeny S. Soldatov 521

40 YEARS OF THE INSTITUTE OF CHEMISTRY AND CHEMICAL TECHNOLOGY OF THE SB RAS

Boris N. Kuznetsov, Vladimir I. Kuzmin 529

IN MEMORIAM

IN MEMORY OF GEORGE A. MARTYNOV

Margarita N. Rodnikova, George G. Malenkov 533



RUSSIAN ACADEMY
OF NATURAL SCIENCES

DEPARTMENT OF
RADIOELECTRONICS,
NANOPHYSICS AND
INFORMATION TECHNOLOGIES
PROBLEMS

REN SIT:

RADIOELECTRONICS.
NANOSYSTEMS.
INFORMATION
TECHNOLOGIES.
2021, VOL. 13, NO. 4

FOUNDED IN 2009

4 ISSUES PER YEAR

MOSCOW

Editor-in-Chief

Vladimir I. Grachev

grachev@cpclie.ru

Deputy Chief Editor

Vladimir A. Makarov, DrSci, MSU

Deputy Chief Editor

Sergey P. Gubin, DrSci, IGIC RAS

Executive Secretary

Rostislav V. Belyaev, PhD, IRE RAS

belyaev@cpclie.ru

EDITORIAL BOARD

Anatoly V. Andreev, DrSci, MSU

Vladimir A. Bushuev, DrSci, MSU

Vladimir A. Cherepenin, DrSci, c-mRAS, IRE

Alexander S. Dmitriev, DrSci, IRE

Yuri K. Fetisov, DrSci, MIREA

Yuri V. Gulyaev, DrSci, acad.RAS, IRE

Yaroslav A. Ilyushin, DrSci, MSU

Anatoly V. Kozar, DrSci, MSU

Vladimir V. Kolesov, PhD, IRE

Albina A. Kornilova, PhD, MSU

Alexander V. Okotrub, DrSci, SB RAS

Aleksey P. Oreshko, DrSci, MSU

Igor B. Petrov, DrSci, c-m RAS, MIPT

Alexander A. Potapov, DrSci, IRE

Vyacheslav S. Rusakov, DrSci, MSU

Alexander S. Sigov, DrSci, c-m RAS, MIREA

Eugeniy S. Soldatov, DrSci, MSU

Lkhamsuren Enkhtoor, DrSci (Mongolia)

Yoshiyuki Kawazoe, DrSci (Japan)

Kayrat K. Kadyrhanov, DrSci (Kazakhstan)

Peter Paul Mac Kenn, DrSci (USA)

Jiao Licheng, Ph.D. (China)

Deleg Sangaa, DrSci (Mongolia)

Andre Skirtach, DrSci (Belgium)

Enrico Verona, DrSci (Italy)

ISSN 2414-1267

The journal on-line is registered by the Ministry of Telecom and Mass Communications of the Russian Federation. Certificate El. no. FS77-60275 on 19.12.2014

All rights reserved. No part of this publication may be reproduced in any form or by any means without permission in writing from the publisher.

©RANS 2021

EDITORIAL BOARD ADDRESS

218-219 of., 7 b., 11, Mokhovaya str.,
125009 MOSCOW, RUSSIAN FEDERATION,
TEL. +7 495 629 3368
FAX +7 495 629 3678 FOR GRACHEV

Installation for studying the parameters of localization of an electromagnetic wave in a waveguide of variable cross-section in the framework of the predictions of the 5-D extended space model

^{1,2}Dmitry Yu. Tcipenyuk, ¹Sergey I. Derzhavin, ¹Yaroslav V. Kravchenko

¹Prokhorov General Physics Institute of Russian Academy of Sciences, <http://gpi.ras.ru/>
Moscow 119991, Russian Federation

²Moscow Polytechnic University, <https://new.mospolytech.ru/>
Moscow 107023, Russian Federation

E-mail: tsip@kapella.gpi.ru, derzh@kapella.gpi.ru, kravch@kapella.gpi.ru

Mikhail R. Bogdanov

Moscow Polytechnic University, <https://new.mospolytech.ru/>
Moscow 107023, Russian Federation

E-mail: bogdanov_m_r@mail.ru

Received August 24, 2021, peer-reviewed September 14, 2021, accepted on September 27, 2021

Abstract: The paper describes the creation and testing of an experimental setup for studying the parameters of localization of electromagnetic microwave radiation with a power of 0.001-0.004 W in the range of 36.0-79.0 GHz when propagating radiation in metal waveguides of variable cross-section. Measurements will also be carried out under conditions of filling the waveguide with dielectric materials with refractive indices from 1.46 to 4.0 for microwave radiation of the specified range. The installation is designed to measure the parameters of the localization of microwave radiation when it passes through a waveguide of variable cross-section, filled with materials with different refractive indices. Interpretation of the results will be carried out within the framework of the 5-D extended space model (ESM). The extended space model is formulated in (1+4)-dimensional space time-coordinate-interval. An additional spatial coordinate in the ESM is the interval. In the conjugate 5-D space, the energy-momentum-mass interval in the ESM corresponds to mass. In the ESM formalism, the question of the appearance of a nonzero variable mass in a photon and its localization under the influence of an external field is studied.

Keywords: localization of the electromagnetic field, waveguide, microwave radiation, (1+4)D extended space model, variable photon mass, interval

PACS: 11.10.Kk, 03.50.-Z, 03.65.Pm

For citation: Dmitry Yu. Tcipenyuk, Sergey I. Derzhavin, Yaroslav V. Kravchenko, Mikhail R. Bogdanov. Installation for studying the parameters of localization of an electromagnetic wave in a waveguide of variable cross-section in the framework of the predictions of the 5-D extended space model. *RENSIT: Radioelectronics. Nanosystems. Information technologies*, 2021, 13(4):407-418. DOI: 10.17725/rensit.2021.13.407.

CONTENTS

- 1. INTRODUCTION (407)**
- 2. POTENTIALS AND CURRENTS IN THE FRAMEWORK OF THE EXTENDED SPACE MODEL APPROACH (409)**
 - 2.1. LOCALIZATION OF FIELDS AND PARTICLES WITHIN THE FRAMEWORK OF THE ESM APPROACH (410)**
- 3. DESCRIPTION OF INSTALLATION AND METHODS OF MEASUREMENT (412)**

4. RESULTS OF CALIBRATION AND TEST

MEASUREMENTS (414)

5. CONCLUSION (416)

REFERENCES (416)

1. INTRODUCTION

In modern science, the problem of combining gravitational and electromagnetic fields into one is actively discussed. Historically, this topic has been discussed for over 100 years.

Most of the attempts to build a unifying field model are implemented by constructing geometric models of physical interactions and interpreting physics within the framework of geometry in spaces of a larger number of dimensions. A review of the literature on the topic of multidimensional theories can be found, for example, in [1].

At the very beginning of the 20th century, Felix Klein [2] considered the Hamilton-Jacobi theory as optics in spaces of a greater number of dimensions. Klein's ideas did not receive further development at the time of creation. Interest in the problem of the geometrization of physics was again caused by the creation of the General Theory of Relativity (GR) [3]. Efforts have been made by researchers to describe electromagnetism in geometric terms similar to gravity. The authors of these works tried to expand the already created general relativity scheme in various ways instead of creating new models.

The models of Klein [4] and O. Kaluza [5] became famous. We can also mention the work of Fock [6] and Mandela [7]. Note that a 5-dimensional space was used to build these models. Nevertheless, no clear physical interpretation of the fifth coordinate was made in these works. In the future, attempts to develop 5-dimensional models were undertaken by many scientists, including Einstein, de Broglie, Gamow and Rumer [8,9], however, some interesting results did not work out.

We believe that the reason for the relative failure of these approaches was the lack of new physical hypotheses and the basis for a formal generalization of the existing models.

An interesting opinion about the reasons for the failures in the creation of a unified theory of the Fock field is from his letter to Rumer on February 14, 1950: "The success of

the idea of geometrization in Einstein's theory of bodies with a sufficiently small mass move according to the same law. The movement of charged bodies in an electromagnetic field depends on the ratio of charge to mass. Therefore, the geometrization of the corresponding concepts can be successful only for one particle. This is also the reason for the complete failure of all "unified" field theories" [10, p. 78].

We also note Einstein's opinion regarding the shortcomings of the 5-dimensional Rumer theory (the Extended Space Model - ESM model [14-18] is close to Rumer's idea, but differs significantly from it in that the ESM considers the interval S as a non-compactified 5th coordinate), expressed in Einstein's letter M. Born from 12/14/1929: "I really liked Mr. Rumer. His idea of attracting multidimensional sets is original and formally well implemented. The weakness is rooted in the fact that the laws found in this way are not complete and the paths for logical support and completeness are not foreseen" [10, p. 163; 11].

Although in Rumer's 5-optics the fifth coordinate is introduced in the form of an action and a 5-dimensional space with the metric (+, -, -, -, -) is considered, but no transformations in this space that would confuse the coordinate with the other four coordinates of the Minkowski space, he does not consider. Accordingly, in the conjugate 5-dimensional space with coordinates, the mass also remains constant and is not converted into energy and momentum.

It is also necessary to note the theory of gauge fields, in which electromagnetism, gravity and other interactions are considered from a single geometric point of view [12]. In the work of Landau [13], estimates of the value of the "radius" of elementary

particles were obtained, proceeding from the limit of applicability of electrodynamic representations in quantum mechanics. Note that the "radius" of the electron in this case turned out to be equal to zero.

The approach proposed in the ESM [14-18] is fundamentally different from all the above and similar theories. The ESM is based on the physical hypothesis that mass (rest mass) and its conjugate value - action (interval) are dynamic variables. The magnitude of these variables is determined by the interaction of fields and particles. In this respect, such a model is a direct generalization of the Special Theory of Relativity (SRT). In SRT, the interval and rest mass of particles are invariants, and they can vary in the ESM. In particular, a photon can acquire a mass, both positive and negative. This mass can appear and change due to electromagnetic interaction and generate gravitational forces. It is this circumstance that allows us to consider gravity and electromagnetism as a single field in the ESM.

A similar ESM 5-dimensional model was developed by Paul Wesson et al. [19-22]. P. Wesson suggested using "mass" as the fifth coordinate, complementary to time and three spatial coordinates: [19, p.10]. "We ... consider mass on the same basis as time and space ..." [19, p. 191, equation (7.40)]. "This means that the role of the uncharged 4D mass in the 5D geometry is played by an additional coordinate".

This approach seems counterintuitive to us. In this case, this leads to difficulties in generalizing the 4D energy-momentum tensor to the 5D energy-momentum-mass tensor in 5-dimensional space.

Of course, mass can be used as a fifth coordinate, but not in coordinate space. Mass should be considered in momentum space,

i.e., as an additional quantity to the energy and three components of the momentum. And in coordinate space, the fifth coordinate must be another value related to mass. As a result of considering mass as the fifth coordinate in addition to time and space in [19-22], it was difficult to establish a connection between m and real experiments.

Recently James Overduin (co-author Paul Wesson) and R.C. Henry in [23] proposed the same idea of introducing the 5th coordinate as Tsipenyuk D.Yu. and Andreev V.A. in 2000 [14].

The presented work is devoted to the description of the experimental setup we created and its subsequent testing. The installation is designed to study the parameters of localization of electromagnetic microwave radiation with a power of 0.001-0.004 W in the range of 36.0-79.0 GHz during propagation of radiation in metal waveguides of variable cross-section. These parameters of the facility should allow experimentally testing the prediction of the ESM in the region of localization of electromagnetic waves when they hit media with a high refractive index.

2. POTENTIALS AND CURRENTS IN THE FRAMEWORK OF THE ESM APPROACH

Within the framework of the extended space model, the process of localization of the electromagnetic field was described when an electromagnetic wave from a vacuum enters an external field (for example, an electron) or into a converging waveguide.

In the ESM, the assumption is made that the relationship between energy, momentum and mass is 5-dimensional if we take into account the possibility of mass change in physical processes:

$$E^2 - c^2 p_x^2 - c^2 p_y^2 - c^2 p_z^2 - m^2 c^4 = 0. \quad (1)$$

The generalization of Einstein's special theory of relativity (STR) to (1+4)D-dimensional space (T, \bar{X}, S) , with the metric (+ - - -), where the fifth coordinate is the interval S , which has the physical meaning of action, is considered. The basis for this generalization is the fact that in SRT the masses of particles are scalars and do not change during their elastic interactions. It is well known that a photon can be considered a massless particle and described by a plane wave only in infinite empty space. If a photon enters a medium or finds itself in a limited space (in a resonator or waveguide), then it acquires a nonzero mass.

The length of the Lorentz-covariant 5-vector corresponding to objects satisfying (1) in the ESM is equal to zero:

$$(ct)^2 - x^2 - y^2 - z^2 - s^2 = 0. \quad (2)$$

In contrast to (1+3)D Minkowski space, where the particle is associated with a 4-dimensional isotropic for massless particles and anisotropic for massive particles, the energy-momentum vector $(E/c, P(x), P(y), P(z))$, in the (1+4)D ESM particle is assigned an isotropic Lorentz-covariant for all particles 5-dimensional energy-momentum-mass vector $(E/c, P(x), P(y), P(z), mc)$ whose length is zero.

The 5-dimensional current vector generating a single electromagnetic-gravitational field has the form:

$$\vec{\rho} = (j_0, \vec{j}_1, j_4) = \left[\frac{emc}{\sqrt{1-\beta^2}}, \frac{em\vec{v}}{\sqrt{1-\beta^2}}, emc \right]. \quad (3)$$

This is an isotropic vector $\vec{\rho}^2 = 0$.

The equation of continuity, as in the usual case, is expressed by the equality to zero of the 5-divergence of the 5-current

$$\sum_{i=0}^4 \frac{\partial j_i}{\partial x_i} = 0. \quad (4)$$

If the charge is at rest, then the continuity equation takes the form

$$\frac{\partial m}{\partial t} + \frac{\partial m}{\partial x_4} = 0. \quad (5)$$

Current (3) generates an electromagnetic-gravitational field in the expanded space $G(1,4)$. This field is given by the 5-vector potential A :

$$A = (A_0, A_x, A_y, A_z, A_s) = (A_0, A_1, A_2, A_3, A_4) \quad (6)$$

Here and below, we use the notation $t = x_0$, $x = x_1$, $y = x_2$, $z = x_3$, $s = x_4$.

The components of this vector potential are determined by the equations

$$\Pi_{(5)} A_0 = -4\pi\rho, \quad (7)$$

$$\Pi_{(5)} \vec{A} = \frac{-4\pi}{c} \vec{j}, \quad (8)$$

$$\Pi_{(5)} A_s = \frac{-4\pi}{c} j_s. \quad (9)$$

Here

$$\Pi_{(5)} = \frac{\partial^2}{\partial s^2} + \frac{\partial^2}{\partial x^2} + \frac{\partial^2}{\partial y^2} + \frac{\partial^2}{\partial z^2} - \frac{1}{c^2} \frac{\partial^2}{\partial t^2}. \quad (10)$$

Note that in the case when there is no dependence on the coordinate s and the mass m entering the current components (3) is constant, the system of equations (7)-(9) splits into two independent parts. Equations (7), (8) specify the usual potentials of the electromagnetic field, and equation (9) specifies the potential of the scalar gravitational field. These fields exist independently of each other. They are combined into one field only when the mass m becomes variable and there is a dependence on the variable s [18].

2.1. LOCALIZATION OF FIELDS AND PARTICLES WITHIN THE FRAMEWORK OF THE ESM APPROACH

Localization of fields and particles within the framework of the ESM approach is considered in detail in [17,18]. Some of the

results of this work are presented below. Note that the approach is based on an analogy when comparing the dispersion relation of a free particle

$$E^2 = (c\vec{p})^2 + m^2 c^4. \quad (11)$$

and the dispersion relation of the wave in the mode of a hollow metal waveguide

$$\omega^2 = \omega_{kr}^2 + (c\xi)^2. \quad (12)$$

Here, ω_{kr} is the critical frequency of the waveguide mode, and ξ is the wave propagation constant. De Broglie, Feynman, and other authors drew attention to the similarity of relations (11) and (12). The critical frequency ω_{kr} is associated with a parameter that has the dimension of mass

$$m = \frac{\hbar\omega_{kr}}{c^2}, \quad (13)$$

The mass that an electromagnetic field acquires when it enters a waveguide.

In particular, if the waveguide has a square shape with a side of size a , then this connection has the form

$$a = \frac{\sqrt{2}\pi\hbar}{mc}. \quad (14)$$

We propose to consider this value as a linear parameter associated with a massless particle when it acquires mass m . We believe that at the same time as, when hitting an external field, a massless particle acquires a nonzero mass, the corresponding infinite plane wave is compressed to a finite size. And this final size is characterized by the localization parameter

$$l = \frac{2\pi\hbar}{mc}. \quad (15)$$

In appearance, quantity (15) resembles the Compton wavelength of an electron, however, its physical meaning is completely different. In the formula for the Compton wavelength of an electron, the parameter m - is the electron rest mass, and in formula (15)

m - is the mass that a photon acquires when it is exposed to external influences.

In the ESM, the external influence is described by means of rotations in the expanded space $G(1,4)$. Since the linear parameter l is expressed using formula (14) in terms of the photon mass, it can be used to find the dependence of this parameter on the quantities that specify these rotations.

So, in the case of hyperbolic rotations in the plane (TS), the dependence of the photon mass on the rotation angle θ is determined by the formula $m^2 = \hbar\omega sh\theta$. Substituting this expression into formula (15), we obtain an expression for the parameter l through the angle θ

$$l = \frac{2\pi c}{\omega \cdot sh\theta}. \quad (16)$$

In the case of Euclidean rotations in the (XS) plane, the dependence of the photon mass on the rotation angle ψ is determined by the formula $m^2 = \hbar\omega sin\psi$.

With its help, we obtain an expression for the parameter l through the angle ψ .

$$l = \frac{2\pi c}{\omega \cdot sin\psi}. \quad (17)$$

The speed of propagation of a wave c in vacuum is related to the propagation of speed in a medium or a waveguide v refractive index n by the ratio $v = c/n$.

In the case of rotations (TS), a photon under the influence of an external field acquires a mass related to the refractive index by the relation

$$m_{(TS)} = \frac{\hbar\omega}{c^2} \cdot sh\theta = \frac{\hbar\omega}{c^2} \sqrt{n^2 - 1}. \quad (18)$$

The physical meaning of turns (TS) is that we do not make spatial movements, we are always at the same point, but the optical density at this point changes over time. Thus, in this case, the transformation

(*TS*) means a transition to a different point in time and a different optical density. This can be interpreted in such a way that an external field arises in space, which, acting on a particle and performing work, changes its energy and mass. All movements occur along cones and hyperboloids and are transitive in nature. Since there is no spatial motion, the momenta of the particles must be conserved.

In the case of rotations (*XS*), a photon under the influence of an external field acquires a mass related to the refractive index by the relation

$$m_{(XS)} = \frac{\hbar\omega}{c^2} \cdot \sin\psi = \frac{\hbar\omega}{c^2 n}. \quad (19)$$

The rotation (*XS*) corresponds in the ESM to the transition from a space with one optical density to a space with a different optical density. In this case, no time processes occur, everything is considered at the same time. Therefore, the energy of the particles is conserved, and all processes occurring with them are reduced to internal rearrangements. Conventionally, this can be understood so that a particle, falling into a denser medium, is deformed in an elastic manner, and leaving it, restores its characteristics. In this case, there is no exchange of energy and momentum between the medium and the particle.

So, from the point of view of the ESM, the transition from a medium with one refractive index to a medium with a different refractive index can be interpreted as a movement along the fifth coordinate of the Expanded space. In other words, this (1+4)-dimensional space can be understood as a set of 1+3-dimensional Minkowski spaces, each of which is characterized by some parameter, such as the refractive index n . And the transition from a medium with an index n_1 to a medium with a refractive index n_2 can be

interpreted as a transition in 1+4-dimensional space from one 1+3-dimensional subspace to another 1+3-dimensional subspace. Thus, the geometry of the Expanded Space turns out to be related to the physics of the processes that we study in each specific problem. Namely, with fields and environments that participate in these processes. The distribution of these media and fields in our ordinary Minkowski space determines the distribution of the "refractive index" in the Expanded space, i.e. its geometry.

In [36], a solution to the system of equations (7)-(10) was found in the form

$$U(s, x, y, z, t) = u(s, x, y, z) \cdot e^{-iks} \cdot e^{i\omega t}, \quad k = \frac{2\pi}{\lambda}, \quad (20)$$

Assuming that the sought-for function is stationary in time and varies slowly along the s -axis in comparison with the change along the x, y, z axes. In this case, the solution has the form of a 3-dimensional Gaussian wave

$$u = u_0 \left(\frac{w_0}{w} \right)^{3/2} \exp[-i(ks + \varphi)] - (x^2 + y^2 + z^2) \left(\frac{1}{w^2} + \frac{ik}{2R} \right). \quad (21)$$

Here w_0 is the minimum radius of the wave at a point $s = 0$; w - is the diameter of the wave at point s_1 and R is the radius of curvature of the wavefront at this point.

When a plane electromagnetic wave hits a medium or an external field, the ESM predicts that, in accordance with (21), the plane wave is localized into a sphere of radius w_0 , taking into account the above assumptions.

3. DESCRIPTION OF INSTALLATION AND METHODS OF MEASUREMENT

To experimentally check the correctness of the ESM predictions about the parameters of the localization of an electromagnetic wave in a waveguide with a variable cross section,

we assembled a specialized experimental microwave setup. This setup is also supposed to measure the microwave localization parameter when radiation hits dielectric media with a refractive index greater than unity.

The installation diagram is shown in **Fig. 1**.

Radiation in the microwave frequency range from 36 to 79 GHz is generated by interchangeable generators 1 model Г4-141 (generation region 36-54 GHz) or Г4-142 (generation region 53-79 GHz). The instability of the output frequency is not more than 10^{-3} , the adjustable output signal power is up to $4 \cdot 10^{-3}$ W, the range of the output power level is not less than 30 dB. The limit of instability of the output power level is ± 0.3 dB. Standard operating modes of generators: 1) continuous generation; 2) internal modulation by rectangular symmetric pulses with a repetition rate 1 ± 0.2 kHz and a duty cycle of 2 ± 0.4 ; 2) electrical remote frequency tuning by digital code.

After the generator, microwave radiation propagates through a silver-plated copper waveguide having a rectangular cross-section of $a \times b = 5.5 \times 2.5$ mm for the case of the

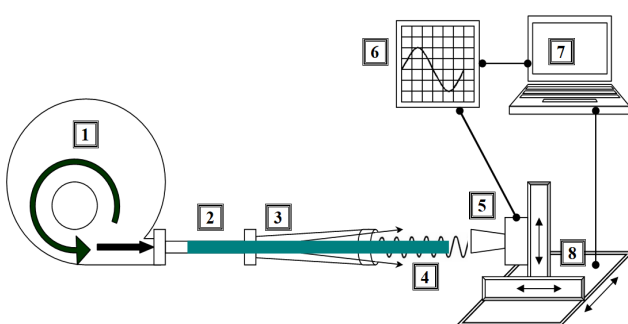


Fig. 1. Installation diagram. 1 - microwave generator 36-79 GHz, 2 - rectangular waveguide, 3 - output horn/sectoral antenna, 4 - Teflon or silicone dielectric insert of variable cross-section, 5 - microwave receiver, 6 - digital oscilloscope, 7 - computer, 8 - receiver 3D positioning system.

Г4-141 generator (option 3.8×1.9 mm when using the Г4-142 generator) with a length $l =$ from 30 to 50 mm.

Inside the waveguide 2, if necessary, a dielectric rod 4 made of Teflon or silicone and completely filling the waveguide can be installed and, if necessary, coming out from the waveguide by 150-200 mm outside. At the same time, we made a series of dielectric rods with a length having both a constant cross-section along the length and converging evenly in one or two directions. For example, to work with the Г4-141 generator (the generation region is 36-54 GHz, which approximately corresponds to the microwave radiation wavelength from 8.32 to 5.55 mm), Teflon rods of various profiles were made: No. 1 with a cross-section of 5.5×2.5 mm at the beginning up to 2.2×1.6 mm at the end of a rod 200 mm long; No. 2 with a section from 5.5×2.5 mm at the beginning to 0.5×2.5 mm at the end of a 180 mm long rod and No. 3 with the same section 5.4×2.4 mm along the entire rod 200 mm long.

Further, the installation has the ability to install a horn antenna 3, as well as a waveguide 2 with a wall thickness of 1.2 mm, made of copper and silver-plated from the inside. We have the ability to install various horn antennas at the output 3 or at the input of the receiver 5. We have horn antennas of the following types and sizes: 1) horn antennas of the pyramidal type, measuring the length of the horn - 90 or 75 mm and the size of the output aperture 45×45 mm or 40×40 mm; 2) horn antennas with a circular output section with dimensions (length x output diameter): 55×36 ; 110×44 ; 116×51 and 160×50 mm.

The received modulated low frequency 1 kHz microwave signal from the receiver 5, after digitizing its parameters on the DS-1052 oscilloscope, is transmitted for recording and

further processing to the computer 7. The receiver 5 can be precisely moved in three spatial directions using the 3-dimensional positioning system of the receiver 8.

Direct measurement by the parameter of a high-frequency signal in the continuous generation mode with a resolution in the range of 36-79 GHz on the assembled installation is impossible. For this reason, it was decided to measure the parameters of the microwave signal resulting from internal modulation by rectangular symmetric pulses with a repetition rate 1 ± 0.2 kHz and a duty cycle of 2 ± 0.4 . A low-frequency modulated microwave signal is confidently recorded by a receiver coupled to a digital oscilloscope at a distance of 10-800 mm from the output waveguide. When the maximum signal output power level is set at $4 \cdot 10^{-3}$ W, the amplitude of the recorded useful signal reaches 700 mV at a distance of about 100 mm.

Measurement of the useful signal with an accuracy of less than 0.1 mV on the created setup seems to be impractical. This conclusion was made based on the results of experimentally measured signal fluctuations caused by various factors in total. Such factors can be the instability of the signal from the generator (the level of parasitic amplitude low-frequency modulation of the output signal is about 1% according to the technical description), mechanical vibrations of the installation, air flows, etc.

Thus, we have a range of the useful signal of the order of 10^4 , which seems to be sufficient for the purposes of our experiment. The positioning accuracy of the receiver of our installation is not worse than 0.1 mm, is sufficient taking into account the characteristic distances at which there is a significant change in the signal for microwave waves in the 3-8 mm range.

4. RESULTS OF CALIBRATION AND TEST MEASUREMENTS

On the created experimental stand, in the period from April to June 2021, we carried out several series of test and calibration measurements, the results of which are described below.

The power of the output signal of the Г4-141 and Г4-142 generators can be changed with a special regulator, while the signal level indicator shows current changes in the range of 0-100 mV. The connection between the readings of the dial indicator and the real level of the output signal was measured. In Fig. 2 shows the data showing the measured relationship between the readings of the dial indicator installed on the Г4-141 generator with the level of the microwave signal recorded at a distance of 200 mm. The measurements were carried out at two frequencies at frequencies of 36 and 52 GHz.

Changes in the linearity of the connection between the indicator readings and the real output signal level were carried out for two frequencies 36 and 52 GHz. It can be seen that changes in the output signal occur with

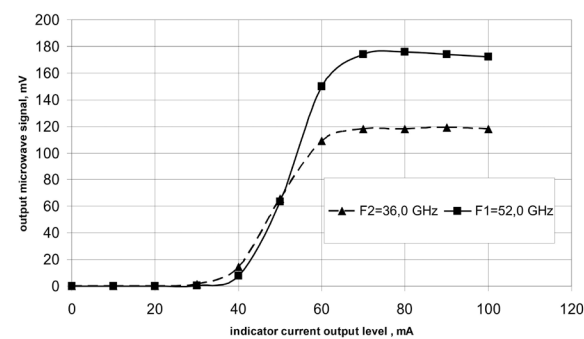


Fig. 2. The linearity level of the measured output microwave signal at a distance of 200 mm from the output waveguide, depending on the readings of the dial gauge of the output level installed on the Г4-141 generator.

changes in the regulator current in the range of 30-70 mA. The measurement accuracy of the microwave signal is from 0.1 to 2.0 mV at various signal amplitudes.

Fig. 3 shows the change in the signal with a linear shift of the receiver along the direction of propagation of the microwave signal by 50 mm relative to the Teflon insert.

The receiver moves towards the emitter relative to a 200 mm long Teflon insert of constant cross-section partially inserted into the output waveguide, see Fig. 1. The frequency of the emitter in two series of measurements was 36.0 and 52.0 GHz, the current set on the output power regulator was 70 mA, which corresponds to the maximum output power, see Fig. 2. The measurement accuracy of the microwave amplitude in this signal series was 0.5-2.0 mV.

It can be seen that the number of periods of stationary microwave waves established in the receiving waveguide is proportional to the frequencies of the initial radiation: the ratio of the initial frequencies $52.0/36.0 = 1.44$ coincides, taking into account the

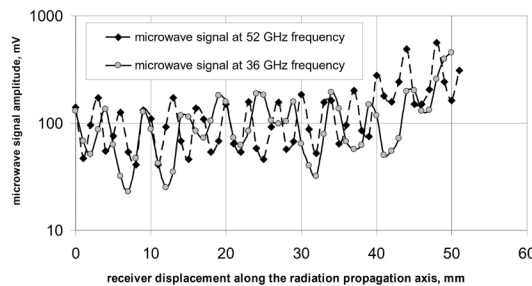


Fig. 3. The structure of standing waves generated in the waveguide connected to the receiver input when the receiver is moved towards the emitter by 0-51 mm. The measurements were carried out at two radiation frequencies of 36.0 and 52.0 GHz.

accuracy of the measurements, with the ratio of the number of periods measured when the receiver is moved to a length of 51 mm $16/11 = 1.45$.

We also measured the number of maxima of a steady-state microwave wave in air in the absence of a dielectric rod. In these measurements, the sensor was moved along the axis of wave propagation at a distance of 70 mm. The frequency range for which the number of maxima in the air is investigated is from 37 to 52 GHz. The results are shown in **Fig. 4**.

The achieved measurement accuracy in this experiment is estimated at 0.4 mm and is displayed on the graph. The microwave radiation power in this series was $2 \cdot 10^{-3}$ W, the distance of the source to the receiver was from 100 to 180 mm.

From the results shown in Fig. 4 it can be seen that a good qualitative and quantitative agreement has been achieved between the calculated and experimentally measured graphs of the change in the microwave wavelengths depending on the frequency.

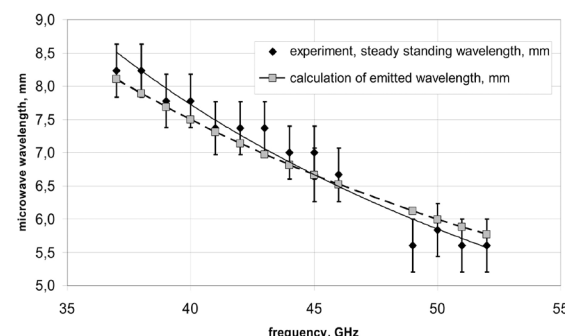


Fig. 4. The lengths of the steady-state microwave wave in the air obtained by counting the number of maxima measured when the receiver is shifted by 70 mm, depending on the frequency of 36-52 GHz. Also, for comparison, the calculated graph of the wavelength emitted by the generator versus frequency is shown.

We plan to compare the results of measurements carried out on the created experimental stand with the calculations of the electromagnetic field for microwave antennas, carried out using programs based on the method of moments. For example, the common programs NEC2 and MININEC3. It is also possible to use a more modern program for modeling MMANA-GAL - this is a program for calculating and analyzing antennas. Any antenna that can be thought of as an arbitrary set of thin wires. The computational basis of the program is MININEC3 (revised and modified for modern means) [32,33]. The possibility of using the electrodynamic modeling and design system HFSS (High Frequency Structure Simulator), IE3D, Microwave Office, Microwave Studio [34,35] will also be studied.

5. CONCLUSION

Let us formulate the main provisions of the ESM, which lead to the localization of the photon and the appearance of new fields in it. According to the ESM, a photon, falling into a medium, or into an external field, acquires mass. Simultaneously with this, its localization takes place. In empty Minkowski space, an infinite plane wave is associated with a photon, which contains components of both electric and magnetic fields. After a photon is exposed to an external influence, it localizes, acquires mass and, in addition to the fields and, it has new field components: a vector field and a scalar field. These 10 fields form a single object, they satisfy the extended system of Maxwell's equations and can transform into each other. Each of them interacts with the environment in its own way and, due to the presence of additional components, they can penetrate such barriers that are inaccessible

to a conventional electromagnetic field. In this case, an important role is played by the fact that photons have mass, and in addition to electromagnetic interaction, there is also a gravitational interaction between photons and the external environment.

The appearance of a nonzero mass in a photon and a simultaneous change in the mass of other particles leads to a change in the picture of their interaction. The developed formalism of the ESM makes it possible to take these changes into account.

The developed setup for measuring the parameters of the microwave field when radiation hits waveguides of variable cross-section or an external field will make it possible to compare the experimental results with the predictions made within the framework of the ESM. The experimental data that we plan to obtain on the created installation will allow us to compare the predictions of the (1+4)D ESM with standard calculations made in the framework of classical calculations carried out in the (1+3)D Minkowski space.

REFERENCES

1. Vladimirov YuS. Prostranstvo-vremya: yavnye i skrytye razmernosti [Space-Time: Explicit and Hidden Dimensions]. Moscow, LIBROKOM Publ., 2010, 208 p.
2. Klein Felix. Über neuere englische Arbeiten zur Gesammelte mathematische Abhandlungen. *Zeitschrift für Mathematik und Physik*, 1901, 46:375.
3. Einstein A. Die Grundlage der allgemeinen Relativitätstheorie. *Annalen der Physik*, 1916, 49:769-822.
4. Klein Oskar. Quantentheorie und fünfdimensionale Relativitätstheorie. *Zeitschrift für Physik*, 1926, 37(12):895-906; doi: 10.1007/BF01397481.

5. Kaluza Th. Zum Unitätsproblem in der Physik. *Sitzungsberichte der Königlich Preussischen Akademie der Wissenschaften*, 1921:966-972.
6. Fock VA. Über die invariante Form der Wellen und der Bewegungsgleichungen für einen geladenen Massenpunkt. *Zeitschrift für Physik*, 1926, 39:226-232.
7. Mandel H. Über den Zusammenhang zwischen der Einsteinischen Theorie des Fern. Parallelismus und der Fünfdimensionalen Fieldtheorie. *Zeitschrift für Physik*, 1926, 39:136-145.
8. Einstein A, Bergmann P. Generalization of Kaluza's Theory of Electricity. *Ann. Math.*, Ser. 2, 1938, 39:683-701.
9. Rumer YuB. *Issledovaniya po pyatimernoy optike* [Studies on five-dimensional optics]. Moscow, URSS Publ., 2010, 152 p.
10. Kraineva IA et.al. *Yuri Borisovich Rumer: Physics, XX century*. Novosibirsk, ARTA Publ., 2013, 592 p.; <https://www.iis.nsk.su/files/book/file/rumer.pdf>.
11. Frankfurt UI (ed.). *Einstein sbornik-1972*. Moscow, Nauka Publ., 1974, p. 15.
12. Rubakov VA. *Klassicheskie kalibrovochnye polya. Bozonnye teorii* [Classical gauge fields. Bosonic theories]. Moscow, URSS Publ., 1999, 336 p.
13. Landau LD. On the "radius" of elementary particles. *Soviet Physics JETP*, 1940, 10:718-722.
14. Tsipenyuk DYu, Andreev VA. Structure of Extended Space. *Bulletin of the Lebedev Physics Institute*, 2000, 6:23-34; arXiv:gr-qc/0106093, 2001; doi: 10.24412/0455-0595-2000-6-23-34.
15. Tcipenyuk DYu, Andreev VA. Elektrodinamika v rasshirennom prostranstve [Electrodynamics in extended space]. *Preprint IOFAN-1999*, No 9, 26 p.; doi: 10.24412/FhITben9-y4 (in Russ.).
16. Andreev VA, Tcipenyuk DYu. Mechanism of the Dark Matter and Condensed Bubble Objects Formation in the Model of Extended Space. *Bulletin of the Lebedev Physics Institute*, 2004, 9:13-25; arXiv:physics/0506002.
17. Andreev VA, Tcipenyuk DYu. The Mass and Size of Photons in the 5-Dimensional Extended Space Model. *Journal of Modern Physics*, 2016, 7:1308-1315; doi: 10.4236/jmp.2016.711116.
18. Andreev VA, Tcipenyuk DYu. Electromagnetic field in the extended space 5-dimensional model, its localization and interaction with waveguide. *RENSIT: Radioelectronics. Nanosystems. Information technologies*, 2019, 11(2):93-102; doi: 10.17725/rensit.2019.11.093.
19. Wesson PS. *Space, Time, Matter: modern Kaluza-Klein theory*. Singapore, World Scientific Publ., 1999, 209. Available: <https://archive.org/details/spacetime matterm000wess>.
20. Wesson PS. *Five-Dimensional Physics. Classical and Quantum Consequences of Kaluza-Klein Cosmology*. Singapore, World Scientific Publ., 2006, 232 p.
21. Wesson PS. *Int. J. Mod. Phys. D*, 2015, 24:1530001.
22. James Overduin, Paul Wesson. Kaluza-Klein Gravity. *Physics Reports*, 1997, 283:303-378.
23. Overduin J, Henry RC. *Physics and the Pythagorean Theorem*. arXiv:2005.10671v2; 2020.
24. Andreev VA, Tcipenyuk DYu. Properties of the 5-Dimensional Extended Space Model with Variable Photons Mass and Size. *New Insights into Physical Science*, 2020, 7(12); doi: 10.9734/bpi/nips/v7.
25. Tcipenyuk DYu. Non-isotropic objects in extended space. *Engineering Physics*,

- 2017, 6:20-26; <http://infiz.tgizd.ru/en/arhiv/16434>.
26. Tsiplenyuk DYu, Belayev WB. Bubble structures in microphysical objects in 5-D extended space model. *RENSIT: Radioelectronics. Nanosystems. Information technologies*, 2019, 11(3):249-260; doi: 10.17725/rensit.2019.11.249.
27. Tsiplenyuk DYu, Belayev WB. Dependence of universe deceleration parameter on cosmological constant: mechanism of vacuum pressure excitation by matter. *Romanian Reports in Physics*, 2020, 72:113; <http://www.rrp.infim.ro/2020/AN72113.pdf>.
28. Tsiplenyuk DY, Belayev WB. Astrophysical and microcosm's applications of 2hv photon gravitational mass. *Indian J Phys*, 2021; doi: 10.1007/s12648-021-02104-2.
29. Voropinov AV, Tsiplenyuk DYu, Shevchenko MA et.al. *LaserPhys. Lett.*, 2021, 18:075301; doi: 10.1088/1612-202X/ac063a.
30. Pshirkov M, Vasilyev V, Postnov K. Fermi bubbles around the M31 galaxy. *EPJ Web of Conferences*, 2016, 125:03010; doi: 10.1051/epjconf/201612503010.
31. Predehl P, Sunyaev RA, Becker W. Detection of large-scale X-ray bubbles in the Milky Way halo. *Nature*, 2020, 588:227-231; doi: 10.1038/s41586-020-2979-0.
32. Description MMANA-GAL program. *Web-site MMANA-GAL, DL2KQ & DL1PBD*; <http://gal-ana.de/basicmm/ru/>.
33. Goncharenko IV. *Antenny KV i UKV. Part 1. Komp'yuternoe modelirovanie. MMANA*. Moscow, IP RadioSoft, Journal "Radio", 2004, 126 p. (in Russ.).
34. *High Frequency Structure Simulation*. Manuals, Agilent, 2000.
35. Sirkeli AI, Drach VE. *Obzor SAPR modelirovaniya SVCH-ustrojstv*.
- Interaktivnaya nauka*, 2017, 1(11):139-141, doi: 10.21661/r-116149 (in Russ.).
36. Andreev VA, Tsiplenyuk DYu. The 5-dimensional Extended space model. Localization of a plane wave and its interaction with a point charged particle. *Pramana-J. Phys*, 2021, in press; <https://www.ias.ac.in/Journals/Pramana%E2%80%93Journal of Physics/>.

DOI: 10.17725/rensit.2021.13.419

Investigation of thin films for fabrication of Nb/AlN/NbN tunnel junctions and microstrip lines of NbTiN-SiO₂-Al

Artem M. Chekushkin, Lyudmila V. Filippenko, Vadim V. Kashin, Mikhail Yu. Fominskiy, Valery P. Koshelets

Kotelnikov Institute of Radioengineering and Electronics of RAS, <http://www.cplire.ru/>
Moscow 125009, Russian Federation

E-mail: chekushkin@hitech.cplire.ru, lyudmila@hitech.cplire.ru, vkashin@cplire.ru, demiurge@hitech.cplire.ru, valery@hitech.cplire.ru

Received November 03, 2021, peer-reviewed November 10, 2021, accepted November 17, 2021

Abstract: The surface of thin films of Nb, Al, NbTiN, SiO₂, Al₂O₃ is investigated in this work. These films are necessary for the fabrication of high-sensitive devices of THz range. The fabrication processes of such devices are described briefly. All films were fabricated using a Kurt J. Lesker magnetron sputtering system. The study of the film surface roughness was carried out using a Bruker Ikon atomic force microscope. The surface quality of films is determined not only deposition mode, but plasma etching process also. The best values of the root-mean-square deviation of the surface profile $R_q = 2 \text{ nm}$ were obtained for the used NbTiN film with a thickness of 325 nm. Thin Al-layers that is used for tunnel barrier formation is studied. It is shown than Al films with a thickness of more than 6 nm are already continuous. The surface roughness of the single-layer and multilayer films has been studied

Keywords: superconductivity, tunnel junctions, magnetron sputtering, thin films, surface roughness

UDC 539.231

Acknowledgements: The study is supported by the Russian Science Foundation (project No. 19-19-00618). The equipment of USU "Cryointegral" was used to carry out the research; USU is supported by a grant from the Ministry of Science and Higher Education of the Russian Federation, agreement No. 075-15-2021-667. We thank S. Kraevsky (Carl Zeiss, Moscow, Russia) for performing AFM imaging.

For citation: Artem M. Chekushkin, Lyudmila V. Filippenko, Vadim V. Kashin, Mikhail Yu. Fominskiy, Valery P. Koshelets. Investigation of thin films for fabrication of Nb/AlN/NbN tunnel junctions and microstrip lines of NbTiN-SiO₂-Al. *RENSIT: Radioelectronics. Nanosystems. Information technologies*, 2021, 13(4):419-426. DOI: 10.17725/rensit.2021.13.419.

CONTENTS

- 1. INTRODUCTION (419)
- 2. FABRICATION TECHNOLOGY OF SIS JUNCTIOS (420)
- 3. INVESTIGATION OF FILMS SURFACE (421)
- 4. CONCLUSION (425)
- REFERENCES (425)

1. INTRODUCTION

It is important to know and control the parameters of the thin films used for fabrication of receiving structures for the terahertz (THz) range. Thin films of the needed parameters (surface roughness, resistivity, critical temperature) are required for the microstrip lines and for the superconductor-insulator-

superconductor (SIS) Josephson junction. Nb and NbN are used as superconductors for SIS-junctions: Nb-AlO_x-Nb with a limiting frequency of 700 GHz and Nb-AlN-NbN with a limiting frequency of 1.4 THz [1,2]. NbTiN and Al are used as electrodes for the microstrip line and SiO₂ as dielectric.

Niobium-based tunnel SIS-junctions are the main elements for fabrication of high-sensitive detectors for radio astronomy tasks [3,4]. The surface quality of the films used to make devices directly affects their properties. For example, in [5], it was demonstrated that an NbTiN film with a more developed crystal structure (the film roughness is determined by larger crystallites) also has a lower Tc and a higher resistivity, which negatively affects on the operation of the device at high frequencies (more than 1 THz). This article is a continuing work on optimisation of fabrication of thin films for superconducting devices [5] and is aimed to determining the quality of their surface.

2. FABRICATION TECHNOLOGY OF SIS JUNCTIONS

All structures are formed on two types of substrates: high-ohmic polished silicon or quartz. The latter is necessary to achieve the best parameters for waveguide SIS-structures since it's dielectric constant is significantly less than that of silicon. Quartz with a thickness of 200 μm after sample preparation is polished to a thickness of about 40 μm for receiving structures with an operating frequency of 1 THz. A 100 nm thick Al₂O₃ layer is deposited onto the selected substrate over the entire surface. This buffer layer acts as a stop-layer in the

subsequent etching of NbTiN in fluorinated gases and avoids etching of the substrate. All films were deposited by magnetron sputtering.

The first layer of the working structure is a bottom electrode from NbTiN 325 nm thick. This thickness is due to the London penetration depth in this material [6]. The NbTiN layer is sputtered over the entire area of the substrate, and then etched over a resistive mask using plasma-chemical etching in tetrafluoromethane (CF₄). The same etching process is used for the Nb and NbN etching. The etching process provides a flat electrode edge, in contrast to the «lift-off» lithography technology, which, under conditions of magnetron sputtering and at similar thicknesses, can leave “walls” of metal along the edges. In addition, this layer is the lower layer of the NbTiN-SiO₂-Al microstrip line, in which high-frequency currents flow. Since the penetration depth of the field is large, inhomogeneities of the order of 10 nm are not very important. For aluminum, which is the upper electrode of the microstrip line, currents flow along the lower surface; therefore, the upper film roughness is also not important.

The next step in fabrication is deposition of three-layer Nb-AlN-NbN (80 nm-7 nm-80 nm) structure over the entire area of the substrate and etching over a resistive mask right through to the NbTiN layer. As a result, “columns” of a three-layer structure are formed on the surface of the lower electrode, which are SIS junctions. The area of the tunnel junction can be from 0.5 to 40 μm^2 , which is determined by the tasks. At this step, it is important to stop the etching of the bottom layer in the three-layer structure

(Nb) in time to avoid etching of the NbTiN layer. After that the process of anodisation in a solution of ammonium tetraborate with glycol is happens. It's necessary to protect the sides of the SIS-junctions and surface of NbTiN from the short connection with upper electrode. The same resistive mask is used to deposit an insulator layer 250 nm thick, which is necessary both as a dielectric layer in a microstrip line and as an insulating layer from the shorts between the SIS junction and the upper electrode. The upper electrode is formed from a 450 nm thick aluminum layer.

3. INVESTIGATION OF FILMS SURFACE

The morphological analysis has been carried out through a Bruker Dimension Icon AFM, equipped with a Nanoscope V controller operated in PeakForce Tapping® mode. The measurements have been performed using N-doped Si probes (Bruker Scanasyst-air).

The main parameters in determining the film roughness are the arithmetic mean deviation of the surface profile R_a and standard deviation of the surface profile R_q .

The surface roughness of a thin film depends significantly on the quality of the surface and the material on which it is deposited. We investigated the surface of Al₂O₃ 100 nm thick, deposited with an RF magnetron on a silicon substrate. For this film $R_q = 1.02$ nm, $R_a = 0.8$ nm were obtained. The AFM image is shown in **Fig. 1**. For comparison, for the surface of optical quartz polished by the mechanical-chemical method $R_a = 0.2$ nm [7].

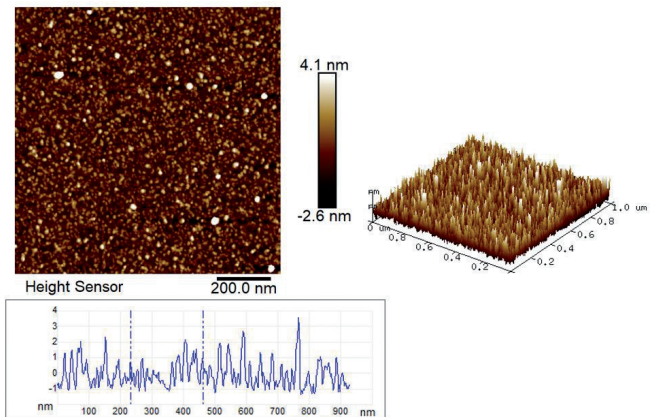


Fig. 1. AFM images of an 100 nm Al₂O₃ film. Scanning area 1×1 μm^2 . At the top left is a 2D scan view, at the top right it is in 3D, at the bottom is a cross-section in the center of the scan.

A 325 nm thick NbTiN layer was deposited on a silicon substrate. For the scan area 90×90 μm^2 $R_q = 2$ nm, $R_a = 1.3$ nm were obtained. For the same sample $R_q = 2.24$ nm, $R_a = 1.81$ nm were obtained for the scan area 4 μm^2 . The scan profile is shown in **Fig. 2**.

The NbTiN surface was also monitored after plasma chemical etching procedures. A sample was prepared, on which an 80 nm thick Nb layer was deposited, and

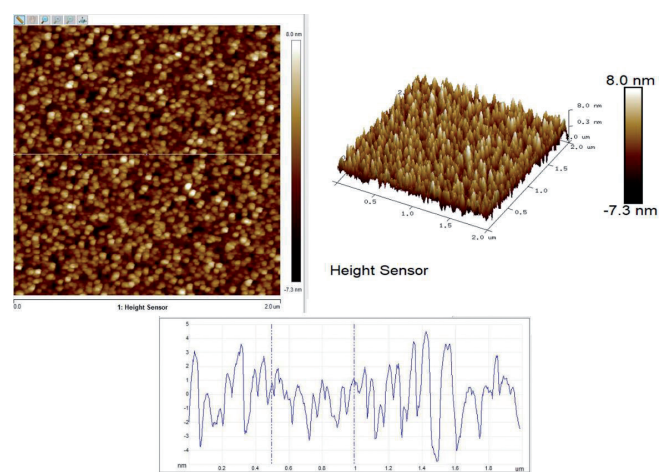


Fig. 2. AFM images of NbTiN with a thickness of 325 nm. Scanning area 1×1 μm^2 . At the top left is a 2D scan view, at the top right it is in 3D, at the bottom is a cross-section in the center of the scan.

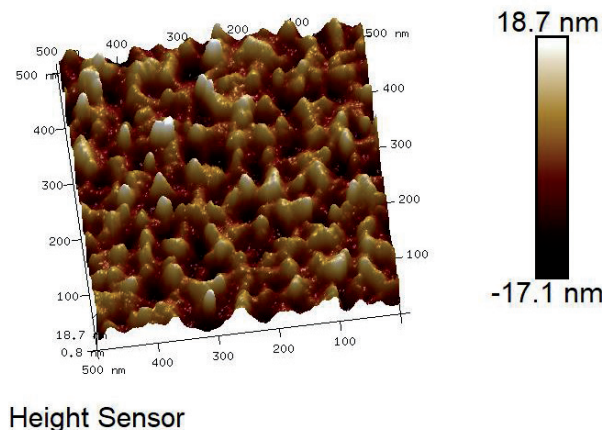


Fig. 3. Surface of NbTiN after Nb etching. Scanning area is $0.5 \times 0.5 \mu\text{m}^2$.

then etched into CF_4 . **Fig. 3** shows the NbTiN surface after etching the Nb layer. We note that the film roughness became significantly higher: $R_q = 5.2 \text{ nm}$, $R_a = 4.14 \text{ nm}$.

The NbTiN surface was also studied after etching the Nb/AlN/NbN structure. For the scan area $10 \times 10 \mu\text{m}^2$ $R_q = 11.6 \text{ nm}$, $R_a = 8.2 \text{ nm}$ were obtained (see **Fig. 4**). We conclude that the NbTiN surface is significantly damaged by etching through the overlying layers, which may be associated with anisotropic etching of the material. We are planning to use a thin Al layer (up to 5 nm)

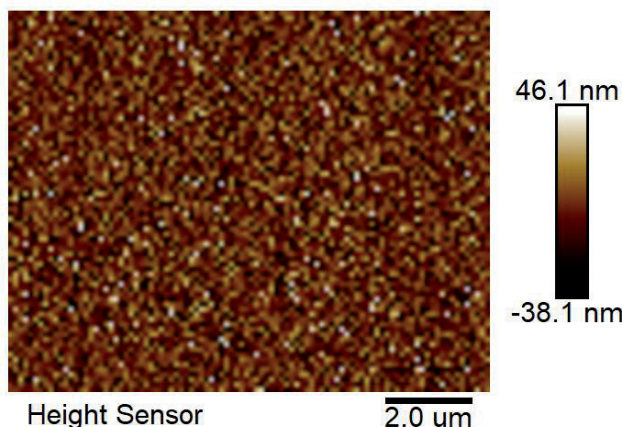


Fig. 4. NbTiN surface after Nb/AlN/NbN etching. Scanning window area $10 \times 10 \mu\text{m}^2$.

as a stop layer to prevent etching of NbTiN in fluorine-containing gases in further studies. In addition, there is information in the literature that the Al layer can wet the NbTiN or Nb layer, which will reduce the surface roughness [8].

According to the technological map, the Nb layer is deposited on top of the NbTiN layer. The fabrication of this layer on a magnetron sputtering system is possible using both a DC magnetron and an RF magnetron. It was shown in [9,10] that in the case of using a DC magnetron, the surface of the films is smoother, which is better suited for fabrication of high quality Josephson junctions. In this work, the roughness of an Nb film with a thickness of 200 nm deposited on a silicon substrate was investigated, as well as the roughness of an Nb film with a thickness of 80 nm deposited over the NbTiN layer. For the first case, the values $R_q = 0.78 \text{ nm}$ and $R_a = 0.62 \text{ nm}$ were obtained. The AFM images (2D and 3D) are shown in **Fig. 5**. In the second case, R_q and R_a were 1.86 nm and 1.48 nm on a scan area of $1 \mu\text{m}^2$ (see **Fig. 6**). The surface roughness of Nb film deposited on top of the NbTiN layer has better R_q and R_a values in comparison with the roughness of the NbTiN film.

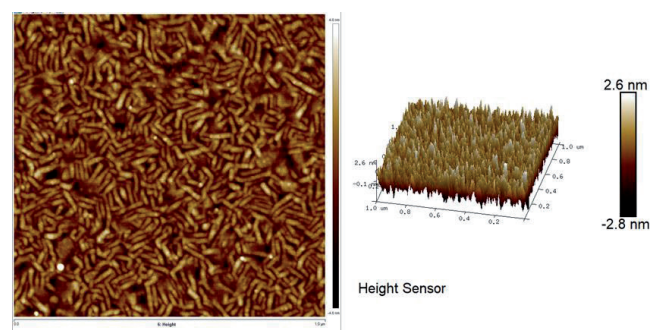


Fig. 5. Nb 200 nm thick, scan area is $1 \times 1 \mu\text{m}^2$ and its 3D image.

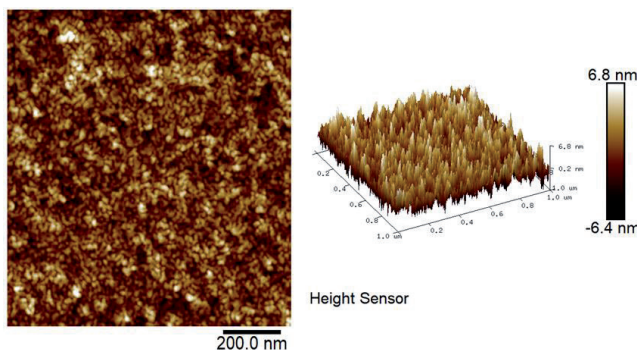


Fig. 6. Nb 80 nm thick, scan area is $1 \times 1 \mu\text{m}^2$ and its 3D image.

We studied thin Al films with a thickness of 3 nm, 6 nm, 20 nm, 124 nm, deposited on a silicon substrate with a buffer layer of 100 nm Al₂O₃. Thin films with thicknesses of 3, 6 and 20 nm is sputtered with a low deposition rate (0.2 nm/s) and with a reduced power supplied to the magnetron (300 W), thicker Al films sputter at a magnetron power of 500 W, the deposition rate is 1 nm/s.

Typical thickness of the barrier layer in the SIS junction is 1-1.5 nm, and its formation occurs in the vacuum chamber without breaking the vacuum between the superconducting layers. In these conditions we can't studied surface of AlO_x or AlN directly because additional oxidation occurs at the atmospheric pressure. First, a thin layer of Al 5-7 nm is deposited [8,11], then either oxidation in an oxygen atmosphere at a characteristic pressure of 10^{-1} mbar, or nitridisation in a high-frequency nitrogen plasma (pressure $6 \cdot 10^{-3}$ mbar, power 75 W). **Fig. 7** shows a AFM image of $1 \times 1 \mu\text{m}^2$ of an Al film with a thickness of 3 nm. For this film vertical peak-to-peak distance is 3 nm. It means that this film has island structure. In this case $R_q = 0.9 \text{ nm}$, $R_a = 0.75 \text{ nm}$, but we should keep in mind that due to island

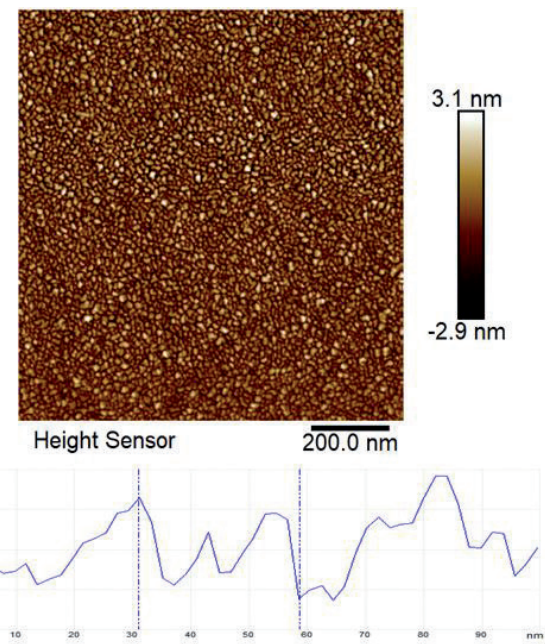


Fig. 7. Al film, 3 nm thick and its cross section, scan area is $1 \times 1 \mu\text{m}^2$.

structure this film repeats the relief of the lower layer-Al₂O₃.

The AFM image of a 6 nm Al film is shown in **Fig. 8**. Here, as in the 3 nm Al

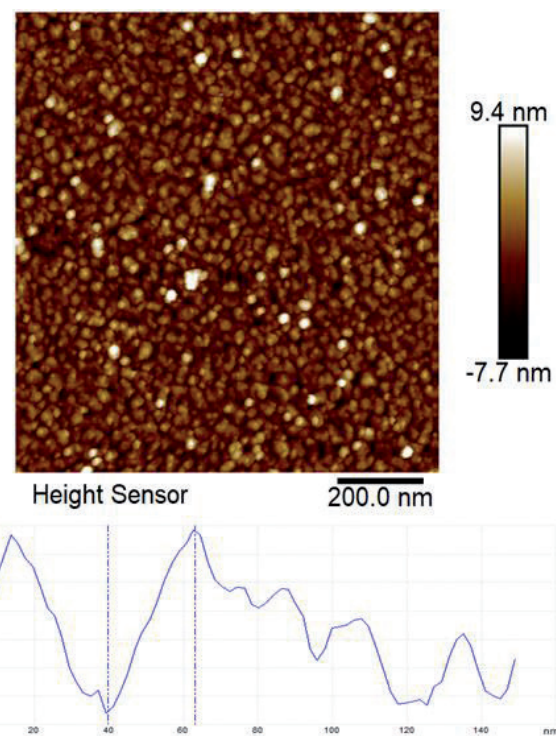


Fig. 8. Al film, 6 nm thick and its cross section, scan area is $1 \times 1 \mu\text{m}^2$.

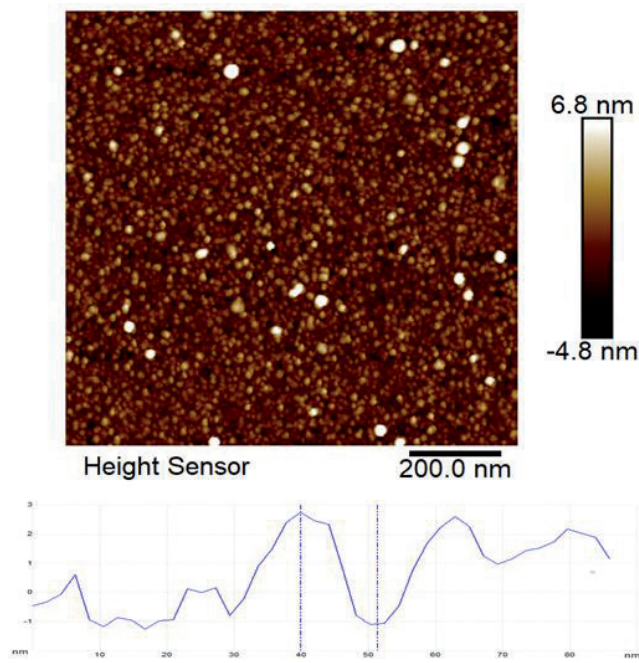


Fig. 9. *Al film, 20 nm thick and its cross section, scan area is $1 \times 1 \mu\text{m}^2$.*

film, it can be seen that the distance between the peaks reaches 6 nm, but the film grains are already much larger. For this film the values $R_q = 2.3 \text{ nm}$ and $R_a = 1.7 \text{ nm}$ were obtained.

The AFM image of a 20 nm thick Al film is shown in **Fig. 9**. The maximum peak-to-peak vertical distance for this film is 4 nm, $R_q = 1.5 \text{ nm}$ and $R_a = 1.1 \text{ nm}$, that is less than for 6 nm films. It means that this film has already continuous.

Aluminum films deposited at higher speeds and thicknesses have significantly greater roughness. For Al with a thickness of 124 nm on a silicon substrate covered by a 100 nm Al_2O_3 film $R_q = 2.57 \text{ nm}$, $R_a = 2 \text{ nm}$ (**Fig. 10**, top), but if we take into account a strong feature that can manifest itself at large thicknesses, then $R_q = 4.5 \text{ nm}$, $R_a = 3 \text{ nm}$ (Fig. 10 bottom).

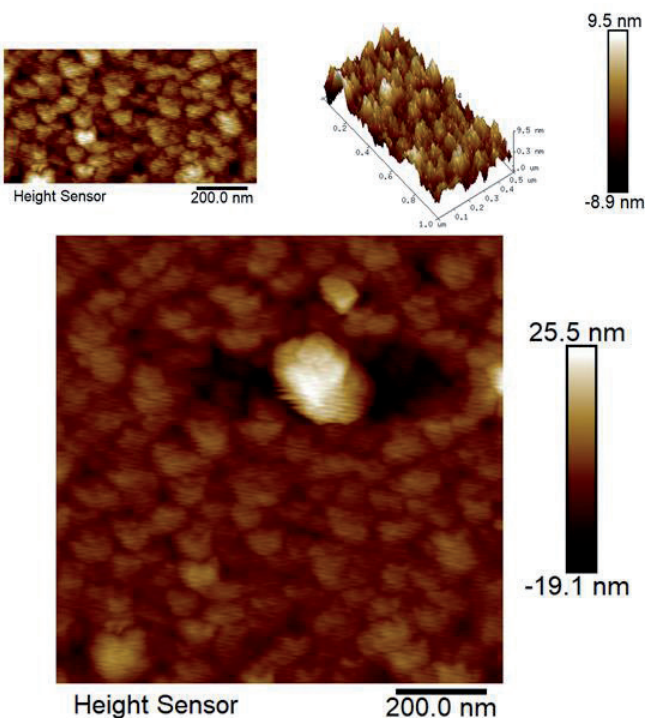


Fig. 10. *Al, thickness 124 nm. Top: scan area with a uniform surface, bottom - with a feature that appears periodically throughout the film.*

We studied the SiO_2 surface, deposited after etching a three-layer structure, on top of the NbTiN layer: $R_q = 4.0 \text{ nm}$, $R_a = 3.0 \text{ nm}$, which is better than the NbTiN surface after etching. The scan result is shown in **Fig. 11**.

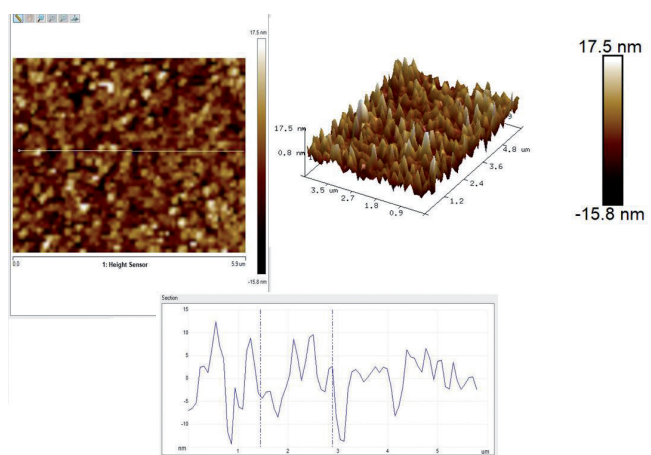


Fig. 11. *Scan $6 \times 6 \mu\text{m}^2$ of SiO_2 surface deposited on top of NbTiN. On the top left is a 2D view, on the right it is in 3D, below is a cross-section.*

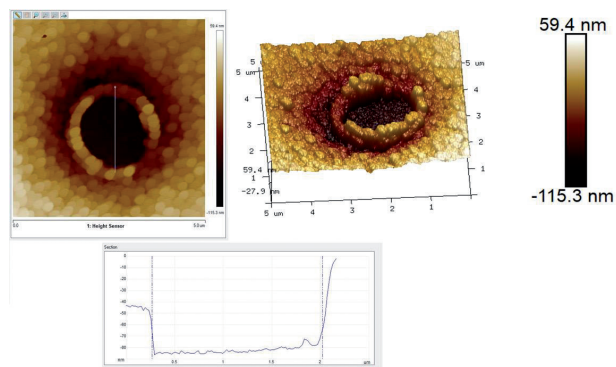


Fig. 12. SiO_2 surface and SIS junction. Scanning window size $5 \times 5 \mu\text{m}^2$. Top left view in 2D, top right it is in 3D, bottom cross-section along the SIS-junction.

We also studied the SiO_2 surface directly near the formed SIS junctions: the diameter of junction is $1.8 \mu\text{m}$, the characteristic size of the SiO_2 granules is 250 nm (Fig. 12).

4. CONCLUSION

Atomic force microscopy was used to study surface roughness of films: Al, Nb, NbTiN, SiO_2 , Al_2O_3 , which are necessary to fabricate devices that operate in the terahertz range. The measured values of R_q and R_a show that the surfaces of these films are suitable for further work on the fabrication of SIS junctions. It is noticed that the NbTiN surface strongly depends on the subsequent technological operations, namely, on the plasma-chemical etching. It is proposed for further work to use a thin aluminum layer, which should prevent the etching of NbTiN after etching of Nb. It is demonstrated that the required thickness for the formation of a continuous Al film is more than 6 nm .

REFERENCES

1. Jackson BD, de Lange G, Zijlstra T, Kroug M, Klapwijk TM, Stern JA, Klapwijk TM. Low-noise 0.8-0.96- and 0.96-1.12-THz superconductor-insulator-superconductor mixers for the Herschel Space Observatory. *IEEE transactions on microwave theory and techniques*, 2006, 54(2):547-558.

2. Jackson BD, de Lange G, Zijlstra T, Kroug M, Kooi JW, Stern JA, Klapwijk TM. Low-noise 0.8-0.96- and 0.96-1.12-THz superconductor-insulator-superconductor mixers for the Herschel Space Observatory. *IEEE transactions on microwave theory and techniques*, 2006, 54(2):547-558.
3. Kerr AR, Pan SK, Claude SM, Dindo P, Lichtenberger AW, Effland JE, Lauria EF. Development of the ALMA band-3 and band-6 sideband-separating SIS mixers. *IEEE Transactions on Terahertz Science and Technology*, 2014, 4(2):201-212.
4. Baryshev AM, Hesper R, Mena FP, Klapwijk TM, Van Kempen TA, Hogerheijde MR, Jackson BD, Adema J, Gerlofsma GJ, Bekema ME, Barkhof J, de Haan-Stijkel LHR, van dem Bemt M, Koops A, Keizer K, Pieters C, van het Jagt JK, Schaeffer HHA, Zijlstra T, Kroug M, Lodewijk CFJ, Wielinga K, Boland W, de Graauw MWM, van Dishoeck EF, Jager H, Wild W. The ALMA Band 9 receiver-Design, construction, characterization, and first light. *Astronomy & Astrophysics*, 2015, 577:A129.
5. Chekushkin AM, Filippenko LV, Lomov AA, Liu Dong, Sheng-Cai Shi, Koshelets VP. Optimizatsiya protsessov izgotovleniya plenok Nb, NbN, NbTiN i vysokokachestvennykh tunnel'nykh perekhodov dlya priyemnykh struktur teragertsovogo diapazona [Optimization of the production processes of Nb, NbN, NbTiN and high-quality tunnel junctions for receiving structures in the terahertz range]. In: *Nanostructured materials and nanosystems: physical and chemical properties and applications*. Naukova Dumka, Kyiv, 2015. pp. 11-20.

- of fabrication processes for Nb, NbN, NbTiN films and high-quality tunnel junctions for terahertz receiving circuits]. *ZhTF*, 2021, 91(10):1577-1582 (in Russ).
6. Lap BNR, Khudchenko A, Hesper R, Rudakov KI, Dmitriev PN, Khan F, Koshelets VP, Baryshev AM. Characterization of superconducting NbTiN films using a dispersive Fourier transform spectrometer. *Applied Physics Letters*, 2021, 119(15):152601.
 7. Bo D, Jianwei Z, Yuling L, Mingbin S, Yufeng Z. Surface roughness of optical quartz substrate by chemical mechanical polishing. *Journal of Semiconductors*, 2014, 35(11):116001.
 8. Imamura T, Hasuo S. Fabrication of high quality Nb/AlO_x/Al/Nb Josephson junctions. II. Deposition of thin Al layers on Nb films. *IEEE Transactions on applied superconductivity*, 1992, 2(2):84-94.
 9. Imamura T, Shiota T, Hasuo S. Fabrication of high quality Nb/AlO_x/Al/Nb Josephson junctions. I. Sputtered Nb films for junction electrodes. *IEEE Transactions on applied superconductivity*, 1992, 2(1):1-14.
 10. Gurvitch M, Washington MA, Huggins HA. High quality refractory Josephson tunnel junctions utilizing thin aluminum layers. *Applied Physics Letters*, 1983, 42(5):472-474.
 11. Rowell JM, Gurvitch M, Geerk J. Modification of tunneling barriers on Nb by a few monolayers of Al. *Physical Review B*, 1981, 24(4):2278.

DOI: 10.17725/rensit.2021.13.427

Using Additive Technologies to Create Broadband Antennas with Fractal Geometry

Andrey V. Smirnov, Alexander S. Fionov, Ilia A. Gorbachev, Elizaveta S. Shamsutdinova, Iren E. Kuznetsova, Vladimir V. Kolesov

Kotelnikov Institute of Radioelectronics and Electronics of RAS, <http://www.cplire.ru/>
Moscow 125009, Russian Federation

E-mail: andre-smirnov-v@yandex.ru, fionov@cplire.ru, iliyagor36@gmail.com, shes1996@bk.ru,
kuziren@yandex.ru, kvv@cplire.ru

Received November 24, 2021, peer-reviewed November 30, 2021, accepted December 06, 2021

Abstract: The paper presents the results of a study of the frequency dependence of the S_{11} parameters of antenna samples with fractal geometry, created using 3D printing technology, followed by the deposition of a conductive copper coating by galvanization. It is shown that changing the dimension of the fractal at different iterations, shifting and dividing the resonant frequencies, it is possible to flexibly form the working bands of antennas in any frequency range and any width. The developed designs can be used to create broadband rectennas.

Keywords: fractal, fractal dimension, additive technologies, rectenna

UDC 621.396.67

Acknowledgments: Work was partially supported by the Ministry of Science and Higher Education of the Russian Federation (State Order # 0030-2019-0016), supported by the Council for Grants of the President of the Russian Federation (Project No. MK-1503.2020.8) and the Russian Foundation for Basic Research (Project No. 18-29-23042 MK).

For citation: Andrey V. Smirnov, Alexander S. Fionov, Ilia A. Gorbachev, Elizaveta S. Shamsutdinova, Iren E. Kuznetsova, Vladimir V. Kolesov. Using Additive Technologies to Create Broadband Antennas with Fractal Geometry. *RENSIT: Radioelectronics. Nanosystems. Information technologies*, 2021, 13(4):427-434. DOI: 10.17725/rensit.2021.13.427.

CONTENTS

- 1. INTRODUCTION (427)**
- 2. EXPERIMENTAL TECHNIQUE (429)**
- 3. RESULTS AND DISCUSSION (431)**
- 4. CONCLUSION (434)**

REFERENCES (434)

1. INTRODUCTION

Since obtaining a patent for the first photopolymer printer in 1986, additive printing (or 3D printing) technology has evolved significantly. Over the past 5-7 years, a large number of affordable

commercial products have appeared on the 3D technology market. This is due to a significant reduction in the cost of technology and the emergence of its various variations. One of the important advantages of the technology is the ability to create parts of complex geometric shapes in one technological cycle, without the manufacture of additional equipment. 3D printing can significantly increase the flexibility of production and has already proven itself for the manufacture of not only instrument cases, but also for the creation of functional

parts of electronics, microwave circuits and antennas [1-3].

However, the suitability of the technology for creating broadband antennas requires further research. In the case of antennas, the material must have good conductive properties. Existing samples of conductive plastics used for 3D printing do not have them. Therefore, to create experimental samples of antennas using additive technologies, it is necessary to create a conductive coating. Surface metallization can be carried out by various methods: vacuum deposition (magnetron, cathode-arc), electroplating, conductive paint. Vacuum spraying allows to obtain a uniform dense metal coating, however, in the case of parts with complex shapes, it has a disadvantage in the form of a shadow effect. Conductive paint does not have good electrical conductivity, so a promising option is the use of galvanization technology [4,5].

In the modern world, the concept of wireless sensor systems is rapidly developing, consisting of hundreds and thousands of miniature autonomous sensor elements. One of the options for providing such elements with electricity are systems for collecting background electromagnetic energy based on rectennas [6-8]. The main criterion applicable to such rectennas is a wide frequency range of operation. Thanks to which a sufficient level of energy is provided, despite its low density at one, specific frequency. The criterion of wide-range is met by rectennas, which are based on the elements of fractals.

Unlike traditional methods, when smooth dipole antennas are synthesized, the theory of synthesis of fractal antennas

is based on the idea of realizing the characteristics of radiation with a repeating structure on arbitrary scales [9]. This makes it possible to create new regimes in fractal electrodynamics. The complex structure of fractal antennas provides such extremely important properties as broadband and multi-band [10].

The principle of constructing a common H-fractal begins with a figure in the form of the letter H, in which the vertical and horizontal segments are equal. Then, to each of the 4 ends of the figure, a copy of it, reduced in half, is attached. To each end (there are already 16 of them) is attached a copy of the letter H, already reduced by 4 times. Etc. In the limit, a fractal will turn out, which visually almost fills a certain square. In it, the H-fractal is dense everywhere. That is, in any neighborhood of any point of the square, there are fractal points. The H-fractal completely fills its square (space-filling curve). Therefore, its fractal dimension is equal to 2 [11]. The total length of all segments in an ideal fractal structure is infinite. In antenna technology, tree structures of the H-fractal type are used if it is necessary that a large number of elements in a complex circuit receive the same signal at the same time.

Placed at the end of a whip antenna, the tree-like elements increase the bandwidth and somewhat shorten the antenna at a constant frequency due to the length of their branches. The main advantage of the H-tree is its ability to efficiently fill the space. This property manifests itself in both two-dimensional and three-dimensional versions.

In this paper, we consider the process of creating rectennas based on the

geometric fractal H-tree by 3D printing on a photopolymer printer, followed by the application of a conductive copper coating by galvanization.

2. EXPERIMENTAL TECHNIQUE

In Fig. 1a shows the basic structures used to build 3D models. In Fig. 1b shows images of modeled tree-like rectennas used to create 3D models. Antenna mock-ups were created using SLA technology (laser stereolithography) on an Anycubic photon S photopolymer 3D printer with a UV source with a wavelength of 405 nm. The print resolution was 50 μm in the xy plane

and 10 μm in the z axis. Photopolymer resin Anycubic Gray 405 nm UV Resin was used. The photopolymerization of the resin was carried out in layers, the thickness of one layer was 50 μm , the exposure time was 110 s for the first 5 layers and 10 seconds for the subsequent ones. At the end of the formation process, the model was separated from the metal table, washed in a solution of a mixture of acetone (puriss.) and isopropyl alcohol (puriss.) with a component ratio of 1:1 by weight. Then it was placed in a UV camera for 3 hours for additional polymerization under the influence of UV radiation with a wavelength of 405 nm.

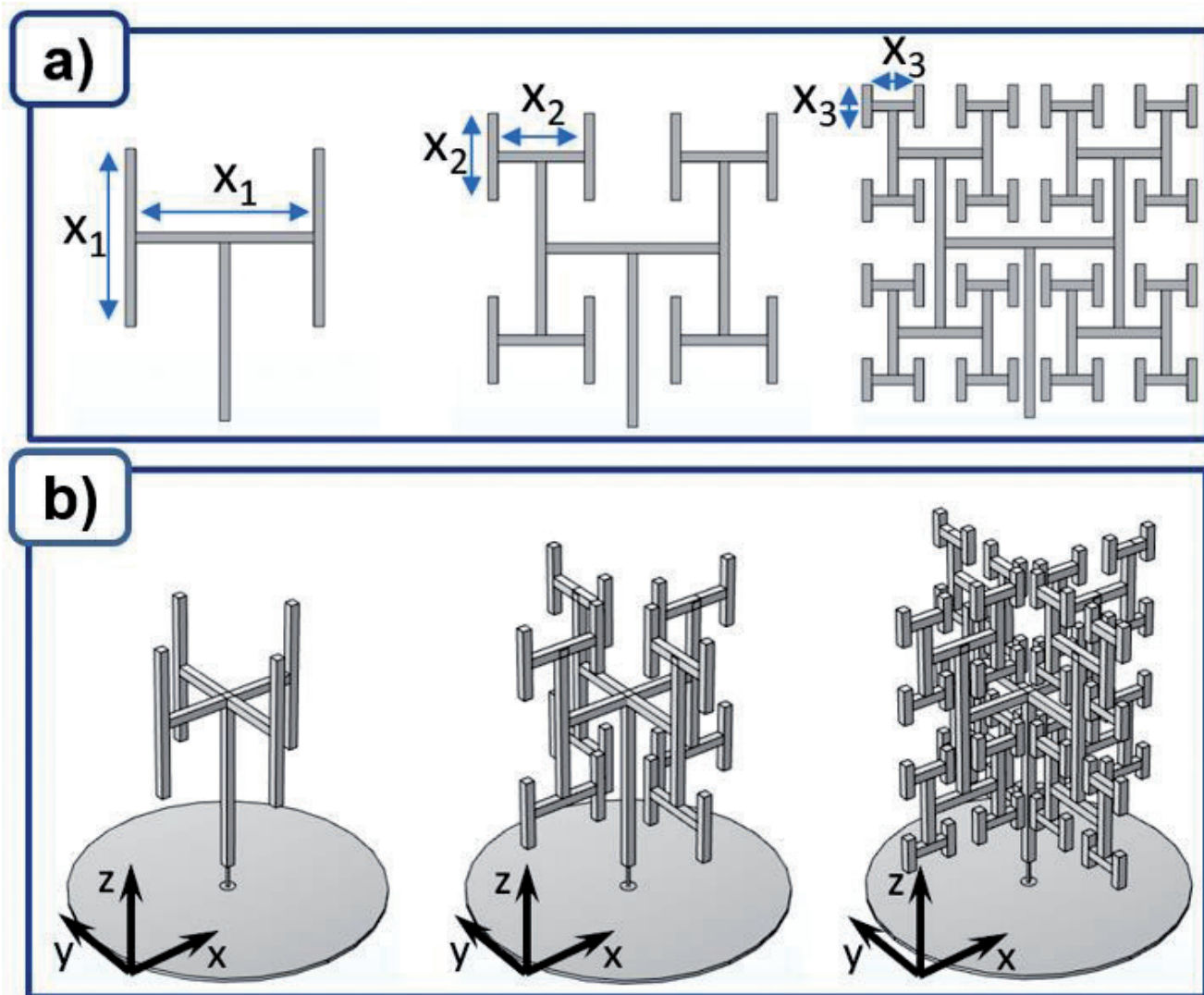


Fig. 1. Image: (a) the basic structure underlying the antenna ($x_1 = 40 \text{ mm}$, $x_2 = 20 \text{ mm}$, $x_3 = 10 \text{ mm}$); (b) models used for radiation pattern modeling and 3D printing.

In Fig. 2a shows photographs of samples of tree rectennas obtained as a result of 3D printing.

The antenna was coated with a conductive copper coating by the classical galvanization method. For this, the antenna surface was preliminarily coated with a conductive graphite varnish (Solins GRAPHITE). To prepare the electrolyte solution, 1 L of pure distilled water, 180 g of copper sulfate (pure), 25 g of sulfuric acid, and 10 ml of ethyl alcohol (pure) were taken. The anode was a 3 mm thick copper plate located along the perimeter of the

container with the electrolyte; the cathode was a model placed in the center of the container. The current density was 0.15 A/dm² at the first stage – the formation of a conductive layer on the entire surface of the model (6 hours) and 0.5 A/dm² at the second stage – increasing the thickness over the entire surface of the model (20 hours).

The construction of radiation patterns corresponding to the field strength in the far zone for the models considered in this work was carried out by modeling by the finite element method.

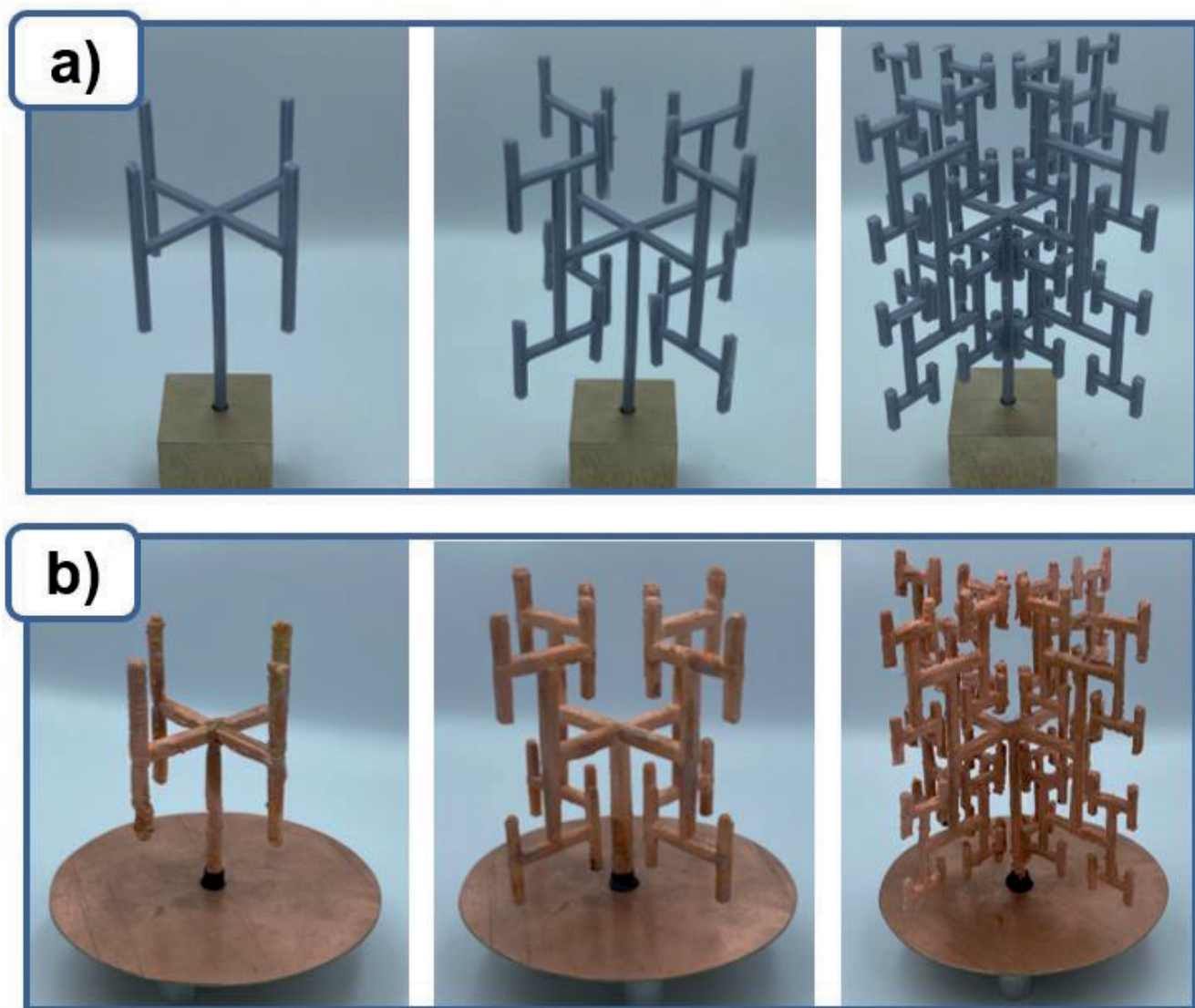


Fig. 2. Photos: (a) 3D models obtained as a result of printing; (b) collected experimental antenna samples, after copper plating by galvanization.

The frequency dependences of the reflection coefficient (parameter S_{11}) in the coaxial transmission line loaded on the antenna were investigated.

The measurements were carried out in two types of transmission lines:

- N-type, using a Tektronix 506 A vector network analyzer (VNA), frequency range 1...6 GHz;

- K-type, using Anritsu vector network analyzer (VNA), frequency range 1...30 GHz.

These types of transmission lines have a characteristic impedance of 50Ω and differ in the size of the coaxial line, the type of connectors (N-type and K-type, respectively) and broadband – the limiting upper operating frequency, at which acceptable matching parameters are still maintained (11 GHz for the N-type transmission line and 45 GHz for K-type transmission line). An increase in the limiting frequency is achieved by using a smaller coaxial line [12].

The measurement process included the calibration of the analyzer in the used frequency range, the connection of the investigated object to the measurement

transmission line, and the recording of the frequency response of the S_{11} parameter.

The obtained frequency characteristics are shown in **Fig. 3** (VNA Tektronix, N-type transmission line) and **Fig. 5** (VNA Anritsu, K-type transmission line).

3. RESULTS AND DISCUSSION

In different regions of the frequency range, the structure of a fractal antenna works simultaneously both as a single conductor and as a set of smaller conductors. If the signal is transmitted and received at the lower frequency of the range, then the entire structure is involved. If higher frequencies are used, then smaller structural elements corresponding to shorter wavelengths are used. The number of resonances increases with the number of fractal iterations.

The broadband of fractal antennas is ensured by the fact that their structure works simultaneously both as a whole and as a set of smaller antennas. The larger the number of fractal iterations, the finer structures the antenna will contain, and the higher in frequency the resonances will be. However, with

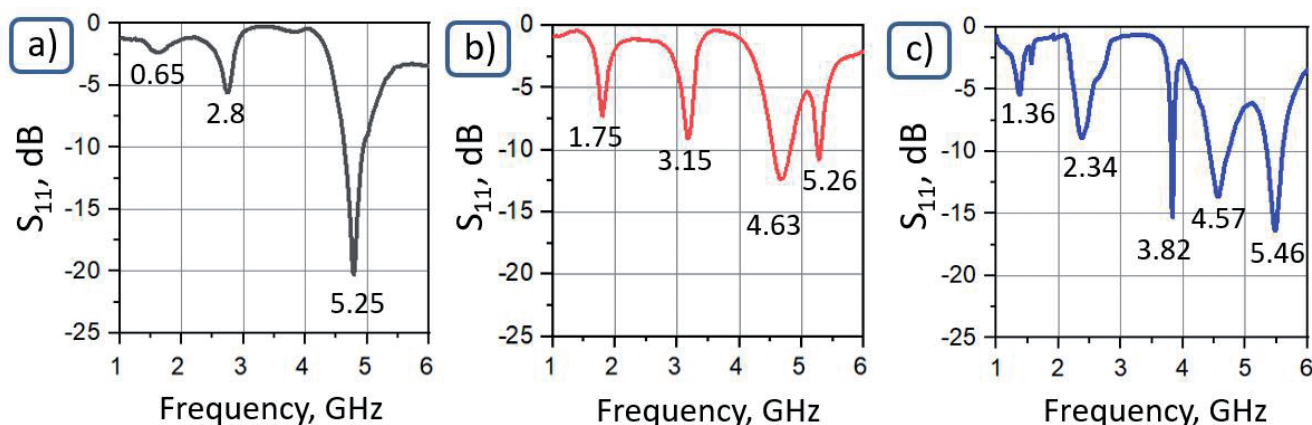


Fig. 3. Frequency dependence S_{11} of the parameters of antennas with different iterations in the range of 1-40 GHz in the N-type transmission line a) 1; b) 2; c) 3.

an increase in iterations, the effective length of the antenna decreases, the antenna sections are moved to another plane of polarization and often form

countercurrents, which reduces the gain at each specific frequency.

In **Fig. 4** show the radiation patterns for tree-like fractal antennas of 3 iterations

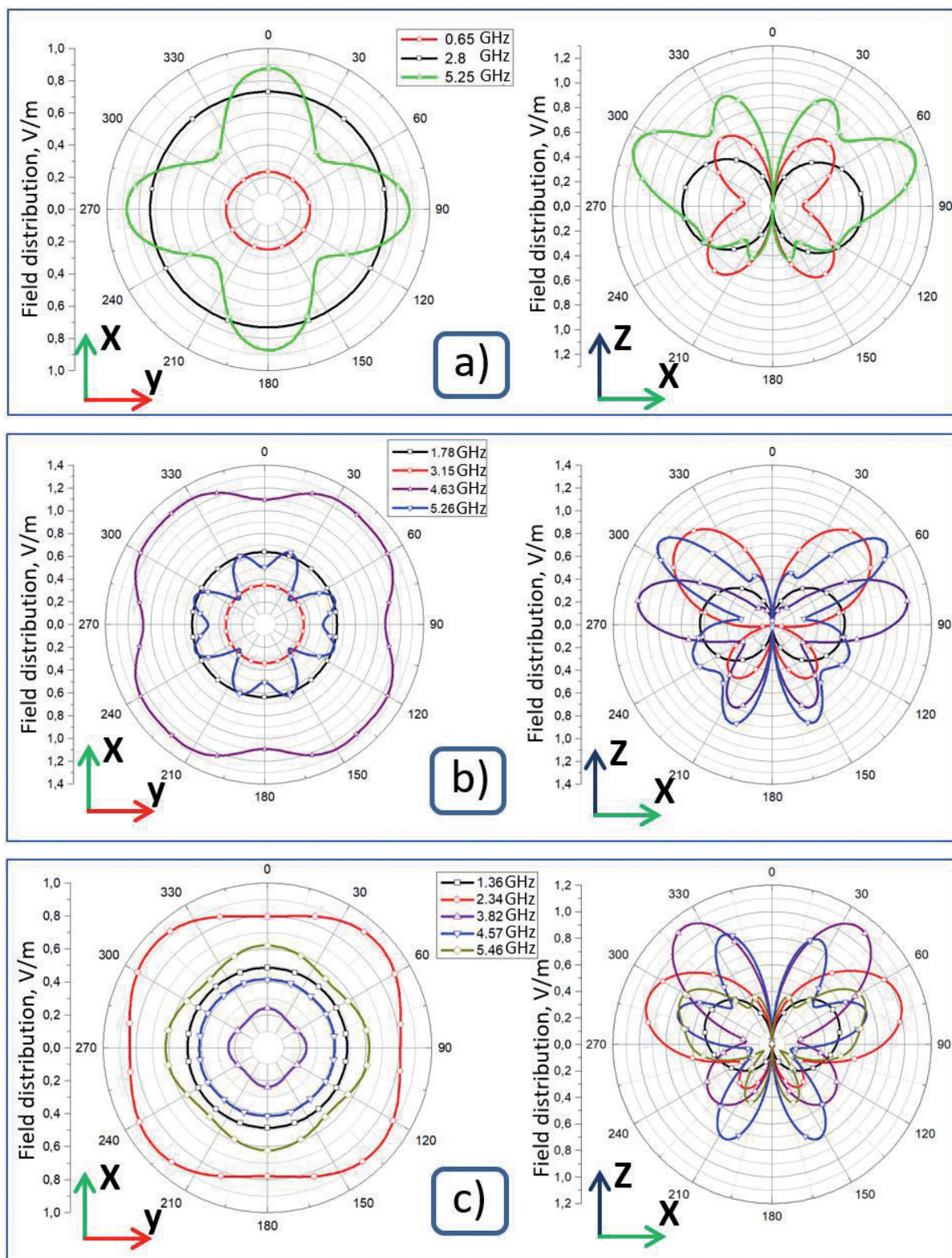


Fig. 4. Antenna radiation patterns corresponding to the field strength in the far-field with iteration a) 1, b) 2 and c) 3.

based on the 3D model of the H-fractal in different planes and in different frequency ranges.

The radiation pattern of any fractal antenna will be frequency dependent, since at different frequencies, different parts of the structure will resonate; when the frequency changes, the phase of the signal and the strength of the current flowing through these structures will change. It can be seen from the figures that the antenna

directivity pattern in the horizontal plane is uniform at almost all frequency ranges, which ensures signal reception from all directions.

The low-frequency (1 ... 6 GHz) region is characterized by a set of high-quality peaks, the number of which increases with an increase in the iteration order of the fractal structure. The intensity of the peaks in absolute value does not exceed 20 dB. This pattern is seen on both VNA Tektronix

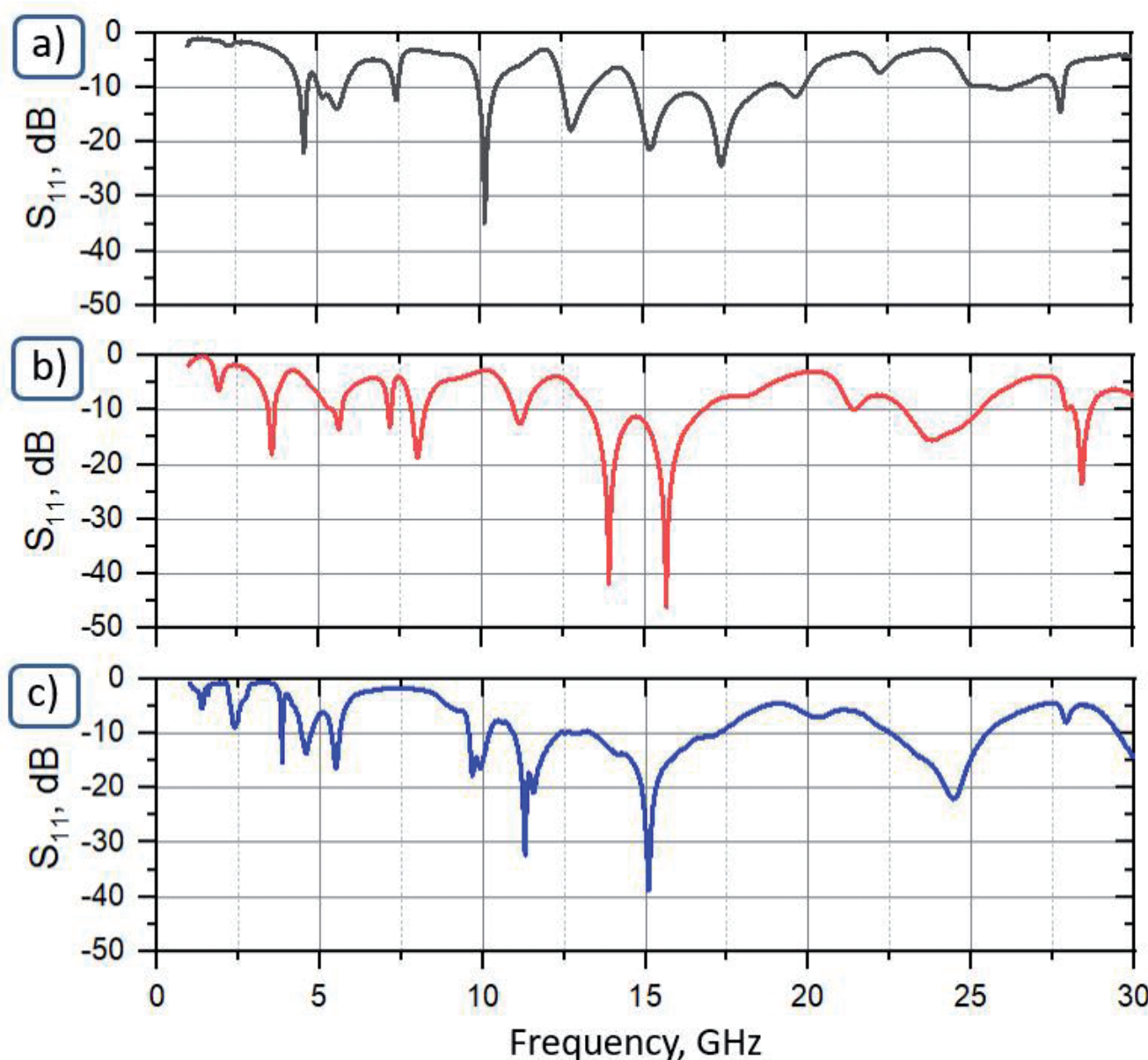


Fig. 5. Frequency dependence S_{11} of the parameters of antennas with different iterations in the range of 1-30 GHz in the K-type transmission line a) 1; b) 2; c) 3.

(N-type transmission line) and Anritsu VNA (K-type transmission line).

In the frequency range 7.5... 30 GHz, bands are observed formed by individual peaks with different center frequency and quality factor. An increase in the iteration order leads to an increase in the intensity of individual peaks and an expansion of the total frequency band, in which the absolute value of the parameter $S_{11} = 10$ dB or more. It should be noted that this Raman spreading occurs both in the lower and upper parts of the range.

4. CONCLUSION

The revealed electrodynamic properties of the investigated fractal antennas make it possible to conclude that the investigated fractal antennas are broadband and multirange, as well as the dependence of the number of resonances on the order of iterations of the fractal curve. This mechanism allows to control the antenna pattern and resonances by manipulating the dimension and the number of fractal iterations. Changing the dimension of the fractal at different iterations, shifting and dividing the resonant frequencies, it is possible to flexibly form the working bands of antennas in any frequency range and any width.

REFERENCES

- Le Sage GP. 3D printed waveguide slot array antennas. *IEEE Access*, 2016, 4:1258-1265.
- Du G. et al. 3-D printing implementation of an X-band Eaton lens for beam deflection. *IEEE Antennas and Wireless Propagation Letters*, 2016, 15:1487-1490.
- Gjokaj V, Chahal P, Kempel LC, Rothwell E. A novel 3D printed half-width microstrip leaky-wave antenna. *Proc. IEEE International Symposium on Antennas and Propagation & USNC/URSI National Radio Science Meeting*, pp. 1249-1250. San Diego, CA, USA, 9-14 July 2017. IEEE Publ., 2017. DOI: 10.1109/APUSNCURSINRSM.2017.8072667.
- Zhang S, Cadman D, Vardaxoglou JYC. Additively manufactured profiled conical horn antenna with dielectric loading. *IEEE Antennas and Wireless Propagation Letters*, 2018, 17(11):2128-2132.
- Angel K. et al. Selective electroplating of 3D printed parts. *Additive Manufacturing*, 2018, 20:164-172.
- Kolesov VV, Reshetilov AN. Mikroenergetika: sistemy s nakopleniem energii dlya mikroelektronnykh ustroystv [Microenergy: energy storage systems for microelectronic devices]. *Radiotekhnika*, 2015, 8:66-72 (in Russ.).
- Smirnov AV, Gorbachev IA, Gorbunova AV, Fionov AS, Kolesov VV, Kuznetsova IE. Fractal rectenna for collecting energy in the Wi-Fi range. *Radioelectronics. Nanosystems. Information Technology (RENSIT)*, 2020, 12(3):313-318. DOI: 10.17725/rensit.2020.12.313.
- Smirnov AV, Gorbachev IA, Gorbunova AV, Kolesov VV, Kuznetsova IE. Modelirovanie fraktalnoy rekteny metodom konechnykh elementov dlya sbora RCh energii v Wi-Fi diapazone [Simulation of fractal rectenna by the finite element method for collecting RF energy in the Wi-Fi range]. *Matematicheskie metody v tekhnike i tekhnologiyakh-MMTT*. 2020, 12-1:28-31 (in Russ.).
- Potapov AA. *Fraktały w radiofizyce i radiolokacji. Topologia wyborki* [Fractals in radiophysics and radar: Sample topology]. Moscow, Universitetskaya kniga Publ., 2005, 848 p.
- Belyaev RV, Vorontsov GM, Kislov VYa, Kolesov VV, Krupenin SV, Popov AM, Ryabenkov VI. Complex chaotic discrete signals in telecommunications, radar, and navigation systems. *Journal of Communications Technology and Electronics*, 2006, 51(9):1052-1063; doi: 10.1134/S1064226906090063.
- Kaloshin V, Saprykina M. An example of a nearly integrable Hamiltonian system with a trajectory dense in a set of maximal Hausdorff dimension. *Communications in mathematical physics*, 2012, 315(3):643-697.
- Dzhurinsky KB. *Miniatyurnye koaksialnye radiokomponenty dlya mikroelektroniki SVCh* [Miniature coaxial radio components for microwave microelectronics]. Moscow, Tekhnosfera Publ., 2006, 216 p.

DOI: 10.17725/rensit.2021.13.435

Passive Measurements of the Refractive Index of Liquid Nitrogen and Free-flowing Substances by the Prism Method in the Millimeter Wavelength Range

Valery A. Golunov, Konstantin V. Gordeev, Konstantin N. Rykov

Kotelnikov Institute of Radioelectronics and Electronics of RAS, Fryazino Branch, <http://fire.relarn.ru/> Fryazino 141190, Moscow region, Russian Federation

E-mail: golsnow@mail.ru, gordeer@yandex.ru, constrykov@yandex.ru

Received August 17, 2021, peer-reviewed August 27, 2021, accepted September 06, 2021

Abstract: It is proposed to use the classical prism method in the millimeter wavelength range for measuring the refractive index of liquid and free-flowing substances, including mixtures with particle sizes comparable to the wavelength. The method is implemented using a hollow radio transparent rectangular prism filled with a test substance. The measurements were carried out in the thermal radiation mode using radiometers with horn-lens antennas at frequencies of 37.5 and 94 GHz. To measure the deflection of the refracted beam, a linear scanner with a black body mounted on it, cooled with liquid nitrogen, was used. The distance between the prism and the scanner was 1 m. The refractive index of liquid nitrogen, sand, gravel, marble chips and granular polyethylene were measured. Using the refractive formula and the Landau-Lifshitz-Looeng formula for calculating the dependence of the refractive index of binary mixtures on the bulk density of particles, estimates of the refractive index of the material of the particles that make up the substances under study are obtained. They are in satisfactory agreement with the known experimental data for quartz, feldspar, granite, and marble.

Keywords: prism method, refractive index, millimeter waves, thermal radiation, mixtures of particles commensurate with the wavelength

UDC 535.36, 621.396.11

Acknowledgements: Work was supported by the Ministry of Science and Higher Education of the Russian Federation (State Order No. 0030-2019-0008).

For citation: Valery A. Golunov, Konstantin V. Gordeev, Konstantin N. Rykov. Passive Measurements of the Refractive Index of Liquid Nitrogen and Free-flowing Substances by the Prism Method in the Millimeter Wavelength Range. *RENSIT: Radioelectronics. Nanosystems. Information technologies*, 2021, 13(4):435-442. DOI: 10.17725/rensit.2021.13.435.

CONTENTS

1. INTRODUCTION (435)
2. SCHEME, TECHNIQUE AND EQUIPMENT FOR MEASUREMENTS (436)
3. MEASUREMENT RESULTS (438)
4. DISCUSSION OF RESULTS (439)
5. CONCLUSION (440)
- REFERENCES (440)

1. INTRODUCTION

The refractive index is one of the most important characteristics of solid, liquid and gaseous media that determine their electrodynamic properties [1]. To measure the refractive index, a variety of methods have been developed that take into account both the features of the media under study and the technical capabilities of the used

wavelength range. For example, in the range of millimeter (MM) waves, methods are used that are implemented using active waveguide, resonator, quasi-optical and open systems [2-7]. In the optical range, since Newton's time, the prism method has been widely used, based on its property, due to refraction, to decompose white light into spectral components.

The possibility of evaluating the dielectric constant (DC) of a solid from the measured values of the permittivity of a mixture of its particles with air, and vice versa, is of certain practical importance. The widely used formulas for calculating the dependence of the DC of binary mixtures on the volume density of particles, such as Maxwell Garnett, Polder-van Santen, were developed within the framework of the effective medium theory in the approximation of particles small in comparison with the wavelength [8,9]. This condition is satisfied, for example, by the results of measurements performed on coaxial, waveguide and resonator devices, since negligible particle sizes are a necessary condition for correct measurements using these devices. However, even the fulfillment of this condition does not guarantee satisfactory agreement of the experimental data with the results of calculations performed according to any of the above formulas. The reason is that at average values of the volume density, these formulas lead to diverging values of the dielectric constant [10].

With increasing particle size, multiple scattering occurs between individual particles, that affects the dielectric properties of the medium. However, strict accounting of the scattering effect, carried out within the framework of the theory of strong fluctuations [11,12], the quasicrystalline approximation (QCA), and the quasicrystalline approximation with a coherent potential (QCA-CP) [13], insignificantly increases the permissible ratio of particle size to wavelength. When MM waves propagate in such granular media as

sand, snow, gravel, the particle sizes can be commensurate with the wavelength that, on the one hand, can lead to the appearance of the multiple scattering effects, and, on the other hand, limits the use of waveguide and resonator devices for measuring their DC. In this work, to measure the refractive index of liquid and granular weakly absorbing media, including mixtures with particles whose sizes are commensurate with the wavelength, a variant of the implementation of the prism method on MM waves in the passive mode is proposed. Liquid nitrogen, sand, granular polyethylene, marble chips and gravel were used as media under study. Refractive index was measured at 37.5 and 94 GHz.

2. SCHEME, TECHNIQUE AND EQUIPMENT FOR MEASUREMENTS

Using the refractive properties of a prism to measure the refractive index of substances assumes that these substances have a prismatic shape. If, in the study of solids, such a form is made due to their appropriate processing, then in the study of liquids and loose substances, a preliminary preparation of a prismatic container is necessary. In the proposed study, in order to give such samples the required prismatic shape, triangular hollow prisms were created with input and output edges for radiation, made of 20 mm thick Penoplex foam sheet, which provided both the necessary stiffness of the prism and almost absolute transparency for MM waves. The base of the prism is made of wood in the shape of a right-angled triangle. A drawing of a prismatic cell is shown in Fig. 1.

Fig. 2 shows the path of rays in a rectangular prism filled with a substance with a refractive index n at normal incidence of a plane wave from above. The angle of incidence on the lower face α and the angle of refraction $\alpha + \beta$ are related by the Snell relation:

$$n \sin \alpha = \sin (\alpha + \beta) \quad (1)$$

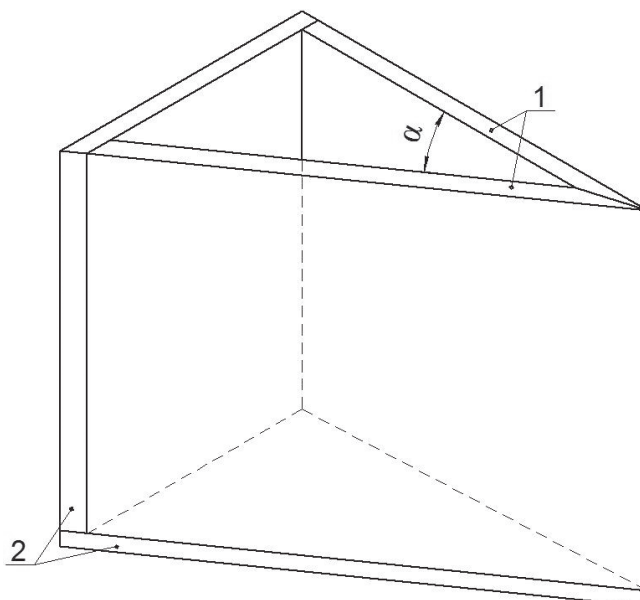


Fig. 1. Rectangular prism design: 1 – foam, 2 – wood.

At a distance $OB = L$ from the refracting face, the beam is displaced in the transverse direction by a distance $AB = x$. If L and x are known, then the refractive index in accordance with (1) is determined as follows:

$$n = \frac{\sin(\beta + \alpha)}{\sin \alpha} = \frac{\sin[\arctg(x/L) + \alpha]}{\sin \alpha}. \quad (2)$$

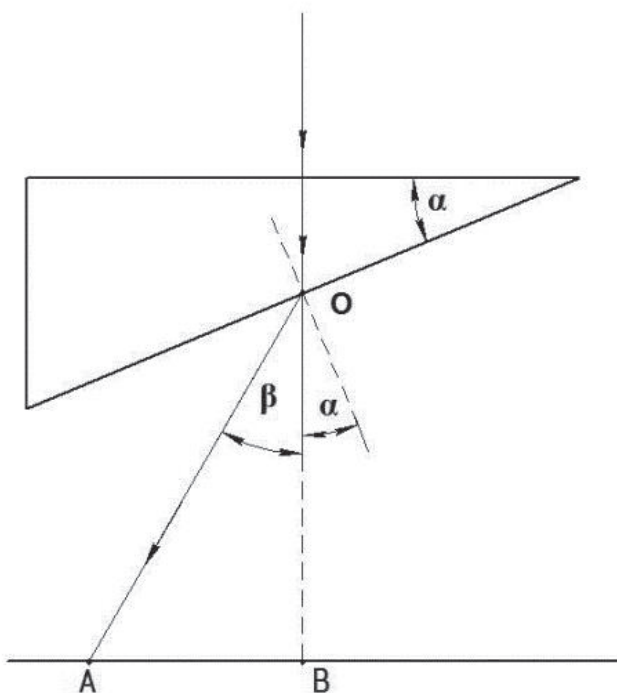


Fig. 2. Ray path in a prism.

Relation (2) is, in fact, a classical algorithm for measuring the refractive index of substances. The novelty of the measurement technique proposed below is the implementation of the algorithm in the thermal radiation mode.

The measurement scheme is shown in **Fig. 3**. The receiving system consisted of a radiometer with a horn-lens antenna with an aperture of 180×160 mm and a lens focal length of 400 mm. As a radiation source, a black body (BB) with a size of 100×200 mm, cooled with liquid nitrogen, was used. The BB was installed on a moving platform of a linear scanner with a stroke length of 1 m. Scanning was carried out perpendicular to the optical axis of the antenna at a distance of up to 1.5 m from a prism mounted almost close to the lens. The dimensions of the prism face adjacent to the lens were 250×200 mm. To study substances, depending on their dielectric and attenuating properties, three prismatic cells were used, differing only in the values of the angle α (10° , 25° , and 40°) shown in Fig. 1.

The BB thermal radiation was received by broadband radiometers with sensitivities no worse than 0.2 K at a time constant of 1 s, operating at 37.5 and 94 GHz. The output signals of the radiometers were recorded using an ADC and a computer.

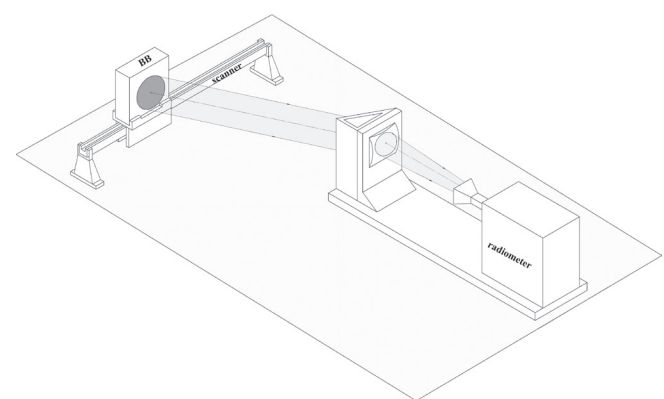


Fig. 3. Refractive index measurement circuit.

3. MEASUREMENT RESULTS

The prism cell, as noted above, is designed to measure the refractive index of liquids and loose materials. Let us first consider the results of measuring the refractive index of liquid nitrogen, the dielectric properties of which are of particular interest in connection with its wide application in radiometry for cooling black bodies used to calibrate radiometers. **Fig. 4** shows the records of the output signals of the radiometers at frequencies of 37.5 and 94 GHz when the BB moved along the perpendicular to the optical axis of the lens antenna (see Fig. 3). At each frequency, two records of the output signal were performed, one of which (calibration) corresponded to the case of a hollow prism, the other - the case of the prism filled with liquid nitrogen. The cell angle $\alpha = 25^\circ$, the distance L at 37.5 and 94 GHz was equal to 1.28 m and 1.31 m, respectively (see Fig. 2).

The displacements x of the refracted rays relative to the direct rays, determined as the difference between the maximum of the corresponding output signals of the radiometers, were 11.55 cm at 37.5 GHz and 11.84 cm – at 94 GHz. As a result of calculations using formula (2) at both frequencies, practically coinciding values

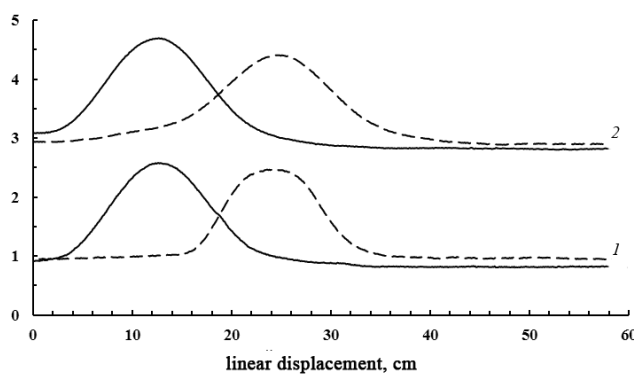


Fig. 4. Output signals of radiometers at frequencies of 37.5 GHz (1) and 94 GHz (2) when the FT moves along the perpendicular to the optical axis of the lens antenna with an hollow prism (solid lines) and prism is filled with liquid nitrogen (dashed lines).

Table
Experimental values of the refractive index of free-flowing substances

| | Substance | Particles size, mm | n | ρ_v | ρ , g/sm ³ | ρ_0 , g/sm ³ | α , angular degree |
|----|--------------|--------------------|-------|----------|----------------------------|------------------------------|---------------------------|
| 1 | sand | <0.5 | 1.67 | 0.67 | 1.67 | 2.49 | 10 |
| 2 | sand | <1 | 1.62 | 0.62 | 1.59 | 2.4 | 10 |
| 3 | gravel | <1 | 1.64 | 0.59 | 1.55 | 2.63 | 10 |
| 4 | gravel | 1-2 | 1.62 | 0.56 | 1.55 | 2.8 | 10 |
| 5 | gravel | 3-4 | 1.665 | 0.57 | 1.65 | 2.9 | 10 |
| 6 | marble | 1-2 | 1.748 | 0.48 | 1.28 | 2.65 | 10 |
| 7 | Polyethylene | 3 | 1.34 | 0.6 | 0.575 | 0.96 | 30 |
| 8 | Polyethylene | 4 | 1.32 | 0.64 | 0.615 | 0.96 | 30 |
| 9 | Polyethylene | 5 | 1.23 | 0.4 | - | - | 40 |
| 10 | Polyethylene | 5 | 1.32 | 0.625 | 0.6 | 0.96 | 30 |

of the refractive index of liquid nitrogen were obtained, equal to $n = 1.189$, which corresponds to the value of the real part of the DP $\epsilon' = 1.41$. The fact that equal values of n were obtained at both frequencies was to be expected, since nitrogen, as it is known, is a neutral gas. For comparison on the Internet for liquid nitrogen values $\epsilon' = 1.4 \dots 1.5$ are given, but there is no information on the methods used to measure DP.

The **Table** lists the values of the refractive index of sand, gravel, marble chips and granular polyethylene measured at 37.5 GHz. In addition, the table lists the values of the volume density of the particles ρ_v , the density of the mixture ρ , the density ρ_0 of the solid material of the particles, and the angle of the prism α at which the measurements were carried out.

The density of the solid material of particles ρ_0 and their volume density ρ_v are related by the ratio:

$$\rho_0 = \frac{\rho}{\rho_v}, \quad (3)$$

where ρ is the density of the mixture, defined as the ratio of the mixture mass M to its volume V_0 :

$$\rho = \frac{M}{V_0}. \quad (4)$$

Thus, if the density of the particle material is known, then the bulk density is determined using the results of measurements of M , V_0 and relations (3)-(4). This approach was used to calculate the volume density of marble chips and polyethylene, since their density has been known.

The volume density of sand and gravel, which could include various minerals with an unknown concentration, was determined as:

$$\rho_V = \frac{V_0 - V_w}{V_0}, \quad (5)$$

where V_0 is the total volume of the mixture, V_w is the volume of pores determined by method of filled with water.

In the theory of random dense media and applications requiring a wide choice of density, a large set of mixing rules was introduced [10], for example, by writing the "power law" approximation, which in the case of a mixture of particles with air is written in the form:

$$\varepsilon_{\text{eff}}^{\eta} = 1 + \rho_V (\varepsilon_m^{\eta} - 1), \quad (6)$$

where ε_{eff} is the effective DP of the mixture, ε_m is the DP of the particle material, η is the exponent. Validation of formulas for mixtures is carried out by comparison with a radiophysical experiment. From a large number of published works, we single out studies [14,16], in which it was shown that the experimental dependences ε_{eff} (ρ_V) both in the case of liquid and powder binary mixtures are best approximated using the refraction formula [17] and the Landau-Lifshitz-Looyenga formula [18,19].

The refraction formula is written in the form (6) at $\eta = 1/2$:

$$\sqrt{\varepsilon'_{\text{eff}}} = 1 + \rho_V (\sqrt{\varepsilon'_m} - 1). \quad (7)$$

For weakly absorbing particles $\varepsilon'_m \gg \varepsilon''_m$, therefore $\sqrt{\varepsilon'_{\text{eff}}} = n_{\text{eff}}$, $\sqrt{\varepsilon'_m} = n_m$ and (7) is transformed to the form:

$$n_{\text{eff}} = 1 + (n_m - 1)\rho_V. \quad (8)$$

Thus, the refractive model corresponds to the linear dependence of the refractive index of the mixture on the volume density of the particles, while the proportionality coefficient equal to $(n_m - 1)$ is determined by the refractive index of the material of the particles. Therefore, by measuring the refractive index of the mixture with known volume density of the particles, the refractive index of the particles material can be determined.

The Landau-Lifshitz-Looyeng formula is applicable for a mixture of dissimilar particles with an arbitrary shape and is written in the form (6) at $\eta = 1/3$:

$$\varepsilon_{\text{eff}}^{1/3} = 1 + \rho_V (\varepsilon_m^{1/3} - 1)$$

or

$$n_{\text{eff}} = [1 + \rho_V (n_m^{2/3} - 1)]^{3/2}. \quad (9)$$

It follows from (9) that the refractive index depends nonlinearly on the volume density. **Fig. 5** shows the experimental data obtained in this work and plots of the dependence of the refractive index on the volume density of particles, calculated using formulas (8) and (9). It is seen that the nonlinearity of the dependence of the refractive index on the bulk density, corresponding to formula (9),

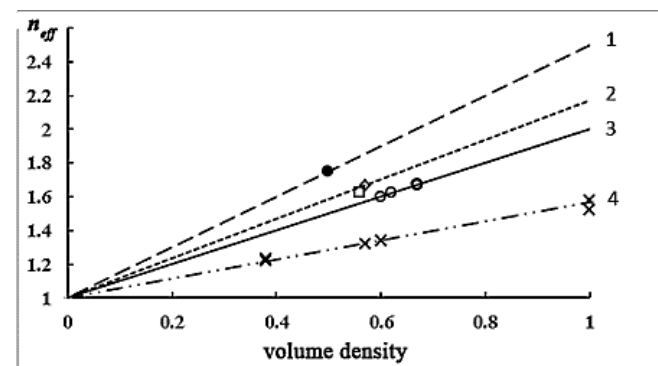


Fig. 5. Graphs of the dependence of the refractive index on the volume density of particles: 1 – marble, 2 – gravel ($d = 2 \dots 4 \text{ mm}$), 3 – gravel ($d < 2 \text{ mm}$) and sand, 4 – polyethylene ($d = 3 \dots 5 \text{ mm}$). Solid lines – calculated by the refractive formula, dashed lines – by the Landau-Lifshitz-Looyenga formula. Discrete symbols – experimental data.

manifests itself the stronger, the higher the refractive index of the particle material. In the case of polyethylene granules, both formulas lead to practically coinciding graphs at the value of the refractive index of polyethylene $n_m = 1.58$ ($\epsilon_m = 2.49$). This value turned out to be slightly overestimated in comparison with the reference data $\epsilon_m = 2.3 \dots 2.4$.

4. DISCUSSION OF RESULTS

An interesting fact is the coincidence of the experimental data for sand and fine gravel. This means that the sand and fine gravel had similar mineral components. The refractive index of the material of their particles, calculated using the refractive formula, turned out to be equal to $n_m = 2$ ($\epsilon_m = 4$), and calculated using the Landau-Lifshitz-Looyeng formula – $n_m = 2.05$ ($\epsilon_m = 4.2$). Gravel grains can contain quartz, feldspars, and other minerals. From various sources (for example, [20,22]) it follows that the refractive index of quartz is estimated within 1.9...2.1, feldspar – over 2.25. Thus, the results of measuring the refractive index of sand and fine gravel are in satisfactory agreement with the known data on the assumption that quartz is the main mineral in their composition.

The refractive index of gravel with particle sizes $d = 2 \dots 4$ mm turned out to be noticeably higher than for sand and finer gravel ($d = 1 \dots 2$ mm). The reason for this may be the increased concentration in the material of larger particles of such minerals as feldspar and granite, the refractive index of which is higher than that of quartz [20,22].

The refractive index of white marble chips turned out to have the highest value. The refractive index of marble, calculated using the refractive formula, is $n_m = 2.57$ ($\epsilon_m = 6.6$), and calculated by the Landau-Lifshitz-Looyenga formula – $n_m = 2.7$ ($\epsilon_m = 7.29$). It is known [23] that the dielectric properties of marble, even white, which is considered one of the purest calcites, strongly depend on its

chemical composition. The values $\epsilon_m = 6.8 \dots 7.2$ measured at frequencies of 40-50 GHz for marble with unknown composition are given in [24]. These values are in satisfactory agreement with the data obtained in this work and presented above.

Thus, a comparative analysis of the experimental data obtained for a number of granular substances showed that the use of a prismatic cuvette makes it possible to measure their refractive index by the prism method using the mode of receiving thermal radiation.

5. CONCLUSION

In this work, the features of the application of the classical prism method in the range of MM waves for measuring the refractive index of loose materials with particle sizes comparable to the wavelength have been investigated. It is shown that the method is implemented using a hollow radio transparent prismatic cell filled with a test substance. In addition, the proposed method can be implemented in a passive mode. The values of the refractive index of mixtures of sand, gravel, marble chips and polyethylene with air, measured by the prism method at a frequency of 37.5 GHz, are in satisfactory agreement with the known experimental data for quartz, feldspar, polyethylene, and marble.

REFERENCES

1. Rytov SM, Kravtsov YuA, Tatarskii VI. *Vvedenie v statisticheskuyu radiofiziku* [Introduction to statistical radiophysics]. Pt. 1-2. Moscow, Nauka Publ., 1978.
2. Valitov RA, Dyubko SF, Kamyshan VV, Kuz'michev VM, Makarenko BI, Sokolov AV, Sheiko VP. *Tekhnika submillimetrovых волн* [Submillimeter wave technique]. Moscow, Sovetskoe Radio Publ., 1969, 477 p.
3. Parkhomenko MP, Kalenov DS, Fedoseev NA, Eremin IS, Kolesnikova VM, Kovtykov

- DA et al. The improved resonator method for measuring the complex permittivity of materials. *J. Commun. Technol. Electron.*, 2017, 62(7):759-764.
4. Parkhomenko MP, Kalenov DS, Eremin IS, Fedoseev NA, Kolesnikova VM, D'yakonova OA. Improving the accuracy in measuring the complex dielectric and magnetic permeabilities in the microwave range using the waveguide method. *J. of Commun. Technol. Electron.*, 2020, 65(8):894-898.
 5. Parkhomenko MP, Kalenov DS, Eremin IS, Fedoseev NA, Kolesnikova VM, Barinov YuL. Usage and experimental tests of the modified waveguide method for measurement of the complex permittivity and permeability of materials. *Physics of Wave Phenomena*, 2019, 27(4):299-306.
 6. Sato K, Manabe T, Polivka J, Ihara T, Kasahima Y, Yamaki K. Measurement of the complex refractive index of concrete at 57.5 GHz. *IEEE Trans. Antennas and Propagation*, 1996, 44(1):35-40.
 7. Derov JS, Turchinetz BW, Crisman EE, Drehman AJ, Best SR; Wing RM. Free space measurements of negative refraction with varying angles of incidence. *IEEE Microwave and wireless components letters*, 2005, 15(9):567-569.
 8. Sihvola AH, Kong JA. Effective permittivity of dielectric mixtures. *IEEE Trans. Geosci. Remote. Sens.*, 1988, 26(4):420-429.
 9. Tuncer E; Serdyuk YV, Gubanski SM. Dielectric mixtures: electrical properties and modeling. *IEEE Trans. Dielectrics and Electrical Insulation*, 2002, 9(5):809-828.
 10. Sihvola AH. Mixing rules with complex dielectric coefficient. *Subsurface Sensing Technologies and Applications*, 2000, 1(4):393-415.
 11. Ryzhov YuA, Tamoykin VV, Tatarsky VI. O prostranstvennoy dispersii neodnorodnykh sred [On the spatial dispersion of inhomogeneous media]. ZhETF, 1965, 48(2):656-665 (in Russ.).
 12. Zhuck NP, Schünemann K, Shulga SN. Effective permittivity of a statistically inhomogeneous medium with strong permittivity fluctuations. *J. Electromagnetic Waves and Applications*, 2004, 18(3):357-359.
 13. Tsang L, Kong JA, Shin R. *Theory of Microwave Remote Sensing*. New York, Wiley-Interscience, 1985, 632 p.
 14. Dube DC. Study of Landau-Lifshitz-Looyenga's formula for dielectric correlation between powder and bulk. *J. Applied Phys.*, 1970, 3(11):1648-1652.
 15. Zhou P-H, Deng L-J, Wu B.-I, Kong JA. Influence of scatter's geometry on power-law formula in random mixing composites. *Progress In Electromagnetics Research*, 2008, 85:69-82; doi: 10.2528/PIER08081705.
 16. Sheen J, Hong Z-W. Microwave measurements of dielectric constants by exponential and logarithmic mixture equations. *Progress In Electromagnetics Research*, 2010, 100:13-26; doi: 10.2528/PIER09091706.
 17. Kraszewski A, Kulinski S, Matuszewski M. Dielectric properties and a model of biphasic water suspension at 9.4 GHz. *J. Applied Phys.*, 1976, 47:1275-1277.
 18. Landau LD, Lifshitz EM. *Elektrodinamika sploshnykh sred* [Electrodynamics of continuous media]. Moscow, Fizmatgiz Publ., 1959, 532 p.
 19. Looyenga H. Dielectric constants of heterogeneous mixtures. *Physica*, 1965, 31(3):401-412.
 20. Zheng Y, Wang S, Feng J, Ouyang Z, Li X. Measurement of the complex permittivity of dry rocks and minerals: application of polythene dilution method and Lichtenecker's mixture formulae. *Geophys. J. Intern.*, 2005, 163(3):1195-1202.

21. Arcone SA, Boitnott GE. Complex permittivity of common minerals and one soil at low water contents. *Proceed. of the XIII Intern. Conf. Ground Penetrating Radar* (Lecce, Italy, 2010). IEEE, 2010; doi: 10.1109/ICGPR.2010.5550133.
22. Manouchehri HR, Rao KH, Forssberg KSE. Triboelectric charge, electrophysical properties and electrical beneficiation potential of chemically treated feldspar, quartz and wollastonite. *Physical Separation in Science and Engineering*, 2002, 11:9-32; doi: 10.1155/2002/46414.
23. Sengwa RJ, Sony A. Dielectric dispersion and microwave dielectric study of marbles in support of radar investigations. *Indian J. of Pure@Applied Physics*, 2005, 43:777-782.
24. Shao Yu., Liao Xi., Wang Yang. Complex permittivity of typical construction materials over 40-50 GHz. *Proc. 2018 IEEE Intern. Symp. on Antennas and Propagation & USNC/URSI National Radio Science Meeting* (Boston, MA, USA, 2018). N.Y., 2018. DOI: 10.1109/APUSNCURSINRSM.2018.8608541.

DOI: 10.17725/rensit.2021.13.443

Millimeter-wave band subsurface sounding module

Gennady I. Khokhlov, Roman N. Denisiuk

Kotelnikov Institute of Radioelectronics and Electronics of RAS, Fryazino branch, <http://fire.relarn.ru/>
Fryazino 141190, Moscow Region, Russian Federation

E-mail: khokhland@rambler.ru, ro-d@yandex.ru

Received May 26, 2021, peer-reviewed June 10, 2021, accepted June 15, 2021

Abstract: Radio-wave devices are used for many environmental and material research tasks. These devices and the development of relatively simple and affordable quasi-optic radio wave receivers and transmitters of millimeter and terahertz bands are important for numerous applications. Results of the design of a terahertz-band quasioptical transmitter-receiver module are presented. The module is intended for the remote detection of various objects and for measuring the depolarized field components backscattered by various long objects hidden behind obstacles (building materials and/or everyday items that prevent visual contact with the objects). These may be interfaces between materials with different dielectric constants, fiber optic cables, electric cables, and other objects. Results of full-scale experimental testing of the module on the detection of electric cables buried under plater in the wall of a building are presented.

Keywords: microwave module, millimeter and terahertz bands, quasi-optical devices, waves depolarization effect

UDC 621.396:96:537.874.4

Acknowledgements: The work was carried out according to the state order of the Kotelnikov IRE of RAS, topic number 0030-2019-0014.

For citation: Gennady I. Khokhlov, Roman N. Denisiuk. Millimeter-wave band subsurface sounding module. *RENSIT: Radioelectronics. Nanosystems. Information technologies*, 2021, 13(4):443-448. DOI: 10.17725/rensit.2021.13.443.

CONTENTS

- 1. INTRODUCTION (443)**
- 2. PURPOSE OF THE DEVICE (444)**
- 3. OPERATION PRINCIPLE (444)**
- 4. DESIGN AND COMPOSITION OF THE DEVICE (MICROWAVE MODULE) (445)**
- 5. OPERATION OF THE MODULE WITH A LENS-OBJECTIVE (446)**
- 6. CONCLUSIONS (447)**
- REFERENCES (447)**

1. INTRODUCTION

With the development of solid-state electronics, millimeter and terahertz band waves are being intensively used for solving scientific and engineering problems. The development of relatively simple and

inexpensive terahertz-band quasi-optical transmitter-receiver systems is important for many applications. These may be spectroscopy, detection and visualization of various objects hidden in building structures or under clothes, new methods of diagnostics in medicine, atmospheric control, and many other applications. Of great importance is studying the electrodynamic parameters of various materials, detection and localization of small-size objects, not only metallic, but also dielectric ones.

The purpose of this work is to present the results of the development of a receiving-transmitting radio-wave quasi-optical terahertz module for problems of subsurface sensing.

2. PURPOSE OF THE DEVICE

The module is designed for remote detection of reflections and measuring the reflection coefficients of various objects in the millimeter and terahertz wavelength ranges. These can be dielectric or metal objects and interfaces between materials with different dielectric constants. The module can be used both for studying the internal structure of spatially inhomogeneous media and measuring the depolarized field component backscattered by various linear (elongated) objects, including microwires, wires, fiber-optic cables, etc., and for detecting objects hidden behind building structures (drywall, plywood, brick, wallpaper, etc.) or behind fabrics, leather and other non-transparent household materials.

3. OPERATION PRINCIPLE

Metallic or dielectric objects in optically opaque media with dielectric constant different from the dielectric constant of the objects can be detected by radio wave transmission or reflection radio wave methods [1,2]. The thickness of building structures limits the applicability of transmission methods due to the losses in the building materials. To detect hidden anomalies at shallow depths, one can apply the radar method, which significantly reduces the effect of absorption in the environment. However, in such schemes, wave reflections at the interfaces have a great interfering effect. In order to get rid of this, it is proposed to use the phenomenon of radio wave depolarization in the case of scattering by linear inhomogeneities.

The operating principle of this method is described in [2]. It consists in the fact

that if the orientation of the linear object differs from the polarization direction of the incident wave, then the reflected wave has a component with polarization orthogonal to the polarization of the incident wave. The receiver of the reflected wave has a polarizing filter that transmits only the depolarized field component. This allows one to get rid of the interference of reflections at the interfaces of building structures, to significantly reduce the noise level, and, accordingly, to increase the signal-to-noise ratio of the signal reflected from objects hidden behind building structures. To substantiate this method of detecting objects behind obstacles, we measured the reflection coefficients and the polarization conversion coefficients of a number of objects [2]. The measurement results showed that the use of the depolarized component of the reflected wave to detect small-diameter wires does not lead to a loss of the energy potential of the device.

The microwave part of the module contains a linearly polarized microwave source (transmitter), as well as a linearly polarized microwave radiation receiver with polarization orthogonal to that of the transmitter [2]. The development of such a module on the basis of ordinary waveguides would lead to a bistatic location system, which significantly complicates the design, or to the use of ferrite microwave elements, which are currently little used in the terahertz range. Therefore, we decided to implement such a module in a quasi-optical version.

4. DESIGN AND COMPOSITION OF THE DEVICE (MICROWAVE MODULE)

The diagram of the device (microwave module) is given in [2]. It consists of a microwave oscillator, a waveguide-to-beam-guide converter (WBC), a beam-guide module, a beam splitter, a lens that forms the output microwave beam, and a receiver. The receiver includes a polarizing filter, waveguide-beam converter, a detector head, and an amplifier. The device also includes a power supply and a microwave modulator. The microwave power is modulated through the feeding circuit of a Gunn oscillator with operating frequency of 1 kHz.

A plane linearly polarized wave from a microwave oscillator formed by a waveguide-beam converter into a quasi-optical beam is incident on a plane grating of linear conducting elements, which is located at an angle of 45° to the direction of wave propagation. The conductors of the grating are parallel to the electric field of the wave and completely reflect the wave toward the boundary of the test medium. The wave of orthogonal polarization arising from scattering by the object is not reflected by the grating, but is completely transmitted to the receiver. The receiver consists of a polarizing filter, a waveguide-beam transducer, and a detector head.

Consider the design features of some elements of the microwave module. The microwave oscillator, detector heads, and power supply are purchased items.

The beam-guiding module or, as we call it, a prism, is made of Plexiglas and is the supporting structure. We called this element (prism) a beam-guiding because it contains

cylindrical channels in which a microwave beam propagates. All other elements of the microwave module are mounted to this prism: the oscillator with the WBGC, the beam-splitting grating (in some cases a beam-splitting film), the polarizing filter, the detector head (with the WBGC). The diameter of the quasi-optical beam was chosen to be 16 mm. It is known that the amplitude distribution of the field in the horn opening is similar to the distribution of the field in the feed waveguide, and the phase in the aperture changes according to the quadratic law. Therefore, to form a wave with a plane front, a phase corrector is placed in the horn opening. In our case, this is a Teflon lens. The quasi-optical system should satisfy the condition $ka \gg 1$, where $k = 2\pi/\lambda$ and a is the transverse size of the beam. The ratio $C = ka/L$ is a parameter characterizing the diffraction spread of the beam during its propagation in the path [3]. L is the length of the beam or the distance to the working area. At small L , the diffraction losses are also small. These and some minor circumstances forced us to choose a quasi-optical beam diameter of 16 mm.

A variety of devices made of wire gratings or thin dielectric plates to control wave propagation in quasi-optical systems have been described in the literature [4,5]. If a grating is placed at an angle of 45° to the direction of wave propagation and its conductors are parallel to the electric field vector, then the field is completely reflected from the grating, while if the conductors are perpendicular, then the wave completely passes through the grating. In our module, we use a small-period wire grating. It is glued to a special frame inserted into a groove in the prism at an angle of 45° to the incident

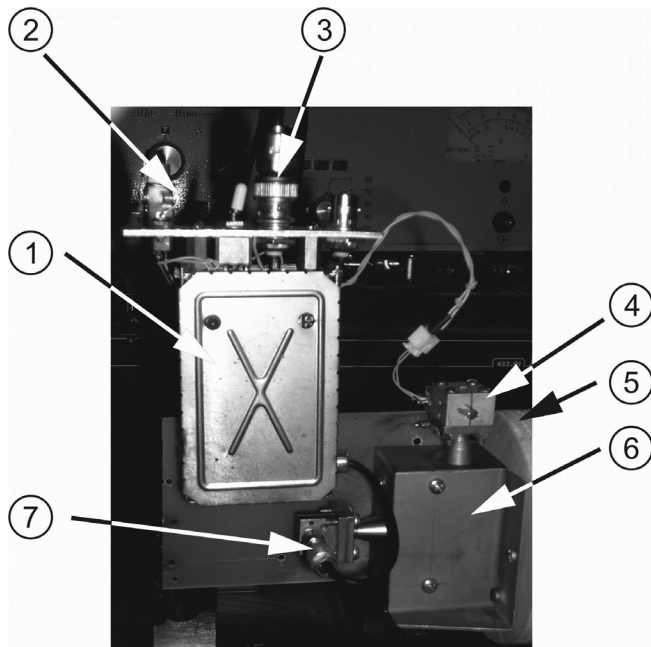


Fig. 1. Photo of the microwave module with a tube for the lens antenna 1 – amplifier and modulator of the supply voltage, 2 – power connector of the amplifier and the Gunn diode, 3 – amplifier output connector, 4 – Gunn oscillator, 5 – tube for mounting the lens-objective, 6 – prism, and 7 – detector.

wave and deflects the beam. **Fig. 1** shows a photograph of the microwave module with all the elements of the module, including the tube on which the lens-objective is mounted. The lens-objective is a receiving-transmitting antenna for a quasi-optical beam and allows focusing the beam at the required distance.

The operation of the module with a lens antenna is discussed below in Section 5.

5. OPERATION OF THE MODULE WITH A LENS-OBJECTIVE

For remote measurements, it is necessary to form a beam focused at a certain distance from the microwave module. **Fig. 2** shows a diagram of a single-channel module operating at a frequency of 100 GHz with a lens-objective (antenna) forming a focused

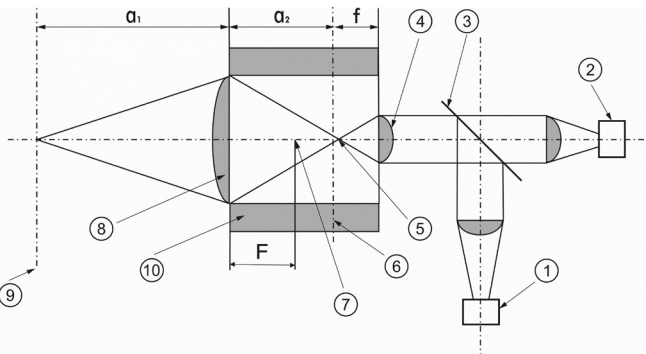


Fig. 2. Scheme of the microwave module with a lens-antenna (objective). 1- oscillator, 2 - receiver, 3- grating, 4 - ocular lens, 5 - ocular focus, 6 - image plane, 7 - objective focus, 8 - objective, 9 - object plane, and 10 - tube.

beam. This scheme was implemented in laboratory conditions.

The lens antenna is calculated by the formula [6]:

$$F = \{[D/2(n-1) - t](n+1)\}/2t.$$

The antenna is made of Teflon F-4 with a refractive index of $n = 1.427$. The lens diameter is $D = 70$ mm. The focal length of the lens $F = 90$ mm was chosen for the convenience of using the microwave module with the lens. The lens thickness at the center is $t = 13.5$ mm.

The ocular is a spherical lens made of Teflon F-4 with thickness at the center $t = 2.3$ mm. The lens diameter is $d = 16$ mm. The lens was calculated by the formula

$$f = (d/2)/2t(n-1).$$

The focus of the lens is 32.5 mm.

The image plane passes through the focus of the ocular lens (perpendicular to the optical axis). For optimal use of the lens aperture, the latter was placed at a distance a_2 from the image plane, which is calculated by the formula

$$a_2 = D \cdot f / d.$$

This distance turned out to be $a_2 = 142.2$ mm.

Now, we find a_1 – the distance from the lens to the plane of the object:

$$a_1 = (a_2 \cdot f) / (a_2 - f).$$

The plane of the object is located at a distance $a_1 = 244.4$ mm from the objective lens.

Thus, a point of the object is mapped to a point on the image plane, which passes through the ocular focus perpendicular to the optical axis of the system. Then, the signal corresponding to this point is converted into a signal from the detector by the waveguide-optical system of the module.

A point of an object on the optical axis is irradiated by a wave formed by the WBGC, the grating, the ocular lens, and the objective lens (antenna). The tube is a foam plastic tube that structurally integrates the lens and the module. The length of the tube is $a_2 + f = 174.2$ mm. The optical scheme was tested on the resolution of two conductors. Two conductors 0.5 mm in diameter without insulation and 0.07 mm in diameter (MGTP wire in Teflon insulation with a diameter of 0.5 mm) were attached to the back side of a plate 8-mm-thick foam plastic at a distance of 10 mm from each other. When the foam plate was moved in the plane of the object (at a distance of ~ 240 mm from the objective), the signal at the receiver output has a two-hump shape, the dip between the humps being about 3 dB. In natural conditions, the device was tested to find electrical wiring hidden behind plaster in the wall of an industrial building. The excess of the signal from the cables of the wiring system was also 3 dB.

If, instead of a polarizing reflective grating placed in the module at an angle of

45° (see Fig. 2), we place a dielectric (Mylar) film in the prism of this microwave module, and turn the receiver to receive the main polarization emitted by the oscillator, then the module can be used as a reflectometer to measure not only external boundaries, but also internal inhomogeneities of various materials.

6. CONCLUSIONS

This design of the device expands the possibilities of its application in detecting linear objects buried in building structure and improves the resolution and other technical characteristics necessary for further modifications of microwave modules for subsurface sounding.

REFERENCES

1. Kharkovsky S, Zoughi R and Hepburn FL. High Resolution Millimeter Wave Imaging of Space Shuttle External Fuel Tank Spray-on Foam Insulation. *Materials Evaluation*, 2007, 65(12):1220-1229.
2. Chigryay EE, Khokhlov GI, Ignatov BG, Kovalev AV, Fedchishin VG, Matveev VI, Bazhanov AS, Skopin VI, Krichevsky VI. Radio wave introscope in the millimeter range. *Electromagnetic waves and electronic systems*, 2010, 15(1):50-54.
3. Katselenbaum BZ. *High-frequency electrodynamics*. Moscow, Nauka Publ., 1966, 240 p.
4. Valitov RA, Dyubko SF, Kamyshan VV, Kuzmichev VM, Makarenko BI, Sokolov AV, Sheiko VP. *Technique of submillimeter waves*. Moscow, Sov. radio Publ., 1969, 299 p.

5. Chigryay EE, Khokhlov GI, Nikitin IP. Deliteli kvaziopticheskogo puchka na tonkikh dielektricheskikh plenkakh v millimetrovom i submillimetrovom diapazonakh dlin voln [Quasi-optical beam splitters on thin dielectric films in the millimeter and submillimeter wavelength ranges]. *Radioelektronika* (electronic journal) 2016, No. 6: <http://jre.cplire.ru/jre/jun16/9/text.pdf> (282kB).
6. Skolnik M (ed.). *Radar Handbook*, vol. 2. Radar antenna devices, p.11. Moscow, Sov. radio Publ., 1977.

DOI: 10.17725/rensit.2021.13.449

Simulation of the characteristics of low-voltage gates on combined cylindrical surrounding gate field-effect nanotransistors

Nikolae V. Masalsky

Research Institute of System Researches of RAS, <http://www.niisi.ru/>
Moscow 117218, Russian Federation

E-mail: volkov@niisi.ras.ru

Received May 26, 2021, peer-reviewed June 10, 2021, accepted June 15, 2021

Abstract: The applicability of the architecture of a nanoscale surrounding gate field-effect transistor with a combined cylindrical working area for low-voltage applications is discussed. At the same time, the licensed TCAD Sentaurus instrument and technological modeling system is used as a tool. The transistor architecture under consideration involves combining the working zones of n-channel and p-channel transistors with one common gate. At the same time, the efficiency of suppressing short-channel effects is maintained and a high level of transistor current is provided in the strong inversion mode. Based on this architecture, a TCAD model of the NAND gate has been developed, the design of which contains two independent surrounding gates one combined working area. The use of the proposed gate architecture makes it possible to reduce the number of required transistor structures per gate by three times. This leads to a decrease in the switched capacity and power dissipation. From the simulation results, the gate geometric parameters with a working area length of 25 nm and a diameter of 8.5 nm, which can function at control voltages of 0.5 V in the frequency range up to 20 GHz with high gain, are determined. The switching time delay is 0.81 ps. The TCAD model of a half-adder is developed in the basis 2NAND. According to the simulation results, the efficiency of the prototype, which performs binary code addition operations with a delay of 4.2 ps at a supply voltage of 0.5 V and a frequency of 20 GHz, is shown. The obtained results create a theoretical basis for the synthesis of low-voltage complex functional blocks with high performance and minimal occupied area, which meets modern requirements for digital applications.

Keywords: nanoscale MOSFET, silicon on insulator, surrounding gate, short-channel effects, logic gate, low supply voltage

UDC 621.382.323

Acknowledgments: The work was carried out within the framework of the state assignment for SRISA RAS "Conducting fundamental scientific research (47 GP)" on topic No. FNEF-2021-0001 "Software and tools for modeling, design and development of elements of complex technical systems, software telecommunication networks in various problem-oriented areas. 0580-2021-0001", reg. No. 121031300047-6.

For citation: Nikolae V. Masalsky. Simulation of the characteristics of low-voltage gates on combined cylindrical surrounding gate field-effect nanotransistors. *RENSIT: Radioelectronics. Nanosystems. Information technologies*, 2021, 13(4):449-456. DOI: 10.17725/rensit.2021.13.449.

Contents

1. Introduction (450)

2. Simulation result of the 2NAND gate (451)

3. Simulation of the characteristics of a half adder (453)
4. Conclusion (454)
- References (455)

1. INTRODUCTION

The main direction of development of modern microelectronics – "More Moore and more than Moore" also covers the creation of nanotransistor architectures that can provide ultra-high performance and an exorbitant degree of integration [1]. Among them, those in which the active zone (channel) is completely surrounded by a gate predominate [1-5]. One of these is the architecture with cylindrical geometry [6]. It is characterized by a twofold superiority in suppressing short-channel effects (SCE) in comparison with traditional transistor architectures. It also features improved subthreshold performance and increased current density in strong inversion mode [6-9]. A creative development of a cylindrical architecture with a fully surrounding gate is the concept of combining *n*- and *p*-type transistors into a single whole [10], that is shown on **Fig. 1**.

In this case, the source and drain regions are divided into two highly alloyed *n*- and *p*-types, the working region is universal

for charge carriers (electrons and holes). The entire transistor structure is placed on a SOI (silicon on insulator) substrate. A distinctive feature of such a design is the ability to significantly increase the degree of integration [11,12], and also allows for a wide variety of design designs [1,2,10-14], which will greatly simplify the task of designing complex-functional logic gates [2,10]. To achieve high conductivity of the considered transistor structure, it is necessary that its working region be low-alloyed. Ideally, its conductivity will be close to the intrinsic conductivity of silicon [7,15,16]. When the supply voltage (U_{dd}) is applied to the source, the process of carrier injection into the combined working region is activated [10,17]. Their distribution in the channel depends on the gate voltage (U_g). Thus, at $U_g - U_{th} > 0$, electrons prevail in the channel, and at $U_g - U_{th} < 0$ – these are holes, where U_{th} is the threshold voltage. Therefore, the considered transistor structure is a single-stage logic gate, whose input is the gate, the output is a common drain [6,9].

On the basis of the developed transistor, it is possible to synthesize a more complex logic gate NAND. **Fig. 2** shows a functional diagram of a two-input NAND gate based on one transistor with two independent fully surrounding gates.

The current flows through the gate only if the voltage corresponding to the level of the logical unit U_1 ($U_1 = U_{dd}$) is applied to both gates at the same time. Then the voltage at the output (drain) will be low, close to zero, equal to the logic zero level U_0 . For all other combinations of gate voltages, in the ideal case, no current will flow through the gate,

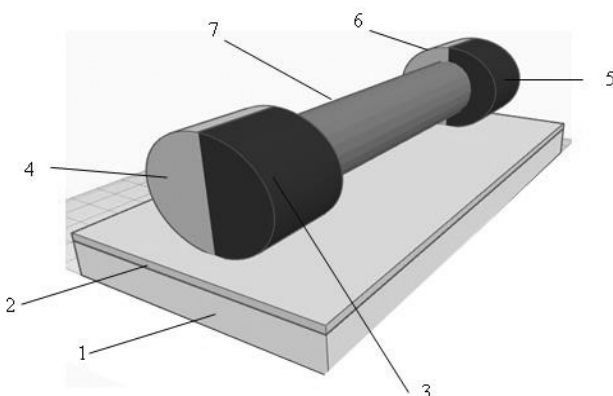


Fig. 1. Block diagram of the combined transistor. Here 1 is the silicon substrate, 2 is the silicon oxide, 3 is the *n*⁺-source, 4 is the *p*⁺-source, 5 is the *n*⁺-drain, 6 is the *p*⁺-drain, 7 is the combined working region.

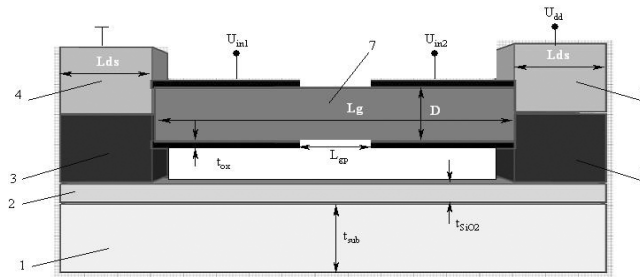


Fig. 2. Block diagram of the 2NAND gate, where the numerical designations correspond to Fig. 1. Here, L_g is the length of the working area, D is the diameter of the working area, L_{ds} is the size of the source and drain regions, t_{ox} is the thickness of the gate dielectric, L_{gp} is the size of the gap between of independent gates, t_{SiO2} is the isolating silicon oxide thickness, t_{sub} is the silicon substrate thickness, U_{dd} is supply voltage, $U_{in1(2)}$ is control voltage.

and the output voltage will be high, at a logic-one level.

The structure we study is characterized by effective suppression of SCE and low capacitance value. This, together with a reduction in the footprint, leads to a decrease in the level of dissipated power [2,6,7,9], which fully meets the requirements for modern digital circuits [1,4,18].

In this paper, we investigate the possibility of synthesizing complex logic gates combined in nanotransistors with a fully enclosing gate for low-voltage digital applications. The solution of this problem is carried out using the software package of instrument-technological modeling TCAD [19].

2. SIMULATION RESULT OF THE 2NAND GATE

Computer simulation of the electro-physical characteristics of transistor structures was carried out using the DESSIS program of the ISE TCAD package [19]. A TCAD

model has been developed for a combined SOI CMOS nanotransistor with a cylindrical geometry and a fully surrounding gate. In the course of numerical experiments, devices with different geometric dimensions of the working region were analyzed, the main parameters of which are given in **Table 1**. The "planar" and "vertical" versions of the gate design were considered, taking into account the surface recombination of charge carriers according to the Shockley-Reed-Hall mechanism, high degradation of the field mobility, and without taking into account quantum effects. The following designations are adopted in Table 1. Here t_{ox} is the gate oxide thickness (silicon oxide), t_{SiO2} is the silicon oxide thickness, t_{sub} is the silicon substrate thickness, n_i is the intrinsic carrier concentration, L_{ds} is the drain and source length, N_{ds} is the source and drain alloying concentration, v_{SRH} is the surface recombination rate by the mechanism Shockley-Reed-Hall, t_{SRH} is the lifetime of minority charge carriers according to the Shockley-Reed-Hall mechanism, A_d is the output function.

In our calculations the diameter D , the gate length L_g , and the length of the gap between the gate oxide of independent gates L_{gp} are varied. When choosing the parameters L_g and D , it is necessary to fulfill the condition of complete suppression of the SCE [6]. It should be borne in mind that with a decrease in the diameter, the

Table 1
The main parameters of prototypes

| Parameter | Value | Parameter | Value |
|-----------------------------|---------------------|---------------------------|----------------|
| L_g , nm | 22...32 | D , nm | 8...12 |
| L_{gp} , nm | 5...8 | t_{ox} , nm | 1.2 |
| t_{SiO2} , nm | 20 | t_{sub} , μm | 0.6 |
| L_{ds} , nm | 100 | n_i , cm^{-3} | 10^{13} |
| N_{ds} , cm^{-3} | $3.5 \cdot 10^{19}$ | v_{SRH} , cm/s | $3 \cdot 10^5$ |
| t_{SRH} , μs | 10 | A_d , eV | 4.65 |

capacitance of the drain-source junction decreases, and accordingly the threshold voltage increases, and, consequently, the response time of the transistor [16,17,20]. When choosing the topological parameters of the prototypes of the gate, it is necessary to take into account that during scaling, a decrease in the total number of carriers participating in the transfer process will be critical. The direct increase in the diameter of the active region is limited due to the fact that the efficiency of suppression of the SCE decreases [7]. An increase in the alloy level of the source and drain is limited by an exponential increase in the forward tunneling current between the source and drain [4,17,21] and a decrease in the breakdown voltage [20].

At the simulation it is assumed that the boundaries of the working region and the source/drain are sharp. There is no overlap between the gate and the source and drain regions. The t_{ox} thickness is chosen in such a way as to exclude the influence of the constant tunneling current of the gate [7].

From the simulation results, we selected a prototype with the following set a parameters for further research: L_g is equal 25 nm, D is equal 8.5 nm, L_{gp} is equal 6 nm, since ratio of the its ON/OFF currents was maximum, more than 10^6 , which is the main criterion for choosing structures for digital applications [10, 22].

Fig. 3 shows the TCAD simulation result of the distribution of carriers in the working region of the chosen gate for the control gate voltages $U_{in1} = U_{in2} = U_0$ and the supply voltage $U_{dd} = 0.5$ V. In this case, the working region is mainly filled with holes and its electronic conductivity is very low.

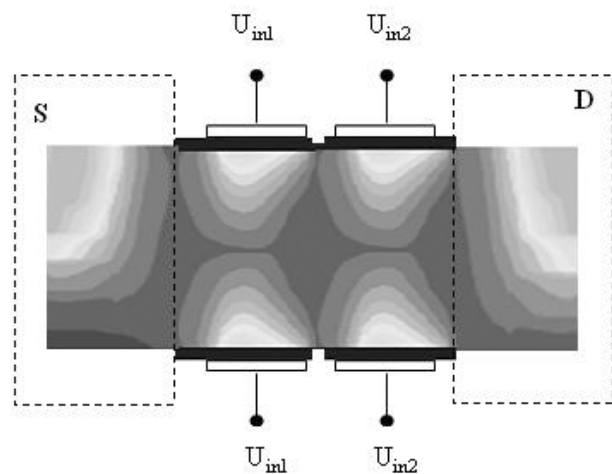


Fig. 3. Fragment of the distribution of carriers in its active region of the NAND gate.

Fig. 4 shows the simulation results of the transfer and transient characteristics of the chosen gate. The transfer characteristics of the gate show that it can operate in the

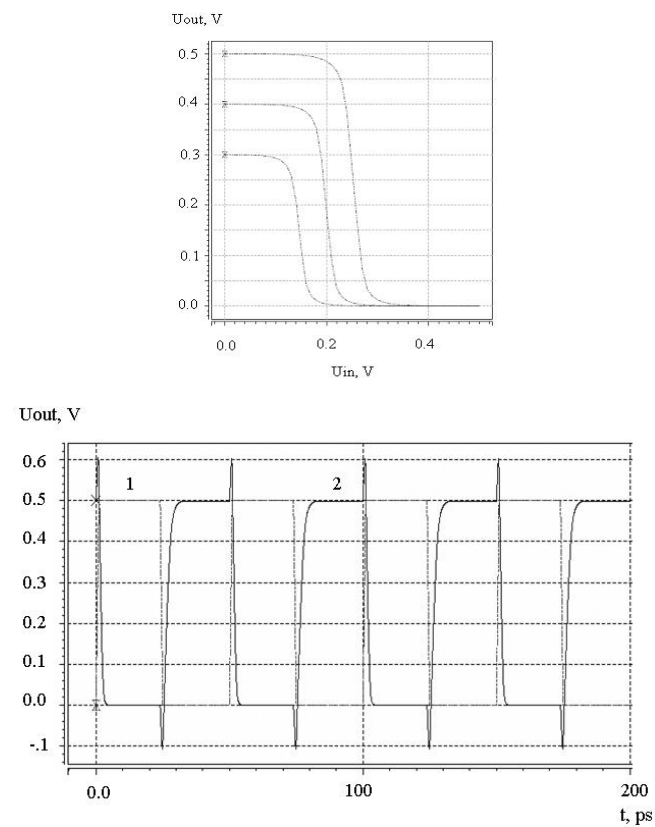


Fig. 4. (top) A family of transfer characteristics of the gate at U_{dd} from 0.5 to 0.3 V; (bottom) The transient response of the gate at $U_{in2} = U_{dd} = 0.5$ V, where 1 is the input signal U_{in1} , 2 is the output signal (solid line).

region of low supply voltages (less than 0.5 V) with a high voltage gain. In the given case of the transient response, the gate is triggered and a logical unit signal is generated at its output. The switching time delay at 20 GHz is 0.81 ps. In all other combinations of gate voltages, the voltage at the output of the device corresponds to the logic zero level. In the general case, the response time of the gate is limited by the time response of the transistor structure, which can be optimized by selecting the topological parameters.

3. SIMULATION OF THE CHARACTERISTICS OF A HALF ADDER

The logic element half adder is the main component of a one-digit full adder. It has two inputs a_1 and a_2 for two terms and two outputs: S – sum, P – carry. It is not single-stage due to its logical function. **Fig. 5** shows the implementation of a half adder in the NAND basis. It should be noted that one of the gates in the circuit is used as an inverter, and there are five inverting operations in total. The use of the considered gate architecture leads to a sharp reduction of footprint (at least five times), which increases the fast performance by

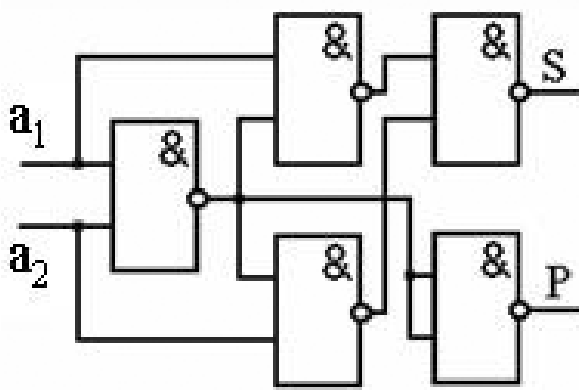


Fig. 5. Structural circuit of half adder.

switched capacitance, and causes a decrease in the dissipated power.

On the basis of the model of the NAND gate, a TCAD model of the half adder was developed. On **Fig. 6** is shown the simulation results one of its possible dynamic characteristics.

Here, at $U_{dd} = 0.5$ V, the voltage at the input a_1 (U_{a1}) is at a low level "U₀" (0 V) and the voltage at the input a_2 (U_{a2}) is switched from U₀ (zero) to U₁ (one), the output S (US) is switched to the high level of U₁, and the output P (UP) remains at the low level U₀. In the case under consideration, this process occurs with a clock frequency of 20 GHz. Switching time delay is 4.2 ps, switching power is 0.66 μ W, static power is 21.5 pW. Depending on the voltage level at the gate inputs, the outputs are maintained either low/low, high/low, or low/high. The presence of peaks is associated with transients in the circuit, the maximum peak value directly depends on the value of the supply voltage.

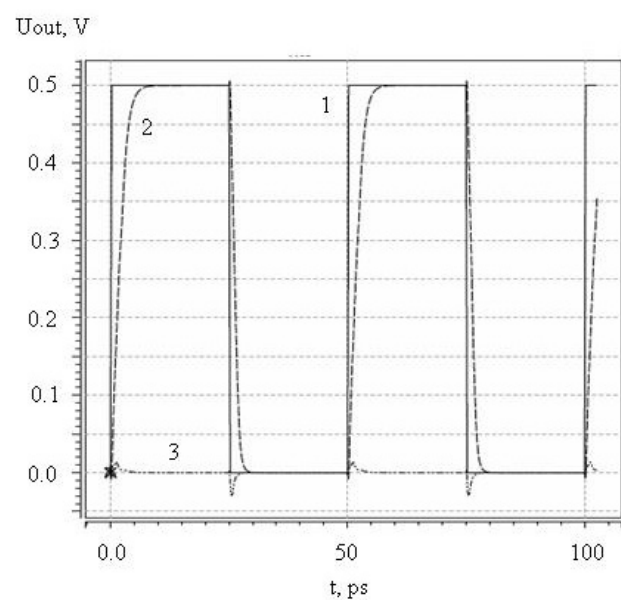


Fig. 6. Dynamic characteristic of a half adder at $U_{a1} = U_{dd} = 0.5$ V and a clock frequency of 20 GHz, where 1 – U_{a2} , 2 – U_S , 3 – U_P .

Fig. 7 shows a timing diagram of the voltages at the inputs and outputs of the half adder. The duration of the pulses supplied to each input a_1 (U_{a1}) and a_2 (U_{a2}) is the same. The frequency of their repetition is exactly two times different. This entails the superposition of pulses from the low-frequency sequence U_{a1} on the even pulses of the high-frequency sequence U_{a2} . It is in these cases that the transition of the output P occurs and a signal of a logical unit is formed on it, and a signal of a logical zero is formed at the output S.

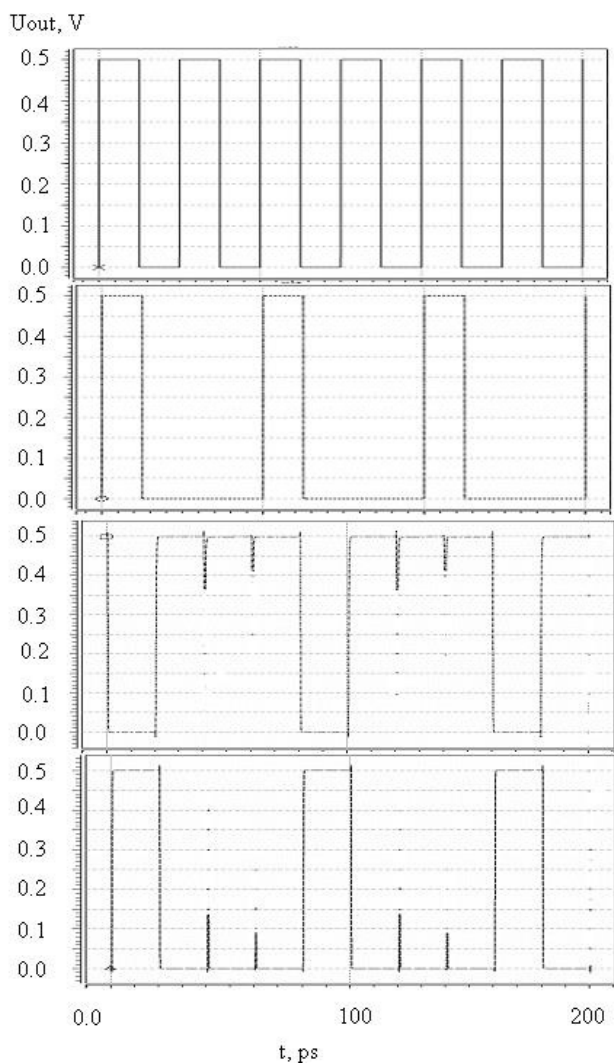


Fig. 7. Timing diagram of voltages at the inputs and outputs of the half adder, where the two upper figures are the voltage at the inputs a_1 and a_2 , the middle one is at the output S, the lower one is at the output P.

In all other cases, the voltage at the S output corresponds to the level of a logical unit, at the P output – to a logical zero.

Summarizing the results obtained, it can be assumed that devices based on the considered gate architecture can be used in the development of analog and digital circuits applicable for both high-frequency and low-voltage applications.

4. CONCLUSION

The high potential for applicability in low-voltage digital applications of the surrounding gate field-effect nanotransistor architecture with a cylindrical combined working area is shown. At the same time, the licensed instrument and technological modeling system TCAD is used as a tool. Based on this architecture, a TCAD model of the NAND gate has been developed, the design of which contains two independent surrounding gates one combined working area. The use of the proposed gate architecture makes it possible to reduce the number of required transistor structures per gate by three times. From the simulation results, the gate geometric parameters with a working area length of 25 nm and a diameter of 8.5 nm, which can function at control voltages of 0.5 V and lower in the frequency range up to 20 GHz with a high gain, are determined. The switching time delay is equal 0.81 ps at control voltages are equal 0.5 V.

The TCAD model of a half-adder is developed in the basis 2NAND. According to the simulation results, the efficiency of the prototype, which performs binary code addition operations with a delay of 4.2 ps at a supply voltage of 0.5 V and a frequency of 20 GHz, is shown. In this case, the active power is 0.66 μ W, the static power is 21.5 pW.

The obtained results create a theoretical basis for the synthesis of low-voltage complex functional blocks with high performance and minimal occupied area, which meets modern requirements for digital applications.

REFERENCES

1. Radamson HH, Zhu H, Wu Z, He X, Lin H, Liu J, Xiang J, Kong Z, Xiong W, Li J, Cui H, Gao J, Yang H, Du Y, Xu B, Li B, Zhao X, Yu J, Dong Y, Wa G. State of the art and future perspectives in advanced CMOS technology. *Nanomaterials*, 2020, 10(8):1555-1641.
2. Rahman F, Shakya B, Xu X, Forte D, Tehrani poor M. Security beyond CMOS: fundamentals, applications, and roadmap. *IEEE Trans. Very Large Scale Integr. (VLSI) Syst.*, 2017, 25(12):3420-3433.
3. Hsieh D, Lin J, Kuo P, Chao T. Comprehensive analysis on electrical characteristics of Pi-Gate poly-Si junctionless FETs. *IEEE Trans. Electron Dev.*, 2017, 64(8):2992-2998.
4. Majzoub S, Taouil M, Hamdioui S. System-level sub-20 nm planar and FinFET CMOS delay modelling for supply and threshold voltage scaling under process variation. *J. of Low Power Electron.*, 2019, 15(1):1-10.
5. Dharshan V, Balamurugan NB, Arun Samuel TS. An analytical modeling and simulation of surrounding gate TFET with an impact of dual material gate and stacked oxide for low power applications. *J. of Nano Research*, 2019, 57(4):68-76.
6. Ferain I, Colinge CA, Colinge J. Multigate transistors as the future of classical metal–oxide–semiconductor field-effect transistors. *Nature*, 2011, 479:310-316.
7. Lu W. Nanowire transistor performance limits and applications. *IEEE Trans. on Electron Dev.*, 2008, 55(11):2859-2876.
8. Dastjerdy E, Ghayour R, Sarvari H. Simulation and analysis of the frequency performance of a new silicon nanowire MOSFET structure. *Physica E*, 2012, 45(8):66-71.
9. Schwierz F, Wong H, Liou JJ. *Nanometer CMOS*. Singapore, Pan Stanford Publishing, 2010, 350 p.
10. Kaushik BK (ed.). *Nanoelectronics: Devices, Circuits and Systems*. Elsevier, 2018, 476 p.
11. Yoon JS, Rim T, Kim J, Meyyappan M, Baek CK, Jeong YH. Vertical gate-all-around junctionless nanowire transistors with asymmetric diameters and underlap lengths. *J. Appl. Phys.*, 2014, 105(10):102105.
12. Guerfi Y, Larrieu G. Vertical silicon nanowire field effect transistors with nano scale gate-all-around. *Nanoscale Res. Lett.*, 2016, 11(1):210-217.
13. Neamen D. *Semiconductor physics & devices: basic principles*. New York, McGraw-Hill, 2011, 784 p.
14. Masal'skii NV. Modeling the CMOS characteristics of a completely depleted surrounding-gate nanotransistor and an unevenly doped working region. *Rus. Microelectron.*, 2019, 48(6):394-398.
15. Verma JHK, Haldar S, Gupta RS, Gupta M. Modelling and simulation of subthreshold behaviour of cylindrical surrounding double gate MOSFET for enhanced electrostatic integrity. *Superlattices Microstruct.*, 2015, 88(3):354-364.
16. Gupta SK. Threshold voltage model of junctionless cylindrical surrounding gate MOSFETs including fringing field

- effects. *Superlattices Microstruct.*, 2015, 88(2):188-197.
17. Nayak K, Agarwal S, Bajaj M, Murali KV, Rao VR. Random dopant fluctuation induced variability in undoped channel Si gate all around nanowire n-MOSFET. *IEEE Trans. Electron Dev.*, 2015, 62(2):685-688.
18. Yoon JS, Jeong EY, Baek CK, Kim YR, Hong JH, Lee JS, Baek RH, Jeong YH. Junction design strategy for Si bulk FinFETs for system-on-chip applications down to the 7-nm node. *IEEE Trans. Electron Dev. Lett.*, 2015, 36(10):994-996.
19. ISE TCAD Release 10. [Online]. Available: <https://www.synopsys.com/silicon/tcad/device-simulation/sentaurus-device.hlm>, access data 15.06.2019.
20. Wang H, Liu Y, Han G, Shao Y, Zhang C, Feng Q, Zhang J, Hao Y .Performance enhancement in uniaxially strained Germanium–Tin FinTFET: Fin direction dependence. *IEEE Trans. Electron Dev.*, 2017, 64(6):2804-2811.
21. Samoju VR, Mahapatra K, Tiwari PK. Analytical modeling of subthreshold characteristics by considering quantum confinement effects in ultrathin dual-metal quadruple gate (DMQG) MOSFETs. *Superlattices Microstruct.*, 2017, 111(6):704-713.
22. Kumari Amrita, Kumar Subindu, Tarun Kumar Sharma, Mukul Kumar Das. On the C-V characteristics of nanoscale strained gate-all-around Si/SiGe MOSFETs. *Solid-State Electron.*, 2019, 154(4):36-42. DOI: 10.1016/j.sse.2019.02.006.

DOI: 10.17725/rensit.2021.13.457

Structure and electrical conductivity of polyvinyl alcohol films with multi-walled carbon nanotubes cured in a magnetic field

Sergey V. Vasin, Azat M. Nizametdinov, Viacheslav A. Sergeev

Kotelnikov Institute of Radioelectronics and Electronics of RAS, Ulyanovsk branch, <http://ulireran.ru/>
Ulyanovsk 432071, Russian Federation

E-mail: vs0902@mail.ru, anizametdinov@yandex.ru, sva@ulstu.ru,

Michael S. Efimov

Ulyanovsky State Technical University, <https://www.ulstu.ru/>

Ulyanovsk 432027, Russian Federation

E-mail: efimovmix@mail.ru

Received August 25, 2021, peer-reviewed Sept. 10, 2021, accepted Sept. 15, 2021

Abstract: The results of the study of the effect of the permanent magnetic field of a neodymium magnet on the polymerization process and the electrophysical characteristics of polyvinyl alcohol (PVA) films with the inclusion of multi-walled carbon nanotubes (MWCNTs) are presented. When studying the morphology of films using a scanning electron microscope, it was found that nanocomposite films with a thickness of 30 microns, cured in the presence of a magnetic field with the direction of the magnetic induction vector perpendicular to the surface of the films, have a homogeneous structure, while a significant number of MWCNTs agglomerations are observed in control samples of films. Measurements of the conductivity of films in the direction of the MWCNTs orientation at direct and alternating current showed that the conductivity of films obtained in a magnetic field significantly (by almost two orders of magnitude) exceeds the conductivity of control samples. The obtained results are analyzed on the basis of known models of electrical conductivity of nanocomposites with oriented MWCNTs. The degree of orientation of the MWCNTs during the curing of films in a magnetic field is estimated, taking into account the increase in the viscosity of the nanocomposite during the curing process.

Keywords: polymer nanocomposites, orientation of carbon nanotubes, magnetic field, nanocomposite films, electrical conductivity

UDC 678.744.72; 537.312.6

Acknowledgments: The work was carried out within the framework of a state assignment with partial financial support from the Russian Foundation for Basic Research and the Government of the Ulyanovsk Region, project No. 19-42-730011.

For citation: Sergey V. Vasin, Azat M. Nizametdinov, Viacheslav A. Sergeev, Michael S. Efimov.

Structure and electrical conductivity of polyvinyl alcohol films with multi-walled carbon nanotubes, cured in a magnetic field. *RENSIT: Radioelectronics. Nanosystems. Information technologies*, 2021, 13(4):457-464. DOI: 10.17725/rensit.2021.13.457.

CONTENTS

1. INTRODUCTION (458)

2. MATERIALS AND METHODS (458)

3. RESULTS AND DISCUSSION (459)

4. CONCLUSION (462)

REFERENCES (463)

1. INTRODUCTION

The excellent mechanical and electrical properties of carbon nanotubes (CNTs) have made them one of the best fillers for nanocomposites [1]. Even a small amount of CNTs added to the polymer matrix is significantly changes the functional properties of nanocomposite polymer structures [2]. However, the observed improvements in the mechanical and electrical properties of nanocomposites are lower than expected [3]. The random orientation of CNTs in the matrix cannot properly transfer the desired unique properties of CNTs to the composite, since these properties are, as a rule, localized along the axis of the CNTs. It has been shown that CNTs alignment is an effective way to transfer these properties to the surrounding matrix [4-5]. Moreover, the alignment of CNTs in nanocomposites can lead to a significant decrease in their proportion to achieve the desired results [6].

A number of methods are used to align CNTs in a polymer matrix: self-assembly [7], the Langmuir-Blodgett method [8], exposure to electric [9] or/and magnetic field [3,5,6,10], etc. Since ordinary CNTs have a low magnetic susceptibility, fields of about 10-25 T are required to align CNTs in a magnetic field. [3,5,11]. In [11], for example, for the orientation of CNTs in a polypropylene-based nanocomposite, repeated exposure to a magnetic field pulse with magnetic induction at a maximum of 10 T and a duration of about 1 ms was used.

To solve this problem, CNTs containing magnetic impurities are usually used. Such CNTs exhibit high magnetic susceptibility and can be aligned in magnetic fields not

exceeding 1 T and easily achievable in conventional laboratories [10]. It should be noted that CNTs obtained by standard methods (such as, for example, CVD) and not subjected to additional purification can contain a sufficiently large amount of impurities, including ferromagnetic catalysts (for example, iron compounds), which increase the magnetic susceptibility of CNTs. Most of these impurities are encapsulated between CNT molecules, and some are inside them, and they can only be removed using complex multi-stage purification methods. This allows us to expect that commercially produced CNTs can have increased magnetic susceptibility and can be aligned in a polymer matrix with using magnetic fields below 1 T.

This paper presents the results of a study of the influence of the magnetic field of a conventional neodymium magnet on the polymerization process and the electrophysical characteristics of polyvinyl alcohol (PVA) films with the inclusion of multi-wall carbon nanotubes (MWCNTs).

2. MATERIALS AND METHODS

For the production of the nanocomposite, we used commercially available PVS 17-99 and MWCNTs of the «Taunit» brand produced by NanoTechCenter LLC (Tambov, Russia). According to the manufacturer, the MWCNTs had a diameter of 20-50 nm, a length of the order of 2 μm , and the total amount of impurities did not exceed 10%. PVA is a widely used polymer and one of the best and widely used materials as a polymer matrix for creating film nanocomposite structures [12].

An aqueous solution of PVA was prepared in deionized water by continuous

stirring in a magnetic stirrer for an hour at a temperature of 90°C. The MWCNTs were dispersed in deionized water in the required ratio using an ultrasonic disperser. To improve the compatibility of the MWCNTs with the polymer matrix, the so-called non-covalent functionalization was used: 0.1% sodium dodecyl sulfate (SDS) was added to the water before dispersing MWCNTs. Then both solutions were mixed in the proportion necessary to obtain a given concentration of MWCNTs in relation to the weight of PVA, mixed in a magnetic stirrer for 30 minutes and cooled. The required amount of solution was poured into Petri dishes and dried at room temperature for 48 hours. During drying, one of the samples (hereinafter referred to as "m-film") was dried on the surface of a neodymium magnet, the second sample ("c-film") was dried without exposure to a magnetic field. The magnetic field strength near the surface of the neodymium magnet we used was measured by the ATE-8702 magnetometer (Aktacom) and was 0.3 T.

After evaporation of the solvent, nanocomposite films with a thickness of 30 microns were obtained. Square-shaped samples with dimensions of 1×1 cm were cut from the obtained films, which were clamped between flat brass contacts for electrical measurements. Measurements of current-voltage (I-V) characteristics were carried out on a setup including a programmable power supply APS-7313 (Aktakom), a DM4040 multimeter (Tektronix), and an A2-4 picoammeter (MNIPI). Frequency dependences of conductivity in the frequency range 50 kHz - 15 MHz were measured on an E7-29 meter (MNIPI). The surface morphology of the films was investigated using an

optical and scanning electron microscope (SEM, Phenom).

3. RESULTS AND DISCUSSION

To confirm the sensitivity of the MWCNTs used by us to the magnetic field, a glass with an aqueous suspension of a small amount of MWCNTs was placed in close proximity to a neodymium magnet. After 3 hours, the bulk of the MWCNTs in the suspension was grouped near the magnet (**Fig. 1**), which indicates that the used MWCNTs contain a significant amount of ferromagnetic impurities, which noticeably increase the magnetic susceptibility of MWCNTs.

Fig. 2 shows the SEM images of the obtained samples of PVA films containing 1% of the mass fraction of MWCNTs. The photographs clearly show that the



Fig. 1. Aqueous dispersion of MWCNTs after 3 hours of exposure to a neodymium magnet.

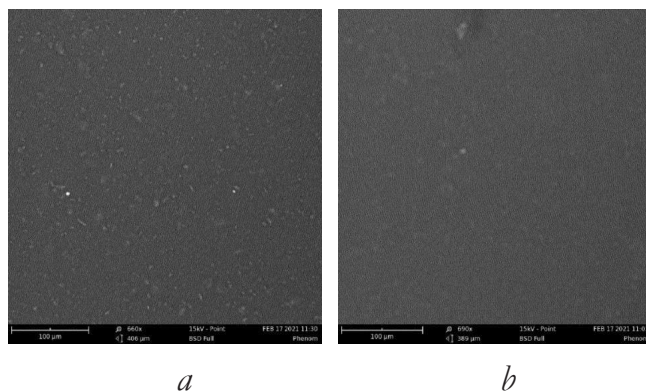


Fig. 2. SEM images of control nanocomposite films (c-film) (a) and films produced under the influence of a magnetic field (m-film) (b).

control films contain a large number of agglomerations several microns in size. At the same time, the films in which polymerization took place under the influence of a magnetic field have a fairly homogeneous structure.

Since in our experiment the m-film during the curing process was located coplanar to the surface of the magnet, then under the influence of the magnetic field the MWCNTs should be oriented along the field, that is, perpendicular to the surface of the film. With this orientation of the MWCNTs, the resolution of the SEM used by us, unfortunately, was not enough to directly reveal the fact of alignment of the MWCNTs.

An indirect confirmation of the alignment of the MWCNTs in the direction of the magnetic field can be a change in the conductivity of the films. **Fig. 3a** shows the I-V characteristics of the studied samples of films with a concentration of 1% MWCNTs measured at constant current. It can be seen that the current in films cured in a magnetic field is almost two orders of magnitude higher than the current in control samples. This ratio is maintained up to an MWCNTs

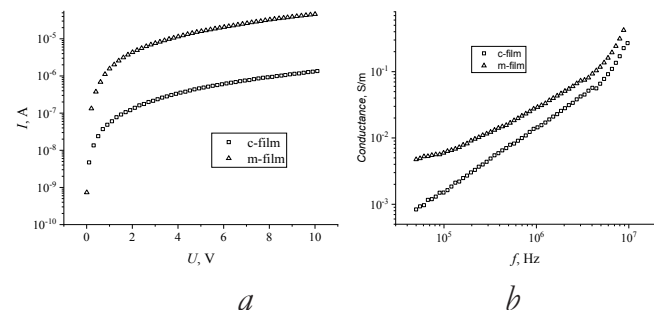


Fig. 3. Current-voltage characteristics (a) and frequency dependences of conductivity (b) of a control nanocomposite film (c-film) and a film cured under the influence of a magnetic field (m-film).

concentration of about 0.1%, when the resistivity becomes close to that of pure PVA, and it is no longer possible to detect a significant difference between the control samples and the samples exposed to the magnetic field.

Measurements of the conductivity of the films at alternating current (Fig. 3b) showed that the frequency dependence of the conductivity has a form characteristic of polarized dielectrics, namely, with an increase in frequency, a noticeable increase in conductivity is observed. In the entire frequency range, the conductivity of the films obtained in a magnetic field is noticeably higher than the conductivity of the control samples. At a frequency of 50 kHz, this difference was more than an order of magnitude, and with an increase in frequency, the difference decreases.

A similar frequency dependence of the conductivity was observed in epoxy nanocomposite films with oriented CNTs [13].

In the known models of electrical conductivity of nanocomposites [9,13], it is shown that the conductivity of a nanocomposite strongly depends on

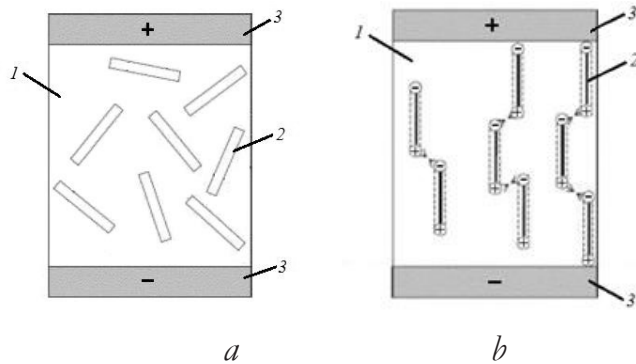


Fig. 4. Model of a film with unoriented (a) and ideally oriented (b) CNTs: 1 – polymer matrix; 2 – carbon nanotube; 3 – brass contacts.

the orientation angle of the CNTs with respect to the direction of the applied electric field. The schematic models of PVA films with randomly and oriented CNTs and metal contacts are shown in **Fig. 4**. At a low concentration of CNTs, an increase in electrical conductivity in films with oriented CNTs is explained by the appearance of an additional number of percolation chains of CNTs along the axis of their orientation.

In turn, the angle of CNTs orientation is determined by the intensity and time of application of the external magnetic field. To estimate, we will use a simplified model of the orientation of CNTs in a magnetic field, given in [14]. According to this model, CNT with a magnetic moment vector p_m and located in a magnetic field with a magnetic induction vector B (**Fig. 5**) are subjected to a torque $M = [p_m \cdot B]$, and the angle θ between the vectors of magnetic induction and magnetic moment of the CNT is determined from the equation

$$8\pi r^3 \eta \frac{d\theta}{dt} = p_m B \sin \theta, \quad (1)$$

where t is the time of exposure to the magnetic field; η is the viscosity of the polymer nanocomposite; r is the radius of a

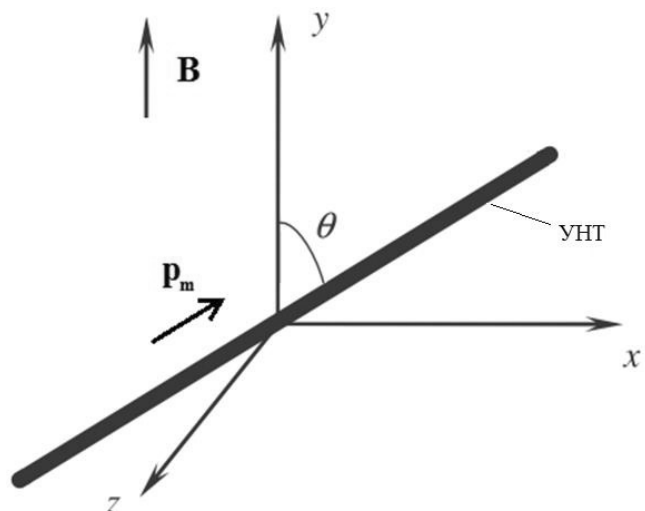


Fig. 5. Geometry of the CNT orientation problem in a magnetic field.

sphere with a volume equal to the volume of a carbon nanotube.

The numerical example given in [14], shows the possibilities of application for the alignment of the CNT field with the magnetic induction 0.28 T. For estimates in [14] the polymer viscosity was 30 Pa·s, however, the initial viscosity of real solutions of monomers before curing is significantly less and increases during the curing process. Let us estimate the change in the orientation angle taking into account the change in the viscosity of the polymer during the curing process. The simplest and, in our opinion, adequate law of viscosity change during polymer curing is the exponential law [15]:

$$\eta(t) = \eta_0 \exp(kt) = \eta_0 \exp\left(\frac{t}{\tau_0}\right), \quad (2)$$

where $k^{-1} = \tau_0$ is the characteristic time that determines the curing rate, during which the viscosity increases by a factor of e .

Equation (1) with such a law of change in viscosity is reduced to the form

$$\frac{d\theta}{\sin \theta} = \frac{p_m B}{8\pi r^3 \eta_0} \exp\left(-\frac{t}{\tau_0}\right) dt. \quad (3)$$

Integrating both parts of (3) over the curing time, we obtain the following transcendental equation for the orientation angle:

$$\begin{aligned} \log \left[\operatorname{tg} \left(\frac{\theta_{\text{cure}}}{2} \right) \right] - \log \left[\operatorname{tg} \left(\frac{\theta_0}{2} \right) \right] = \\ = \frac{p_m B \tau_0}{8\pi r^3 \eta_0} \left(1 - \exp \left(-\frac{t_{\text{cure}}}{\tau_0} \right) \right), \end{aligned} \quad (4)$$

where t_{cure} – is the curing time of the polymer, θ_0 – is the initial angle between the magnetic moment of the CNT and the vector B , θ_{cure} – orientation angle of the CNT in a cured nanocomposite.

To estimate, we take the initial orientation of CNT $\theta_0 = 90^\circ$, and the curing time is much greater than τ_0 , then we obtain a general expression for finding θ_{cure}

$$\log \left[\operatorname{tg} \left(\frac{\theta_{\text{cure}}}{2} \right) \right] = \frac{p_m B \tau_0}{8\pi r^3 \eta_0}. \quad (5)$$

After substituting in (5) the approximate numerical values of the sizes of the used MWCNTs: $r = 20 \text{ nm}$, $l = 10 \mu\text{m}$; magnetic induction $B = 0.3 \text{ T}$, and, taking according to [14] the value of $p_m = 1.0 \text{ meV/T}$, we obtain the following expression for estimating the angle θ_{cure} of the CNT orientation in the field of a neodymium magnet:

$$\log \left[\operatorname{tg} \left(\frac{\theta_{\text{cure}}}{2} \right) \right] \approx -4 \cdot 10^{-4} \frac{\tau_0}{\eta_0}. \quad (6)$$

As can be seen from (6), with the accepted model law of the change in the viscosity of the mixture and prolonged curing, the orientation angle of the CNT does not depend on the curing time, but is determined, other things being equal, by the initial viscosity of the solution and the curing time constant. The values of these parameters were not determined by us, but

taking for example $\tau_0 \approx 2400 \text{ s}$ (i.e. 40 min) and the initial viscosity of the solution $\eta_0 = 1 \text{ Pa}\cdot\text{s}$ for the orientation angle θ_{cure} , from (6) we obtain the value 10° . With an increase in the initial viscosity the orientation angle will increase. Expression (6) is convenient to use for a qualitative assessment of the expected angle of orientation of MWCNTs in PVA solutions cured in the field of a neodymium magnet, depending on the initial viscosity of the solution.

4. CONCLUSION

As a result of the studies carried out on the effect of a constant magnetic field on the properties of nanocomposite PVA films with MWCNTs during their curing, it was shown that films, obtained under the influence of a magnetic field have a more homogeneous structure, while in the control samples there is a significant amount of agglomerations of MWCNTs. In the study of the electrical conductivity of the obtained samples, it was found that the films obtained in a magnetic field have a conductivity in the direction of the MWCNT orientation, which significantly exceeds the conductivity of the control samples.

A significant increase in the conductivity of nanocomposite films, cured under the influence of a magnetic field, can serve as an indirect fact confirming the alignment of MWCNTs along the direction of the magnetic field, which is well explained on the basis of existing models of electrical conductivity of polymer nanocomposites with oriented CNTs and qualitatively corresponds to the results obtained by other authors on other polymer nanocomposites.

REFERENCES

1. Sahoo NG, Rana S, Cho JW, Li L, Chan SH. Polymer nanocomposites based on functionalized carbon nanotubes. *Progress in polymer science*, 2010, 35(7):837-867. DOI: 10.1016/j.progpolymsci.2010.03.002.
2. Vasin SV, Efimov MS, Sergeev VA. Characteristics of Current Transfer in PVA Films with Dispersed Multiwall Carbon Nanotubes on Silicon Substrates. *Tech. Phys. Lett.*, 2020, 46(6):595-598.
3. Camponeschi E, Vance R, Al-Haik M, Garmestani H, Tannenbaum R. Properties of carbon nanotube–polymer composites aligned in a magnetic field. *Carbon*, 2007, 45(10):2037-2046.
4. Zhao X, Ye L. Structure and properties of highly oriented polyoxymethylene/multi-walled carbon nanotube composites produced by hot stretching. *Compos. Sci. Technol.*, 2011, 71(10):1367-1372.
5. Kimura T, Ago H, Tobita M, Ohshima S, Kyotani M, Yumura M. Polymer Composites of Carbon Nanotubes Aligned by a Magnetic Field. *Adv. Mater.*, 2002, 14(19):1380-1383.
6. Larijani MM, Khamse EJ, Asadollahi Z, Asadi M. Effect of aligned carbon nanotubes on electrical conductivity behaviour in polycarbonate matrix. *Bull. Mater. Sci.*, 2012, 35(3):305-311.
7. LeMieux MC, Roberts M, Barman S, Jin YW, Kim JM, Bao Z. Self-Sorted, Aligned Nanotube Networks for Thin-Film Transistors. *Science*, 2008, 321(5885):101-104.
8. Li X, Zhang L, Wang X, Shimoyama I, Sun X, Seo W-S, Dai H. Langmuir-Blodgett Assembly of Densely Aligned Single-Walled Carbon Nanotubes from Bulk Materials. *J. Am. Chem. Soc.*, 2007, 129(16):4890-4891.
9. Monti M, Natali M, Torre L, Kenny JM. The alignment of single walled carbon nanotubes in an epoxy resin by applying a DC electric field. *Carbon*, 2012, 50(7):2453-2464.
10. Moaseri E, Fotouhi M, Bazubandi B, Karimi M, Baniadam M, Maghrebi M. Two-dimensional reinforcement of epoxy composites: alignment of multi-walled carbon nanotubes in two directions. *Adv. Compos. Mater.*, 2020, 29(6):547-557.
11. Kazemikia K, Bonabi F, Asadpoorhallo A, Shokrzadeh M. Influence of the concentration of carbon nanotubes on electrical conductivity of magnetically aligned MWCNT–polypyrrole composites. *Bull. Mater. Sci.*, 2016, 39(2):457-462.
12. Vasin SV, Efimov MS, Sergeev VA, Frolov IV. Current transfer mechanisms in polyvinyl alcohol films with inclusions of multi-walled carbon nanotubes. *J. Phys. Conf. Ser.*, 2020, 1697:012104. DOI: 10.1088/1742-6596/1697/1/012104.
13. Ladani RB, Wu S, Kinloch AJ, Ghorbani K, Zhang J, Mouritz AP, Wang CH. Improving the toughness and electrical conductivity of epoxy nanocomposites by using aligned carbon nanofibres. *Compos. Sci. Technol.*, 2016, 117:146-158.
14. Latypov ZZ. Anizotropnoe usilenie svoystv nanokompozitov metodami elektromagnitnoy orientatsii nanochastits v matritse [Anisotropic enhancement of the properties of nanocomposites

- by methods of electromagnetic orientation of nanoparticles in a matrix]. *Nauchnoe priborostroenie*, 2011, 1:50-52, (in Russ.).
15. Roller MB. Rheology of Curing Thermosets: A Review. *Polym. Eng. Sci.*, 1986, 26(6):432-440.

DOI: 10.17725/rensit.2021.13.465

Influence of different types of solvents on morphology, optical and conductive properties of PCBM films

Olga A. Krokhina, Nikita E. Podolsky

St. Petersburg State University, <https://spbu.ru/>

St. Petersburg 199034, Russian Federation

E-mail: olga.a.kro@gmail.com, Npodolsky48@gmail.com

Andrey S. Tyutyunik, Vladimir S. Gurchenko

Vernadsky Crimean Federal University, <https://cfuv.ru/>

Simferopol 295007, Russian Federation

E-mail: tyutyunikas@mail.ru, gurchenko_v@mail.ru

Received July 26, 2021, peer-reviewed August 15, 2021, accepted August 25, 2021

Abstract: The article deals with the influence of various types of solvents on the spectral characteristics and conductive properties of films [6,6] -methyl phenyl-C₆₁-butyric acid, precipitated from solutions. It is clearly shown that the effect of the nature of the solvent affects the morphology of the film surface. Analysis of the spectra of the optical range showed the presence of a maximum of the absorption coefficient in the frequency range of 340-490 nm. The calculation of the optical band gap clearly demonstrates the possibility of modernizing the atomic structure of films by using various types of solvents. A study of the current-voltage characteristics showed the presence of a photocurrent in carbon films deposited with dichloromethane, toluene, and chloroform.

Keywords: PCBM, thin films, optical band gap, current-voltage characteristics, photoelectric effect

PACS: 61.48.+c, 73.61.-r, 78.20.-e

Acknowledgments: The authors are grateful to the MST-Nano company for providing the PCBM source material. The reported study was funded by RFBR, project number 19-32-90038.

For citation: Olga A. Krokhina, Nikita E. Podolsky, Andrey S. Tyutyunik, Vladimir S. Gurchenko.

Influence of different types of solvents on morphology, optical and conductive properties of PCBM films. *RENSIT: Radioelectronics. Nanosystems. Information technologies*, 2021, 13(4):465-470. DOI: 10.17725/rensit.2021.13.465.

CONTENTS

- 1. INTRODUCTION (465)
- 2. SYNTHESIS AND DEPOSITION OF CARBON FILMS, EXPERIMENTAL TECHNIQUE (466)
- 3. OPTICAL PERFORMANCE (467)
- 4. CURRENT-VOLTAGE CHARACTERISTICS (468)
- 5. CONCLUSION (468)
- REFERENCES (468)

1. INTRODUCTION

Over the past decade, the interest of researchers in organic photovoltaics has increased [1-3]. This is due to the relative low cost of manufacturing combined with the ease of production of the final product, which is an indisputable advantage over more expensive and difficult-to-manufacture analogues [4,5]. For example, the

use of roll-to-roll technology makes it possible to produce microcircuits by directly “printing” electronic circuits at a high speed [6]. Due to its excellent electron-acceptor properties, fullerene has established itself as a promising component in organic electronics [7]. In particular, fullerene C₆₀ is a fairly good n-type semiconductor, which demonstrates a high electron mobility 11 cm²V⁻¹s⁻¹; therefore, it is widely used in the creation of OFET (Organic field-effect transistor) [8]. The use of fullerene as a transfer layer for electrons makes it possible to improve the electrical characteristics of organic light-emitting diodes (OLEDs) [9].

Along with fullerene C₆₀, its derivatives, for example, [6,6]phenyl-C₆₁-butyric acid methyl ester (PCBM), have also become very popular.

Currently, PCBM is widely used in pharmaceuticals and organic photovoltaic systems [10-11]. More recently, the energy conversion efficiency for solar cells using PCBM and polymer materials has reached 7-8% [12-15]. Nevertheless, despite the extensive list of works devoted to the creation of devices using PCBM, the question of choosing the optimal solvent for obtaining thin-film structures with the maximum photocurrent remains relevant. Considering all of the above, it was these prerequisites that prompted this study, in which we considered how the use of various types of solvents affects the electrophysical and electrodynamic properties of carbon thin-film structures deposited by the method of watering from solution onto dielectric substrates [16].

2. SYNTHESIS AND DEPOSITION OF CARBON FILMS, EXPERIMENTAL TECHNIQUE

PCBM was synthesized according to a modified method proposed by F. Wudl [17]. This method is based on the process of 1,3-dipolar addition of methyl ester of δ -phenylbutyric acid to the fullerene core. The main benefit of the final product is the increase in PCE (power conversion efficiency) up to 5.3%.

The formation of films from the initial PCBM powder material was carried out by pouring from a solution onto substrates. Non-aromatic solvents were used: dichloromethane (CH_2Cl_2), chloroform (CHCl_3), carbon tetrachloride (CCl_4) and aromatic: toluene ($\text{C}_6\text{H}_5\text{CH}_3$), benzene (C_6H_6). The concentration of the starting substance in the solution was 0.5 mg/ml. After thorough mixing and holding (at least 48 h at room temperature), the resulting suspensions were applied to dielectric and conductive substrates, with a volume of 1 ml of the latter. Cover glasses with geometric parameters of 18×18 mm were used as dielectric substrates. To measure the conducting characteristics, indium tin oxide (ITO) with a resistivity of 16-18 Ω/sq was used as a contact group, as well as thin aluminum films obtained by vacuum deposition

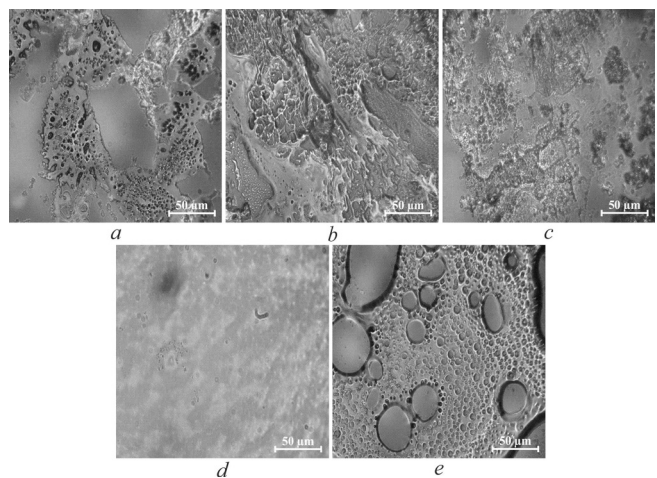


Fig. 1. Surface morphology of PCBM films depending on the type of solvent: a - dichloromethane; b - chloroform; c - carbon tetrachloride; d - toluene; e - benzene.

on sittall, having high uniformity, low roughness with resistivity 20 Ω/sq .

The analysis of the surface relief and volumetric irregularities was carried out by means of transmission and reflection microscopy based on a LOMO Mii-4M microinterferometer using additional illumination with a semiconductor laser and an extended optical path on a camera with a 1/2FF 10MP matrix (Fig. 1). To determine the electrodynamic characteristics, a GBC Cintra-4040 spectrophotometer was used to study the interaction of electromagnetic radiation in the optical range and obtain the transmission, absorption (Fig. 2) and reflection coefficients. A distinctive feature of this device is the presence of a double monochromator in the Czerny-Turner configuration. Tungsten and deuterium lamps were used as radiation sources. Due to this, the range of incident radiation was from 250 to 850 nm. During the experiment, a

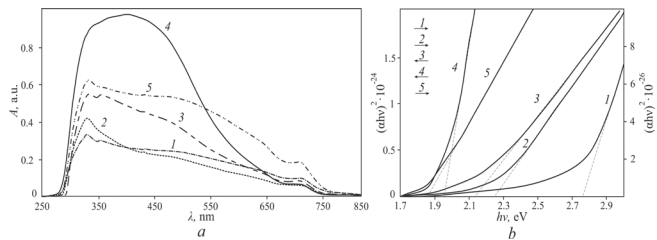


Fig. 2. Absorption spectra of the optical range (a) and the optical band gap (b) of films depending on the solvent: 1) dichloromethane, 2) chloroform, 3) tetrachloromethane, 4) toluene, 5) benzene.

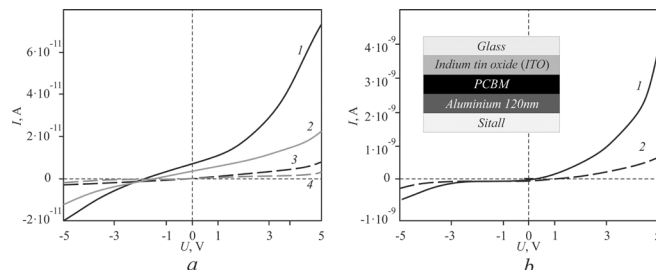


Fig. 3. (a) Current-voltage characteristics of PCBM, where: 1 - light PCBM in toluene; 2 - light PCBM in dichloromethane; 3 - dark PCBM in toluene; 4 - PCBM in dichloromethane. (b) Current-voltage characteristics of PCBM in chloroform, where: 1 - light; 2 - dark.

clean substrate was used as a normalization basis. The study of current-voltage characteristics (**Fig. 3**) was carried out using a keysight B1500A semiconductor analyzer. To analyze the photoactivity of the studied carbon films, an LED matrix was used as an illumination source, with a flux density of about 300 W/m² and an incoming power of 60 mW. All measurements were carried out at least ten times at room temperature not exceeding 30°C using a shielding chamber and subsequent averaging of the results obtained.

As a result of surface analysis, it was found that the use of various types of solvents significantly affects the final surface morphology of PCBM films. For example, films deposited with dichloromethane (CH_2Cl_2) are characterized by an "island-like" structure (Fig. 1a). Moreover, its thickness varies in the range from 8 to 25 μm . A more uniform surface is observed for films deposited with chloroform (CHCl_3). It is worth noting the formation of "cells" with a diameter of 10-15 μm on the surface of the film. The thickness of the film itself is 4-5 μm (Fig. 1b). PCBM films synthesized with tetrachloromethane (CCl_4) also showed the presence of an "island-like" structure, 5-10 μm thick (Fig. 1c). The highest homogeneity of the PCBM film was achieved using toluene ($\text{C}_6\text{H}_5\text{CH}_3$) as a solvent (Fig. 1d). The thickness of such films is about 500-600 nm. The use of benzene (C_6H_6) made it possible to obtain a relatively uniform film with a thickness of about 5-6 μm (Fig. 1e).

Thus, the nature of the solvent effect on the final homogeneity and morphology of the carbon film is clearly shown.

3. OPTICAL PERFORMANCE

Due to the variety of the surface morphology of the films and the characteristic feature of each type of samples, it is necessary to evaluate the optical properties, in particular, the absorption spectra (Fig. 2a). Analysis of the optical characteristics showed that the highest absorption coefficient is possessed by PCBM films obtained with the use of toluene. Absorption maximum ~ 0.9 a.u. falls on the wavelength range of 340-490 nm and is accompanied by a further decline to the near infrared spectral range. The next largest film in terms of absorbing properties is benzene, with a maximum absorption coefficient of ~ 0.6 a.u. The use of tetrachloromethane made it possible to obtain an absorption maximum of ~ 0.5 a.u. The remaining two types of images differ insignificantly from each other, with the absorption coefficient at the peak: for chloroform ~ 0.4 a.u., for dichloromethane ~ 0.3 a.u.

Considering the similarity of the frequency dependences of the optical range and the insignificant difference in the structures of the obtained films, one should assume the presence of an optical gap in the experimental samples. Assuming that the main transitions between the valence and conduction bands are indirect allowed transitions, depending on the absorption coefficient on the incident photon energy, according to the Tauc formula, let us take a power exponent m equal to two [18,19]:

$$\alpha \sim \frac{1}{hv} (\hbar v - E_g)^m,$$

where α is the absorption coefficient; hv is the energy of the optical quantum; E_g is the band gap of the material. In this case, the optical band gap: PCBM in dichloromethane – 2.75 eV; PCBM in chloroform – 2.26 eV; PCBM in tetrachloromethane – 2.14 eV; PCBM in toluene

– 1.95 eV; PCBM in benzene – 1.84 eV (Fig. 2b). The results obtained clearly demonstrate the possibility of modernizing the atomic structure of carbon films by using various types of solvents.

4. CURRENT-VOLTAGE CHARACTERISTICS

To research the electrical parameters, PCBM carbon films were formed in the form of a "sandwich" structure: Al-PCBM-ITO. The geometric parameters of both layers (Al and ITO) were 10×10 mm (inset in Fig. 3b). The use of thin-film aluminum and tin indium oxide as a contact group is due to the fact that the electron work function of ITO is comparable to that of polymers, which provides ohmic contact with the organic layer, while Al forms a rectifying barrier due to a lower work function [20].

The primary study of the charge kinetics was carried out by analyzing the current-voltage characteristics (I-V characteristics) in the range from –5 to 5 V. For PCBM deposited with toluene, the current-voltage characteristic is nonlinear and asymmetric at forward currents of 8 pA and reverse currents of 2.6 pA (Fig. 3a). Using dichloromethane, the currents flowing in the film were 1.3 pA for the forward leg and 0.7 pA for the reverse leg (Fig. 3a). For the samples: CHCl₃, CCl₄, C₆H₆, the limiting values of the currents in the forward branch were 3.5 nA, 5 pA, 4.8 pA, respectively, the reverse currents were 0.4 nA, 9 pA, 7 pA.

It is worth noting the presence of light sensitivity in three of the five types of images, when the latter is irradiated with an electromagnetic wave of the optical range (Fig. 3a,b). The greatest increase in the charge kinetics upon irradiation was recorded in films deposited with toluene (an increase of 8.8 times) and dichloromethane (an increase of 8.5 times). The smallest increase was recorded for PCBM in chloroform (5.8 times increase). Comparison of the I-V characteristic with the surface

morphology makes it possible to conclude that a galvanic bond is formed between individual centers of agglomerators growth that form the basis of carbon films.

5. CONCLUSION

Thus, the paper considers the electrical properties of PCBM-based carbon films deposited using 5 types of solvents. The main feature is the presence of light sensitivity in three of the five types of samples. For samples precipitated using toluene, the increase in kinetics was ~ 8.8 times, for dichloromethane ~ 8.5 times, for chloroform – 5.8 times. It is also worth noting that the mobility of charge carriers is not determined over the entire surface of the "film" structure, but is formed by separate sections and agglomerations, which are successive connected chains.

Analysis of the surface morphology clearly showed that when using toluene, the result is the most uniform film surface. The analysis of the optical characteristics showed that the maximum of the absorption spectrum for all types of carbon films is observed in the wavelength range of 340-490 nm. The highest absorption (~ 0.9 a.u.) is possessed by the PCBM film deposited with toluene. The smallest absorption coefficient was recorded for the film in dichloromethane (~ 0.3 a.u.). The calculation results of the optical band gap clearly demonstrate the possibility of modernizing the atomic structure of carbon films by using various types of solvents.

REFERENCES

1. Kim JY, Lee K, Coates NE, Moses D, Nguyen TQ, Dante M, Heeger AJ. Efficient tandem polymer solar cells fabricated by all-solution processing. *Science*, 2007, 317(5835).
2. Nguyen LH, Hoppe H, Erb T, Günes S, Gobsch G, Sariciftci NS. Effects of Annealing on the Nanomorphology and Performance of Poly(alkylthiophene):Fullerene Bulk-Heterojunction Solar Cells. *Advanced functional materials*, 2007, 17(7):1071-1078.

3. Ruderer MA, Prams SM, Rawolle M, Zhong Q, Perlich J, Roth SV, Müller-Buschbaum P. Influence of annealing and blending of photoactive polymers on their crystalline structure. *J Phys Chem B.*, 2010, 114(47):1545.
4. Ruderer MA, Guo S, Meier R, Chiang H-Y, Körstgens V, Wiedersich J, Perlich J, Roth SV, Müller-Buschbaum P. Solvent-Induced Morphology in Polymer-Based Systems for Organic Photovoltaics. *Advanced Functional Materials*, 2011, 21(17):3382-3391.
5. Gusev AN, Mazinov AS, Tyutyunik AS, Gurchenko VS. Spectral and conductive properties of film heterostructures based on fullerene-containing material and 4-methylphenylhydrazone N-isoamilisatine. *Radioelectronics. Nanosystems. Information Technologies (RENSIT)*, 2019, 11(3):331-336. DOI: 10.17725/rensit.2019.11.331.
6. Gusev AN, Mazinov AS, Shevchenko AI, Tyutyunik AS, Gurchenko VS, Braga EV. The Voltage–Current Characteristics and Photoelectric Effect of Fullerene C₆₀–N-Isoamylisatin 4-Methylphenylhydrazone Heterostructures. *Pisma v zhurnal tehnicheskoy fiziki*, 2019, 45(10):997-1000 (in Russ.).
7. Brabec CJ, Sariciftci NS, Hummelen JC. Plastic Solar Cells. *Advanced functional materials*, 2001, 11(1):15-26.
8. Mazinov AS, Tyutyunik AS, Gurchenko VS. Changes in the spectral and conducting properties of fullerene films depending on the type of solvent. *Prikladnaya fizika*, 2020, 2:64-70 (in Russ.).
9. Mazinov AS, Tyutyunik AS, Gurchenko VS, Ilina VYu. Effect of masses of active layers of C₆₀-4-methylphenylhydrazone N-isoamylisatin fullerene heterostructures on their rectifying characteristics. *RENSIT*, 2020, 12(3):361-368. DOI: 10.17725/rensit.2020.12.361.
10. Mchedlov-Petrossyan NO. Fullerenes in Molecular Liquids. Solutions in “Good” Solvents: Another View. *Journal of Molecular Liquids*, 2011, 161(1):1-12.
11. Mchedlov-Petrossyan NO. Fullerenes in Liquid Media: An Unsettling Intrusion into the Solution Chemistry. *Chem. Rev.*, 2013, 113:5149-5193.
12. Min J, Zhang Z, Zhang S, Zhang M. Synthesis and Photovoltaic Properties of D–A Copolymers Based on Dithienosilole and Benzotriazole. *Macromolecules*, 2011, 44(19):7632-7638.
13. Su M-S, Kuo C-Y, Yuan M-C, Jeng US, Su C-J, Wei K-H. Improving Device Efficiency of Polymer/Fullerene Bulk Heterojunction Solar Cells Through Enhanced Crystallinity and Reduced Grain Boundaries Induced by Solvent Additives. *Advanced Materials*, 2011, 23:3315.
14. Price SC, Stuart AC, Yang L, Zhou H, You W. Fluorine substituted conjugated polymer of medium band gap yields 7% efficiency in polymer-fullerene solar cells. *J. Am. Chem. Soc.*, 2011, 133:4625.
15. Piliego C, Holcombe TW, Douglas JD, Woo CH, Beaujuge PM, Fréchet JMJ. Synthetic control of structural order in N-alkylthieno[3,4-c]pyrrole-4,6-dione-based polymers for efficient solar cells. *J. Am. Chem. Soc.*, 2010, 132:7595.
16. Gusev AN, Mazinov AS, Shevchenko AI, Tyutyunik AS, Gurchenko VS, Braga EV. Research of heterojunctions based on the system of fullerene and hydrazone. *Prikladnaya fizika*, 2019, 6:48-53 (in Russ.).
17. Ito T, Ohno T, Iwai T, Matsumoto F, Hida K, Moriwaki K, Mizuno T. Facile Synthesis of [6,6]-Phenyl-C₆₁/71-Butyric Acid Methyl Esters via Sulfur Ylides for Bulk-Heterojunction Solar Cell. *Synlett*, 2013, 24(15):1988-1992.
18. Tan ST, Chen BJ, Sun XW, Fan WJ, Kwok HS, Zhang XH, Chua SJ. Blueshift of optical

- band gap in ZnO thin films grown by metal-organic chemical-vapor deposition. *Journal of Applied Physics*, 2005, 98:013505.
19. Gusev AN, Mazinov AS, Tyutyunik AS, Fitaev IS, Gurchenko VS, Braga EV. Effect of Doping with N, Br, and F Atoms on Electrodynamic Characteristics and Physical Properties of Isatin- β -anil. *Zhurnal tehnicheskoy fiziki*, 2021, 66(1):84-92 (in Russ.).
20. Pandey RK, Singh AK, Prakash R. Enhancement in performance of polycarbazole-graphene nanocomposite Schottky diode. *AIP Advances*, 2013, 3(12):122120.

DOI: 10.17725/rensit.2021.13.471

Hybrid superconducting heterostructures with magnetic interlayers

Karen Y. Constantinian, Gennady A. Ovsyannikov, Yulii V. Kislinski, Andrey M. Petrzhik

Kotelnikov Institute of Radioelectronics and Electronics of RAS, <http://www.cplire.ru/>
Moscow 125009, Russian Federation

E-mail: karen@hitech.cplire.ru, gена@hitech.cplire.ru, yulii@hitech.cplire.ru, petrzhik@hitech.cplire.ru

Anton V. Shadrin

Moscow Institute of Physics and Technology, <https://mipt.ru/>

Dolgoprudny 141701, Moscow Region, Russian Federation

E-mail: anton_sh@hitech.cplire.ru

Alexei S. Kalaboukhov

Chalmers University of Technology, <https://www.chalmers.se/>

SE-412 96 Göteborg, Sweden

E-mail: alexei.kalaboukhov@chalmers.se

Received October 20, 2021, peer-reviewed October 27, 2021, accepted November 08, 2021

Abstract: Electron transport processes in oxide superconducting heterostructures with epitaxially grown magnetic thin-film interlayers, in which the interaction of superconducting correlations and magnetic ordering occurs due to superconducting and magnetic proximity effects, have been studied experimentally. Hybrid mesa-heterostructures were prepared from thin-film bottom cuprate superconductor (S), magnetic (M) interlayer made of manganite or an antiferromagnetic cuprate, and the upper electrode made from an ordinary superconductor. When the cuprate antiferromagnetic material was replaced by a ferromagnetic manganite interlayer, the superconducting current was suppressed, although the thin magnetic film was several times thinner, 5 nm, and the temperature was lowered to 0.3 K. At low temperatures dependences of differential resistance vs. voltage for mesa-heterostructures with manganite interlayer featured mini-gap low-energy states.

Keywords: superconducting heterostructures, thin films, manganites, cuprates, differential conductivity, exchange energy

PACS: 74.45.+c, 74.72.-h, 75.47.Lx, 73.63.-b

Acknowledgments: This work was supported by the Ministry of Science and Higher Education of the Russian Federation (Agreement No. 075-15-2021-990).

For citation: Karen Y. Constantinian, Gennady A. Ovsyannikov, Anton V. Shadrin, Yulii V. Kislinski, Andrey M. Petrzhik, Alexei S. Kalaboukhov. Hybrid superconducting heterostructures with magnetic interlayers. *RENSIT: Radioelectronics. Nanosystems. Information technologies*, 2021, 13(4)471-478. DOI: 10.17725/rensit.2021.13.471.

CONTENTS

1. INTRODUCTION (472)
2. EXPERIMENTAL MESA-HETEROSTRUCTURES (473)
 3. RESULTS OF MEASUREMENTS AND DISCUSSION (473)
 - 3.1. SPECIFIC RESISTANCE OF MHS WITH

MANGANITE INTERLAYERS (473)

- 3.2. CHARACTERISTICS OF MHS WITH $\text{Ca}_x\text{Sr}_{1-x}\text{CuO}_2$ ANTIFERROMAGNETIC LAYER (476)

4. CONCLUSION (477)

REFERENCES (477)

1. INTRODUCTION

The coexistence of superconducting and magnetic ordering leads to an unusual behavior of the superconducting pair potential. In ferromagnetic (*F*) and superconducting (*S*) junctions the oscillatory behavior of the paired potential took place [1,2], and as a consequence, a π -state occurs in *S/F/S* structures as predicted in [3] and experimentally confirmed on niobium superconducting structures with copper-nickel interlayers [4]. The interest to *S/F/S* structures is caused by opportunities of obtaining non-sinusoidal current-phase relation, π -junctions, systems with spin valve properties, electronic transport with spin-triplet superconducting correlations with nonzero spin projection, long-range proximity effect and a number of other effects.

A lot number of papers have been devoted to the physical mechanisms for the development of *S/F/S* structures with metallic *F*-layers (see, for example, reviews [5,6]). The case of the *S/AF* boundary formed between a superconductor and an antiferromagnet (*AF*) is no less interesting [7-9]. However, the creation of structures based on metallic layers with *S*, *F* and *AF* properties encountered technological problems, the solution of which are associated with the design and development of technology of heterostructures fabrication with epitaxially grown interfaces between thin films of oxide materials with the required functionalities.

Note, when polycrystalline films are used for preparation of *F/S* interfaces, the influence of the crystal structure on contacting materials leads to that a number of interesting effects cannot be observed.

For example, the anomalously strong proximity effect was absent in the junctions with the *AF* interlayers, which manifests itself in a magnetic layered structure with the *AF* ordering of interlayer [7,8].

A number of specific properties of manganites [10] and antiferromagnetic cuprates have led to increasing interest in heterostructures with epitaxially grown interlayers of magnetically active materials characterized by identical crystal structure and similar crystallographic parameters. As shown in [11,12], thin-film interfaces of manganite/superconducting cuprate $\text{La}_{0.7}\text{Ca}_{0.3}\text{MnO}_3/\text{YBa}_2\text{Cu}_3\text{O}_x$ (LCMO/YBCO) or $\text{La}_{0.7}\text{Sr}_{0.3}\text{MnO}_3/\text{YBa}_2\text{Cu}_3\text{O}_x$ (LSMO/YBCO) can be made very smooth on atomic level and free of defects. Chemical diffusion of the boundary elements was absent within the experimental error, and measurements [13] showed a minor migration of manganese ions within 1 nm. The high degree of polarization of manganites indicates that superconducting structures containing manganite interlayers with ferromagnetic ordering, as well as antiferromagnetic oxides, are very interesting for studies of spin-dependent electronic transport and proximity effects in multilayer heterostructures.

This paper presents the results of experimental studies of hybrid *S/M/S_d* mesa-heterostructures (MHS) $\text{Nb}/\text{Au}/\text{M}/\text{YBa}_2\text{Cu}_3\text{O}_x$ in which an Nb/Au bilayer was used as the *S* superconductor with *s*-symmetry of order parameter and an epitaxial film of $\text{YBa}_2\text{Cu}_3\text{O}_x$ (YBCO) superconducting cuprate with a dominant order parameter with *d*-wave symmetry, used as the *S_d* superconductor. The magnetically active layer (*M*) was prepared from a manganite

film with optimal $\text{La}_{0.7}\text{Ca}_{0.3}\text{MnO}_3$ doping, or from non-doped manganite film LaMnO_3 . The optimal doping level means the level of doping at which the Curie temperature is maximal.

The results of resistivity measurements of MHS with manganite interlayers at low temperatures $T = 2 \text{ K}$, 1 K and 0.3 K will be compared to the dependences obtained in [14], calculated taking into account the impact of exchange interaction energy b . Another type of MHS studied in this work has the M -layer material made from antiferromagnetic $\text{Ca}_x\text{Sr}_{1-x}\text{CuO}_2$ cuprate with doping level $x = 0.5$ (CSCO).

2. EXPERIMENTAL MESA-HETEROSTRUCTURES

The superconducting cuprate YBCO film with critical temperature $T_c = 88\text{-}89 \text{ K}$ was prepared by laser ablation at $700\text{-}800^\circ\text{C}$ and pressure 0.3 mbar on $(110)\text{NdGaO}_3$ (NGO) substrate. A thin $d_M = 5\text{...}20 \text{ nm}$ manganite M -layer film was epitaxially grown in the same vacuum chamber at high temperature and then coated with a thin ($20\text{-}30 \text{ nm}$) gold (Au) layer after cooling to room temperature. A subsequent layer of niobium (Nb) was deposited by magnetron sputtering. The protective Au film used to reduce oxygen diffusion from the contacting oxides. The proximity effect between the superconducting (Nb) and metallic (Au) films gave the critical bilayer temperature $T_c = 8.5\text{...}9 \text{ K}$, close to the critical temperature of the Nb film (9.2 K). The LCMO M -layer manganite thin film at temperatures $T < 100 \text{ K}$ has the properties of a ferromagnetic metal. In the case of manganite LaMnO_3 , very thin M -layer at low temperatures may exhibit properties of an antiferromagnet [10,13], however, at thicknesses which

exceed the thickness of pin-holes ($d_M > 1 \text{ nm}$) it becomes a weak ferromagnet.

The topology of the mesa-heterostructures was formed by photolithography, plasma-chemical, and ion-beam etching methods [15]. A protective layer of SiO_2 insulator was deposited by high-frequency magnetron sputtering and then a square-shaped planar geometry was formed, defining the MHS area varied from $A = 10 \times 10 \mu\text{m}^2$ to $50 \times 50 \mu\text{m}^2$. For comparison, a similar fabrication procedure was used for structures without M -layer [16]. To avoid the appearance of pin-holes (short circuits for electric current), the deposited M films were thicker than the surface roughness of the YBCO layer. Direct deposition of Nb on top of the YBCO film results in an Nb/YBCO interface with high resistivity due to oxidation of the Nb film. Thus, if the Au layer locally damaged due to the finite surface roughness of the M/S_d interface, then niobium oxide is formed directly there, which prevents pin-hole formation.

3. RESULTS OF MEASUREMENTS AND DISCUSSION

3.1. SPECIFIC RESISTANCE OF MHS WITH MANGANITE INTERLAYERS

The temperature dependences of the resistivity of epitaxial LMO and LCMO films deposited on NGO substrate were investigated [15] to evaluate their contribution to the MHS resistivity. Note that the resistance of the LMO film is much higher than that of the doped ferromagnetic manganite film, particularly, the LCMO. The increase in resistance with decreasing temperature indicates nonmetallic conductivity.

A detailed analysis of the temperature dependence shows that on the dependence $R(T)$ the Mott insulator behavior with two

components can be distinguished, which are described by an expression $\rho \propto \exp(T_0/T)^{1/4}$ with different characteristic temperatures $T_0 = 34 \cdot 10^6$ K at $T > T_{\text{CU}}$ and $T_0 = 4 \cdot 10^6$ K at $T < T_{\text{CU}}$, where T_{CU} is the Curie phase transition temperature. The difference in T_0 parameter below and above T_{CU} can be described using a polaron model of hopping conduction at high temperature [16] for which the dependence $\rho = \alpha \exp(T_0^*/T)^{1/4}$, where T_0^* is the activation temperature and the parameter α depends on the concentration of charge carriers and the jump length.

The *MHS* resistance is described by sum of resistances $R = R_{\text{YBCO}} + R_{\text{M/Y}} + R'_{\text{M}} + R_b + R_{\text{Nb/Au}} + R_{\text{Nb}} + R_{\text{Au}}$, where R_{YBCO} is the YBCO electrode resistance, $R_{\text{M/Y}}$ is the *M*/YBCO interface resistance, R'_{M} is the *M*-layer resistance, R_b is the Au/*M* barrier resistance, and R_{Nb} and R_{Au} are the Nb electrode and Au film resistances, respectively. Usually, the contribution from the Au thin film resistance can be neglected [16].

At temperatures above the superconducting critical temperature ($T_c = 70 \div 80$ K) of the YBCO film ($T > T_c$), the temperature dependence of the MHS resistance $R(T)$ is similar to that of a single YBCO film. MHS with *M*-layer of a manganite film had no superconducting critical current, although the thickness d_M was reduced to 5 nm. In the case of LSMO manganite *M*-layer its impedance in MHS, calculated from the resistivity of the single film, is much higher than the total impedance of the MHS. Consequently, there is a significant decrease in the resistivity of the *M*-layer in the MHS.

Taking the calculated maximum resistance of the interface between Au and manganite and assuming that the contribution of the *M*-layer resistance is insignificant, we find

that the determining factor in the MHS resistance comes from the manganite/YBCO interface. **Fig. 1** shows the family of dependences of characteristic resistances $R_N A(V)$ for MHS with an LMO layer with thickness $d_M = 6$ nm and size $L = 20 \mu\text{m}$, measured at temperatures $T = 17.8$ K, 25.9 K, 30.2 K, and 39.3 K, all above the critical temperature of the Nb film. An asymmetry with respect to $V = 0$ with a shift of the maximum about 10 mV can be seen, which can be explained by the influence of LMO ferromagnetism on the tunneling characteristics of MHS [17].

Although the resistivity of the single LMO film is significantly higher than that of the LCMO film at reduced temperatures, the resistance of the MHS with an LMO layer is significantly lower than the calculated R'_M contribution. With a further decrease in temperature to $T = 6$ K, which is already below the superconducting transition temperature of the Nb film the singularity feature of resistance with a minimum at $V = 0$ is manifested more clearly. However, the question whether it relates to the

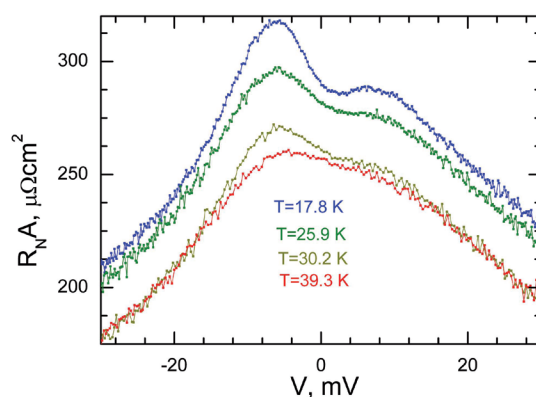


Fig. 1. Family of characteristic resistivity dependences $R_N A(V)$ for MHS with LMO layer of thickness $d_M = 6$ nm and $L = 20 \mu\text{m}$, measured at temperatures $T = 17.8$ K, 25.9 K, 30.2 K and 39.3 K, which are higher than the critical temperature of the Nb film.

appearance of superconducting current remained open.

Measurements at lower temperatures are shown in **Fig. 2**, which shows $R_N A(V)$ dependences for MHS, taken at $T < 4.2$ K. At low temperatures, the M -layer contribution from the LCMO to the MHS resistance is small due to the metal-insulator transition of the LCMO film. For the case of LMO film, on the contrary, as mentioned above, there is an increase in R'_M resistance with decreasing temperature, but the $R_{M/Y}$ contribution is more significant because the transparency D of the LCMO/YBCO and LMO/YBCO interface is smaller than for Au/LCMO or Au/LMO.

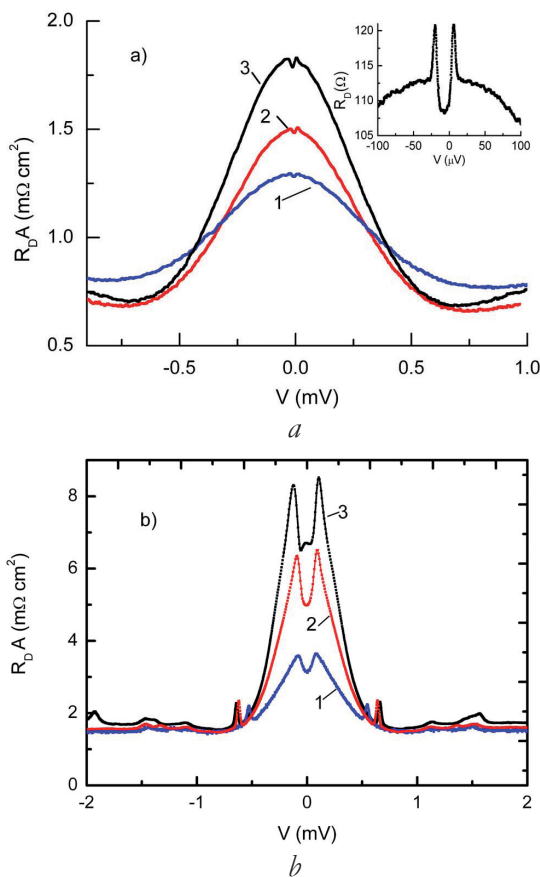


Fig. 2. Family of dependences of $R_N A(V)$ at the temperatures $T = 2 \text{ K}$, 1 K and 0.3 K for (a) MHS with LMO interlayer $d_M = 6 \text{ nm}$, the inset shows a more detailed dependence at $T = 0.3 \text{ K}$; (b) MHS with LC MO interlayer with thickness $d_M = 20 \text{ nm}$.

So, we are dealing with the structures with two low transparent barriers, which can strongly suppress the superconducting current (or critical I_C current) in proportion to the square of the D_2 transparency. The absence of superconducting current is indicated by the dependence $R_D(V)$ shown in the inset in Fig. 2a. It can be seen that even at $T = 0.3 \text{ K}$ there is an increase in resistance at $V = 0$, and low-energy sub-gap features on the dependence $R_D(V)$ distinctly registered.

It is possible to evaluate the influence of exchange interaction by values of the normalized conductivity ratio σ_0/σ_N , where σ_0 is taken at $V = 0$, and σ_N corresponds to conductivity of MHS in the normal conducting state. **Fig. 3** shows the temperature dependences of experimental values for σ_0/σ_N , taken from data on Fig. 2 and calculated using approach [14] taking values of exchange interaction $b = 0.1$ and $b = 1$ at fixed all other parameters of modeling. From Fig. 3 one may conclude that the

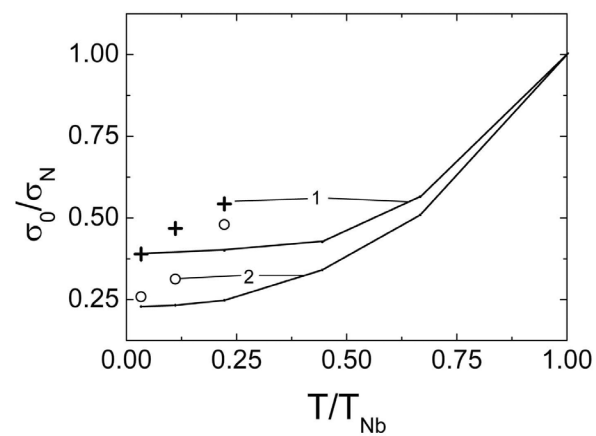


Fig. 3. Temperature dependence of the normalized conductivity σ_0/σ_N at $V = 0$ for MHS with LMO (1) and LC MO (2) interlayers. Experiment: crosses (LMO), light circles (LCMO), theoretical curves correspond to exchange energy $b = 0.1$ (1) and $b = 1$ (2).

ferromagnetism in the LMO layer is much weaker than in the LCMO.

3.2. Characteristics of MHS with

$\text{Ca}_x\text{Sr}_{1-x}\text{CuO}_2$ antiferromagnetic layer

Replacement of the ferromagnetic interlayer with an antiferromagnetic one is manifested in appearance of a superconducting current.

Fig. 4 shows the temperature dependence of the resistance of three MHS with M layer made of $\text{Ca}_{0.5}\text{Sr}_{0.5}\text{CuO}_2$ (CSCO) for different interlayer thicknesses $d_M = 80, 50$, and 20 nm. The inset on the same figure shows the superconducting transition for the MHS with $d_M = 20$ nm.

The superconducting current I_C was observed at $T = 4.2$ K for MHS with interlayer thickness up to $d_M = 50$ nm, detectable by the differential conductivity peak on the dependence of $R_D(V)$ at $V=0$. In contrast to the manganite interlayers characterized by the nonzero energy of exchange interaction $b > 0$, in the case of the antiferromagnetic (AF) interlayer, the main contribution to the reduction of the superconducting current comes from the transparency of the Au/CSCO

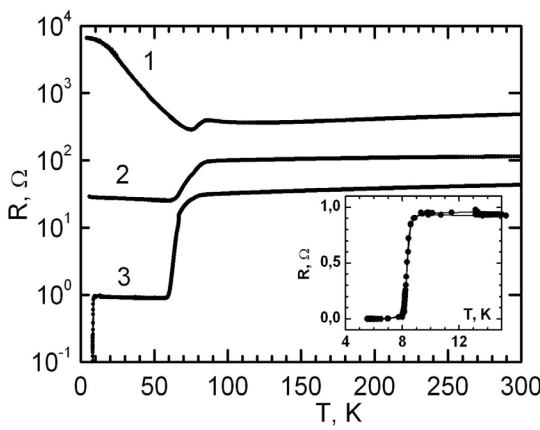


Fig. 4. Temperature dependence of the resistance of three MHS with CSCO. The curve (1) corresponds to $d_M = 80$ nm, (2) $d_M = 50$ nm, (3) $d_M = 20$ nm. The inset shows the transition to the superconducting state of MHS (3).

and YBCO/CSCO barriers. We consider that the barrier thickness condition for existence of superconducting current is satisfied as for the case of $S/N/S$ junctions, when I_C exponentially decreases with the ratio d_N/ξ_N (ξ_N is the coherence length in the normal metal interlayer).

Thus, MHS can be considered as $S_d/M/S$ structures, where S_d is a YBCO electrode with a dominant d -wave order parameter, S is a superconducting Nb/Au bilayer (due to the strong proximity effect in thin Au film of thickness $d_{Au} < 1$, smaller than the free path length l).

Fig. 5 shows a simplified model for YBCO/CSCO/Au/Nb MHS in which the antiferromagnetic interlayer is represented as a normal metal with an antiferromagnetic ordering N(AF) and the CSCO/Au barrier with transparency $D < 1$ is an insulator with thickness d_0 and dielectric permittivity ϵ . The barrier layer in the inset is given as white gap between the CSCO and Au films, in which there is

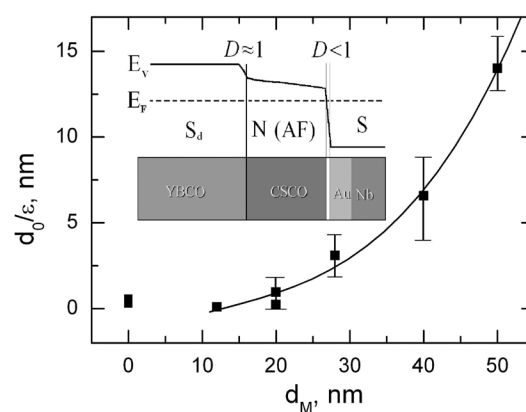


Fig. 5. Dependence of the barrier parameter d_0/ϵ vs. the CSCO layer thickness d_M . The inset shows the band diagram for the YBCO/CSCO/Au/Nb hybrid mesa-heterostructure with different values of interface transparency D . The E_V energy denotes the valence zone, and the E_F is the Fermi energy shown as a dashed line.

drown an abrupt change in the energy level E_v characterizing the valence zone. As can be seen from Fig. 5, the parameter d_0/ε grows exponentially with thickness d_M , calculated from the capacity $C = A\varepsilon/4\pi d_0$ of the MHS, which was estimated from the hysteresis of I-V characteristics which were observed in experiment.

4. CONCLUSION

Hybrid planar mesa-heterostructures with three types of the oxide barrier layer epitaxially grown on top of the $\text{YBa}_2\text{Cu}_3\text{O}_x$ cuprate superconductor were experimentally studied, and the Au/Nb bilayer was used as the upper superconducting electrode. In the case of a barrier layer of ferromagnetic manganite $\text{La}_{0.7}\text{Ca}_{0.3}\text{MnO}_3$ or LaMnO_3 , the exchange interaction prevented flow of superconducting current even when the mesa-heterostructures were cooled to temperature $T = 0.3 \text{ K}$ and the layer thickness was reduced to $d_M = 6 \text{ nm}$ - a value which guarantees the absence of pinholes. In the case of the $\text{Ca}_{0.5}\text{Sr}_{0.5}\text{CuO}_2$ antiferromagnetic cuprate interlayer, superconducting current was detected at $T = 4.2 \text{ K}$ increasing the interlayer thickness up to $d_M = 50 \text{ nm}$. At low temperatures $T < 4.2 \text{ K}$, the dependences of differential resistance vs. voltage for mesa-heterostructures with manganite interlayers exhibited features which could be attributed to the appearance of low-energy sub-gap states.

REFERENCES

1. Fulde P and Ferrell RA. Superconductivity in a strong spin-exchange field. *Phys.Rev.*, 1964, 135:A550-A563.
2. Larkin AI and Ovchinnikov YN. Inhomogeneous state of superconductors. *Sov.Phys.JETP*, 1965, 20:762-769.
3. Bulaevskii LN, Kuzii VV, and Sobyanin AA. Superconducting system with weak coupling with a current in the ground state. *JETP Lett.*, 1977, 25:290-294.
4. Ryazanov VV, Oboznov VA, Rusanov AYu, Veretennikov AV, Golubov AA, and Aarts J. Coupling of two superconductors through a ferromagnet: Evidence for a π -junction. *Phys.Rev.Lett.*, 2001, 86:2427-2430.
5. Buzdin AI. Proximity effects in superconductor-ferromagnet heterostructures. *Rev.Mod.Phys.*, 2005, 77(3):935-976.
6. Bergeret FS, Volkov AF, Efetov KB. Odd triplet superconductivity and related phenomena in superconductor-ferromagnet structures. *Rev.Mod.Phys.*, 2005, 77(4):1321-1373.
7. Gor'kov L, Kresin V. Giant magnetic effects and oscillations in antiferromagnetic Josephson weak links. *Appl.Phys.Lett.*, 2001, 78(23):3657-3659.
8. Zaitsev AV. Peculiarities of the proximity effect in superconductor-multilayered ferromagnet structures with collinear magnetizations in ferromagnetic layers. *JETP Lett.*, 2009, 90(6):475-479.
9. Zaitsev AV, Ovsyannikov GA, Constantinian KY, Kislynskii YV, Shadrin AV, Borisenko IV and Komissinskiy PV. Superconducting current in hybrid structures with an antiferromagnetic interlayer. *JETP*, 2010, 110(2):336-344.
10. Dorr K. Ferromagnetic manganites: spin-polarized conduction versus competing interactions. *J.Phys.D: Appl. Phys.*, 2006, 39:R125-R150.
11. Pena V, Sefrioui Z, Arias D, Leon C, Santamaria J, Varela M, Pennycook SJ and

- Martinez JL. Coupling of superconductors through a half-metallic ferromagnet: Evidence for a long-range proximity effect. *Phys. Rev. B*, 2004, 69(22):224502.
12. Moran O, Bacab E, Perez FA. Depression of the superconducting critical temperature and finite-size scaling relation in $\text{YBa}_2\text{Cu}_3\text{O}_{7-\delta}/\text{La}_{2/3}\text{Ca}_{1/3}\text{MnO}_3$ bilayers. *Microelectronics Journal*, 2008, 39(3-4):556-559.
13. Salamon MB, Jaime M. The physics of manganites: Structure and transport. *Rev. Mod. Phys.*, 2001, 73(3):583-628.
14. Petrzhik AM, Ovsyannikov GA, Shadrin AV, Konstantynyan KI, Zaitsev AV, Demidov VV, and Kislinskii YuV. Electron Transport in Hybrid Superconductor Heterostructures with Manganite Interlayers. *JETP*, 2011, 12 (6):1042-1050.
15. Ovsyannikov GA, Constantinian KY, Kislinskii YuV, Shadrin AV, Zaitsev AV, Petrzhik AM, Demidov VV, Borisenco IV, Kalaboukhov AV, and Winkler D. Proximity effect and electron transport in oxide hybrid heterostructures with superconducting/magnetic interfaces. *Supercond. Sci. Technol.*, 2011, 24(5):055012.
16. Komissinskiy PV, Ovsyannikov GA, Constantinian KY, Kislinskii YuV, Borisenco IV, Soloviev II, Kornev VK, Goldobin E and Winkler D. High-frequency dynamics of hybrid oxide Josephson heterostructures. *Phys. Rev. B*, 2008, 78(2):024501.
17. Ovsyannikov GA, Kislinskii YuV, Constantinian KY, Shadrin AV, Demidov VV, and Petrzhik AM. Spin-Filter Tunneling in Superconducting Mesa Structures with a Ferromagnetic Manganite Interlayer. *JETP*, 2017, 124(4):628-634.

DOI: 10.17725/rensit.2021.13.479

Spin current and spin magnetoresistance of the heterostructure iridate/manganite interface

Gennady A. Ovsyannikov, Karen Y. Constantinian, Vladislav A. Shmakov, Yulii V. Kislinski, Andrey P. Orlov, Peter V. Lega

Kotelnikov Institute of Radioengineering and Electronics of RAS, <http://www.cplire.ru/>
Moscow 125009, Russian Federation

E-mail: gena@hitech.cplire.ru, karen@hitech.cplire.ru, shmakov-va@hitech.cplire.ru, yuli@hitech.cplire.ru, orl@cplire.ru, lega_peter@list.ru

Anton V. Shadrin

Moscow Institute of Physics and Technology, <https://mipt.ru/>
Dolgoprudny 141701, Moscow Region, Russian Federation

E-mail: shadrinant@mail.ru

Nikolay V. Andreev, Filipp O. Milovich

National Research Technological University "MISIS", <https://misis.ru/>
Moscow 119049, Russian Federation

E-mail: andreevn.misa@gmail.com, filippmilovich@mail.ru

Received Oktober 20, 2021, peer-reviewed Oktober 27, 2021, accepted November 08, 2021

Abstract: The paper presents the results of fabrication and structural study of $\text{SrIrO}_3/\text{La}_{0.7}\text{Sr}_{0.3}\text{MnO}_3$ heterostructures. The results of experimental studies of the spin current arising in the regime of ferromagnetic resonance are presented. The spin-orbit interaction present in 5d-oxides of transition metals, which is SrIrO_3 , provides an effective conversion of spin current to charge current due to the inverse spin Hall effect. The angular dependence of spin magnetoresistance makes it possible to determine the angle of the spin Hall effect.

Keywords: spin-orbit interaction, heterostructures, transition metals, topological symmetry, magnetoelectric effects

PACS: 75.47.Lx, 75.25.-j

Acknowledgments: This work was carried out within the framework of the state task of the Kotelnikov Institute of Radioengineering and Electronics of Russian Academy of Sciences and Russian Foundation for Basic Research No.19-07-00143. The study was carried out using the Unique Science Unit "Cryointegral" (USU #352529), which was supported by the Ministry of Science and Higher Education of Russia (Project No. 075-15-2021-667). Structural investigations were carried out using the equipment of the Center "Material Science and Metallurgy" with the financial support of Ministry of Education and Science of Russian Federation (№ 075-15-2921-696).

For citation: Gennady A. Ovsyannikov, Karen Y. Constantinian, Vladislav A. Shmakov, Anton V. Shadrin, Yulii V. Kislinski, Nikolay V. Andreev, Filipp O. Milovich, Andrey P. Orlov, Peter V. Lega. Spin current and spin magnetoresistance of the heterostructure iridate/manganite interface. *RENSIT: Radioelectronics. Nanosystems. Information technologies*, 2021, 13(4):479-486.
DOI: 10.17725/rensit.2021.13.479.

CONTENTS

- 1. INTRODUCTION (480)**
 - 2. MANGANITE/IRIDATE HETEROSTRUCTURES (480)**
 - 3. SPIN CURRENT (482)**
 - 4. SPIN MAGNETORESISTANCE (483)**
 - 5. CONCLUSION (484)**
- REFERENCES (484)**

1. INTRODUCTION

Significant progress in microelectronics in the field of informatics is due to the use of the charge properties of electrons. The use of electron spins opens up new opportunities in microelectronics, especially in the field of heat dissipation from submicron-sized elements. Spintronics elements enable solutions to the heat dissipation problem because there is no heat dissipation for spin transfer (spin current).

The detection and generation of spin current requires a completely different approach to the problem. A challenging task is the conversion of the spin current into a charge current, which is used in modern systems. The spin Hall effect is used to describe the conversion of spin current to charge current and vice versa in paramagnetic metals [1]. The conversion efficiency is determined by a parameter, the spin Hall effect angle θ_{SH} , which is defined as the ratio of the spin Hall resistance and the charge conduction of the paramagnetic metal. θ_{SH} can be determined from non-local magnetotransport measurements (see, for example [2]).

The most common method is to use spin pumping in a ferromagnetic resonance (FMR) mode in a paramagnetic metal/ferromagnet heterostructure [3-6]. However,

a large number of parameters determining the magnitude of the spin current cannot be determined with good accuracy. As a result there is a strong scatter of experimentally obtained values of θ_{SH} for the same heterostructure. The number of parameters in the relationship between θ_{SH} and spin magnetoresistance is much smaller. As a result of spin resistance measurements it is possible to determine the value of θ_{SH} with greater accuracy.

The paper presents the results of fabrication and structural study of $\text{SrIrO}_3/\text{La}_{0.7}\text{Sr}_{0.3}\text{MnO}_3$ heterostructures, the results of experimental studies of the spin current arising in the regime of ferromagnetic resonance and magnetoresistance. The influence of anisotropic magnetoresistance and Rashba-Edelstein parameter on the parameters of heterostructures are discussed.

2. MANGANITE/IRIDATE HETEROSTRUCTURES

Thin films of strontium iridate SrIrO_3 and manganite $\text{La}_{0.7}\text{Sr}_{0.3}\text{MnO}_3$ of nanometer thickness were deposited on single-crystal substrates $(110)\text{NdGaO}_3$. Epitaxial films were grown by magnetron sputtering at substrate temperatures of 770-800°C in Ar and O_2 gas mixture at a total pressure of 0.3 mBar [5,6].

The crystal structure of the obtained heterostructures has been studied by X-ray diffraction analysis and transmission electron microscopy (TEM). A relatively thick platinum film was deposited on top of the heterostructure to avoid charge build-up. We will describe the crystal lattice of SrIrO_3 and $\text{La}_{0.7}\text{Sr}_{0.3}\text{MnO}_3$ as a distorted pseudo-cube with lattice parameters $a_{\text{SIO}} = 0.396 \text{ nm}$ and $a_{\text{LSMO}} = 0.389 \text{ nm}$ respectively [6].

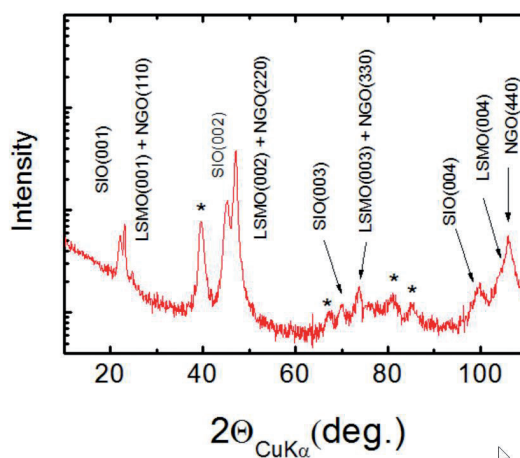


Fig. 1. X-ray diffractogram of $\text{Pt}/\text{SrIrO}_3/\text{La}_{0.7}\text{Sr}_{0.3}\text{MnO}_3/\text{NdGaO}_3$. The reflections from the platinum film marked with an asterisk.

Fig. 1 shows a X-ray Bragg diffractogram of the obtained heterostructure. Multiple reflections from plane (001) of SrIrO_3 film, reflections (110) of NdGaO_3 substrate coinciding with reflections from plane (001) of $\text{La}_{0.7}\text{Sr}_{0.3}\text{MnO}_3$ as well as reflections from platinum film can be seen. Thus, it is possible to draw a conclusion that the growth of heterostructure is carried out by the "cube upon cube" mechanism with the following ratios: (001) $\text{SrIrO}_3||$ (001) $\text{La}_{0.7}\text{Sr}_{0.3}\text{MnO}_3||$ (110) NdGaO_3 and [100] $\text{SrIrO}_3||$ [100] $\text{La}_{0.7}\text{Sr}_{0.3}\text{MnO}_3||$ [001] NdGaO_3 [6].

Fig. 2 shows a TEM image of a cross section of a heterostructure obtained with a transmission electron microscope JEM -2100 at 200 kV. Elemental analysis was performed by X-ray energy dispersive system (OXFORD Instruments, INCA Energy). The cross section slice plate for transmission electron microscopy was made by using a focused ion beam in a Carl Zeiss CrossBeam Neon 40 EsB scanning electron-ion microscope equipped with an auto-emission electron and a gallium ion gun with a resolution of 1 and 7 nm. The

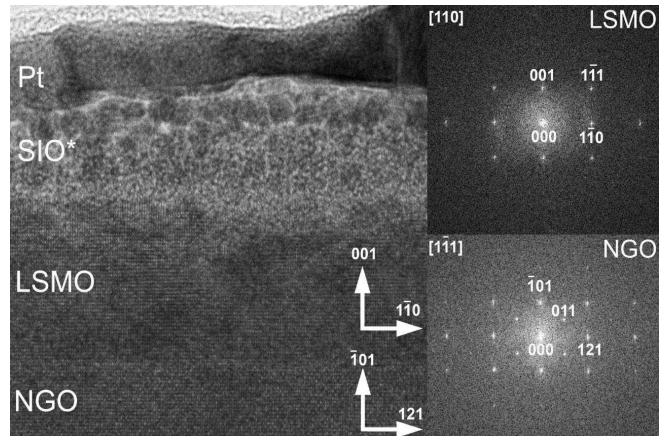


Fig. 2. TEM image of a cross section of a $\text{SrIrO}_3/\text{La}_{0.7}\text{Sr}_{0.3}\text{MnO}_3/\text{NdGaO}_3$ ($\text{Pt}/\text{SIO}/\text{LSMO}/\text{NGO}$) heterostructure covered with a thick layer of platinum. The electron diffraction from the NdGaO_3 substrate regions and $\text{La}_{0.7}\text{Sr}_{0.3}\text{MnO}_3$ films are shown on the right.

unit was equipped with a micromanipulator and gas injection system for local precursor gas (Pt, W, etc.) deposition.

A layer of metal mask (Pt) up to $2 \mu\text{m}$ thick was formed on the sample surface to protect from damage. Ga^+ ions with an energy of 30 keV were used to obtain the slice and its thinning (polishing) with a gradual decrease of the etching current from 5 nA to 5 pA. To remove the amorphous layer at the final stage, the ion energy was decreased to 5 keV.

Presumably, during the preparation of the sample for TEM, the upper layer of SrIrO_3 was damaged - amorphized during the interaction with the beam of gallium ions. At the same time, the layer $\text{La}_{0.7}\text{Sr}_{0.3}\text{MnO}_3$ remained undamaged. In the high-resolution image, we can observe a clearly pronounced even boundary between the $\text{La}_{0.7}\text{Sr}_{0.3}\text{MnO}_3$ layer and the NdGaO_3 substrate. Hence, an epitaxial correspondence between the layer and the substrate is observed. The inset to the figure shows Fourier images from the

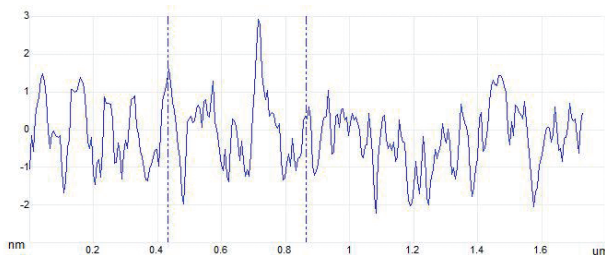


Fig. 3. $\text{La}_{0.7}\text{Sr}_{0.3}\text{MnO}_3$ film surface taken on an atomic force microscope.

regions of the figure corresponding to the substrate and $\text{La}_{0.7}\text{Sr}_{0.3}\text{MnO}_3$ layer, also confirming the epitaxial growth.

Fig. 3 shows a cross section of the $\text{La}_{0.7}\text{Sr}_{0.3}\text{MnO}_3$ film surface obtained using an atomic force microscope. Vertical irregularities 1-2 nm do not exceed the thickness of the upper SrIrO_3 film. Horizontally, the size of the irregularity is 50-70 nm.

3. SPIN CURRENT

The ferromagnetic resonance (FMR) line width characterizes the attenuation of the spin precession. In a ferromagnetic/normal metal heterostructure, an increase is observed due to the generation of a spin current across the interface [7]. Under microwave action in the FMR mode, a spin current j_s flows across the boundary in the ferromagnetic film, which is determined by the spin conductance of the boundary $g^{\uparrow\downarrow}$ and the amplitude of the magnetic moment precession m induced by the microwave magnetic field [4,8,9].

$$j_s = \frac{h}{8\pi} (mdm/dt)^2. \quad (1)$$

The value of the spin conductivity is usually determined from the increase in spin damping caused by the flow of a spin current. In our case the expression for the spin conductivity of the SrIrO_3 /

$\text{La}_{0.7}\text{Sr}_{0.3}\text{MnO}_3$ interface looks as follows:

$$g^{\uparrow\downarrow} = \frac{4\pi\gamma_g M_s t_{\text{LSMO}}}{g\mu_B\omega_f} (\Delta H_{\text{SIO/LSMO}} - \Delta H_{\text{LSMO}}), \quad (2)$$

where $\text{La}_{0.7}\text{Sr}_{0.3}\text{MnO}_3$ film magnetization $M_s = 300$ Oe determined from resonance magnetic field value of FMR, $t_{\text{LSMO}} = 12$ nm film thickness $\text{La}_{0.7}\text{Sr}_{0.3}\text{MnO}_3$, $\mu_B = 9.274 \cdot 10^{-21}$ erg/G is the Bohr magneton, $g = 2$, $\gamma_g = 17.605 \cdot 10^6$ s⁻¹G⁻¹ is the gyromagnetic ratio for free electrons and $\omega_f = 2\pi \cdot 9.51 \cdot 10^9$ s⁻¹ is the microwave frequency. At room temperature, the increase in the $\Delta H_{\text{SIO/LSMO}} - \Delta H_{\text{LSMO}} = 20$ Oe width is 20 Oe, which gives $g^{\uparrow\downarrow} = 1 \cdot 10^{18}$ m⁻² for $\text{SrIrO}_3/\text{La}_{0.7}\text{Sr}_{0.3}\text{MnO}_3$ heterostructures. Note that $= 1.3 \cdot 10^{18}$ m⁻² was obtained in [10] for $\text{SrIrO}_3/\text{La}_{0.7}\text{Sr}_{0.3}\text{MnO}_3$ heterostructure obtained by laser ablation.

Inverse spin Hall effect is used to detect spin current [3,8]. According to the effect the ratio of spin and charge currents is determined by a dimensionless parameter – the spin Hall angle θ_{SH} :

$$\vec{j}_{\text{ISH}} = \theta_{\text{SH}} \frac{e}{\hbar} [\vec{n} \times \vec{j}_s^0], \quad (3)$$

where \vec{n} is unit vector of spin momentum direction.

The voltage dependence on the upper film $V(H)$ is measured when the magnetic field is swept close to the resonance value of the FMR. **Fig. 4** shows the magnetic-field voltage dependence on the SrIrO_3 film under ferromagnetic resonance conditions at 2.6 GHz. The experimental dependence is well approximated by the following formula taking into account the effect of spin current and the contribution from anisotropic magnetoresistance (AMR) [11,12]:

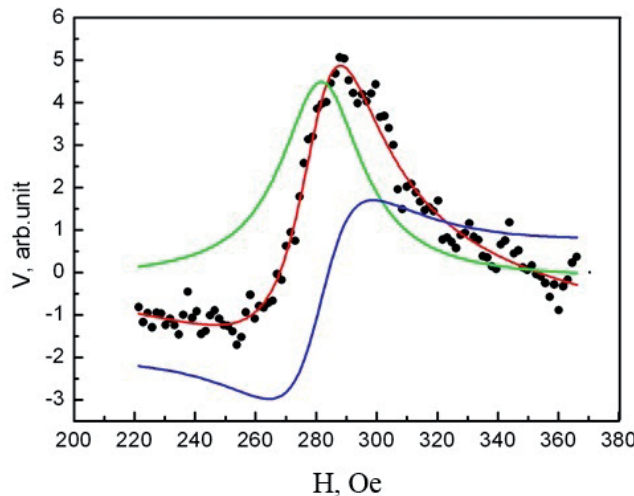


Fig. 4. Spectrum of voltage induced by spin current, $f = 2.6 \text{ GHz}$, $T = 300 \text{ K}$. Red curve – approximation by Lorentz line and antisymmetrical component of anisotropic magnetoresistance, blue curve – antisymmetrical part of anisotropic magnetoresistance, green curve – sum of symmetrical part of anisotropic magnetoresistance and spin current signal.

$$V = [V_{AMR}^S L(H) + V_{AMR}^A L'(H)] \sin 2\varphi_0 \sin \varphi_0 + \\ + V_Q L(H) \cos \varphi_0, \quad (4)$$

where $L(H) = \Delta H^2 / [(H - H_0)^2 + \Delta H^2]$ is the symmetric Lorentz function, $L'(H) = \Delta H(H - H_0) / [(H - H_0)^2 + \Delta H^2]$ is the asymmetric Lorentz function, V_{AMR}^S and V_{AMR}^A are the amplitudes of both symmetric and asymmetric parts of the AMR contribution, $V_Q(H)$ is the voltage on the SrIrO_3 film, caused by spin current flowing through the interface, φ_0 is angle between external magnetic field and normal to voltage direction caused by reverse spin Hall effect. For $\varphi_0 = 45^\circ$ assuming a ratio $V_{AMR}^A / V_{AMR}^S = -\tan \varphi_I \approx -1$ [11], where φ_I is the phase difference between microwave current and microwave magnetization from the amplitude V_{AMR}^A we obtain that the

contribution from the spin current is less than 10% of the V_{AMR}^S .

4. SPIN MAGNETORESISTANCE

Magnetic-field dependence of the change in the normalised magnetoresistance (MR) of the heterostructure is shown in **Fig. 5b**. The normalisation is given for resistance at $H = 0$. Directions of magnetic field change are indicated by arrows. The

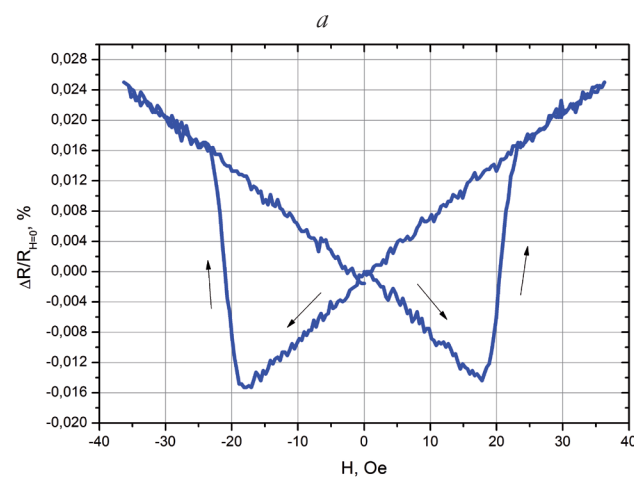
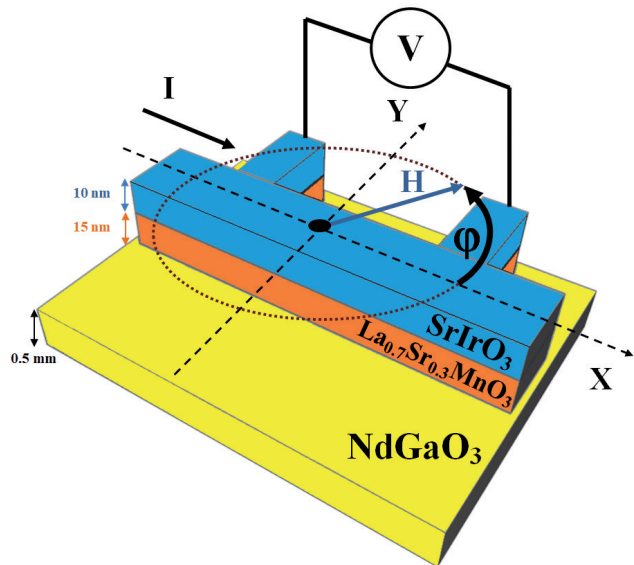


Fig. 5. (a) The topology of the measurements $\text{SrIrO}_3/\text{La}_{0.7}\text{Sr}_{0.3}\text{MnO}_3$, (b) Magnetic-field dependence of variation of normalized magnetoresistance of heterostructures. The normalization is given for resistance at $H = 0$. The directions of magnetic field change are indicated by arrows.

hysteresis of the magnetoresistance change can be seen. The maximum value of the MR variation is 0.032%. The field was directed perpendicular to the direction of the current flow (angle $\varphi = 90^\circ$ in the Fig. 5a).

The MR field dependence follows the manganite magnetisation curve [13]. The small value of the hysteresis loop width is probably caused by the proximity effect (penetration of the magnetic order parameter in the $\text{La}_{0.7}\text{Sr}_{0.3}\text{MnO}_3$ film into SrIrO_3).

Following the theory [14] taking into account conductivity of $\text{La}_{0.7}\text{Sr}_{0.3}\text{MnO}_3$ film the expression for spin resistance (SMR) is as follows [15]:

$$\frac{\Delta R}{R} = \frac{\theta_{\text{SH}}^2 \lambda_s g_R \tanh^2(t_{\text{SIO}} / 2\lambda_s)}{(1+\eta)t_{\text{SIO}}[1+g_R \coth(t_{\text{SIO}} / \lambda_s)]}, \quad (5)$$

where θ_{SH} and λ_s are the spin angle and spin diffusion length in the SrIrO_3 film correspondingly. $\eta = \rho_{\text{SIO}} t_{\text{LSMO}} / \rho_{\text{LSMO}} t_{\text{SIO}} = 0.33$ are determined by the resistivities of iridate and manganite $\rho_{\text{SIO}} = 3 \cdot 10^{-4}$ Ωcm and $\rho_{\text{LSMO}} = 1.1 \cdot 10^{-3}$ Ωcm , and the thicknesses of these films $t_{\text{LSMO}} = 12$ nm and $t_{\text{SIO}} = 10$ nm, $g_R = h\rho_{\text{SIO}} \lambda_s g^{\uparrow\downarrow} / e^2$. Using the data for the spin resistance value of the boundaries [6] $g^{\uparrow\downarrow} = 10^{18} \text{ m}^{-2}$ and the value $\lambda_s = 1$ nm we obtain $g_R = 0.12$. Under the condition $t_{\text{SIO}} \gg \lambda_s$ relation (5) is simplified. Substituting the parameters calculated above we obtain $\theta_{\text{SH}} \approx 0.2$. Assuming that the anisotropic magnetoresistance (AMR) gives an additive contribution to the resistivity of the heterostructure together with the spin current we obtain that the value must be reduced to the root of the relationship between the amplitude of the symmetric AMR signal and the spin current

signal in the ferromagnetic resonance $\sqrt{V_Q / V_{\text{AMR}}^S} = 0.3$ [6].

Along with the spin magnetoresistance there is the Rashba-Edelstein magnetoresistance which results from the processes occurring at the boundary with broken symmetry of the inversion [16-18]. Recently this effect has been investigated experimentally in a $\text{Bi}/\text{Ag}/$ ferromagnetic multilayer [19] caused by nonequilibrium spin accumulation at the interface

5. CONCLUSION

The structural parameters of the fabricated $\text{SrIrO}_3/\text{La}_{0.7}\text{Sr}_{0.3}\text{MnO}_3$ heterostructure were studied. Epitaxial growth of two films on NdGaO_3 substrate was observed by transmission electron microscope and confirmed by X-ray diffraction structure measurements. The value of the spin Hall angle was determined by two methods by direct measurement of the voltage induced by the spin current induced in the ferromagnetic resonance mode and by measuring the spin resistance. A strong influence of anisotropic magnetoresistance on the spin transport parameters was observed.

REFERENCES

1. Zhang S. Spin Hall Effect in the Presence of Spin Diffusion. *Phys. Rev. Lett.*, 2000, 85:393.
2. Mihajlovic G, Pearson JE, Garcia MA, Bader SD, and Hoffmann A. Negative Nonlocal Resistance in Mesoscopic Gold Hall Bars: Absence of the Giant Spin Hall Effect. *Phys. Rev. Lett.*, 2009, 103:166601.

3. Saitoh E, Ueda M, Miyajima H, and Tatara G. Conversion of spin current into charge current at room temperature: Inverse spin-Hall effect. *Appl. Phys. Lett.*, 2006, 88:182509.
4. Mosendz O, Vlaminck V, Pearson JE, Fradin FY, Bauer GEW, Bader SD, and Hoffmann A. Detection and quantification of inverse spin Hall effect from spin pumping in permalloy/normal metal bilayers. *Phys. Rev. B*, 2010, 82:214403.
5. Shaikhulov TA, Ovsyannikov GA, Demidov VV, Andreev NV. Magnetic and Resistive Properties of Magnetite/Iridate Heterostructures. *Journal of Experimental and Theoretical Physics*, 2019, 129:112.
6. Ovsyannikov GA, Shaikhulov TA, Stankevich KL, Khaydukov Yu, Andreev NV. Magnetism at an iridate/manganite interface: Influence of strong spin-orbit interaction. *Phys. Rev. B*, 2020, 102:144401.
7. Shaikhulov TA, Ovsyannikov GA. Attenuation of Spin Precession in Manganite/Normal Metal Heterostructures. *Physics of the Solid State*, 2018, 60:2231.
8. Tserkovnyak Ya, Brataas A, Bauer GEW. Enhanced Gilbert damping in thin ferromagnetic films. *Phys. Rev. Lett.*, 2002, 88:117601.
9. Fengyuan Yang and P. Chris Hammel. FMR-driven spin pumping in Y_3Fe5O_{12} -based structures. *J. Phys. D: Appl. Phys.*, 2018, 51:253001.
10. Crossley S, Swartz AG, Nishio K, Hikita Y, and Hwang HY. All-oxide ferromagnetic resonance and spin pumping with $SrIrO_3$. *Phys. Rev. B*, 2019, 100:115163.
11. Azevedo A, Vilela-Leao LH, Rodriguez-Suarez RL, Lacerda Santos AF, Rezende SM. Spin pumping and anisotropic magnetoresistance voltages in magnetic bilayers: Theory and experiment. *Phys. Rev. B*, 2011, 83:144402.
12. Atsarkin VA, Borisenco IV, Demidov VV, Shaikhulov TA. Temperature dependence of pure spin current and spin-mixing conductance in the ferromagnetic—normal metal structure. *J. Phys. D*, 2018, 51:245002.
13. Ovsyannikov GA, Petrzhik AM, Borisenco IV, Klimov AA, Ignatov YA, Demidov VV, Nikitov SA. Magnetotransport characteristics of strained $La_{0.7}Sr_{0.3}MnO_3$ epitaxial manganite films. *Journal of Experimental and Theoretical Physics*, 2009, 108:48.
14. Chen Y-T, Takahashi S, Nakayama H, Althammer M, Goennenwein STB, Saitoh E, and Bauer GEW. Theory of spin Hall magnetoresistance. *Phys. Rev. B*, 2013, 87:144411.
15. Du Ye, Takahashi Saburo and Nitta Junsaku. Spin current related magnetoresistance in epitaxial Pt/Co bilayers in the presence of spin Hall effect and Rashba-Edelstein effect. *Phys. Rev. B*, 2021, 103:094419.
16. Manchon A, Koo HC, Nitta J, Frolov S M, and Duine RA. New perspectives for Rashba spin-orbit coupling. *Nat. Mater.*, 2015, 14:871.
17. Emori Satoru, T Nanianxiang, Belkessam Amine M, Wang Xinjun, Matyushov Alexei, Babroski D, Christopher J, Gao Yuan, Lin Hwaide, and Sun Nian X. Interfacial spin-orbit torque without bulk

spin-orbit coupling. *Phys. Rev. B*, 2016,
93:18040.

18. Akio Asami, Hongyu An, Akira Musha,
Makoto Kuroda, and Kazuya Ando. Spin
absorption at a ferromagnetic-metal/
platinum-oxide interface. *Physical Review
B*, 2019, 99:024432.

19. Kim J, Chen Y-T, Karube S,
Takahashi S, Kondou K, Tatara G,
and Otani Y. Evaluation of bulk-
interface contributions to Edelstein
magnetoresistance at metal/
oxide interfaces. *Phys. Rev. B*, 2017,
96:140409(R).

DOI: 10.17725/rensit.2021.13.487

Characteristic form of dynamics equations of Cosserat medium

George G. Bulychev

MIREA-Russian Technological University, <https://www.mirea.ru/>

Moscow 119454, Russian Federation

E-mail: geo-bulychev@mail.ru

Received August 26, 2021, peer-reviewed September 10, 2021, accepted September 15, 2021

Abstract: In this paper, we construct the characteristic form of the equations of dynamics of the Cosserat medium and the Cosserat pseudocontinuum for bounded bodies. The method of matrix transformations proposed by the author is used for construction and allows obtaining the necessary relations using identical transformations. The obtained equations are compared with those for a symmetrically elastic isotropic homogeneous body. A method is proposed for selecting the necessary equations for computational schemes at the internal and boundary points of the body. A sequence of operations is proposed for iterative calculations of stresses, particle velocities, moment stresses, and angular velocities of particles in a coupled model of the Cosserat medium.

Keywords: dynamic processes, spatial characteristics method, numerical modeling, Cosserat medium

UDC 537.311.3, 539.23, 546.26

For citation: George G. Bulychev. Characteristic form of dynamics equations of Cosserat medium.

RENSIT: Radioelectronics. Nanosystems. Information technologies, 2021, 13(4)487-494. DOI: 10.17725/rensit.2021.13.487.

CONTENTS

1. INTRODUCTION (487)

2. CONSTRUCTION OF CHARACTERISTIC EQUATIONS OF DYNAMICS (488)

3. MODELING (492)

4. CONCLUSION (493)

REFERENCES (494)

1. INTRODUCTION

One of the first models of moment elasticity was the brothers Cosserat model [1], developed by them in 1909 (see also [2]). For quite a long time, this model was not in demand and only in the sixties of the last century, applications were found for it, and a significant number of works appeared, one way or another, developed this model [3,4,5]. In particular, in [5] great attention was paid to the kinetics of the medium of Cosserat and, using generating functions, was constructed fundamental solution of the task of elastokinetics and thermoelectrokinetics for this medium. The formulas for the dispersion of the phase velocity of transverse torsion waves were also derived there and the possibility of

bifurcation of these waves at different rotational frequencies of medium particles was shown.

The current model Cosserat widely used where the classic theory does not give good agreement with experiment. Thus, when investigating the theory of brittle fracture of metals, Morozov [6] draws on this mathematical theory to describe stresses near the tip of the crack, Zhilin [7] uses the model Cosserat in the theory of non-classical shells, Erofeev and Kunin [8,9] based on nonlinear theory Cosserat studies solitons in solids and develops a polar theory of media with microstructure. There are still a number of works where moment theories are used too study the movement of grains in ferromagnets, thermodiffusion, complicated models of crystal lattices, etc.

In this paper, a matrix and scalar characteristic form of linear medium dynamics equations is constructed on the basis of the matrix method developed by the author for Cosserat line medium and pseudo-continuum Cosserat and discussed the possibilities and sequence of their numerical implementation.

2. CONSTRUCTION OF CHARACTERISTIC EQUATIONS OF DYNAMICS

Following [5], the equations of dynamics for the Cosserat medium can be written as a system consisting of equations of motion

$$\begin{aligned} \partial_j p_{ji} + f_i &= \rho \partial_t^2 u_i, \\ \epsilon_{ijk} p_{jk} + \partial_j \mu_{ji} + y_i &= J \partial_t^2 \Omega_i, \end{aligned} \quad (1)$$

equations for non-symmetric deformation tensor and bending-torsion

$$\begin{aligned} \gamma_{ji} &= \partial_j u_i - \epsilon_{kji} \Omega_k, \\ \chi_{ji} &= \partial_j \Omega_i, \end{aligned} \quad (2)$$

and the defining equations

$$\begin{aligned} p_{ji} &= (\mu + a) \gamma_{ji} + (\mu - a) \gamma_{ij} + \lambda \gamma_{kk} \delta_{ji}, \\ \mu_{ji} &= (\varphi + \varepsilon) \chi_{ji} + (\varphi - \varepsilon) \chi_{ij} + \beta \chi_{kk} \delta_{ji}. \end{aligned} \quad (3)$$

Here μ, λ are the Lame constants, $a, \varphi, \varepsilon, \beta$ new elastic constants, p_i asymmetric stresses, γ_{ji} asymmetric deformations, χ_{ji} bending-torsion tensor, u_i displacement, Ω_i rotation angles, f_i internal forces, y_i internal moments, ϵ_{ijk} Levi-Chevita tensor, δ_{ij} the unit tensor, $i, j, k = 1, 2, 3$; $\partial_i = \partial/\partial x_i$, $\partial_t^2 = \partial^2/\partial t^2$, t time, x_i Cartesian coordinates, for repeated Roman indices are summed up here and then.

Note that systems (2) and (3) are constructed in such a way that

$$\begin{aligned} p_{\alpha\alpha} &= \sigma_{\alpha\alpha}, \quad p_{\alpha\beta} + p_{\beta\alpha} = 2\sigma_{\alpha\beta}, \\ \gamma_{\alpha\alpha} &= \varepsilon_{\alpha\alpha}, \quad \gamma_{\alpha\beta} + \gamma_{\beta\alpha} = 2\varepsilon_{\alpha\beta}, \end{aligned} \quad (4)$$

where $\sigma_{\alpha\alpha}, \sigma_{\alpha\beta}, \varepsilon_{\alpha\alpha}, \varepsilon_{\alpha\beta}$ are the stresses of the classical elasticity theory, $\alpha, \beta, \gamma, \alpha \neq \beta \neq \gamma$, there is no summation here and further along the echoing Greek indices. The indices $\alpha, \beta, \gamma = 1, 2, 3$ and form a circular permutation of the numbers 1, 2, 3, i.e. $\epsilon_{\alpha\beta\gamma} = 1$, and $\epsilon_{\beta\alpha\gamma} = -1$.

Remark (4) allows us to reduce some gradient problems of Cosserat medium dynamics (for example, the problem of bound thermoelasticity) to problems of classical momentless mechanics, if, of course, we do not consider asymmetric tangent deformations and stresses separately. Another consequence (4) is that the normal stresses and deformations of the Cosserat medium are equal to the corresponding stresses and deformations of the classical elastic theory, and the interaction of ordinary and moment stresses occurs only through tangent stresses.

Let's proceed to the construction of the matrix form of equations (1)-(3), for which we will enter the row matrices

$$\begin{aligned} P &= \begin{vmatrix} p_{11} & p_{22} & p_{33} & p_{12} & p_{13} & p_{21} & p_{23} & p_{31} & p_{32} \end{vmatrix}, \\ \Gamma &= \begin{vmatrix} \gamma_{11} & \gamma_{22} & \gamma_{33} & \gamma_{12} & \gamma_{13} & \gamma_{21} & \gamma_{23} & \gamma_{31} & \gamma_{32} \end{vmatrix}, \\ M &= \begin{vmatrix} \mu_{11} & \mu_{22} & \mu_{33} & \mu_{12} & \mu_{13} & \mu_{21} & \mu_{23} & \mu_{31} & \mu_{32} \end{vmatrix}, \\ X &= \begin{vmatrix} \chi_{11} & \chi_{22} & \chi_{33} & \chi_{12} & \chi_{13} & \chi_{21} & \chi_{23} & \chi_{31} & \chi_{32} \end{vmatrix}, \\ U &= \begin{vmatrix} u_1 & u_2 & u_3 \end{vmatrix}, \quad \Omega = \begin{vmatrix} \Omega_1 & \Omega_2 & \Omega_3 \end{vmatrix}, \\ F &= \begin{vmatrix} f_1 & f_2 & f_3 \end{vmatrix}, \quad Y = \begin{vmatrix} y_1 & y_2 & y_3 \end{vmatrix} \end{aligned} \quad (5)$$

and two additional matrices-rows

$$e_i = \begin{vmatrix} \delta_1 & \delta_2 & \delta_3 \end{vmatrix} \text{ and}$$

$q_{ij} = \begin{vmatrix} \delta_{ii} \delta_{1j} & \delta_{2j} \delta_{2j} & \delta_{3j} \delta_{3j} & \delta_{1i} \delta_{2j} & \delta_{1i} \delta_{3j} & \delta_{2i} \delta_{1j} & \delta_{2i} \delta_{3j} & \delta_{3i} \delta_{1j} & \delta_{3i} \delta_{2j} \end{vmatrix}$, with which you can select components from matrix rows (5) and restore these matrix rows by their components, for example,

$$e_a U^T = u_a, \quad e_i^T u_i = U^T, \quad q_{\alpha\beta} P^T = p_{\alpha\beta}, \quad q_{ij}^T p_{ij} = P^T, \quad (6)$$

obviously, $e_\alpha e_\beta^T = \delta_{\alpha\beta}$, $e_i^T e_i = I_3$, $q_{\alpha\beta} q_{cd}^T = \delta_{\alpha c} \delta_{\beta d}$, $q_{ij}^T q_{ij} = I_9$, where I_3 and I_9 are unit matrices of 3-rd and 9-th order.

Using matrices (5) and auxiliary matrices e_i and q_{ij} construct the matrix form of equations (1) - (3), using the form of row matrices (5), additional matrices, and properties (6) of additional matrices.

In this case, equations (1) will take the form:

$$Q_i \partial_i P^T + F^T = \rho \partial_t V^T, \quad (7)$$

$$-S_i Q_i P^T + Q_i \partial_i M^T + Y^T = J \partial_t \omega^T,$$

where $V^T = \partial_t U^T$, $\omega^T = \partial_t \Omega^T$, matrices $Q_i = e_i^T q_{ij}$ and $S_i = -\epsilon_{ijk} e_j^T e_i$ are known to us by [10] and characterize the matrix form of differential invariants *grad*, *div* and *rot*. In matrix form Q_i and S_i have the form

$$\begin{aligned} Q_i &= \begin{vmatrix} \delta_{1i} & 0 & 0 & 0 & 0 & \delta_{2i} & 0 & \delta_{3i} & 0 \\ 0 & \delta_{2i} & 0 & \delta_{1i} & 0 & 0 & 0 & 0 & \delta_{3i} \\ 0 & 0 & \delta_{3i} & 0 & \delta_{1i} & 0 & \delta_{2i} & 0 & 0 \end{vmatrix}; \\ S_i &= \begin{vmatrix} 0 & -\delta_{3i} & \delta_{2i} \\ \delta_{3i} & 0 & -\delta_{1i} \\ -\delta_{2i} & \delta_{1i} & 0 \end{vmatrix}. \end{aligned}$$

Equations (2), differentiated by t , are written in the matrix representation as

$$\partial_t \Gamma^T = Q_i^T (\partial_i V^T + S_i \omega^T), \quad (8)$$

$$\partial_t X^T = Q_i^T \partial_i \Omega^T.$$

Equations (3), also differentiated by t , in the matrix representation will take the form

$$\begin{aligned}\partial_t P^T &= \{(\mu+a)I_9 + (\mu-a)q_{ij}^T q_{ji} + \lambda q_{ij}^T q_{kk} \delta_{ij}\} \partial_t \Gamma^T, \\ \partial_t M^T &= \{(\varphi+\varepsilon)I_9 + (\varphi-\varepsilon)q_{ij}^T q_{ji} + \beta q_{ij}^T q_{kk} \delta_{ij}\} \partial_t X^T,\end{aligned}\quad (9)$$

or using (8), finally

$$\begin{aligned}\partial_t P^T &= \{(\mu+a)I_9 + (\mu-a)q_{ij}^T q_{ji} + \lambda q_{ij}^T q_{kk} \delta_{ij}\} \times \\ &\times Q_i^T (\partial_t V^T + S_i \omega^T),\end{aligned}\quad (10)$$

$$\partial_t M^T = \{(\varphi+\varepsilon)I_9 + (\varphi-\varepsilon)q_{ij}^T q_{ji} + \beta q_{ij}^T q_{kk} \delta_{ij}\} Q_i^T \partial_t \omega^T.$$

Equations (7) and (10), written in the matrix representation, define 24 variables, defined by matrix strings P, V, M and ω .

Let's consider an arbitrary element $q_{\alpha\beta}^T q_{\chi\phi} a$, that stands in curly brackets. By selecting the type of matrix rows q_{ij} , where $q_{\alpha\beta}^T$ - the column uses its unit to shows the number of the row where the element a is located, and - $q_{\chi\phi}$ - the string whose unit shows the sequential number of this element in the row. Noticing this, we write down the stiffness C_p and rotation matrices C_m .

$$C_p = \begin{vmatrix} 2\mu+\lambda & \lambda & \lambda & 0 & 0 & 0 & 0 & 0 & 0 \\ \lambda & 2\mu+\lambda & \lambda & 0 & 0 & 0 & 0 & 0 & 0 \\ \lambda & \lambda & 2\mu+\lambda & 0 & 0 & 0 & 0 & 0 & 0 \\ 0 & 0 & 0 & \mu+a & 0 & \mu-a & 0 & 0 & 0 \\ 0 & 0 & 0 & 0 & \mu+a & 0 & 0 & \mu-a & 0 \\ 0 & 0 & 0 & \mu-a & 0 & \mu+a & 0 & 0 & 0 \\ 0 & 0 & 0 & 0 & 0 & 0 & \mu+a & 0 & \mu-a \\ 0 & 0 & 0 & 0 & \mu-a & 0 & 0 & \mu+a & 0 \\ 0 & 0 & 0 & 0 & 0 & 0 & \mu-a & 0 & \mu+a \end{vmatrix},$$

$$C_m = \begin{vmatrix} 2\varphi+\beta & \beta & \beta & 0 & 0 & 0 & 0 & 0 & 0 \\ \beta & 2\varphi+\beta & \beta & 0 & 0 & 0 & 0 & 0 & 0 \\ \beta & \beta & 2\varphi+\beta & 0 & 0 & 0 & 0 & 0 & 0 \\ 0 & 0 & 0 & \varphi+\varepsilon & 0 & \varphi-\varepsilon & 0 & 0 & 0 \\ 0 & 0 & 0 & 0 & \varphi+\varepsilon & 0 & 0 & \varphi-\varepsilon & 0 \\ 0 & 0 & 0 & \varphi-\varepsilon & 0 & \varphi+\varepsilon & 0 & 0 & 0 \\ 0 & 0 & 0 & 0 & 0 & 0 & \varphi+\varepsilon & 0 & \varphi-\varepsilon \\ 0 & 0 & 0 & 0 & \varphi-\varepsilon & 0 & 0 & \varphi+\varepsilon & 0 \\ 0 & 0 & 0 & 0 & 0 & 0 & \varphi-\varepsilon & 0 & \varphi+\varepsilon \end{vmatrix}.$$

Using the constructed matrices C_p and C_m equations (8) and (10) will be written in the form that will be used in the future, i.e. in the form

$$\begin{aligned}\partial_t P^T &= C_p Q_i^T (\partial_t V^T + S_i \omega^T), \\ \partial_t M^T &= C_m Q_i^T \partial_t \omega^T.\end{aligned}\quad (11)$$

Let us construct a matrix form of characteristic equations for stress waves propagating both sides along x_α axis the Cartesian coordinate system $\{x_i\}$. To do this, we multiply the first equation (11) on the left by the matrix Q_α that allocates from the matrix P the stresses acting on the site with the normal to the axis x_α , i.e. $Q_\alpha P^T = [p_{\alpha 1} \ p_{\alpha 2} \ p_{\alpha 3}]^T$, and we

draw the necessary grouping of the terms of this equation:

$$\begin{aligned}\partial_t P_\alpha^T - C_{\alpha\alpha} \partial_t V^T &= C_{\alpha k} (\partial_k V^T + S_k \omega^T) + \\ &+ C_{\alpha\alpha} S_\alpha \omega^T, \quad k = \beta, \gamma,\end{aligned}\quad (12)$$

where $C_{\alpha\beta} = Q_\alpha C_p Q_\beta^T$, example, repeated indices k is carried out by summation.

Note, that all matrices $C_{\alpha\alpha} = \text{diag}(...)$, $\alpha = 1, 2, 3$ and, they have corresponding values $2\mu + \lambda$ and $\mu + \alpha$. Denote by $|D_{\alpha p}| = \sqrt{C_{\alpha\alpha} / \rho}$ the modulus of the velocity matrix of stress waves propagating along the axis x_α .

We also regroup the first of the equations of motion (7)

$$\partial_\alpha P_\alpha^T - \rho \partial_t V^T = -\partial_k P_k^T - F^T, \quad P_k = Q_k P^T. \quad (13)$$

Then multiply (13) from the left by $|D_{\alpha p}|$ and add (12) and (13). We perform a group, selecting the matrix characteristic operator and assuming that the waves propagate in both directions along the axis x_α , we obtain the matrix characteristic equations.

$$\begin{aligned}(I_3 \partial_t \pm D_{\alpha p} \partial_\alpha)(P_\alpha^T \mp \rho D_{\alpha p} V^T) &= \\ &= C_{\alpha k} (\partial_k V^T + S_k \omega^T) + C_{\alpha\alpha} S_\alpha \omega^T \mp \\ &\mp D_{\alpha p} (\partial_k P_k^T + F^T), \quad k = \beta, \gamma.\end{aligned}\quad (14)$$

Characteristic equations (14) is easy to fall into 6 scalar equations. Chosen form of notation shows that, due to the unsymmetry of the matrix S , the scalar equations for normal stresses do not contain ω_i , which is a control of the correctness of calculations.

Before proceeding to scalar equations, we note that the calculation $C_{\alpha\beta}$ of matrices is quite simple: first, three rows are selected from the matrix C_p , corresponding to the position of the units in the matrix Q_α . Then, from the rectangular matrix $Q_\alpha C_p$ obtained in this way, the corresponding to the units in the matrix Q_β are selected, and the result is a matrix $C_{\alpha\beta}$. Due to the symmetry of the matrix C_p , it is also easy to show that $C_{\beta\alpha} = C_{\alpha\beta}^T$, the latter greatly simplifies further calculations. The scalar equations corresponding to (14) have the form.

$$\begin{aligned}(\partial_t \pm c_1 \partial_\alpha)(p_{\alpha\alpha} \mp \rho c_1 V_\alpha) &= \\ &= \lambda (\partial_\beta V_\beta + \partial_\gamma V_\gamma) \mp c_1 (\partial_\beta p_{\beta\alpha} + \partial_\gamma p_{\gamma\alpha} + f_\alpha),\end{aligned}\quad (15)$$

$$\begin{aligned}(\partial_t \pm c_2 \partial_\alpha)(p_{\alpha\beta} \mp \rho c_2 V_\beta) &= (\mu + a) \partial_\beta V_\alpha - \\ &- 2a \omega_\gamma \mp c_2 (\partial_\beta p_{\beta\beta} + \partial_\gamma p_{\gamma\beta} + f_\beta),\end{aligned}\quad (16)$$

$$(\partial_t \pm c_2 \partial_\alpha)(p_{\alpha\gamma} \mp \rho c_2 V_\lambda) = (\mu + a) \partial_\gamma V_\alpha + 2a \omega_\beta \mp c_2 (\partial_\beta p_{\beta\gamma} + \partial_\gamma p_{\gamma\beta} + f_\gamma), \quad (17)$$

where $c_1 \equiv c_{\parallel} = \sqrt{(2\mu + \lambda)/\rho}$ – is the velocity of longitudinal stress waves falling with a similar velocity in an isotropic body, $c_2 = \sqrt{(\mu + a)/\rho}$ – the velocity of transverse stress waves in the model of Cosserat, V_i – components of the particle velocity matrix V .

To construct the characteristics on fixed discontinuities, we will use equations (11) and (12). From equation (12), we select $\partial_\alpha V^T + S_\alpha \omega^T$, and we get

$$\partial_\alpha V^T + S_\alpha \omega^T = C_{\alpha\alpha}^{-1} [\partial_t P_\alpha^T - C_{\alpha k} (\partial_k V^T + S_k \omega^T)]. \quad (18)$$

In order, to obtain equations for P_β^T and P_γ^T , we multiply the first equation (11) sequentially on Q_β and Q_γ ; we get

$$\begin{aligned} \partial_t P_\beta^T &= C_{\beta k} (\partial_k V^T + S_k \omega^T) + C_{\beta\alpha} (\partial_\alpha V^T + S_\alpha \omega^T), \\ \partial_t P_\gamma^T &= C_{\gamma k} (\partial_k V^T + S_k \omega^T) + C_{\gamma\alpha} (\partial_\alpha V^T + S_\alpha \omega^T), \end{aligned} \quad (19)$$

and substituting (18) in (19) and making the grouping, we finally obtain the matrix characteristic form of the equations on fixed discontinuities

$$\begin{aligned} \partial_t (P_\beta^T - C_{\beta\alpha} C_{\alpha\alpha}^{-1} P_\alpha^T) &= (C_{\beta k} - C_{\beta\alpha} C_{\alpha\alpha}^{-1} C_{\alpha k}) (\partial_k V^T + S_k \omega^T), \\ \partial_t (P_\gamma^T - C_{\gamma\alpha} C_{\alpha\alpha}^{-1} P_\alpha^T) &= (C_{\gamma k} - C_{\gamma\alpha} C_{\alpha\alpha}^{-1} C_{\alpha k}) (\partial_k V^T + S_k \omega^T). \end{aligned} \quad (20)$$

Scalar form of equations (20) it consists of six equations

$$\begin{aligned} \partial_t (p_{\beta\alpha} - \eta p_{\alpha\beta}) &= 4a(\mu + a)^{-1} (\mu \partial_\beta V_\alpha + a \omega_\gamma), \\ \partial_t (p_{\beta\beta} - \nu_1 p_{\alpha\alpha}) &= 2\mu[(1 + \nu_1) \partial_\beta V_\beta + \nu_1 \partial_\gamma V_\gamma], \\ \partial_t p_{\beta\gamma} &= \mu(\partial_\beta V_\gamma + \partial_\gamma V_\beta) + a(\partial_\beta V_\gamma - \partial_\gamma V_\beta - 2\omega_\alpha). \\ \partial_t (p_{\gamma\alpha} - \eta p_{\alpha\gamma}) &= 4a(\mu + a)^{-1} (\mu \partial_\gamma V_\alpha + a \omega_\beta), \\ \partial_t p_{\gamma\beta} &= \mu(\partial_\gamma V_\beta + \partial_\beta V_\gamma) + a(\partial_\gamma V_\beta - \partial_\beta V_\gamma + 2\omega_\alpha), \\ \partial_t (p_{\gamma\gamma} - \nu_1 p_{\alpha\alpha}) &= 2\mu[\nu_1 \partial_\beta V_\beta + (1 + \nu_1) \partial_\gamma V_\gamma]. \end{aligned} \quad (21)$$

where $\eta = (\mu - a)/(\mu + a)$, $\nu_1 = \lambda/(2\mu + \lambda)$.

To control the calculations, note that all the equations for normal stress components do not depend on ω_i , and add the third equation (21) with the fifth equation, we obtain the equation known from classical linear elasticity.

$$\partial_t (p_{\beta\gamma} + p_{\gamma\beta}) = 2\mu(\partial_\gamma V_\beta + \partial_\beta V_\gamma). \quad (22)$$

Equations (15)-(17) and (21) form a system of 12 scalar characteristic equations, for the 12 components of matrix-strings P and V , and, given an external vector ω , can be used to determine them.

By sequentially assigning the values 1,2,3, we obtain 36 scalar equations, of which, in numerical simulation, we must select 12.

As it was theoretically proved in [11] for two-dimensional problems of dynamics of a solid body and practically verified for three-dimensional problems by the author, in order to ensure the stability of the count at the inner point of the medium, it is necessary to choose equations on moving discontinuities for normal stresses $p_{\alpha\alpha}$ and particle velocities V_α . The other equations are selected from the context of the problem, usually they are equations on fixed discontinuities. At the boundary point of the medium, according to [12], boundary conditions, equations on discontinuities moving normally to the boundary under consideration, and equations on fixed discontinuities are used.

Considering equations (15)-(17) and (21), you can notice that:

1. In all equations ω_i , it is included in combinations $a\omega$, and for small a or small ω_i it can be ignored and, thus, the connection between the equations for ordinary and moment stresses can be broken. However, if in the first case we arrive at the classical equations of the dynamics of an symmetrically elastic isotropic body, then in the second case the equations correspond to an unsymmetrically elastic body.
2. Equations of the form (22) can be used to reduce the number of equations connecting ordinary and moment stresses, as a result, the number of equations that includes ω_i can be reduced to three.
3. All equations for normal stresses $p_{\alpha\alpha}$ do not depend on ω_i and coincide with the equations of classical elasticity.
4. From the matrix positivity conditions C_p the value must be in the range from 0 to μ . Hence, the velocity of transverse waves in the Cosserat model is always lower than the velocity of longitudinal waves in an isotropic body.

That is, the longitudinal wave always spreads first, and then cross waves. This speed ratio is necessary and sufficient for the stability of numerical schemes.

Let us now construct a matrix characteristic form of moment stresses. The initial equations are the second equations of systems (7) and (11), i.e. the system of equations

$$\begin{aligned} -S_i Q_i P^T + Q_i \partial_t M^T + Y^T &= J \partial_t \omega^T, \\ \partial_t M^T &= C_m Q_i^T \partial_t \omega^T. \end{aligned} \quad (23)$$

Note that by changing $-S_i Q_i P^T + Y^T$ to F^T, M^T on P^T, J on ρ and ω^T on V^T we come to the first equation (7), and by replacing C_m on C_p with and adding $S_i \omega^T$ to we come to the first equation (11). Therefore, reasoning in the same way as mentioned above, enter the matrix $M_\alpha^T = Q_\alpha M^T$, $C_{\alpha\beta m} = Q_\alpha C_m Q_\beta^T$, $D_{\alpha m} = \sqrt{C_{\alpha\alpha m} / J}$, $\alpha, \beta = 1, 2, 3$. Note that all $C_{\alpha\alpha m}$ and $D_{\alpha m}$ are diagonal.

Then the matrix equation for moment stresses moving along the axis x_α by analogy with (14) takes the form

$$\begin{aligned} (I_3 \partial_t \pm D_{\alpha m} \partial_\alpha)(M_\alpha^T \mp J D_{\alpha m} \omega^T) &= \\ = C_{\alpha km} \partial_k \omega^T \mp D_{\alpha m} (\partial_k M_k^T - S_i Q_i P^T + Y^T). \end{aligned} \quad (24)$$

where $i = \alpha, \beta, \gamma$, $k = \beta, \gamma$.

The equations on fixed discontinuities similar to (19) will take the form

$$\begin{aligned} \partial_t (M_\beta^T - C_{\beta\alpha m} C_{\alpha\alpha m}^{-1} M_\alpha^T) &= \\ = (C_{\beta km} - C_{\beta\alpha m} C_{\alpha\alpha m}^{-1} C_{\alpha km}) \partial_k \omega^T, \quad (25) \\ \partial_t (M_\gamma^T - C_{\gamma\alpha m} C_{\alpha\alpha m}^{-1} M_\alpha^T) &= \\ = (C_{\gamma km} - C_{\gamma\alpha m} C_{\alpha\alpha m}^{-1} C_{\alpha km}) \partial_k \omega^T. \end{aligned}$$

In scalar form, equations (24) and (25) represent 9 equations

$$\begin{aligned} (\partial_t \pm c_3 \partial_\alpha) (\mu_{\alpha\alpha} \mp J c_3 \omega_\alpha) &= \beta (\partial_\beta \omega_\beta + \partial_\gamma \omega_\gamma) \mp \\ \mp c_3 (\partial_\beta \mu_{\beta\alpha} + \partial_\gamma \mu_{\gamma\alpha} + p_{\gamma\beta} - p_{\beta\gamma} + y_\alpha), \\ c_3 &= \sqrt{(2\varphi + \beta) / J}, \\ (\partial_t \pm c_4 \partial_\alpha) (\mu_{\alpha\beta} \mp J c_4 \omega_\beta) &= (\varphi - \varepsilon) \partial_\beta \omega_\alpha \mp \\ \mp c_4 (\partial_\beta \mu_{\beta\beta} + \partial_\gamma \mu_{\gamma\beta} + p_{\alpha\gamma} - p_{\gamma\alpha} + y_\beta), \\ c_4 &= \sqrt{(\varphi + \varepsilon) / J}, \\ (\partial_t \pm c_4 \partial_\alpha) (\mu_{\alpha\gamma} \mp J c_4 \omega_\gamma) &= (\varphi - \varepsilon) \partial_\gamma \omega_\alpha \mp \\ \mp c_4 (\partial_\beta \mu_{\beta\gamma} + \partial_\gamma \mu_{\gamma\gamma} + p_{\beta\alpha} - p_{\alpha\beta} + y_\gamma), \quad (26) \\ \partial_t (\mu_{\beta\alpha} - \eta_m \mu_{12}) &= 4\varepsilon\varphi(\varphi + \varepsilon)^{-1} \partial_\beta \omega_\alpha, \\ \partial_t (\mu_{\beta\beta} - \nu_{1m} \mu_{\alpha\alpha}) &= 2\varphi[(1 + \nu_{1m}) \partial_\beta \omega_\beta + \nu_{1m} \partial_\gamma \omega_\gamma], \\ \partial_t \mu_{\beta\gamma} &= \varphi(\partial_\beta \omega_\gamma + \partial_\gamma \omega_\beta) + \varepsilon(\partial_\beta \omega_\gamma - \partial_\gamma \omega_\beta), \\ \partial_t (\mu_{\gamma\alpha} - \eta_m \mu_{12}) &= 4\varepsilon\varphi(\varphi + \varepsilon)^{-1} \partial_\gamma \omega_\alpha, \\ \partial_t \mu_{\gamma\beta} &= \varphi(\partial_\gamma \omega_\beta + \partial_\beta \omega_\gamma) + \varepsilon(\partial_\gamma \omega_\beta - \partial_\beta \omega_\gamma), \\ \partial_t (\mu_{\gamma\gamma} - \nu_{1m} \mu_{\alpha\alpha}) &= 2\varphi[\nu_{1m} \partial_\beta \omega_\beta + (1 + \nu_{1m}) \partial_\beta \omega_\beta], \end{aligned}$$

where $\eta_m = (\varphi - \varepsilon) / (\varphi + \varepsilon)$, $\nu_{1m} = \beta / (2\varphi + \beta)$.

Just as in the case of ordinary stresses, the relations for moment stresses are valid

$$\partial_t (\mu_{\beta\gamma} + \mu_{\gamma\beta}) = 2\varphi(\partial_\beta \omega_\gamma + \partial_\gamma \omega_\beta). \quad (27)$$

Matrix characteristic equations (14), (20), (24) and (25) fully determine the dynamics of the Cosserat medium. They are redundant and their choice is determined by the context of the task. In the numerical solution, the equations for longitudinal waves are essential for implementation. In this case, the computational schemes are stable. In the case of waves of one direction, the matrix characteristic equations give as many scalar equations as the defined variables. In both cases, the computational process is recurrent. Equations (22) and (27), as well as the fact that the normal stresses do not depend on ω_i , greatly simplify the computational process by reducing the number of scalar equations in which p_{ij} and ω_i they are linked.

A significant simplification of the equations occurs in the case of the condition

$$\Omega^T = \frac{1}{2} \text{rot } u, \quad (28)$$

used for a pseudo-continuum Cosserat.

Recording the operation rot in matrix form [10] and using (8), we write

$$\begin{aligned} \partial_t \Gamma^T &= Q_i^T (\partial_i V^T + S_i \omega^T) = \\ = Q_i^T (\partial_i V^T + \frac{1}{2} S_i S_m \partial_m V^T), \end{aligned} \quad (29)$$

and the characteristic equations for ordinary stresses are not related to the analogous equations for moment stresses.

After calculating (29), we get the matrix-string $\partial_t \Gamma$ as

$$\partial_t \Gamma = \begin{bmatrix} \varepsilon_{11} & \varepsilon_{22} & \varepsilon_{33} & \varepsilon_{12} & \varepsilon_{13} & \varepsilon_{21} & \varepsilon_{23} & \varepsilon_{31} & \varepsilon_{32} \end{bmatrix}, \quad (30)$$

where $\varepsilon_{ij} = 2^{-1}(\partial_i V_j + \partial_j V_i)$, $i, j = 1, 2, 3$ – rates of deformations of the classical elasticity theory.

By entering additional matrices q_{ij} and e_i from formula (5), the method used in constructing the matrix C_p , and by grouping the corresponding terms around operators ∂_i , can be obtained $\partial_t \Gamma^T$ as

$$\partial_t \Gamma^T = \Theta_i^T \partial_i V^T, \quad (31)$$

where

$$\Theta_i = \begin{bmatrix} \delta_{ii} & 0 & 0 & \delta_{2i}/2 & \delta_{3i}/2 & \delta_{2i}/2 & 0 & \delta_{3i}/2 & 0 \\ 0 & \delta_{2i} & 0 & \delta_{ii}/2 & 0 & \delta_{ii}/2 & \delta_{3i}/2 & 0 & \delta_{3i}/2 \\ 0 & 0 & \delta_{3i} & 0 & \delta_{ii}/2 & 0 & \delta_{2i}/2 & \delta_{ii}/2 & \delta_{2i}/2 \end{bmatrix}.$$

The first equation of the system (8) written for the pseudo-continuum Cosserat has the form

$$\partial_t P^T = C_p \Theta_i \partial_i V^T, \quad (32)$$

where from

$\partial_t P = \partial_t [\sigma_{11} \ \sigma_{22} \ \sigma_{33} \ \sigma_{12} \ \sigma_{13} \ \sigma_{21} \ \sigma_{23} \ \sigma_{31} \ \sigma_{32}]$, where σ_{ij} – tensor of classical theory of elasticity. For such stresses, the conditions $\sigma_{\alpha\beta} = \sigma_{\beta\alpha}$ are met, and therefore the characteristic equations for ordinary and moment stresses are not related.

To determine the wave velocity in a pseudo-continuum model let's consider the products of matrices $Q_\alpha C_p \Theta_\alpha^T$, $\alpha = 1, 2, 3$. By calculation, we can see that all these products are diagonal and have their own number $2\mu + \lambda$ and μ , and their corresponding wave velocities are $c_1 = \sqrt{(2\mu + \lambda)/\rho}$ and $c_2^* = \sqrt{\mu/\rho}$, the same as for an ordinary isotropic body. The only difference is that here the stiffness matrix has the form C_p .

The first equation of the system (7) and equation (32) can be used to construct a matrix characteristic form of the dynamics equations of the pseudocontinuum Cosserat. For moment stresses, the construction remains the same, with the difference that the terms $S_i Q_i P^T$ should be excluded from the equations on moving discontinuities.

Let us construct a matrix characteristic form of the pseudocontinuum dynamics equations Cosserat's by method, to be discussed above.

Let's assume as before, the wave propagates in both directions along the axis x_α . Let us perform transformations similar to (12)-(14) and obtain a matrix characteristic equation on moving discontinuities

$$(I_3 \partial_t \pm D_{\alpha p}^* \partial_\alpha) (P_\alpha^T \mp \rho D_{\alpha p}^*) = \\ = C_{\alpha k}^* \partial_k V^T \mp D_{\alpha p}^* (\partial_k P_k^T + F^T), \quad (33)$$

where $D_{1p}^* = \text{diag}(c_1, c_2^*, c_2)$, $C_{\alpha k}^* = Q_\alpha C_p \Theta_k^T$, or in scalar form:

$$(\partial_t \pm c_1 \partial_\alpha) (\sigma_{\alpha\alpha} \mp \rho c_1 V_\alpha) = \lambda (\partial_\beta V_\beta + \partial_\gamma V_\gamma) \mp \\ \mp c_1 (\partial_\beta \sigma_{\beta\alpha} + \partial_\gamma \sigma_{\gamma\alpha} + f_\alpha), \\ (\partial_t \pm c_2^* \partial_\alpha) (\sigma_{\alpha\beta} \mp \rho c_2^* V_\beta) = \mu \partial_\beta V_\alpha \mp \\ \mp c_2^* (\partial_\beta \sigma_{\beta\beta} + \partial_\gamma \sigma_{\gamma\beta} + f_\beta), \\ (\partial_t \pm c_2^* \partial_\alpha) (\sigma_{\alpha\gamma} \mp \rho c_2^* V_\gamma) = \mu \partial_\gamma V_\alpha \mp \\ \mp c_2^* (\partial_\beta \sigma_{\beta\gamma} + \partial_\gamma \sigma_{\gamma\gamma} + f_\gamma). \quad (34)$$

On fixed discontinuities, due to the symmetry of tangent stresses, it remains to determine the three stresses $p_{\beta\beta}$, $p_{\gamma\gamma}$ and $p_{\beta\gamma}$. Enter a matrix N that selects from matrix-string P the above mentioned voltages. Obviously, this matrix must have the form $N = e_1^T q_{\beta\beta} + e_2^T q_{\gamma\gamma} + e_3^T q_{\beta\gamma}$. Then we multiply $\partial_t P^T$ from equation (32) on the left by N and select in the right part the term containing ∂_i ; denoting $P_N^T = NP^T$ and $C_{Ni}^* = NC_p \Theta_i$, $i = 1, 2, 3$ we get the equation

$$\partial_t P_N^T = C_{N\alpha}^* \partial_\alpha V^T + C_{Nk}^* \partial_k V^T, \quad k = \beta, \gamma. \quad (35)$$

Since it is possible to determine all the components of the matrix from formulas (34) P_α , multiply (32) on the left by Q_α and select $\partial_t V^T$ from the resulting equation

$$\partial_\alpha V^T = (C_{\alpha\alpha}^*)^{-1} (\partial_t P_\alpha^T - C_{\alpha k}^* \partial_k V^T). \quad (36)$$

Substituting $\partial_t V^T$ from (36) to (35) and conducting the corresponding grouping, we finally obtain the matrix equation on fixed discontinuities

$$\partial_t (P_N^T - C_{N\alpha}^* (C_{\alpha\alpha}^*)^{-1} P_\alpha^T) = \\ = (C_{Nk}^* - C_{N1}^* (C_{11})^{-1} C_{1k}^*) \partial_k V^T. \quad (37)$$

The scalar form of this equation has the following form

$$\partial_t (\sigma_{\beta\beta} - \nu_1 \sigma_{\alpha\alpha}) = (1 - \nu_1) [(\mu + \lambda) \partial_\beta V_\beta + \lambda \partial_\gamma V_\gamma], \\ \partial_t (\sigma_{\gamma\gamma} - \nu_1 \sigma_{\alpha\alpha}) = (1 - \nu_1) [(\mu + \lambda) \partial_\gamma V_\gamma + \lambda \partial_\beta V_\beta], \\ \partial_t \sigma_{\beta\gamma} = \mu (\partial_\beta V_\gamma + \partial_\gamma V_\beta). \quad (38)$$

The characteristic equations (34) and (38) are identical to the analogous equations for an isotropic symmetrically elastic body, which constructed, for example, as a special case in [13].

3. MODELING

The characteristic equations for the Cosserat model constructed here allow us to solve a whole range of problems with connected and unconnected ordinary and instantaneous stresses. In particular,

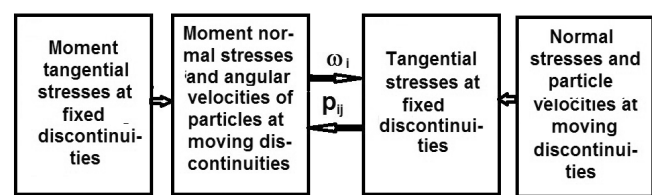


Fig. 1. Scheme of interaction of longitudinal torsional waves with transverse waves of ordinary stresses and velocities of particles.

the theory of pseudocontinuum Cosserat allows you to connect classical and moment mechanics and can serve as the first stage of an iterative process of numerical calculation of the related problem of medium dynamics Cosserat.

Consider the case, when $c_1 > c_3 \geq c_2 > c_4$ the point under consideration is also inside the body. In this case, the longitudinal torsion waves act in turn with the transverse waves of ordinary stresses and velocities of a particles. The interaction diagram is shown in **Fig. 1**.

Taking the pseudocontinuum Cosserat as the initial approximation we have unconnected characteristic equations for ordinary and moment stresses. Having determined the angular velocities of particles ω_i from the left part of the Fig. 1, we substitute them in the equations for tangent stresses; then we return the calculated tangent p_{ij} stresses back to the moment equations on moving discontinuities, thus providing a recurrent calculation ω_i and p_{ij} . At the same time, normal stresses $p_{\alpha\alpha}$, their corresponding velocity V_α and tangent moment stresses $\mu_{\alpha\beta}$ do not directly participate in the exchange, although $\mu_{\alpha\beta}$ they are corrected after each exchange act. To reduce the number of equations involved in the exchange, use equations (22), (25), and (32).

To construct computational schemes at the boundary point of the medium at the same speed sequence, we use the scheme shown in **Fig. 2**.

As indicated above, at the boundary point, we should consider the equations for waves moving inside the body along the normal path to its boundary, equations for fixed discontinuities, and boundary conditions. The sum of these equations and conditions is the same as that of the defined variables, but the sequence of calculations depends significantly on the type of boundary conditions.

Consider the right-hand side of Fig. 2, in which p_{ij} and V_i are calculated. As shown by formulas (15), (21),

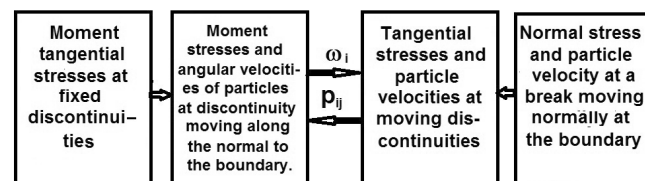


Fig. 2. Scheme for constructing computational circuits at the boundary point of the medium with the same speed calculation sequence.

all normal stresses p_{ii} and the velocity of a particles V_α , directed along the normal to the considered boundary x_α , can be calculated independently of ω_i by the same formulas as in the usual metric theory of elasticity. The order of calculation of the remaining values depends on the corresponding boundary conditions: let, for example, tangent voltage $p_{\beta\alpha}$ is given at the boundary x_α , then, in accordance with the equation

$$\partial_t(p_{\alpha\beta} + p_{\beta\alpha}) = 2\mu(\partial_\beta V_\alpha + \partial_\alpha V_\beta) \quad (39)$$

it is determined $p_{\alpha\beta}$, and from equation (16) it is determined V_β , the plus sign or minus is determined by the position of the boundary: plus corresponds to the boundary $x_{\alpha\max}$, and minus – $x_{\alpha\min}$.

If set at the boundary V_β , then from (16) it is defined $p_{\alpha\beta}$, and then from (39) $p_{\beta\alpha}$

Similarly, $p_{\gamma\sigma}$, $p_{\sigma\gamma}$ and V_γ are calculated.

The values $p_{\beta\gamma}$ of and $p_{\gamma\beta}$ are determined from the system (21) and equation (22)

Now consider the left-hand side of Fig. 2, where the angular velocity of particles ω_i and moment stresses μ_{ij} are calculated. We will also start the review with the internal point of the environment. For the stability of the computational scheme, it is necessary to select all the equations for the normal components of moment stresses $\mu_{\alpha\alpha}$, $\alpha = 1,2,3$ and angular velocities of particles ω_i ; the remaining stresses can be obtained independently from 3 equations on fixed discontinuities

$$\partial_t \mu_{\alpha\beta} = \varphi(\partial_\alpha \omega_\beta + \partial_\beta \omega_\alpha) + \varepsilon(\partial_\alpha \omega_\beta - \partial_\beta \omega_\alpha), \quad (40)$$

and equations (27). At the boundary point, we define 3 equations on discontinuities moving along the normal to the boundary $x_\alpha = \text{const}$ from inside the body, 3 equations on fixed discontinuities, 3 boundary conditions, and 3 equations included in (27). Depending on the boundary condition (ω_i or μ_{ij}) on the moving discontinuities, the remaining variable (μ_{ij} or ω_i) is determined. Then with the help of (27) it is determined μ_{ij} and, finally, the last 3 stresses $\mu_{\beta\beta}$, $\mu_{\gamma\gamma}$ and $\mu_{\beta\gamma}$ are divided by the corresponding equations of the system (26).

4. CONCLUSION

In the article, using the matrix apparatus proposed by the author, we construct the matrix and scalar forms of characteristic equations of medium dynamics Cosserat and pseudo-continuum Cosserat. We used the simplest auxiliary matrices consisting

of zeros and ones, and the same transformations. The order of derivatives was never increased, and no additional conditions were set. The number of constructed equations turned out to be excessive, so then the question of their choice in various cases was considered.

It was shown that the characteristic form of representation of equations for a pseudo-continuum Cosserat reduced to the equations for symmetrical elastic isotropic body, but with the stiffness matrix of the model Cosserat. This circumstance was used in numerical simulation of the dynamics of the Cosserat medium at the same time pseudo-continuum model was considered as an initial approximation for the scheme of sequential calculations of the dynamics of bounded bodies.

According to [11], equations for longitudinal waves propagating in all three directions were used inside the body. At the boundary points, according to [12], we considered all types of waves that fit normally to the boundary of the body from within. Since in each type of wave that approaches the boundary, the same variables (ϕ_{α} , V_i or μ_{α} , ω) change over time as in the corresponding boundary conditions, the choice of variants of interaction of the wave with the boundary conditions is minimal, and this interaction itself it is the simplest and most convenient for numerical calculations.

When approximating the time derivative with a one-way difference and the coordinates with a central difference, the residual terms in all equations have an order $O(\partial_t^2, \partial_{x_i}^3)$ and the calculation errors do not accumulate [13], and the computational schemes are stable.

REFERENCES

1. Cosserat E, Cosserat F. *Theorie des corps deformables*. Paris, Hermann, 1909.
2. Kossera E, Kossera F. Zametka o teorii evklidovskogo deystviya (reprint) [Cosserat E, Cosserat F. A note on the theory of Euclidean action]. *RENSIT*, 2013, 5(1):5-76 (in Russ.); https://www.elibrary.ru/download/elibrary_19429292_61149270.pdf/
3. Kuvshinsky EV, Aero EL. Continuum theory of asymmetric elasticity. *FTT*, 1963, 5(9):2591-2598.
4. Palmov NA. Basic equations of the theory of asymmetric elasticity. *PMM*, 1964, 28(3):401-408.
5. Novatskiy V. *Teoriya uprugosti* [Theory of elasticity]. Moscow, Mir Publ., 1975, p. 852.
6. Morozov NF. *Matematicheskie voprosy teorii theshchin* [Mathematical theory of cracks]. Moscow, Nauka Publ., 1984, p. 256.
7. Zhilin PA. Basic equations of non-classical elasticity theory shells. *Trudy Leningr. polytechn. inst.*, no. 386, 1982, pp. 29-46.
8. Erofeev VI. *Volnovye processy v tverdykh telakh s mikrostrukturoy* [Wave processes in solids with microstructure]. Moscow, Moscow state university Publ., 1999, p. 327.
9. Kunin IA. *Teoriya uprugikh tel s mikrostrukturoy. Nelokalnaya teoriya uprugosti* [Theory of elastic media with microstructure. Nonlocal theory of elasticity]. Moscow, Nauka Publ., 1975, p. 415.
10. Bulychev GG. Characteristic form of equations of dynamics of media of complex structure. *RENSIT*, 2020, 12(2):245-252. DOI: 10.17725/rensit.2020.12.245.
11. Kukudzhanov VN. *Chislennoe reshenie neodnomernykh zadach rasprostraneniya voln napryazhenii v tverdykh telakh* [Numerical solution of inhomogeneous problems of distribution of stress waves in solids]. Moscow, Dorodnicyn Computing Centre of USSR Publ., Issue 6, 1976, 76 p.
12. Butler DS. The numerical solution of hyperbolic systems of partial differential equations in three independent variables. *Proc. Roy. Soc. of London. Series A, Mathematical and Physical Sciences*. 1962, 255(1281):319-343. DOI: 10.2307/2413911.
13. Samarskiy AA. *Teoriya raznostnykh skhem* [Theory of difference schemes]. Moscow, Nauka Publ., 1989, 616 p.

DOI: 10.17725/rensit.2021.13.495

Development of a mathematical model of functioning system communications spacecraft

Mikhail A. Zaytsev, Alexander K. Korovin

The Military Academy of Strategic Rocket Troops after Peter the Great, <https://varvsn.mil.ru/>
Balashikha 143900, Moscow region, Russian Federation

E-mail: mihay-82@mail.ru, shurke@bk.ru

Sergey B. Savilkin

Center of Visualization and Satellite Information Technologies, Scientific Research Institute of System Analysis of the RAS, <https://niisi.ru/>
Moscow 117218, Russian Federation
Moscow Aviation Institute, <https://mai.ru/>
Moscow 125993, Russian Federation

E-mail: savilkin@mail.ru

Andrey V. Sukhov

Moscow Aviation Institute, <https://mai.ru/>
Moscow 125993, Russian Federation

E-mail: avs57@mail.ru

Received July 14, 2021, peer-reviewed July 23, 2021, accepted July 30, 2021

Abstract: The paper discusses a mathematical model of the functioning of communication spacecraft, using systems of differential equations for translational and rotational motion, as well as the process of distributing problems in a constellation of three satellites. The model is implemented by means of the python 3.6 language and the computational method library numpy1.19. A series of computational experiments was carried out in order to estimate the energy costs for the operation of grouping with various orbital parameters and external impact models. The presented results of the experiments suggest the possibility of increasing the life of spacecraft by improving the operating system.

Keywords: communication spacecraft, mathematical model, control system

UDC 519.7

Acknowledgments: The work is made as part of national assignment for SRISA RAS (fundamental scientific research 47 GP) on the topic No. FNEF-2021-0001 (0580-2021-0001), reg. No. 121031300047-6 "Software and tools for modeling, design and development of elements of complex technical systems, software systems and telecommunication networks in various problem-oriented areas"(AAAA-A19-119011790077-1).

For citation: Mikhail A. Zaytsev, Alexander K. Korovin, Sergey B. Savilkin, Andrey V. Sukhov. Development of a mathematical model of functioning system communications spacecraft. *RENSIT: Radioelectronics. Nanosystems. Information technologies*, 2021, 13(4):495-500. DOI: [10.17725/rensit.2021.13.495](https://doi.org/10.17725/rensit.2021.13.495).

CONTENTS

- 1. INTRODUCTION (495)
- 2. THE MODELING METHOD (497)
- 3. THE MODELING RESULTS (498)
- 4. CONCLUSION (499)
- REFERENCES (499)

1. INTRODUCTION

Improving the control system for the exploitation of communication spacecraft is an urgent technical task. One of the important directions in the research of this issue is the optimization of energy costs for maintaining a specified state of

the spacecraft. Depending on the completeness of the factors taken into account, mathematical models of various levels of complexity are used in the research. In practice, under specified constraints, deterministic or stochastic linear models are usually used in the state area.

The state area is formed by a set of vectors with a minimum number of coordinates containing all the necessary information about the motion of the spacecraft. In the state area given in this way, linear mathematical models have a formal representation of the form [1-3]:

$$\dot{x} = A(t)x + B(t)u(t), \quad (1)$$

where $x^T = (x_1, x_2, \dots, x_r)$ – state vector, T – transpose symbol; $A(t)$ – matrix of dynamic model features; $B(t)$ – matrix of intense of control action; $u^T(t) = (u_1, u_2, \dots, u_r)$ – control action.

The behavior of the system (1) over a period of time $[0, t]$ is determined by setting the initial conditions $x(t=0)$ and described by the expression [1,2]:

$$x(t) = N(t, 0)x(0) + \int_0^t N(t, \tau)B(\tau)u(\tau)d\tau, \quad (2)$$

where $N(t, \tau) = \Phi(t)\Phi^{-1}(\tau)$ – matrix of initial system influence; $\Phi(t)$ – fundamental matrix of homogeneous system $\dot{x} = A(t)x(t)$.

It is not possible to find an analytical solution in a general form, so there is a need to present mathematical models of spacecraft motion in finite differences. In discrete form, provided that the control action $u(t)$ retains its value unchanged on the segment $[t_n, t_{n+1}]$, the expression (2) will take the form:

$$x(t_{n+1}) = N(t_{n+1}, t_n)x(t_n) + \\ + u(t_n) \int_{t_n}^{t_{n+1}} N(t_{n+1}, \tau)B(\tau)d\tau. \quad (3)$$

We introduce the following notation:

$$x(t_{n+1}) = x_{n+1},$$

$$u(t_{n+1}) = u_{n+1},$$

$$\int_{t_n}^{t_{n+1}} N(t_{n+1}, \tau)B(\tau)d\tau = \Gamma(t_n) = \Gamma_n,$$

$$N(t_{n+1}, t_n) = N_{n+1, n}.$$

Taking into account the entered notation, the expression (3) will take the form [3]:

$$x_{n+1} = N_{n+1, n}x_n + \Gamma_n u_n.$$

Researching the motion of a spacecraft in real operation, the assumption of the determinism of external influences and functional parameters is acceptable only for relatively short time sampling intervals.

The works of L.S. Pontryagin and his students are devoted to the description of the properties of dynamical systems subject to random perturbations. The further development of ideas about the management of complex technical systems was reflected in the use of artificial intelligence based on information system redundancy [4]. The problem of optimal control in the information space is solved in [6,7].

The main problem of optimal control of the spacecraft is formulated as follows: among all the permissible controls that transfer the image point in the phase space of the system from the initial position to the final one, it is necessary to find such a control at which the minimum of the following functional is achieved [2].

$$I^*(x, u) = \min \sum_{n=0}^{N-1} G_n(x_n, u_n) + \varphi(x_N),$$

where n – number of discrete time step; G – the functional of the costs of managing the spacecraft; in the special case, when the optimality problem is considered for energy consumption for control, the integrand function $G(x, u) \equiv |u|$; $\varphi(x_K)$ – a term that takes into account the ability of the spacecraft to perform the task according to its intended purpose in the final state.

The minimized functional $I(\cdot)$ is an inverse control efficiency. This mapping cannot always be defined as unambiguous, so a more general type of functionality is used.

The solution of the problem by the method of dynamic programming allows us to reduce the problem to a sequential minimization of the

function r of variables (the dimension of the control vector u).

Assume that all the values of the optimal control u_n , except the last one, are found and the system is in the state x_{N-1} . According to the optimality principle, the control u_{N-1} must also be optimal.

This control should provide a minimum of functionality, which, taking into account the restrictions imposed by the requirements for ensuring a communication session on a given section of the spacecraft trajectory, for a section of the trajectory ($N - 1$) has the form [2]:

$$I_{N-1}(x_{N-1}, u_{N-1}) = G_{N-1}[x_{N-1}, u_{N-1}] + \varphi[x_N].$$

Define

$$S_{N-1}(x_{N-1}) = \min_{u_{N-1} \in U} I_{N-1}(x_{N-1}, u_{N-1}).$$

Then the recurrent formula for determining the minimum value of the functional $I_{k-k}(x, u)$ and the corresponding optimal control $\bar{u}(K - k)$ at the k step will have the form:

$$\begin{aligned} S_{K-k}(x_{K-k}) &= \min_{u_{K-k} \in U} \{G_{K-k}(x_{K-k}, u_{K-k}) + \\ &+ S_{K-k+1}f(x_{K-k}, u_{K-k})\}. \end{aligned}$$

The optimal control $\bar{u}(K - k)$ is defined as a function of the coordinates of the state of the system $\bar{u}(K - k) = \bar{u}(x_{K-k})$. Calculating the values of the function $S_{k=k}$ sequentially, we obtain the minimum value of the functional for the entire trajectory. At the same time, the optimal control is determined in the function of the coordinates of the system, i.e. the problem of synthesizing the optimal controller is solved. The specified procedure is performed using a computer. Thus, the application of the optimality principle makes it possible to significantly simplify calculations in comparison with the analytical method of solving the problem for a conditional extremum.

2. THE MODELING METHOD

Consider an open discrete spacecraft control system (Fig. 1). The input of the control device receives a setting action x_n^* , which

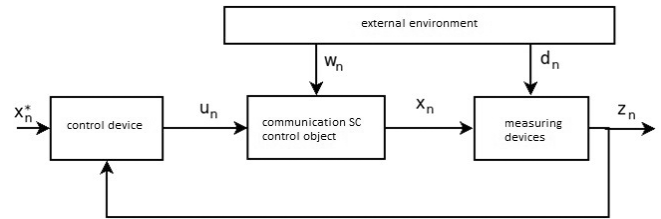


Fig. 1. Model of the spacecraft functioning system.

determines what the desired state of the object should be. The control device generates an r -dimensional control action u_n on the control object (spacecraft). The motion of the spacecraft is influenced by external disturbing factors w_n . The value of the state vector of the spacecraft x_n is determined using measuring devices with an error d_n (measurement noise). The system is considered fully observable if the values of all elements of the state vector x can be found from the measurement vector \tilde{x} :

The state vector of the spacecraft is characterized by the coordinates [1,3]:

$$x = \{x_c, y_c, z_c, v_x, v_y, v_z, m, \psi, \theta, \gamma, \omega_\psi, \omega_\theta, \omega_\gamma, I_\psi, I_\theta, I_\gamma\},$$

where x_c, y_c, z_c – coordinates of the center of mass of the spacecraft; v_x, v_y, v_z – projections of the velocity vector on the coordinate axis; m – spacecraft mass; ψ, θ, γ – projections of the angular velocity of the spacecraft; $I_\psi, I_\theta, I_\gamma$ – projections of the inertia tensor of the spacecraft.

The vector of external disturbances consists of the effects of the unstable gravitational field of the Earth and other cosmic bodies [1, 3]:

$$w = \{F_{Gx}, F_{Gy}, F_{Gz}, \delta F_x, \delta F_y, \delta F_z, \delta M_\psi, \delta M_\theta, \delta M_\gamma\},$$

where F_{Gx}, F_{Gy}, F_{Gz} – the deterministic component of the action of the gravitational attraction of the Earth; $\delta F_x, \delta F_y, \delta F_z$ – random impact of linear forces of cosmic bodies; $\delta M_\psi, \delta M_\theta, \delta M_\gamma$ – random moments of rotation.

The translational and rotational motion of the spacecraft is described by a system of differential equations (SDE) [1]:

$$\dot{x} = x_0 + v_x t,$$

$$\dot{y} = y_0 + v_y t,$$

$$\dot{z} = z_0 + v_z t,$$

$$\dot{v}_x = v_{x0} + \frac{F_{Gx} + \delta F_x}{m} t,$$

$$\dot{v}_y = v_{y0} + \frac{F_{Gy} + \delta F_y}{m} t,$$

$$\dot{v}_z = v_{z0} + \frac{F_{Gz} + \delta F_z}{m} t,$$

$$\psi = \psi_0 + \omega_\psi t,$$

$$\dot{\theta} = \theta_0 + \omega_\theta t,$$

$$\dot{\gamma} = \gamma_0 + \omega_\gamma t,$$

$$\dot{\omega}_\psi = \omega_\psi + \frac{M_\psi}{I_\psi} t,$$

$$\dot{\omega}_\theta = \omega_\theta + \frac{M_\theta}{I_\theta} t,$$

$$\dot{\omega}_\gamma = \omega_\gamma + \frac{M_\gamma}{I_\gamma} t,$$

where x_0, y_0, z_0 – coordinates of the center of mass of the spacecraft at the initial moment of time, $\dot{x}, \dot{y}, \dot{z}$ – coordinates of the center of mass of the spacecraft at a given time, $\dot{v}_x, \dot{v}_y, \dot{v}_z$ – components of the linear velocity of the spacecraft at a given time, $\psi_0, \theta_0, \gamma_0$ – angular position of the spacecraft at the initial moment of time, $\psi, \dot{\theta}, \dot{\gamma}$ – the angular position of the spacecraft at a given time, $\dot{\omega}_\psi, \dot{\omega}_\theta, \dot{\omega}_\gamma$ – the angular velocity of the spacecraft at a given time.

The system is solved using the two-stage Runge-Kutta method (Hoyne method) according to the predictor-corrector scheme [5] of the following type:

Predictor:

$$\tilde{b}_i = b_{i-1} + (a_i - a_{i-1}) f(a_{i-1}, b_{i-1}).$$

Corrector:

$$b_i = b_{i-1} + (a_i - a_{i-1}) \frac{f(a_{i-1}, b_{i-1}) + f(a_i, \tilde{b}_i)}{2}.$$

Pulsed two-parameter three-component correction is carried out in order to maintain the parameters of the spacecraft's orbit and maintain orientation during a communication session. The model uses the hypothesis of an instantaneous change in linear and angular velocities, while

taking into account only the energy costs of correction:

$$E_x = m_{KA} \frac{\Delta V^2}{2},$$

$$E_w = \frac{I_z \Delta \omega^2}{2}.$$

To determine the feed moments and the magnitude of the correction pulses, a quasi-optimal control algorithm was used, which minimizes energy consumption for maintaining the specified orbit parameters.

$$i_c = 00.02.00^{+00.06.00}$$

$$\Omega_c = 00.00.00$$

$$\omega_c = 00.00.00$$

$$e_c = 00.01.16^{+0.0035}$$

$$p_c = 42050$$

$$v_c = 30.00.00^{+00.06.00}.$$

An object-oriented model with three entities has been developed for the presented mathematical model: SpaceShip – spacecraft; Earth – planet Earth; Environment – external environment.

The simulation model is implemented by means of the **python 3.6** language using the **numpy v1.19** library, the visualization is implemented by means of the **matplotlib v3.3.1** library.

3. THE MODELING RESULTS

An experiment was conducted with a grouping of three spacecraft that ensure the fulfillment of the target task within one day. The obtained spacecraft trajectories without modeling external influences are verified with the specified orbit characteristics and with a given relative error not exceeding 10^{-4} for each coordinate.

Taking into account the distribution of the task execution time by purpose (providing signal retransmission) between the three spacecraft, the motion simulation was carried out taking into account the disturbing effects of the external environment (Fig. 2). During the experiment, estimates of energy consumption

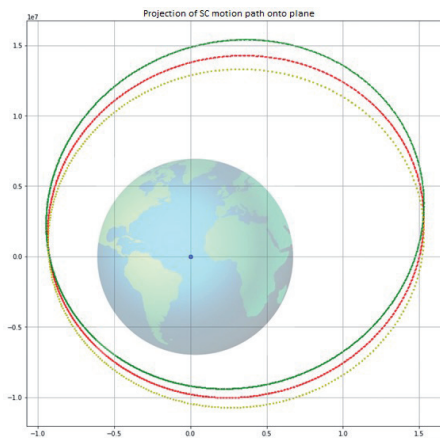


Fig. 2. Projection of the trajectory of the spacecraft on the plane.

for maintaining the specified characteristics of the orbits for spacecraft moving along different trajectories were obtained (**Fig. 3**).

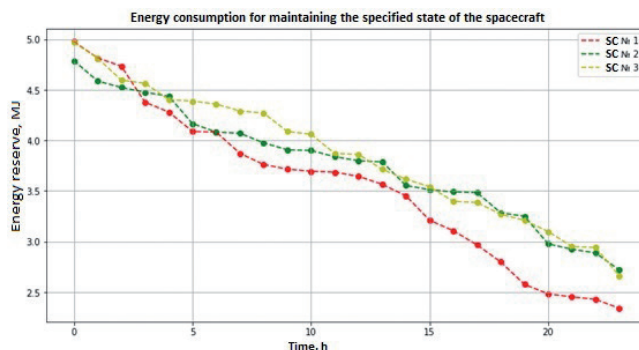


Fig. 3. Energy consumption for maintaining the specified state of the spacecraft.

Based on the empirically obtained average energy consumption of 0.1 MJ/h, an experiment was conducted in which the average operating time of the spacecraft was studied depending on the nature and magnitude of the disturbing effects on it. The results are shown in the graph (**Fig. 4**).

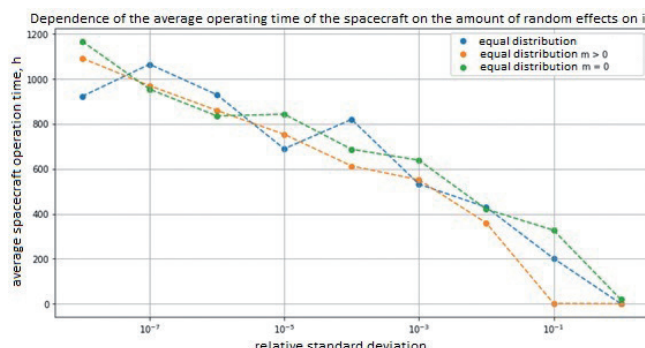


Fig. 4. Average operating time of the spacecraft under various influences.

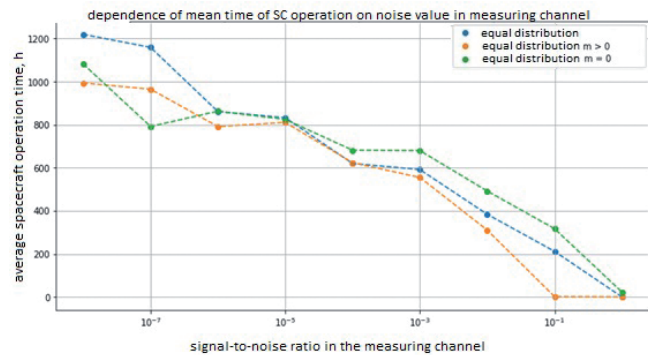


Fig. 5. The average operating time of the spacecraft at various measurement noises.

Based on the empirically obtained average energy consumption of 0.1 MJ/h, an experiment was conducted in which the average operating time of the spacecraft was studied depending on the nature and magnitude of the signal-to-noise ratio in the measuring channel. The results are shown in the graph (**Fig. 5**).

4. CONCLUSION

Thus, the developed model allows us to study the energy efficiency of control algorithms in various modes of operation of both a single spacecraft and a group of space crafts, taking into account the restrictions imposed by the implementation of the communication task. The conducted experiments indicate the possibility of increasing the active life of spacecraft by optimizing the operation system.

REFERENCES

1. Avduevskij VS, Antonov BM, Anfimov NA. *Osnovy teorii poleta kosmicheskikh apparatov* [Fundamentals of the theory of spacecraft flight]. Moscow, Mashinostroenie Publ., 1972, 608 p.
2. Balakin VL, Bayandina TA. *Optimal'noe upravlenie letatel'nymi apparatami* [Optimal control of aircraft]. S.P. Korolev Samara aerospace State University (National Research Institute). Samara, Electron Publ., 2013, 38 p.
3. Krineckij E.A. *Letnye ispytaniya raket i kosmicheskikh apparatov* [Flight tests of rockets

- and spacecraft]. Moscow, Mashinostroenie Publ., 1979, 461 p.
4. Potyupkin AYu., Chechkin AV. *Iskusstvennyj intellekt na baze informacionno-sistemnoj izbytochnosti* [Artificial intelligence based on information system redundancy]. Moscow, Nauka Publ., 2019, 384 p.
 5. Samarskij AA, Gulin AV. *Chislennye metody* [Numerical methods] Moscow, Nauka Publ., 1989, 429 p.
 6. Kachanov AYu., Zaitsev MA, Dubinin DP. Otsenka vozmozhnostej dejstvuyushchej sistemy sputnikovoj svyazi pri reshenii zadach informatsionnogo obmena v informatsionno-kommunikatsionnom prostranstve dlya obespecheniya upravleniya dinamicheskimi ob'ektami [Evaluation of the capabilities of the existing satellite communication system in solving problems of information exchange in the information and communication space to ensure the management of dynamic objects]. In: *RTI Systems of East Kazakhstan Region-2017. Proceedings of the V All-Russian Scientific and Technical Conference*. 2018, pp. 113-119 (in Russ.).
 7. Sukhov AV, Zaitsev MA. Ispol'zovanie entropii pokrytiya pri informacionnom analize rezul'tatov radiomonitoringa sputnikovyh sistem. [Using of coverage entropy in the information analysis of the results of radio monitoring of satellite systems]. *Transportnoe delo Rossii*, 2013, 6:156-159 (in Russ.).

DOI: 10.17725/rensit.2021.13.501

Joint transmutation of stable Cs and Sr isotopes in microbiological systems and prospects for accelerated deactivation of liquid radioactive waste

Alla A. Kornilova, Sergey N. Gaydamaka, Marina A. Gladchenko

Lomonosov Moscow State University, <http://msu.ru/>
Moscow 119991, Russian Federation

E-mail: prfnart@mail.ru, s.gaydamaka@gmail.com, gladmarina@yandex.ru

Vladimir I. Vysotskii

Shevchenko Kiev National University, <http://www.univ.kiev.ua/>
Kiev 01033, Ukraine
E-mail: vivysotskii@gmail.com

Received December 04, 2021, peer-reviewed December 10, 2021, accepted December 14, 2021

Abstract: It was found during the research that in the experimental and control bioreactors, which at the beginning of the experiments contained only cesium and strontium, by the end of the experiments, yttrium and barium were found. These isotopes are formed as a result of low-energy nuclear reactions involving protons. In addition, in experimental bioreactors with an optimal composition, a two to threefold increase in the concentration of yttrium was recorded in comparison with the control non-optimal experiments. Accumulation of strontium and cesium in biomass was registered, which is explained by the process of biosorption. It is known that biosorption is the first step towards nuclear transformation (biotransmutation). At the same time, one of the main conditions for the nuclear transformation of biomass elements is its maximum efficient growth. An unexpected fact discovered during the experiment is that yttrium and barium were also found in the control bioreactor, where no biomass was added before the experiment, but only deionized water, glucose, and the initial stable cesium and strontium salts. It is important to note that these elements were not detected in the analysis of the initial salts, substrates, and deionized water. Most likely, the presence of yttrium and barium is due to inoculation of the control fluid of the bioreactor (where no biomass pellets were added) with microorganisms from the experimental bioreactors during their periodic opening for taking current pH samples and adding glucose. Also, the work recorded a decrease in the content of cesium and strontium in the liquid by 20% and 55%, respectively, which goes beyond the statistical error.

Keywords: bioreactor, biosorption, low energy isotope transmutation, coherent correlated states, seeding with microorganisms

PACS: 25.60.PJ; 25.70.-Z; 28.41.KW; 28.52.-S; 28.60.+S; 82.90.+J; 87.17.-D; 87.17.EE; 87.80.-Y; 89.60.-K

For citation: Alla A. Kornilova, Vladimir I. Vysotskii, Sergey N. Gaydamaka, Marina A. Gladchenko. Joint transmutation of stable Cs and Sr isotopes in microbiological systems and prospects for accelerated deactivation of liquid radioactive waste. *RENSIT: Radioelectronics. Nanosystems. Information technologies*, 2021, 13(4):501-508. DOI: 10.17725/rensit.2021.13.501.

CONTENTS

1. INTRODUCTION (502)

2. SIMULTANEOUS TRANSMUTATION OF STABLE Cs AND Sr ISOTOPES AT LOW ENERGY IN THE PRESENCE OF MICROBIOLOGICAL SUBSTANCES (504)

3. CONCLUSION (506)

REFERENCES (507)

1. INTRODUCTION

It is well known that one of the most actual problems of modern energy and ecology is the deactivation of radioactive waste (RW) generated in large quantities during the normal operation of nuclear reactors. The formation of liquid radioactive waste (LRW) is associated, in particular, with the technology of keeping fuel elements (fuel elements) after their removal from the reactor core for several years for the decay of the shortest-lived radioactive isotopes. An even greater scale of LRW formation is associated with accidents at nuclear power plants. A typical example is the accident at the Fukushima-2 nuclear power plant, on the territory of which, over 10 years after the destruction of the reactor, more than 600000 tons of radioactive water has been accumulated, formed during the continuous cooling of the damaged reactor.

It is also well known that the most dangerous for humans of all long-lived isotopes contained in such wastes are gamma-active cesium Cs¹³⁷ and beta-active strontium Sr⁹⁰, the half-life of which is about 30 years, and the required exposure time to achieve an acceptable conditionally safe radiation level is hundreds of years old.

Coordinated by the IAEA (International Atomic Energy Agency), a technique for the disposal of high-level waste due to their intense irradiation with neutrons with the possibility of converting long-lived radioactive isotopes into rapidly decaying shorter-lived isotopes requires the creation of a large number of very expensive high-current accelerators for high-energy

protons with their subsequent conversion into neutrons.

Simple estimates show that in order to implementation of such solution and utilize of 300-500 thousands of tons of high-level radioactive reactor waste, it is necessary to create in such systems a very large number (thousands of tons (!)) of very fast neutrons, which is very expensive and difficult. This problem was actively discussed 15-20 years ago, and it was shown that only for preliminary work until 2050 for the implementation of such mega-projects in all countries where nuclear power systems are developed, total costs exceeding \$ 200-300 billion are required [1-4]. Now this idea is practically forgotten.

At present, the only real method of RW disposal is a "deferred solution" – primary processing and long-term storage of RW in special storage facilities in order to reduce the specific activity of RW due to the radioactive decay of isotopes contained in RW with subsequent final disposal of RW into deep geological formations (to a depth of about 500 m and more). Such controlled storage requires very large ongoing costs for their maintenance and safety, and is potentially environmentally hazardous due to possible accidents that have repeatedly occurred in the most developed countries of the world when the conditions for servicing the storage facilities are violated. The largest accident occurred at the Mayak chemical plant in 1957 with the release of a large amount of radioactive waste and the formation of the "Kyshtym radioactive trace". It should also be noted that deep geological disposal of radioactive waste is acceptable only for countries with large territories, since the choice of the location for creating a radioactive waste repository must be justified by long-term safety forecasts and certain specific requirements are imposed on the characteristics of geological massifs suitable for disposal of radioactive waste.

Over the past 25 years, we have been investigating a fundamentally different, environmentally friendly and controllable method for the conversion of isotopes at low energy, including the mechanism of disposal of long-lived radioactive waste by converting (transmutation) of radioactive isotopes into stable isotopes of other elements in the process of nuclear transmutation, stimulated by internal topological structural processes in nano-scale (at the level of biomolecules) in growing microbiological systems. It was shown (e.g. in [5,6]) that for atomic and nuclear particles located in nonstationary nanosized potential wells, in the process of deformation of these wells (their rapid expansion or contraction), such quantum-mechanical coherent correlated states (CCS) can arise, which are accompanied by very sharp increase in the probability of one of the interacting nuclei passing through the Coulomb barrier of another nucleus. The presence of this barrier is the main obstacle to nuclear processes at low (thermal) energy of the environment. Such dynamic systems with a rapidly changing internal structure can be created artificially, but it is much more efficient to use fast-growing radiation-resistant microbiological cultures, in which similar processes occur naturally due to, for example, cell division, DNA replication, and ion transport processes at the entrance of heterogeneous channels in membranes. cells, etc.

The physical (quantum mechanical) illustration of such processes is the Schrödinger-Robertson uncertainty relation for different pairs of dynamic variables A and B

$$\sigma_A \sigma_B \geq |<[\hat{A}\hat{B}]>|^2 / 4(1-r^2), \quad (1)$$

which was obtained in 1930 and differs from the "standard" Heisenberg-Robertson uncertainty relation

$$\sigma_A \sigma_B \geq |<[\hat{A}\hat{B}]>|^2 / 4 \quad (2)$$

by the presence of the correlation coefficient $|r| \leq 1$. This coefficient characterizes the

dynamic relationship of these variables A and B and is determined by the relation

$$r = \sigma_{AB} / \sqrt{\sigma_A \sigma_B}, \\ \sigma_{AB} = (<\hat{A}\hat{B} + \hat{B}\hat{A}>) / 2 - <A>, \\ \sigma_C = <(\hat{C} - <C>)^2>, \quad C = A, B. \quad (3)$$

In a particular case

$A = x, B = p, <x - <x>> = 0, <p - <p>> = 0$ (4) this relation is reduced to a modified form of the well-known Heisenberg uncertainty relation with an overdetermined (multiplied by $G = 1/\sqrt{1-r^2}$ times) Planck constant [7]

$$\sigma_p \sigma_x \geq \hbar^2 / 4(1-r^2) \equiv (\hbar^*)^2 / 4, \\ \delta p \delta x \geq \hbar / 2\sqrt{1-r^2} \equiv \hbar^* / 2, \\ \hbar^* = G\hbar, \quad \delta C \equiv \sqrt{\sigma_C}. \quad (5)$$

From these relations, in particular, it follows that when a particle with mass m is within a nonstationary nanowell with a size $\delta x = \sqrt{\sigma_x}$, the fluctuation ΔE of its kinetic energy exceeds the minimum value

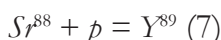
$$\Delta E \approx \sigma_p / 2m \geq \Delta E_{min} = \hbar^2 G^2 / 8m\sigma_x. \quad (6)$$

In particular, if a proton is within this deformable potential well with a size of $\delta x \approx 1$ nm, then in the initial uncorrelated state, for which $r = 0$ and $G = 1$, the amplitude of kinetic energy fluctuations is very small and amounts to 10^{-4} eV, which is much less than the thermal energy at room temperature (~ 0.025 eV). On the other hand, for a really attainable value $G \approx 10^4$ [7], this amplitude exceeds 10 keV, which is sufficient for nuclear fusion and isotope conversion in the presence of microbiological cultures.

The early [5,8-11], as well as subsequent optimized experiments [12], confirmed the reality and high efficiency of such isotope transmutation in the presence of growing microbiological cultures. These experiments were carried out with the participation of light ($Mn^{55} + d = Fe^{57}$), medium-mass ($Na^{23} + P^{31} = Fe^{54}$) and heavy ($Cs^{133} + p = Ba^{134}$) stable isotopes.

2. SIMULTANEOUS TRANSMUTATION OF STABLE Cs AND Sr ISOTOPES AT LOW ENERGY IN THE PRESENCE OF MICROBIOLOGICAL SUBSTANCES

Below are presented the results of the first biostimulated experiments on the implementation of the nuclear transmutation reaction of stable strontium, which is the stable analogue of another extremely dangerous long-lived reactor radioactive Sr⁹⁰ isotope. Taking into account the fact that the main component (82.6%) of stable strontium is the Sr⁸⁸ isotope, and also taking into account that the reactions stimulated by the giant energy fluctuations considered above are most likely to occur when the daughter product of such reactions is a stable isotope [7], it should be expected that the most probable is the transmutation reaction



with the formation of a stable isotope Y⁸⁹.

The fundamental difference and an important feature of the processes under study is that these experiments were first carried out under controlled conditions with the simultaneous presence of stable isotopes of both elements – strontium and cesium. This circumstance is an important prerequisite for the implementation of the disposal process using biotechnology for the joint deactivation of both and the most dangerous radioactive isotopes that are always present in reactor RW.

The experiments were carried out in the following way.

To carry out the experiments, salts containing stable isotopes of cesium and strontium at a concentration of 100 mg/liter were dissolved in deionized water. In identical experimental (basic) bioreactors "1", "2" and "3" (as well as in the control bioreactor "0"), 75 ml of the prepared solution was introduced.

After that, dry granules containing 0.4 gram of dried syntrophic anaerobic microbiological association were added to bioreactors "1-3". The salts Na₂CO₃ and Na₂HPO₄ were added

as necessary trace elements. In bioreactor "0" were introduced similar components, with the exception of the dried microbiological granules.

After that, all bioreactors were placed in a laboratory thermostat, where they were kept for 33 days at a temperature of 55°, which is optimal for these microbiological associations.

On the outer surface of the transparent bioreactors, liquid levels were recorded, and when it decreased, the volume was replenished by adding similar deionized water to the appropriate level during manipulations with the bioreactors throughout the experiment. Every 4 days the bioreactors stayed in a thermostatically controlled chamber, water was added to the initial level, the pH of the liquid in each bioreactor was measured, and 0.05-0.15 ml of glucose was added. The experiment with periodic repetition of such procedures lasted 33 days.

In the course of the experiment, the analysis of similar samples of glucose, salts of the nutrient medium, supernatants and biomasses was also carried out by the method of X-ray fluorescence analysis (XRF) in order to determine the concentration of all chemical elements. The results of such an analysis of the liquid phase taken after centrifugation of the liquid from the bioreactors and separation of the sediment present in the samples are shown in **Table 1**.

It follows from these results that in all bioreactors, including the bioreactor "0", into which no syntrophic association granules were introduced, a large amount of Ba and Y ions was found. It is important to note that the content of Cs and Sr in the liquid phase in the volume bioreactors "1-3" with the optimal composition

Table 1
Results of chemical analysis of the liquid phase after the end of the experiment and after separation of the sediment from the liquid

| Sample name | Concentration, mg/liter | | | |
|---|-------------------------|------|------|------|
| | Cs | Sr | Ba | Y |
| Bioreactor "0" | 107.5 | 93.1 | 0.42 | 0.16 |
| Average values for bioreactors "1", "2" и "3" | 89.2 | 45.2 | 0.23 | 0.23 |

are significantly less than in bioreactor "0", which formally lacked microcultures. This logical conclusion is in good agreement with the initial assumption about the possibility of accelerated biotransmutation reactions in bioreactors "1-3". On the other hand, the presence of Ba and Y ions in the control bioreactor "0", which does not contain syntrophic association granules, requires appropriate explanations.

This interesting circumstance is most likely associated with the uncontrolled ingress of very small amounts of microorganism spores from the working tanks of bioreactors "1"- "3" into a nearby container with bioreactor "0" during short-term but repeated depressurization of these bioreactors during biogas extraction, produced by anaerobic microorganisms. A very small number of such microorganisms that got from the air into the bioreactor "0" could rapidly increase, taking into account the optimal conditions of a long-term experiment, to the amount that would ensure the implementation of the process of sufficiently effective isotope transmutation. This mechanism of self-population of bioreactor "0" is quite reasonable, given the circumstances that under optimal conditions, with all vital components, the absence of competitors and the presence of a comfortable temperature for these microorganisms, 8-10 cycles of extended reproduction of these microorganisms occur during the entire experiment.

For the most complete understanding and explanation of the obtained effects, the X-ray fluorescence analysis of the sediments

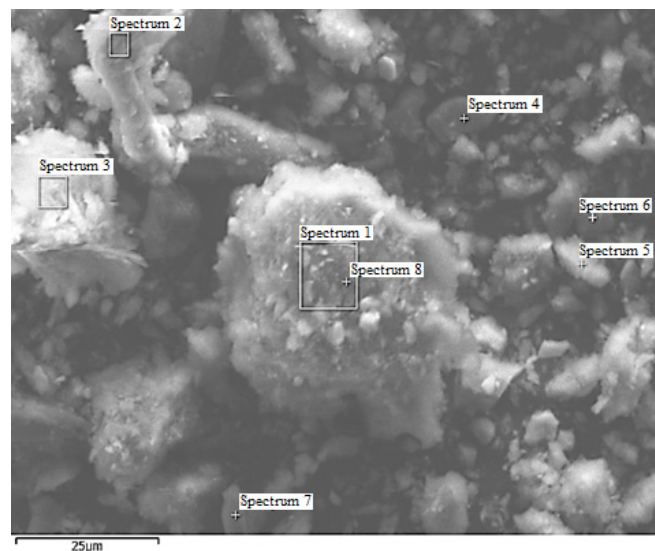


Fig. 1. Electronic image and sampling points in the sediment of bioreactor "1".

in the bioreactors after the completion of the experiments was carried out. The results of the analysis of the sediment previously washed from the mother liquor and dried at a temperature of 100°C in bioreactor "1" are shown in **Fig. 1** and **Fig. 2**, as well as in **Table 2**.

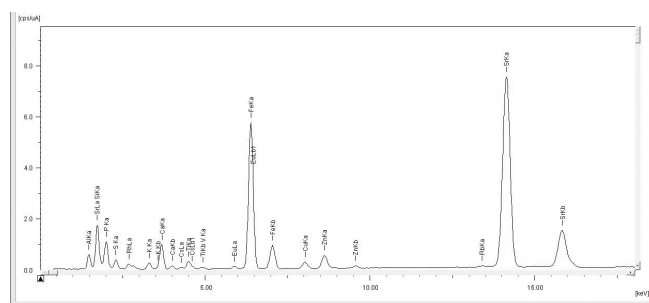


Fig. 2. Roentgenogram of sediment in bioreactor "1".

It follows from these data that almost all studied points of the sediment sample contain Cs and Sr salts, which got there as a result of

Table 2

Elemental (mass %) chemical composition of the sediment in bioreactor "1".

| Spectrum label | Na | Mg | Al | Si | P | S | K | Ca | Ti | Fe | Sr | Y | Cs | Ba | Total |
|----------------|------|------|-------|-------|-------|-------|-------|------|------|------|------|------|------|------|--------|
| Spectrum 1 | 0.95 | 0.91 | 19.04 | 31.06 | 21.81 | 4.64 | 3.34 | 5.08 | 1.26 | 6.48 | 3.70 | 0.56 | 0.83 | 0.34 | 100.00 |
| Spectrum 2 | 1.76 | 0.98 | 17.23 | 31.11 | 19.11 | 5.47 | 3.39 | 6.89 | 1.13 | 7.50 | 3.49 | 0.73 | 1.23 | 0.00 | 100.00 |
| Spectrum 3 | 1.61 | 0.82 | 19.68 | 23.91 | 20.97 | 11.04 | 1.89 | 6.36 | 1.61 | 6.82 | 2.70 | 1.01 | 1.09 | 0.49 | 100.00 |
| Spectrum 4 | 0.33 | 1.06 | 25.11 | 40.05 | 1.44 | 0.29 | 20.62 | 0.48 | 2.01 | 7.00 | 1.09 | 0.26 | 0.16 | 0.11 | 100.00 |
| Spectrum 5 | 1.11 | 1.20 | 21.03 | 35.52 | 20.14 | 3.18 | 2.07 | 3.30 | 1.43 | 4.64 | 3.60 | 1.57 | 1.08 | 0.12 | 100.00 |
| Spectrum 6 | 0.27 | 0.15 | 2.37 | 86.55 | 4.07 | 0.50 | 0.56 | 0.76 | 0.04 | 1.54 | 1.16 | 1.96 | 0.06 | 0.00 | 100.00 |
| Spectrum 7 | 0.26 | 0.21 | 1.77 | 83.24 | 7.02 | 1.00 | 0.00 | 1.36 | 0.44 | 2.69 | 1.61 | 0/41 | 0.00 | 0.00 | 100.00 |
| Spectrum 8 | 0.54 | 0.89 | 16.07 | 33.26 | 19.33 | 6.95 | 2.85 | 5.87 | 1.24 | 6.92 | 4.55 | 0.12 | 0.96 | 0.45 | 100.00 |

sorption into the volume of microcultures. The formal absence of Ba in spectra 2, 6, 7 is most likely associated with its very low concentration due to the selectivity of its sorption or because of the low concentration of Cs at these points.

Similar results were obtained when studying sediments in bioreactors "2" and "3".

For the purpose of "evaluating the purity" of the experiment (the absence of compounds Cs, Sr, Y, and Ba in the reagents), the same RFA of the reagents used in the experiments was carried out. The data of these measurements confirmed the complete absence (with the accuracy guaranteed by the XRF-based measurement technology) of these chemical elements (Fig. 3-5, Table 3, 4).

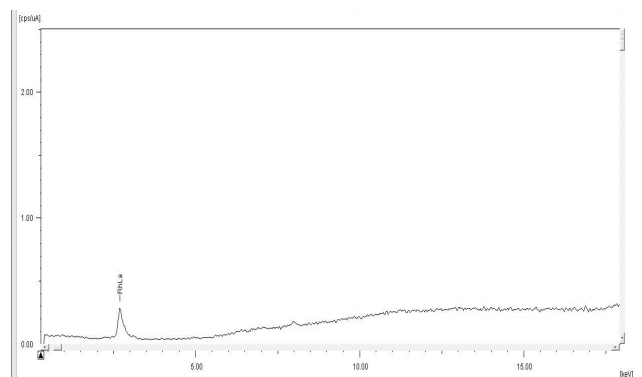


Fig. 3. Roentgenogram of glucose.

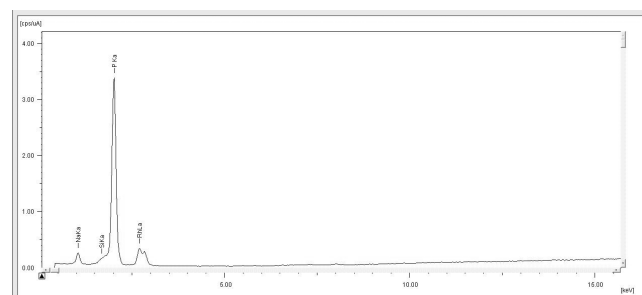


Fig. 4. Roentgenogram of Na_2HPO_4 salt.

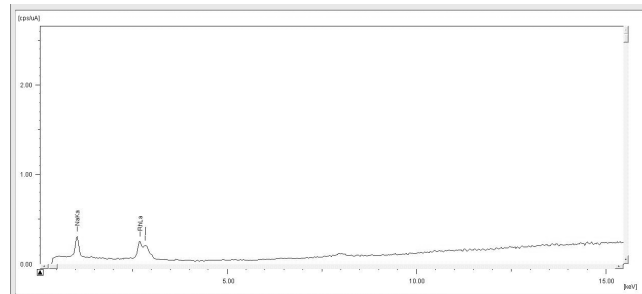


Fig. 5. Roentgenogram of Na_2CO_3 .

Table 3
Results of the elemental chemical composition
 Na_2HPO_4 , mass. %

| | | | | | | | |
|---|-------|----|---------|---------|-----------|------|---------|
| 1 | Elem. | P | 66.302% | (0.087) | Quant.-FP | PKa | 11.2593 |
| 1 | Elem. | Na | 29.599% | (0.176) | Quant.-FP | NaKa | 0.5928 |
| 1 | Elem. | Si | 4.099% | (0.031) | Quant.-FP | SiKa | 0.6122 |

Table 4
Results of the elemental chemical composition
 Na_2CO_3 , mass. %

| | | | | | | | |
|---|-------|----|---------|---------|-----------|------|--------|
| 1 | Elem. | Na | 97.887% | (0.398) | Quant.-FP | NaKa | 0.7087 |
| 1 | Elem. | Ca | 0.864% | (0.045) | Quant.-FP | CaKa | 0.0208 |
| 1 | Elem. | Al | 0.461% | (0.025) | Quant.-FP | AlKa | 0.0100 |
| 1 | Elem. | Mg | 0.278 | (0.063) | Quant.-FP | MgKa | 0.0038 |
| 1 | Elem. | S | 0.266 | (0.010) | Quant.-FP | SKa | 0.0294 |
| 1 | Elem. | Si | 0.245 | (0.011) | Quant.-FP | SiKa | 0.0127 |

3. CONCLUSION

The results of the analysis of the concentration and composition (redistribution) of chemical elements involved in the natural metabolism of microbiological cultures in different solutions allow us to draw the following conclusions.

1. In the mother liquors and in the sediments present in the bioreactors, Ba and Y ions were found, which are completely absent in the initial components. The only mechanism for the formation of these elements is the nuclear fusion reactions.
2. It was shown that in mother liquors there is a significant (at least 20%) decrease in Cs concentration when comparing the results of the study of liquid samples from the optimal bioreactors "1"- "3" and the sample from the control bioreactor "0". This decrease, if we compare these results with the results of our previous experiments [9-11], is directly related to the nuclear transmutation (nuclear fusion reaction $\text{Cs}^{133} + p = \text{Ba}^{134}$) of the Cs^{133} isotope to the Ba^{134} isotope.
3. A very significant (at least 50%) decrease in the concentration of Sr in the optimal bioreactors "1-3" in comparison with the non-optimal system of the bioreactor "0" was found, which can be associated with both its transmutation in Y and sorption

- into sediments containing the bulk of biocultures.
4. In connection with the detected presence of Sr, Ba and Y ions in the sediments, in order to compose the material balance, it is necessary to develop a method for dissolving the sediments in bioreactors.
 5. For a more conclusive confirmation of all the processes under consideration, it is necessary to additionally conduct mass spectrometric measurements of all products of nuclear transformations.
 6. We believe that the simultaneous transmutation of stable Cs and Sr isotopes in the same volume in the presence of microbiological associations makes it possible to predict with a high probability the possibility and high probability of similar processes of transmutation of Cs^{137} and Sr^{90} radioactive isotopes and to effectively deactivate LRW.
 7. The proposed and logically substantiated hypothesis about the possibility of cross-contamination by optimal microbiological associations of initially biologically neutral containers with a radioactive liquid, followed by the optimal transmutation of radioactive isotopes, makes it possible to predict a similar technology for deactivating large volumes of LRW waste without excessive biological load on an industrial scale.
- The authors express their sincere gratitude to the employees of VNIINM JSC V.A. Kashcheev and E.D. Musatov, as well as an employee of TVEL JSC A.I. Ermakov for useful discussion and objective control during these experiments.*

REFERENCES

1. Minato K, Ikegami T, Inoue T. Recent research and development activities on partitioning and transmutation of radioactive nuclides in Japan. *Actinide and Fission Product Partitioning and Transmutation. Eight Information Exchange Meeting*. USA, Las-Vegas, November 2004, p.29-47.
2. Ponomarev LI. Overview of Russia P&T Programme. *Actinide and Fission Product Partitioning and Transmutation. Eight Information Exchange Meeting*. USA, Las-Vegas, November 2004, p. 79-90.
3. Stanculescu A. IAEA Activities in the area of partitioning and transmutation. *Actinide and Fission Product Partitioning and Transmutation. Eight Information Exchange Meeting*. USA, Las-Vegas, November 2004, p.101-108.
4. Savage B. Overview of United States P&T Programme. *Actinide and Fission Product Partitioning and Transmutation. Eight Information Exchange Meeting*. USA, Las-Vegas, November 2004, p. 49-56.
5. Vysotskii VI, Kornilova AA. Transmutation of stable isotopes and deactivation of radioactive waste in growing biological systems. *Annals of Nuclear energy*, 2013, 62:626-633.
6. Vysotskii VI, Kornilova AA. Microbial Transmutation of Cs^{137} and LENR in growing biological systems. *Current Science*, 2015, 108(4):142-146.
7. Vysotskii VI, Vysotsky MV. Features of correlated states and a mechanism of self-similar selection of nuclear reaction channels involving low-energy charged particles. *J. of Experim. and Theor. Phys.*, 2019, 128:856-864.
8. Vysotskii VI, Kornilova AA. *Nuclear fusion and transmutation of isotopes in biological systems*. Moscow, MIR Publ., 2003, 302 p. (in English).
9. Kornilova AA, Vysotskii VI, Gaydamaka SN, Gladchenko MA. Nuclear Reactions in Living Nature: The Possibility of Biological Processing and Deactivation of Liquid Radioactive Waste. *Physical and Mathematical Modeling of Earth and Environment Processes (Springer Proceedings in Earth and Environmental Sciences)*. Springer, Book series (SPEES), 25 March 2019, pp 213-230.
10. Vysotskii VI, Kornilova AA, Gaydamaka SN, Novakova AA, Novikov DS, Vysotskyy VV, Avdonin VV. Creation of Fe isotopes in

- natural geology crusts as the result of self-controlled global biostimulated LENR in oceans and seas. *Journal Condensed Matter Nucl. Science*, 2020, 33:323-332.
11. Vysotskii VI, Kornilova AA. Effective LENR and transmutation of stable and radioactive isotopes in growing biological systems. *Cold Fusion. Advances in Condensed Matter Nuclear Science*, Edited by Jean-Paul Biberian, Elsevier, 2020, Chapter 12, pp. 205-232.
12. Kyu-Jin Yum et all. An Experiment in Reducing the Radioactivity of Radionuclide (Cs^{137}) with Multi-component Microorganisms of 10 Strains. *J. Condensed Matter Nucl. Sci.*, 2019, 28:1-6.

DOI: 10.17725/rensit.2021.13.509

NEW PARADIGM AND PARAMETRY

Gennady V. Mishinsky

Joint Institute for Nuclear Research, <http://www.jinr.ru/>

Dubna 141980, Moscow Region, Russian Federation

E-mail: mysb@jinr.ru

Received Oktober 17, 2021, peer-reviewed Oktober 27, 2021, accepted November 03, 2021

Abstract: Currently, the ongoing paradigm change requires both opening up the main provisions formulated by T. Kuhn and their further development. The article formulates the signs of scientific revolutions and the necessary conditions for their implementation. The history of the new paradigm is given and the periodicity in its emergence is revealed. A conclusion is made about the need to create a new research direction - Parametry. Areas of research are indicated, which scientific results will lead to new scientific revolutions in the foreseeable future.

Keywords: paradigm, scientific revolution, low-energy nuclear reactions, history of science, philosophy of science, metrology

PACS: 01.65.+g; 01.70.+w; 06.20.-f

For citation: Gennady V. Mishinsky. New Paradigm and Parametry. *RENSIT: Radioelectronics. Nanosystems. Information technologies*, 2021, 13(4):509-520. DOI: 10.17725/rensit.2021.13.509.

CONTENTS

1. INTRODUCTION (509)
2. PARADIGM DEFINITION (509)
3. SIGNS OF SCIENTIFIC REVOLUTIONS (510)
4. NEW PARADIGM (511)
5. HISTORY OF EMERGENCE OF NEW PARADIGM (513)
6. PARADIGM SHIFT AND PARAMETRY (515)
7. CONCLUSION (518)
- REFERENCES (518)

1. INTRODUCTION

The science itself that classifies objective knowledge about the world around and formulates the laws of nature obeys objective laws in its development. One of these laws opened and formulated by T.S. Kuhn in his book: "The structure of scientific revolutions" in 1962 is the law of paradigm shift [1]. The last paradigm shift or scientific revolution began with the discovery in 1896 by A. Becquerel of such an "anomalous" phenomenon as the natural radioactivity of uranium salts. Currently, a new paradigm change is taking place associated with the discovery, in 1989-1992, of "impossible", radiationless and low-energy nuclear reactions [2].

The scientific revolution that takes place now is the only one so far after the discovery of the law of paradigm shift. This circumstance led to reflections and some conclusions about the objective properties of the law of the shift of paradigms, about the development history of the last of them and about the need to create new scientific directions, including the parametry of physical objects.

2. PARADIGM DEFINITION

Each new paradigm is generated by a new idea of the structure of Nature.

Each new paradigm describes the World around a human being more and more objectively.

The paradigm is an interconnected, leading system of views, notions and concepts, including postulates, theories and research methods, in accordance with which subsequent scientific constructions and generalizations are carried out, new scientific, technical and industrial technologies arise, thanks to which the civilizational evolution of mankind is carried out. T.Kuhn wrote: "By paradigms, I mean universally recognized scientific achievements that, over a certain time, provide the scientific community

with a model for posing and solving problems." A specific paradigm, adopted as a model for reasonable scientific activity, dominates the scientific community for a certain, limited time, until it is replaced by a new paradigm.

The above definition of the paradigm refers exclusively to the scientific activity of mankind and formulates the most general concept in Science. However, at present, the general concept – the paradigm of Science – has been fragmented and is applied to specific scientific disciplines, for example: a paradigm shift in physics, biology, geology, etc. Moreover, the concept of a paradigm begins to spread to other areas of human activity: engineering and technological paradigms, paradigms in art, social and political paradigms, civilizational paradigms. And if one should reconcile with the "fragmentation and dissemination" of the general concept of a paradigm with the indispensable formulation of definitions in many of its specific manifestations, then the use of the word paradigm, which simply characterizes a change in conditions in any randomly chosen human activity, is unacceptable.

It should be remembered that a paradigm shift in a particular area of human activity means a revolution in this area. Moreover, the results of a revolution in this area will inevitably lead to revolutionary changes in other spheres of human activity. In this article, the concept of paradigm is used in its initial meaning.

A paradigm shift is a rare event. The influence of each of the known paradigms lasted for several generations of scientists who, in their scientific activities, were not aware of their involvement in this paradigm, which is natural.

The today's generation of scientists is in luck! We now know about the law of paradigm shift, and due to scientific specialization, some of us can just observe the process of paradigm change at its initial stage, while others can and should take an active part in the scientific revolution that has come, with an inevitable confrontation, at the beginning, between supporters of old and new

paradigms. The outcome of this confrontation is historically predetermined.

3. SIGNS OF SCIENTIFIC REVOLUTIONS

The scientific revolution, which consists in a change of paradigm, is characterized by three qualitative features [3], and it occurs when:

Firstly, scientists discover anomalous phenomena that cannot be explained using the current paradigm. This is the main feature of an emerging scientific revolution [1];

secondly, a discovery of new particles, new objects, new structures, up to the discovery of new states of matter takes place; and, thirdly, the creation of new theories, the discovery of new laws of interaction between old and new objects, up to the discovery of new types of fundamental interactions takes place.

However, even in the presence of the above signs, the scientific revolution may not take place immediately. A public demand associated with the development of productive forces of society is required for its implementation.

The beginning of the scientific revolution of 1896 coincided with the second industrial, technological revolution of 1870-1960 that was taking place at the same time. The technological revolution was based on advanced scientific discoveries in physics and chemistry and on the desire to introduce scientific achievements into production. The rapidly developing, due to these discoveries social productive forces, in turn, would enthusiastically accept and support any new scientific achievements. Therefore, the 20th century went down in history as the century of scientific and technological progress.

The discovery of natural radioactivity was followed by other, numerous discoveries in physics, the most fundamental of which were: the discovery of new particles: electron, proton, neutron, neutrino and their antiparticles; discovery of new structures: atomic nuclei, atoms, molecules, including organic ones and

biomolecules; the discovery of new states of matter: charge plasma and quark-gluon plasma; creation of quantum mechanics, special and general theory of relativity; discovery of new types of fundamental interactions: strong and weak interactions.

The development of any paradigm is realized in two directions. Within the framework of the first direction, firstly, initial theories are built that explain the anomalous phenomena that gave rise to a new paradigm and, secondly, emerging advanced hypotheses create, both new theories that explain old facts and replace previous theories, and a new toolkit, which allows the creation of new technologies. "The new paradigm means a change in the rules that scientists were guided up to this time in the practice of normal science, which these scientists have already successfully completed. That is why the new paradigm, no matter how special the area of its application, is never just an increment to what was already known. The adoption of a new paradigm requires a restructuring of the previous paradigm and a reassessment of previous facts, an internal revolutionary process that is rarely within the power of one scientist and never takes place within one day [1]".

The second direction is "hidden" theories and technologies, which appear as extensive research is carried out within the framework of the new paradigm. The history of the development of science demonstrates that "hidden" theories, methods and technologies are superior to the initial theories and technologies in their significance for human evolution.

It is obvious from the above that the change of paradigms gives rise to new scientific and technical directions and disciplines in all fields of human activity.

The scientific revolution provides unique opportunities for all generations of scientists, both in restructuring old theories and in the development of "hidden" theories and advanced technologies. It is obvious that the restructuring of old theories and reassessment of old facts

can be carried out faster by scientists who have developed old theories up to the present time and possess a huge amount of empirical data, but who, at the same time, recognize the need for an "internal revolutionary process". It is not enough to declare the beginning of a new scientific revolution, the practical implementation of that revolution is necessary.

4. NEW PARADIGM

Currently, a paradigm shift is taking place; a new scientific revolution has begun, associated,

- firstly, with the discovery of multinuclear, radiation-free and low-energy nuclear reactions: reactions of cold nuclear fusion and reactions of low-energy transmutation of chemical elements [4-7]. Low-energy transmutation reactions are reactions of transformation of some chemical elements into other chemical elements in weakly excited condensed matter;
- secondly, with the discovery of a new state of atomic and nuclear matter: spin nuclide electron condensate [8-9]; and,
- thirdly, with the discovery of a new, fundamental resonant interference exchange interaction (RIEX interaction) [10-11].

It is necessary to understand for the transition to a new paradigm that nuclear reactions occur at low energies in condensed matter, in strong magnetic fields (in the reaction volume $< 10 \text{ eV/atom}$), and they occur everywhere in the Universe [2].

Low-energy nuclear reactions (LENR) were discovered and subsequently reproduced by electrolysis in heavy water; in a glow gas discharge; at electronic melting of zirconium ingots; in explosions of metal targets irradiated by a powerful pulse of electrons; in explosions in liquid dielectric media of metal foils, through which a powerful pulse of electric current was passed; when exposed to a pulsed current on a lead-copper melt; at the passage of electric current in water-mineral media; in ultrasonic treatment of aqueous saline solutions; when

irradiated with braking gamma quanta of condensed gases; in growing biological structures, and in many others [4-7]. It becomes obvious from the above list that the methods of experiments carried out on LENR are extremely diverse and fundamentally different from the methods of nuclear physics. Despite the variety of techniques, the results of LENR experiments are qualitatively similar to each other.

Analysis of experiments on the transmutation of chemical elements and their results showed that they occur in strong, more than 30 T, magnetic fields. It turned out that atomic and nuclear matter in strong and ultrastrong magnetic fields are transformed into a new state of matter: into a spin nuclide electron condensate. A characteristic feature of such a condensate is that pairwise electrons and pairwise protons and neutrons (fermions with spin equal to $S = 1/2\hbar$) are in a bound state, in a state of orthobosons in it, when the total spin of each pair is equal to one, $S = 1\hbar$.

Magnetic fields begin to emerge in ionized, liquid media as a result of the passage of unidirectional flows of electrons with a density of more than 10^{21} cm^{-3} through them [12]. Those magnetic fields owe their origin to the magnetic moments of the electrons μ_e , which are parallel to each other in a unidirectional flow. Since the electron spins in this case are also parallel, then, in addition to the magnetic field, the electrons generate an exchange self-consistent field with a negative potential. Electrons with parallel spins in a negative potential, in order to comply with the Pauli principle, are forced to pair into orthobosons with a spin $S = 1\hbar$. This pairing is carried out because electrons in a magnetic field obtain new, oscillatory quantum numbers [13]. An orthobosonic pair of electrons is a toroidal, ring current of radius R_z , which rotates around a counter flow of positive ions that move at a speed V_i (Fig. 1a). The orthoboson has external and internal strong, more than 30 T, magnetic fields B , and a strong electric field. External magnetic fields connect orthobosons into electronic

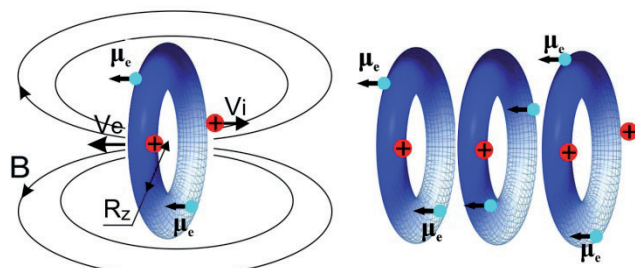


Fig. 1. a – orthoboson, b – “capsule”.

orthoboson “solenoids” - “capsules” (Fig. 1b). “Capsules” can have a different number of orthobosons. They can fly out of the condensed medium. Then the “capsules” are registered as “unknown” particles.

The atoms are transformed into transatoms in internal strong magnetic fields of the “capsules”. Electrons in a transatom are also coupled in pairs to form orthobosons. Atomic electron orthobosons merge into a Bose-Einstein condensate, in which all electron spins and their magnetic moments are parallel to each other (Fig. 2). The magnetic moments of electrons generate ultrastrong magnetic fields inside and around transatoms up to $B_s \sim 10^5\text{--}10^{10} \text{ T}$ [8,14]. The internal ultrastrong magnetic field interacts with the magnetic spin and magnetic orbital moments of nucleons in the nucleus, changes the structure of the nucleus and turns it into a Transnucleus. Nucleons in the transnucleus also form orthobosons with $S = 1\hbar$, but these are already nuclear orthobosons. The transnucleus with the surrounding electron orthoboson Bose-Einstein condensate forms a spin nuclide electron condensate.

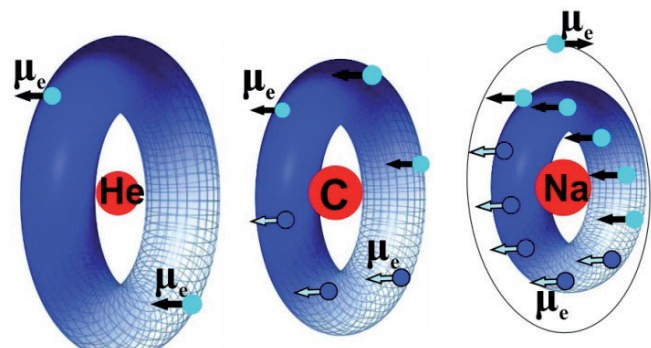


Fig. 2. Examples of transatoms: helium, carbon, sodium.

External ultrastrong magnetic fields of transatoms attract them to each other. Electronic Bose-Einstein condensates of two transatoms are combined into a common condensate. A double nuclear transmolecule is formed from their transnuclei. Other transnuclei can join it. A multinuclear transmolecule is formed, in which multinuclear reactions take place, including those with electron orthobosons. Thus, nuclear-electronic reactions occur, which products are non-radioactive. These reactions occur due to the resonant interference exchange interaction.

The nature of RIEX interaction is associated with the overlap and interference of the wave functions of objects that have resonant R-states. Resonant interference exchange interaction is an exchange interaction between any two or more objects, including between atomic nuclei A, B, C..., which have resonant R-states belonging to a composite system that consists of these objects [2,11]. The wave functions of the nuclei interfere with each other in the R-state. The wave functions of the resonant R-states contain all wave functions of the nuclei A, B, C... It is namely due to the wave functions of R-states that atomic nuclei are simultaneously “in each other” through exchange interactions with each other. Thus, short-range strong and local weak interactions between nuclei become “long-range” interactions. Strong-weak, electromagnetic and inertial-gravitational interactions are realized between the nuclei simultaneously. RIEX interaction is characterized by the interference of all types of interaction.

Thus, multinuclear, radiationless and low-energy nuclear reactions occur due to the RIEX interaction. RIEX interaction is a universal interaction. It includes and controls all the other fundamental interactions. The action of the resonant interference exchange interaction extends to the whole of Nature, from elementary particles to complex biological and social systems.

It is known that low-energy nuclear reactions are accompanied by unknown radiation,

which leaves strange tracks and craters on the “detectors” [15,16]. It is assumed in [12] that the unknown radiation is orthobosonic “capsules” emitted from a condensed matter. It was shown in [16] that the source of unknown particles can be hydrogen-saturated metals and an electric discharge in a hydrogen-containing medium. In addition, the same work demonstrates that the radiation that produces tracks and craters on CDs is generated when a hydrocarbon burns, when an internal combustion engine is running, when charging a smartphone, and in many other processes. In addition to tracks from LENR, background tracks from unknown sources of radiation were recorded, which, apparently, surround us everywhere [15]. We can conclude from the above and from the variety of techniques for low-energy nuclear reactions that they occur throughout the Universe.

The industrial use of low-energy nuclear reactions is associated primarily with the development of new energy sources and with the production of rare elements and their isotopes from cheap and widespread chemical elements.

5. HISTORY OF EMERGENCE OF NEW PARADIGM

Each new paradigm arises in the depths of the old paradigm, due to its scientific and technological achievements; it appears in the form of anomalous phenomena in the beginning. The latter can be perceived by the scientific community as scientific curiosities at its best that require careful research, at worst as “pathological” results of experiments performed by “illiterate” scientists.

As indicated above, the last scientific revolution began in 1896 with the discovery of the natural radioactivity of uranium salts by A. Becquerel. Two years later, E. Rutherford showed that radioactive rays consisted of alpha and beta radiation. A year later, P. Villard discovered gamma radiation. In 1900, A. Becquerel determined that beta rays were electrons, which were discovered by D.D.

Thomson in 1897 while studying the behavior of cathode rays in electric and magnetic fields. In 1903 W. Ramsay and F. Soddy investigated radium emanation by optical spectroscopy and discovered helium lines in it. E. Rutherford proved soon that alpha rays are nothing more than ionized helium. In 1911, Rutherford finally determined, as a result of experiments on alpha particles scattering on gold foil, that an atom consists of a positively charged nucleus and negative electrons surrounding it. Thus, the hypothesis of the transformation of chemical elements in the process of their radioactive decay was substantiated. That hypothesis was put forward by E. Rutherford and F. Soddy as far back as 1903. Soon, in 1913, Rutherford's nuclear model was successfully confirmed by N. Bohr, who formulated postulates about the behavior of atomic systems and created the quantum theory of hydrogen-like atoms.

It became clear that, for the approach of atomic nuclei to the distance of the action of nuclear forces, it is necessary to overcome the Coulomb barrier between these forces, which ranges from tens of keV to hundreds of MeV. This statement was confirmed in 1919 by E. Rutherford, who was the first to carry out a nuclear reaction of nitrogen nuclei with fast alpha particles (helium nuclei): $^{14}_7N + ^4_2He \rightarrow ^{17}_8O + ^1_1H$.

Thus, nuclear physics, that has manifested itself in natural radioactive decay, as low-energy nuclear physics in the input channel, has established itself as high-energy physics due to the creation of a nuclear model of the atom and collisional nuclear reactions [17].

For these reasons, the low-energy experiments by J. Wendt and K. Irion on the alpha decay of tungsten induced by an electric explosion [18] (1922), and the experiments of A. Smiths and A. Karssen on the alpha decay of lead induced by electric current [19] (1925), carried out almost thirty years after the discovery of natural radioactivity, were perceived by the scientific community as impossible, and their results as erroneous.

The experimental works in the next thirty years carried out under the leadership of I.V. Kurchatov, on the launch of thermonuclear reactions with a high-precision discharge in a gaseous medium of hydrogen, deuterium, helium and their mixture, which would lead to the appearance of neutrons and powerful X-rays (1956) [20], as well as the device of I.S. Filimonenko on the electrolysis of heavy water with a palladium cathode, in which electricity was generated due to the reactions of nuclear fusion of helium from deuterium at a temperature of ~ 1150°C (1957) [21], did not arouse wide scientific interest. Probably, such an attitude was due to the fact that the power engineering based on the fission of uranium was developing rapidly at that time, and work on controlled thermonuclear fusion began.

Another thirty years have passed. The nuclear accident at the Chernobyl nuclear power plant (1986), the protracted implementation of controlled thermonuclear fusion, catastrophic environmental pollution and global warming have formed a societal demand for renewable energy sources, alternative to oil, gas and coal. For this reason, the implementation, by M. Fleischman and S. Pons, of the reaction of cold fusion (CF) during the electrolysis of heavy water with a palladium cathode at room temperature (1989) [22] caused a violent reaction of scientists who began to check their results around the world. It was soon discovered that CF reactions are accompanied by reactions of transformation of some chemical elements into other chemical elements, for example, in experiments with a glow discharge of deuterium with a palladium cathode (1992) [23,2]. Moreover, such reactions, called low-energy transmutation reactions, have been recorded in numerous other experiments that have nothing to do with cold fusion [4-7].

Low-energy transmutation of atomic nuclei and cold fusion are united under the general name low-energy nuclear reactions (LENR) or nuclear science in a condensed matter (CMNS - Condensed Matter Nuclear Science).

The absence of a theoretical explanation for LENR, which affected the reproducibility of the experimental results, gave rise to skepticism in the scientific community regarding the possibility of this type of reactions.

It took another thirty years for the Incredible to turn into the Obvious. This transformation occurred, firstly, due to the creation of the theory of pairing of atomic electrons into orthobosons in strong magnetic fields arising in weakly excited condensed matter, and the pairing of identical atomic nuclei in ultrastrong magnetic fields created by the atomic electron Bose-Einstein condensate. And, secondly, due to the discovery of fundamental resonant interference exchange interaction, which manifests itself between objects that are connected by resonant states.

If we consider the implementation of the cold fusion reaction by M. Fleischman and S. Pons as the beginning of a new scientific revolution (1989), then the duration of the previous paradigm from the discovery of natural radioactivity (1896) to the discovery of CF, is equal to approximately 90 years.

It can be seen that the main events in the history of low-energy nuclear reactions took place at intervals of thirty years. Apparently, each time this is associated with the emergence of a new generation of scientists who were not affected by the opposition between normal science and a new, emerging paradigm, and who enthusiastically began on the implementation of the latter paradigm in the practice of their scientific activities. Time will tell whether a thirty-year period is an objective parameter in the history of the emergence of subsequent paradigms.

6. PARADIGM SHIFT AND PARAMETRY

What is the reason that nuclear physics, born as low-energy science, but forgotten for 90 years and also considered a pseudo-science, gave priority to high-energy nuclear physics in scientific research? The reason is in measurements. It turned out that to measure and to determine the parameters

of individual elementary particles under the use a wide variety of detectors, up to devices that consist of many thousands of detectors, was much easier than to perform analytical studies of substances and materials.

For registration of elementary particles, nuclei and individual atoms such detectors as, for example, gas detectors have been developed and are being developed now: Geiger counter, ionization, proportional, streamer detectors; liquid detectors: bubble chambers and scintillation detectors; solid-state detectors: scintillation and semiconductor detectors, microchannel plates and CCDs. These detectors and their combinations make it possible to identify particles: to determine their energy, charge, mass. The main trend today in the development of detecting systems is the development of detectors based on new materials, new technologies and the creation of multi-channel devices on a single basis.

It was necessary to develop analytical instrumentation, computer technologies and to improve the above-mentioned detectors in order to be able to study technical, industrial materials and geological samples, to reliably determine the presence of chemical elements in them and their quantity. The successes achieved in these areas at the end of the last century made it possible to create everywhere analytical laboratories for general use, by means of which researchers have the opportunity to obtain independent, reliable information on the mass and elemental composition of both geological samples and materials gained in various technological and experimental processes.

Thus, quantitative information obtained about the properties of certain objects with a given accuracy and reliability turned out to be a decisive factor in choosing a direction in the development of science at the beginning of the 20th century. In nuclear physics, the choice between low-energy and high-energy reactions has been made in favor of the latter.

The science that deals with measurements, measurement methods and means of ensuring their uniformity is metrology. By metrology, we mean the accuracy of measurement of measures, weights, time and other physical quantities. The role of metrology in the development of science can be understood from the statement of D.I. Mendeleev: "Science begins as soon as they begin to measure. Exact science is unthinkable without measure."

In addition, the determination of the exact numerical values of certain parameters of objects in the formulation of physical experiments allows scientists to make the right choice between various assumptions and theories about the processes with which they are experimenting. It is known that any hypothesis or theory must have predictive power, i.e. be able to anticipate new facts, the numerical values of which can be verified by experience.

We introduce a new concept – Parametry – in this article. Thus, we transfer measurement accuracy to parameters that characterize objects. Objects should be understood as a whole group of objects of the same type.

Parametry is the selection of essential, characteristic parameters of objects that sufficiently describe them and distinguish them from other objects, and the determination of their numerical values. The parametry of the main groups of objects and their relationship with scientific disciplines can be systematized in the following areas:

- the parametry of the physical vacuum (PV);
- parametry of elementary particles, atoms and atomic nuclei (PN) - atomic and nuclear physics;
- parametry of molecules and high-molecular compounds (M) - chemistry, biochemistry;
- parametry of substances and materials (SM) - solid state physics, biology, materials technology;
- parametry of planets (P) - planetology, geophysics, geology;

- parametry of stars and stellar systems (S)
- astrophysics;
- parametry of galaxies (G) - astronomy;
- parametry of the Universe (U) - astronomy.

Parametry objects are located in this list as they increase in size. Since the physics of the microworld – the physics of the physical vacuum, elementary particles and atomic nuclei, is closely related to the physics of the megaworld – the physics of the Universe, then these groups of objects should be connected. Obviously, due to the general universalism of physical laws, all other groups of objects should be connected with each other (**Fig. 3**).

The history of the development of science and the above example show the following: as regards the role of measurements in the choice between low-energy and high-energy nuclear reactions, we can conclude that successes in the parametry of objects are directly related to the emergence of new paradigms and ongoing scientific revolutions. It becomes obvious from the proposed scheme (Fig. 3) that low-energy nuclear reactions could not be discovered and understood without studies of elementary particles, atoms, molecules, without studying high-energy nuclear reactions, i.e. without

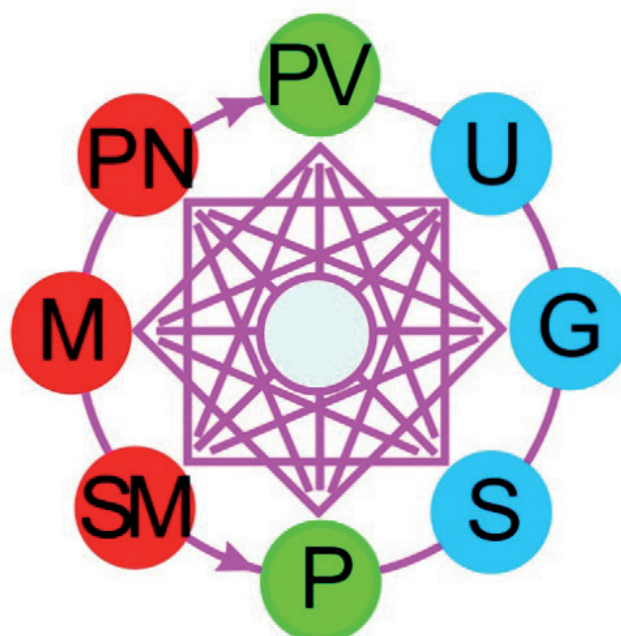


Fig. 3. "Wheel" of objects for research.

scientific and technological achievements realized within the framework of the old paradigm.

At present, the groups of objects highlighted in red (Fig. 3) are sufficiently well studied and continue to be successfully studied by modern science. This cannot be said, due to objective reasons, with respect to other groups of objects, which, despite their ancient history, are in their instrumental studies in their initial positions (green and blue). Obviously, the closest ones for intensive research are, first of all, groups by the size of objects that are adjacent to the already studied groups, namely: the parametry of the physical vacuum and the parametry of the planets, first of all, the parametry of the Earth (green). The creation and formation of the Earth's parametry based on the Earth sciences and Geology is, in addition, a vital direction, since it is associated with the preservation of Mankind as a species, because the mankind continues to irrepressibly and catastrophically pollute their planet.

Full-scale parametry of the physical vacuum and the parametry of the Earth are impossible without a practical revolution in the field of low-energy nuclear reactions. Parametry of the Earth is associated with the emerging new direction in geology – with Quantum geology [24-26]. According to quantum geology, the evolutions of geological processes and ore formation on Earth are determined, among other things by low-energy nuclear reactions: by quantum, nuclear transformations of some chemical elements into others at low energies, in other words, planetary nucleosynthesis. Obviously, quantum geology will not be limited, in its development, only to planetary nucleosynthesis.

A new state of matter that arises in a strong magnetic field – a spin nuclide electron condensate, characterized by ultrastrong, inhomogeneous and anisotropic magnetic and electric fields in which integrals of motion are not preserved, – is a “desktop” laboratory for studying the processes that occur in a physical vacuum, and, therefore, it forms its parametry.

The parametry of the physical vacuum and the parametry of the Earth should develop as intensively as possible and in parallel with the ongoing scientific revolution, caused by low-energy nuclear reactions.

If a thirty-year period in the development of paradigms is an objective parameter, then one should expect the flourishing of resonant technologies based on low-energy nuclear reactions and resonant interference exchange interactions in the fifties of this century. At the same time, the development of the physical vacuum sciences and planetary science will obviously raise the question of a new paradigm shift. Therefore, scientists involved in the study of the physical vacuum and planetology should pay close attention to the registered anomalous phenomena, begin their detailed study and carry out their publication, possibly in special journals.

Two different, “dangerous” directions should be distinguished separately in the group of substances and materials: organic and inorganic, which go still “in parallel” to each other.

- Organic direction: nucleotide-DNA, RNA, protein-cell-organ-Homo sapiens-collective, public consciousness, formed, *inter alia* through social networks - civilization.
- Inorganic direction: transistor-logical element -chip-processor-computer networks-artificial intelligence-collective, network intelligence-AI sphere, AI nationalism.

The danger of the organic direction is associated with the uncontrolled genetic modification of existing biosystems, including humans. The medium and long term consequences of genetic modification are unpredictable and, therefore, there is no guarantee that they do not lead to the death of existing humankind.

The danger of the inorganic direction is associated with the replacement of human consciousness with artificial intelligence, and as a result the loss of human intellectual and conscious properties. It is now obvious that the use of artificial intelligence is required for the study of all groups of objects and the creation

of their parametry, and it is required to put the parametry of the objects under study into the initial data for solving problems with the help of artificial intelligence. It should be noted that public consciousness is being actively formed by social and computer networks, which are now monitored and controlled by artificial intelligence, and in the future, they will possibly be controlled by AI itself!

In order to withstand the emerging threats, the humankind needs to understand: what is the sense of their existence, what is their undeniable advantage over artificial intelligence. It seems impossible to overcome the impending threats without creating the parametry of biosystems, the parametry of human and of whole mankind, and the parametry of artificial intelligence.

7. CONCLUSION

A present paradigm change requires the scientific community to be aware of the ongoing scientific revolution, to explore the main provisions formulated by T. Kuhn and to develop, as soon as possible, new theories and new technologies on the basis of a new paradigm. The peculiarity, attractiveness, but also the danger of the onset stage in the development of Humankind lies in the transition in all spheres of its activity to the widest use of Artificial Intelligence and Resonance Technologies. Both of these areas are methods to obtain maximum results at the lowest cost. The interpenetration of these directions is inevitable.

At present, the evolutionary development of wild life, the biosphere is in a state of noosphere, where the Humankind is an irresistibly growing, powerful Geological force of a planetary scale [27]. The Humankind realized, due to the development of productive forces, the transition to the state of the noosphere, but the Humankind, in its approach to solving emerging crises, in its Consciousness remains at the pre-Christian and even at the pre-Old-Testament level. This unresolved contradiction constantly gives rise to the reproduction of ongoing crises.

Therefore, the creation, by Humankind, of a number of new technologies, the consequences of which are sometimes impossible to predict, for the first time brought the Humankind to the brink of a possible self-destruction. Such a threat comes from probable military, anthropogenic, biogenic, cyber disasters. Moreover, since the emergence of new paradigms leads to the rapid development of the productive forces of society, which, according to the laws of dialectics in history, at a certain stage come into conflict with existing social relations, the beginning scientific revolutions are the forerunners of prompt economic, socio-political crises and crises in the human consciousness. These crises are countered in the form of necessary and inevitable social revolutions and mandatory, traditional or non-traditional world wars. The history of the 20th century demonstrates that these two events are interconnected and proceed at the same time. It becomes more and more obvious that if a Human does not change his own Consciousness in all its manifestations from individual to public – interstate consciousness, no, even the most advanced, technologies are able to prevent impending catastrophes, but they can only bring them closer. The complexity of the forthcoming change in Consciousness is associated with the need to simultaneously preserve the Human as a Conscious, Humanistic, Universal species.

Stagnation in the development of productive forces, as well as the invariableness of Consciousness, and even more so its degradation, lead to the destruction and death of Civilizations. The inevitability of scientific Revolutions makes the creation of a new Consciousness inevitable.

REFERENCES

1. Kuhn TS. *The Structure of scientific revolutions*. University of Chicago Press, 1962, 172 p.
2. Mishinsky GV. Towards a new paradigm. *RENSIT: Radioelectronics. Nanosystems. Information technologies*, 2020, 12(4):529-544. DOI: 10.17725/rensit.2020.12.529.

3. Mishinsky GV. Low-energy nuclear reactions are an integral part of the new scientific paradigm. *Abstracts of the First Russian Scientific Conference "Physical Vacuum – the paradigm of science of the XXI century."* Moscow, Fund for Advanced Technologies and Innovations Publ., 2020, pp. 49-53.
4. *Proceedings of the 1-26th Russian Conferences on Cold Transmutation of Nuclei of Chemical Elements*, 1993-2018.
5. *Proceedings of the 1-23th International Conferences on Condensed Matter Nuclear Science (Cold Fusion, ICCF)*.
6. Balakirev VF, Krymsky VV, Bolotov BV, Vasilieva NV, Vachaev AV, Ivanov NI, Kazbanov VI, Pavlova GA, Solin MI, Trofimov VI, Urutskoev LI. *Vzaimoprevrashcheniya khimicheskikh elementov* [Mutual transformation of chemical elements]. Ekaterinburg, Urals Branch of RAS Publ., 2003, 96 p.
7. Mishinsky GV, Kuznetsov VD, Penkov FM. Nizkoenergeticheskaya transmutatsiya atomnykh yader khimicheskikh elementov. Raspredelenie po elementam v produktakh transmutatsii. nukleosinteza [Low energy transmutation of atomic nuclei of chemical elements. Element distribution in the products of low energy transmutation. Nucleosynthesis]. *International Journal of Unconventional Science (IJUS)*, 2017, 17-18(5):61-81 (in Russ). <http://www.unconv-science.org/>.
8. Mishinsky GV. Magnitnye polya transatomov. Spinovy-nuklidnye-elektronnye kondensaty [Magnetic fields of transatoms. Spin-nuclide-electronic condensate]. *IJUS*, 2017, 15-16(5):6-25 (in Russ).
9. Mishinsky GV. Spin electron condensate. Spin nuclide electron condensate. *RENSIT*, 2018, 10(3):411-424. DOI: 10.17725/rensit.2018.10.411.
10. Mishinsky GV. Theory of cold fusion reactions. *RENSIT: Radioelectronics. Nanosystems. Information technologies*, 2019, 11(2):125-142. DOI: 10.17725/rensit.2019.11.125.
11. Mishinsky GV. Resonant interference exchange interaction. *RENSIT: Radioelectronics. Nanosystems. Information technologies*, 2019, 11(3):261-278. DOI: 10.17725/rensit.2019.11.261.
12. Mishinsky GV. Magnetic Fields and high-temperature superconductivity in excited liquids. Unknown particles. *RENSIT: Radioelectronics. Nanosystems. Information technologies*, 2021, 13(3):303-318. DOI: 10.17725/rensit.2021.13.303.
13. Mishinsky GV. Atom in a strong magnetic field. Transformation of atoms to transatoms. *RENSIT: Radioelectronics. Nanosystems. Information technologies*, 2017, 9(2):147-160. DOI: 10.17725/rensit.2017.09.147.
14. Mishinsky GV. Multinuclear reactions in condensed helium. *RENSIT: Radioelectronics. Nanosystems. Information technologies*, 2017, 9(1):94-105. DOI: 10.17725/rensit.2017.09.094.
15. Zhigalov VA. Strange radiation and LENR: What's the relation? *RENSIT: Radioelectronics. Nanosystems. Information technologies*, 2021, 13(3):329-348. DOI: 10.17725/rensit.2021.13.329.
16. Baranov DS, Zatelepin VN, Panchelyuga VA., Shishkin AL. Transfer of "dark hydrogen" by atomic matter. Methods of diagnostics of "dark hydrogen". *RENSIT: Radioelectronics. Nanosystems. Information technologies*, 2021, 13(3):319-328. DOI: 10.17725/rensit.2021.13.319.
17. Rukhadze AA, Grachev VI. LENR in Russia. *RENSIT: Radioelectronics. Nanosystems. Information technologies*, 2017, 9(1):5-7. DOI: 10.17725/rensit.2017.09.005.
18. Wendt GL, Irion CE. Experimental attempts to decompose tungsten at high temperatures. *J. of the American Chemical Society*, 1922, 44(9):1887-1894.
19. Smits A, Karssen A. Vorläufige Mitteilung über einen Zerfall des Bleiatoms.

- Naturwissenschaft*, 1925, 13:699; Ein Zerfall des Bleiatoms, Zeit Elektrochemie, 1926, 32:577-586.
20. Kurchatov IV. About possibility of creation of thermonuclear reactions in gas discharge. *UFN*, 1956, 59(4):603-618 (in Russ.).
21. Filimonenko IS. Demonstratsionnaya termoemissionnaya ustavka dlya yadernogo sinteza [Demonstrational therm-emission device for nuclear fusion]. *Materials 3 Sci. Symp. "Perestroyka estestvoznaniya [Restructuring of Natural history]"-92*, pp. 17-19. Volgodonsk, Russia, Apr. 1992 (in Russ.).
22. Fleishmann M, Pons S, Hawkins M. Electrochemically induced nuclear fusion of deuterium. *J. Electroanal. Chem.*, 1989, 261:301-308.
23. Karabut AB, Kucherov YaR, Savvatimova IB. Nuclear product ratio for glow discharge in deuterium. *Phys. Letters A*, 1992, 170:265-272.
24. Mishinsky GV. Non-Coulomb nuclear reactions of transatoms. Stellar energy and nucleosynthesis. *RENSIT: Radioelectronics. Nanosystems. Information technologies*, 2018, 10(1):35-52. DOI: 10.17725/rensit.2018.10.035.
25. Krivitsky VA., Mishinsky GV., Starostin VI. Planetary nucleosynthesis and ore formation. Bose-Einstein spin condensate of atomic electrons and atomic nuclei. *Smirnov Proceedings-2019*, pp. 246-265. Moscow, LLC “MAKS Press” Publ., 2019.
26. Mishinsky GV., Krivitsky VA., Starostin VI. Quantum geology. The feasibility of nucleosynthesis not only in stars, but also on planets in the process of their evolution. *Smirnov collection-2020*, pp. 96-136. Moscow, LLC “MAKS Press” Publ., 2021.
27. Vernadsky VI. *The chemical structure of the Earth's biosphere and its environment*. Moscow, Nauka Publ., 1965, 374 p.

DOI: 10.17725/rensit.2021.13.521

HIGH-TEMPERATURE SINGLE-ELECTRON TRANSISTORS BASED ON MOLECULES AND SMALL NANOPARTICLES

Evgeny S. Soldatov

Lomonosov Moscow State University, <http://www.phys.msu.ru/>

Moscow 119991, Russian Federation

E-mail: soldatov.es@physics.msu.ru.

Received November 16, 2021, peer-reviewed November 22, 2021, accepted November 29, 2021.

Abstract: The material of the defense of the dissertation for the degree of Doctor of Physical and Mathematical Sciences – the first in Russia doctoral dissertation on molecular single-electronics is presented. The relevance of the development, creation and research of single-electron transistors with high charge energy and operating temperature for the creation of fundamentally new nanoelectronic devices applicable in wide practice and ensuring breakthrough research in various fields is noted, the necessity of using quantum dots (molecules/nanoparticles) of atomic-molecular scale for this is shown, the formulation of the research problems is formulated, the physical and technological methods of fabrication and analysis used are listed, the main results of the work are presented and their significance for the development of highly sensitive sensing, quantum informatics and quantum metrology is discussed.

Keywords: single-electron tunneling, molecules, clusters, nanoparticles, nanostructures, nanoelectronics, molecular electronics

PACS: 73.23.Hk.

Acknowledgments: This work was supported by the Russian Foundation for Basic Research, Grant No. 19-07-01-91.

For citation: Evgeny S. Soldatov. High-Temperature Single-Electron Transistors Based on Molecules and Small Nanoparticles. *RENSIT: Radioelectronics. Nanosystems. Information technologies*, 2021, 13(4):521-528. DOI: [10.17725/rensit.2021.13.521](https://doi.org/10.17725/rensit.2021.13.521).

July 17, 2021 at the Dissertation Council of the Physics Faculty of Lomonosov Moscow State University Evgeny Sergeevich Soldatov defended his dissertation entitled "High-temperature single-electron transistors based on molecules and small nanoparticles" for the degree of Doctor of Physics and Mathematics.

Tunneling nanosystems with an extremely low capacity based on single molecules and small nanoparticles was **the object** of the study, and the processes of creating such nanostructures, as well as the course and characteristics of tunneling electron transport through them under different experimental conditions was **the subject** of the study.

In general, the work is devoted to the study of the formation of controllable single-electron systems based on single molecules

and small nanoparticles, the development and creation on their basis of single-electron transistors with high charge energy and, accordingly, the operating temperature, as well as the study of electron transport in such transistors at high (more than 77 K) temperatures.

Such nanoelements are absolutely necessary for realizing the possibilities of using in wide practice the unique properties of the effect of correlated (single-electron) electron tunneling, allowing the construction of fundamentally new electronic devices and a dramatic (by several orders of magnitude!) improvement in the characteristics of existing devices. Only the use of such elements can increase the operating temperature of devices based on this effect from the typical level of 50-100 mK for traditional elements

to values of 100-300 K, which are acceptable in practice.

This has led to a great and constantly growing interest in the development of methods for creating planar tunneling single-electron elements based on individual molecules, clusters, small nanoparticles, reproducible production of such elements by technological methods already mastered by modern microelectronics, and the study of their characteristics. In addition to the above-mentioned issues of the experimental implementation of such extremely small nanostructures at the level of individual molecules and atoms, this work also solves the problems of a detailed elucidation of the mechanisms of electron transport through these quantum nanoobjects.

The research in this work is focused on the development and creation of key elements for any single-electronic device – single-electron transistors with high values of the charge energy, which determines the quality and usefulness of such transistors, as well as on the study of the characteristics of these nanoelements at the most convenient for practice, but at the same time extremely high for single-electronics temperatures above 77 K. At the same time, a monotonic improvement in their qualitative parameters and an increase in the operating temperature up to room temperature with a decrease in the size of one-electron elements down to the molecular and even to the atomic level is a main peculiarity of single-electron systems.

The creation of nanoelements was carried out by combining two innovative approaches to the formation of nanoelectronic elements:

- the use of single molecules (and/or small nanoparticles) of the required size as a nanoelement base and

- using a scanning tunneling microscope (STM) as a device both for the formation of tunnel nanosystems based on extremely small objects with sizes from 5 to 50 angstroms, and for studying the electrical characteristics and structure of these systems.

As part of the implementation of these approaches and the achievement of the set goal, three key problems were consistently solved, which stand in the creation of single-electron elements applicable in wide practice and determine the content of the specific main tasks of this work:

1. Investigation of the processes of formation of stable nanostructures based on single molecules/nanoparticles and, as a result, the formation of a methodological and technological basis for the creation of the studied nanoelements.
2. Development and creation of tunnel systems based on single molecules or nanoparticles using STM, as well as experimental and theoretical studies of electron transport through such systems, which has proven its correlated nature even at room temperature.
3. Development, manufacture and research of planar molecular one-electron transistors, efficient at high, up to 300 K, temperature.

In the course of solving the first problem, methods were developed for the formation of stable nanostructures on a solid substrate from extremely small molecules, as well as methods for studying the structure and characteristics of the formed nanostructures using STM. At the same time, two approaches to the formation of such nanostructures tolerant to studies by STM were proposed, developed, and implemented based on the creation of mixed Langmuir monolayers with

molecular-scale objects (1–5 nm) that are promising for single-electronics electronics, stable when they are studied in STM.

In the first approach, ready-made molecules, including non-amphiphilic ones, are included in the classical Langmuir monolayers of surfactants. Its development and implementation has shown the possibility of purposefully and reproducibly obtaining on a substrate measurement-stable samples of the required quality with molecular nanostructures of various dimensions: both 0D (single molecules) and regular 1D (chains) and 2D ensembles. This approach also ensured the creation of research prototypes of nanoelectronic elements using STM, both on the basis of single molecules and on the basis of multimolecular 1- and 2-dimensional systems of molecules. It was found that in 2-dimensional systems of molecules of this type, under certain conditions, their self-organization occurs with the formation of quasi-crystalline planar nanostructures with distinguished crystallographic axes.

In the second approach, the formation of nanostructures that are promising for single electronics is carried out just on a sample during its fabrication by synthesizing nanoparticles with the required properties and characteristics directly in mixed Langmuir monolayers at the water-air interface by carrying out chemical reactions and/or physical effects in them during preparation of a monolayer. This made it possible to controllably obtain, due to the discovered effect of anisotropic growth of nanoparticles in a longitudinal magnetic or electric field, both individual magnetic particles with given sizes (from 3–5 nm and above) and shape, and their chains. The constructed theoretical model of the process of such growth showed good agreement between the calculated

shape, size of nanoparticles and their growth rate with experimental data. This indicates a key role in the growth of interparticle dipole-dipole interactions, which underlie the model, which determines the observed strong dependence of the shape and size of nanoparticles on the orientation of the applied field.

In addition to such magnetic particles, an improved version of this approach made it possible to control both monolayers with separately lying nanoparticles of noble metals (gold and palladium) with a diameter of 1–2 nm, and organized composite polymer films with 1D and 2D ensembles of such *in situ* synthesized nanoparticles. It also made it possible to obtain polymer films with 1D and 2D ensembles of ready-made cluster molecules embedded in a planar monolayer monomolecular dielectric matrix. The sizes of the obtained nanoparticles satisfy the conditions for the realization of the effects of single-electron tunneling at room temperature, which makes it possible to create in this way reliable and stable single-electron nanosystems.

The technological base created in the course of the first key task made it possible, while performing the second key task of the work, to implement a method for creating single-electron elements based on single cluster molecules using STM and for the first time experimentally show the decisive role of the ligand shell of a molecule/nanoparticle in the transformation of the system "STMtip-cluster-substrate" from one-junction to two-junction and, accordingly, in the implementation of the single-electron mode of tunneling electron transport.

With the help of this technique, a single-electron transistor based on a single cluster molecule has been realized for the first time

at room temperature. The experimentally studied main characteristics of the formed transistors showed, despite the significant difference in the structure and electronic spectrum of the studied cluster molecules, the realization in all such nanosystems of the mode of correlated electron tunneling with record high values of the Coulomb blockade of tunneling (more than 500 mV) and charge energy (~ 250 meV). In these systems, a close to 100% modulation of the tunneling current by the control voltage and a charge sensitivity typical of single-electron systems no worse than $\sim 10^{-3}$ e/Hz $^{1/2}$ were obtained. This served as convincing evidence of the correlated nature of the tunneling electron transport in the fabricated molecular systems even at room temperature.

Within the framework of a theoretical study of electron transport through such systems, an approach was proposed and developed to determine and calculate the main parameter for single-electronics – the electric capacitance of extremely small, up to single atoms, quantum objects, and a formula was obtained for calculating the intrinsic effective capacitance of single isolated atomic-scale nanoobjects by the values their ionization potentials and electron affinity. An analysis of its dependence on size, shape and topology showed that with a sufficiently large number of atoms, this dependence is qualitatively similar to the classical case – the capacitance is proportional to the size of the object, and the functional dependence of the intrinsic capacitance of such objects on the number of atoms in them is determined by the dimension of these objects.

Taking these results into account, a theoretical model of tunneling transport through molecular single-electron nanoelements was proposed and developed,

taking into account the quantum discrete nature of the energy spectrum of their basis - a single quantum dot (molecule, small nanoparticle). It also took into account the effects of electron relaxation in a molecule/quantum dot for the first time. On the basis of the developed model, a computer simulation of the characteristics of electron transport of manufactured molecular single-electron nanoelements for cases of extremely fast and extremely slow (compared to the rate of electron tunneling) energy relaxation of electrons in a molecule is carried out. The proposed and implemented efficient scheme for calculating the canonical distribution of electrons in a molecule by the recursive method provided its acceleration by several orders of magnitude in comparison with direct enumeration of combinations and made it possible to simulate and study the I–V characteristics of molecular transistors using conventional laboratory computing power.

Comparison of theoretical and experimental I–V characteristics of molecular single-electron transistors showed their best agreement precisely at slow relaxation of electrons in the molecule. This allows us to conclude that the mode of operation of molecular single-electron transistors fabricated and investigated using STM is correlated tunneling of electrons with their slow energy relaxation in the molecule.

On the whole, this leads to the conclusion that small cluster molecules can serve as a reliable basis for the creation of single-electron nanosystems capable of operating at room temperature as elements of operating fundamentally new nanoelectronic devices. In this case, the greatest progress is provided by the use of the created molecular single-electron transistors for the construction

on their basis of supersensitive charge/field sensors, computer memory elements, fundamental standards (for example, a current standard), qubits, cells of a quantum cellular automaton.

In the course of work on solving the third key problem of this work, in order to ensure a wide and effective practical implementation of the above prospects, which is possible only for planar molecular devices in an integrated design, a method was developed for the manufacture of planar electrodes of a molecular transistor by controlled narrowing of the nanowire formed by electron beam lithography using the effect electromigration.

This technique, due to the use of the created original algorithm for carrying out the electromigration process, provided the production of electrodes with a distance between them required for high-temperature single-electronics electronics of 1.5÷5 nm with a yield of more than 90% usable at a high leakage resistance ($R > 300 \text{ G}\Omega$). These parameters indicate the suitability of such electrodes for creating molecular transistors on their basis.

The developed method of controlled embedding using the dielectrophoresis effect of small (2-4 nm) gold nanoparticles into the fabricated nanogaps between metal electrodes made it possible to ensure the targeting of such embedding and to obtain a high (~20%) yield of suitable samples, which is 3-4 times higher than for the traditional method of drying a solution with nanoparticles.

Measurements of electron transport through such molecular transistors showed a single-electron form of their stability diagrams at $T = 77 \text{ K}$, demonstrated high (more than 150 meV) values of the charge energy of the manufactured single-electron transistors. An oscillating (single-electron)

form of the characteristics of control of electronic transport through them at temperatures of 77 K÷220 K was recorded, and the correlated nature of electron transport in these nanoelements in a wider temperature range of 77 K÷300 K was shown.

Thus, the studies carried out made it possible to obtain the following main new results:

A method for the formation of mixed Langmuir monomolecular layers with a controlled surface density of non-amphiphilic molecules rigidly fixed on the substrate, providing the possibility of non-destructive reproducible study in STM of the structural and electrical characteristics of nanosystems based on such single molecules, has been proposed, developed, and for the first time implemented.

A method for the controlled formation of stable nanostructures on a solid substrate from single gold nanoparticles with a diameter of 1-3 nm promising for high-temperature single-electronics was proposed and implemented for the first time by carrying out chemical reactions of metal reduction directly in a monolayer; self-organization of such nanoparticles into 1-dimensional chains was found. The correlated nature of electron transport through double-junction tunnel systems based on such single nanoparticles at room temperature is shown.

An original method for the controlled formation on a solid substrate of stable 0-dimensional, 1-dimensional and 2-dimensional nanostructures from small (3÷5 nm) magnetic nanoparticles by means of direct decomposition of iron pentacarbonyl and dicobalt octacarbonyl just in the monolayer under the action of ultraviolet radiation with subsequent aggregation is proposed and implemented.

The anisotropic growth of forming magnetic nanoparticles in a longitudinal magnetic or electric field has been discovered and theoretically explained, which makes it possible to controllably obtain magnetic particles of the sizes and shapes required for the formation of nanoelements.

The effect of self-organization of molecules of the thallium derivative of carborane in mixed monomolecular Langmuir films with the formation of two-dimensional quasi-crystalline nanostructures with lattice parameters close to the corresponding parameters of a three-dimensional molecular crystal of this substance is found.

For the first time experimentally demonstrated the fundamental importance for single-electronics of the presence of a ligand shell in a nanoparticle or molecule for the implementation of the single-electron tunneling regime and the correlation of the size of the Coulomb blockade of electron tunneling with the size of the molecule/nanoparticle. At the same time, the possibility of purposefully changing the structure and characteristics of an already finished nanosystem directly on a substrate was demonstrated.

For the first time, a prototype of a molecular single-electron transistor operating at room (300 K) temperature was created and studied, in which a nanosystem with a charge energy of up to 250 meV was created, which provided control of the tunneling current of a single-electron transistor based on a single molecule, and such control was experimentally demonstrated at room temperature.

The proposed theoretical model of correlated electron tunneling in molecular systems taking into account the effects of electron relaxation in a molecule/quantum dot made it possible for the first time to prove

the slowness of electron relaxation in such systems in comparison with the tunneling rate, in contrast to traditional single-electron metallic systems, and to ensure agreement between experimental and theoretical data obtained for molecular transistors.

The proposed and developed method for determining the electrical capacity of quantum objects of atomic-molecular scale showed that the value of the intrinsic capacitance of objects of molecular and atomic scale is directly and closely related to their chemical and spectral properties, with the structure of the electron shells of atoms and the topology of molecules. A formula is obtained for calculating its value from the values of the ionization potential and the electron affinity of molecules and atoms. This allows, when designing and analyzing the operation of practical single-electron devices, to calculate the parameters of quantum nanoelements using a well-developed apparatus of classical electronic circuitry without cumbersome consideration and taking into account the specific quantum properties of such objects, which greatly facilitates the widespread practical implementation of single-electron atomic-molecular devices.

An original technique has been developed for the reproducible formation at room temperature of a key element of molecular single-electron transistors in a planar thin-film design - nanogaps between transistor electrodes with a width of less than 4 nm, a leakage resistance of more than 300 G with a high (90–95%) yield of suitable samples. As a result, this ensured, in the manufacture of planar molecular single-electron transistors, the realization of the main advantage of using molecules/nanoparticles in them – the achievement of a high charge energy and,

accordingly, the operating temperature of such transistors.

For the first time, the quantum dynamics of changes in the conductivity of quantum wires from gold atoms formed at the final stage of the electromigration process was discovered and studied at room temperature. These changes occur during the restructuring of quantum wires due to relaxation of mechanical stresses in them, which ultimately leads to rupture of quantum wires with the formation of nanogaps less than 4 nm wide.

A technique was developed and implemented for the targeted embedding of single small (2-4 nm) gold nanoparticles into the formed nanogaps between the tunnel electrodes of the transistor, which provided the formation of high-temperature molecular single-electron transistors with a yield of suitable samples of about 20%.

For the first time, planar single-electron transistors with a charge energy of up to 150 meV, in which correlated tunneling electron transport is realized at temperatures up to 300 K inclusive, have been manufactured and investigated at temperatures of 77–300 K.

Thus, the main result of this work was the creation of molecular single-electron transistors in a planar design with a high (~ 200 meV) charge energy and parameters that are the best achieved to date for planar single-electron elements. This opens up a wide window of new possibilities for the actual design, manufacture and use of such elements at high operating temperatures, up to room temperature, and, therefore, makes it possible to create on their basis those applicable in a wide practice fundamentally new nanoelectronic devices with unique characteristics and capabilities necessary to

solve the most pressing problems in various fields:

- simple/affordable and fast DNA sequencing – in biology and medicine;
- creation of quantum computers, quantum cellular automata, neural networks – in quantum informatics;
- creation of a quantum standard for a unit of electric current and closure, finally, a "metrological triangle" of quantum standards – «Voltage (Josephson effect) – Current (single-electronics) – Resistance (quantum Hall effect)» – in quantum metrology.

MAIN PUBLICATIONS

1. Soldatov ES, Khanin VV, Trifonov AS, Presnov DE, Yakovenko SA, Khomutov GB, Gubin SP, Kolesov VV. Single-electron transistor based on a single cluster molecule at room temperature. *JETP Letters*, 1996, 64:556-560. <https://doi.org/10.1134/1.567234>.
2. Gubin SP, Soldatov ES, Trifonov AS, Khanin VV. Change in the conductivity of single naked metallic clusters by ligation. *Mendeleev Communications*, 1997, 7(1):30-32; doi: 10.1070/mc1997v007n01abeh000772.
3. Zubilov AA, Soldatov ES, Mevkh NG, Khanin VV. Single-electron tunneling in a two-junction tunneling system based on a single ferritin molecule. *Radiotekhnika i elektronika*, 2000, 45(11):1373 (in Russ.).
4. Shorokhov VV, Johansson P, Soldatov ES. Simulation of characteristics of a molecular single-electron tunneling transistor with a discrete energy spectrum of the central electrode. *J. Appl. Phys.*, 2002, 91:3049.
5. Gubin SP, Gulayev YuV, Khomutov GB, Kislov VV, Kolesov VV, Soldatov

- ES, Sulaimankulov KS, Trifonov AS. Molecular clusters as building blocks for nanoelectronics: the first demonstration of cluster SET transistor at room temperature. *Nanotechnology*, 2002, 13(2):185-194; doi: 10.1088/0957-4484/13/2/311.
6. Soldatov ES, Gubin SP, Kolesov VV, Khomutov GB, Maximov IA, Sergeev-Cherenkov AN, Suyatin DB, Shorokhov VV, Sulaimankulov KS. Molecular cluster based nanoelectronics. *Microelectronic Engineering*, 2003, 69:536.
7. Khomutov GB, Gainutdinov RV, Gubin SP, Kislov VV, Khanin VV, Rakhnyanskaya AA, Sergeev-Cherenkov AN, Soldatov ES, Suyatin DB, Taranov IV, Tolstikhina AL. Organized planar nanostructures from ligand-stabilized nanoclusters: a route to molecular nanoelectronic devices. *Applied Surface Science*, 2004, 226(1-3):149-154.
8. Shorokhov VV, Soldatov ES, Gubin SP. Intrinsic capacitance of nanoscale objects. *Radiotekhnika i elektronika*, 2011, 56(3):352-369 (in Russ.).
9. Dagesyan S, Stepanov A, Soldatov E, Snigirev O. Properties of Extremely Narrow Gaps Between Electrodes of a Molecular Transistor. *Journal of Superconductivity and Novel Magnetism*, 2015, 28(3):787-790; doi: 10.1007/s10948-014-2875-7.
10. Galstyan A, Dagesyan S, Soldatov E. Creating the single-electron transistor by electromigration and electrotrapping. *Proc. of 26-th Int. Conf. Microwave & Telecommunication Technology (Crimico'2016)*, vol. 7, pp. 1520-1526. Russia, Sevastopol, SevSU Publ., 1916.

DOI: 10.17725/rensit.2021.13.529

40 YEARS OF THE INSTITUTE OF CHEMISTRY AND CHEMICAL TECHNOLOGY OF SB RAS

Boris N. Kuznetsov, Vladimir I. Kuzmin

Institute of Chemistry and Chemical Technology of the Siberian Branch of the RAS, <http://www.icct.ru/>
Krasnoyarsk 660036, Russian Federation

E-mail: bnk@icct.ru, kuzmin@icct.ru

Received September 28, 2021, peer-reviewed Oktober 04, 2021, accepted Oktober 18, 2021

Abstract: Information on the organization and activities of the Institute of Chemistry and Chemical Technology of the Krasnoyarsk Scientific Center of the Siberian Branch of the Russian Academy of Sciences is presented. Its scientific directions are highlighted, the results of fundamental scientific and applied research, participation in the creation of technologies for deep processing of mineral and organic resources of Siberia, hydrocarbons and biomass, organization of the development of the scientific potential of the region, international cooperation are noted.

Keywords: coal chemistry, hydrometallurgy, multicomponent raw materials, physical and chemical analysis

UDC 061.75

For citation: Boris N. Kuznetsov, Vladimir I. Kuzmin. 40 years of the Institute of Chemistry and Chemical Technology of SB RAS. *RENSIT: Radioelectronics. Nanosystems. Information technologies*, 2021, 13(4):529-532.
DOI: 10.17725/rensit.2021.13.529.



*Institute of Chemistry and Chemical Technology,
Siberian Branch of the Russian Academy of Sciences,
Krasnoyarsk, Akademgorodok, 50, p. 24*

On September 10, 2021, Krasnoyarsk hosted the celebration of the 40th anniversary of the Institute of Chemistry and Chemical Technology of the Siberian Branch of the Russian Academy of Sciences.

The history of the institute began in 1977. To organize the Institute, the leadership of the SB RAS (academician G.I. Marchuk, academician G.K. Boreskov) invited the Doctor of Chemical Sciences Sergei Pavlovich Gubin, a well-known specialist in the field of coordination and organometallic chemistry, laureate of the USSR

State Prize, to the SB RAS. In the period 1978-1980, he carried out the necessary preparatory work and at the beginning of 1981 the establishment of the Institute was approved by the Decision of the Presidium of the USSR Academy of Sciences. The main task is to develop scientific foundations for solving important problems for the regions of Siberia associated with the deep processing of huge resources of mineral and organic raw materials. Currently, the Institute carries out research in two scientific areas: the physical and chemical foundations of new environmentally friendly metallurgical and chemical-technological processes for the complex extraction of target products from multicomponent raw materials and the physical and chemical foundations of the processes of deep processing of natural organic raw materials, including plant biomass and brown coal.

During the formation of the Institute, a personnel problem immediately arose: it was necessary to find highly qualified employees - doctors and candidates of sciences, specialists with higher and secondary technical education. And then S.P. Gubin and his team began to invite scientists from different cities of the country to

Krasnoyarsk: Moscow, Leningrad, Novosibirsk, etc. The teams and collectives formed at that time are still successfully developing technologies for processing mineral and organic resources.

Now the Institute employs 220 people, of which 100 are research workers (17 are doctors and 65 candidates of sciences), 35 people are young scientists and specialists under the age of 39. At present, the influx of young people is mainly made up of graduates of the Siberian Federal University and the Reshetnev Siberian State University. There are 17 full-time graduate students studying in graduate school, it is planned to create a joint magistracy with Reshetnev SSUST next year.

At the Institute the Doctoral Dissertation Council is successfully working, headed by Doctor of Chemical Sciences, Deputy Director for Scientific Work Nikolai Vasilyevich Chesnokov, in the specialties: physical chemistry, technology of inorganic substances, chemical technology of fuel and high-energy substances.

Initially, the strategy of the Institute in the 80s of the twentieth century was to strengthen cooperation with the "heavyweights" of non-ferrous metallurgy, the largest plants: Norilsk mining and metallurgical, Ust-Kamenogorsk lead-zinc, Balkhash mining and metallurgical, etc. Fundamental research was launched in the field of studying surface phenomena, extraction, sorption, leaching, followed by laboratory and pilot-industrial tests at large enterprises of the country. The first industrial introduction was the sorption extraction of platinum metals from spent electrolytes at the Uglich Watch Plant, then the extraction technology for extracting indium from solutions of zinc production (Chelyabinsk Zinc Plant), extraction schemes for the processing of cobalt raw materials (Norilsk MMC) and others. In 1985, as part of a team of co-authors, the Director of the Institute Anatoly Ivanovich Kholkin and his deputy Gennady Leonidovich Pashkov were awarded the USSR State Prize for the creation of a modern rare metal production at the Ust-Kamenogorsk lead-zinc. In 2008, for the creation and industrial application of new extraction processes and combined hydrometallurgical schemes for the processing of unconventional and

technogenic raw materials and industrial products of the production of rare and non-ferrous metals, as part of a team of co-authors, four employees of the Institute were awarded the prize of the Government of the Russian Federation. The Government Prize was awarded to: Director of the Institute, Corresponding Member of the Russian Academy of Sciences, Doctor of Technical Sciences Gennady Leonidovich Pashkov, Head laboratory, d.ch.s. Vladimir Ivanovich Kuzmin, Head laboratory, Ph.D. Viktor G. Samoilov, Leading Researcher, Ph.D. Isaak Yurievich Fleitlich.

Fundamental research in the field of deep processing of coals of the Kansk-Achinsk basin was started by Doctor of Chemical Sciences, prof. S.P. Gubin in close cooperation with KatekNiiUgol. Subsequently, research in the field of processing coal and wood raw materials at the Institute developed under the leadership of Doctor of Chemical Sciences, prof. Boris Nikolaevich Kuznetsov. The scientific foundations of new effective technologies for thermocatalytic processing of Kansk-Achinsk coals in apparatus with a catalytic fluidized bed were developed. Together with the Institute of Catalysis of the Siberian Branch of the Russian Academy of Sciences and SibVTI, in 1984, a pilot industrial boiler with a fluidized bed furnace was launched, on which the technology of catalytic coal combustion was successfully tested. For his great contribution to the scientific support of the development of KATEK B.N. Kuznetsov was awarded the Order of the Badge of Honor in 1986.

Research in the field of deep processing of renewable wood raw materials is aimed at creating integrated technologies that ensure the transformation of all the main components of woody biomass into a range of in-demand products. The relevance of this topic has sharply increased in recent years, since the processing of biomass into energy carriers and chemical products does not affect the balance of carbon dioxide in the atmosphere and does not aggravate the greenhouse effect. The most important scientific achievements in this area are associated with the development of new catalytic processes for the conversion of woody biomass into valuable chemical products,

biofuels, and functional polymers. The head of these works, Doctor of Chemical Sciences, prof. B.N. Kuznetsov was awarded the honorary title "Honored Scientist of the Russian Federation" in 2008.

The Institute actively participates in international cooperation, was the organizer of 4 international symposia on catalytic transformations of natural polymers.

Over the past years, more than 90 candidate and 28 doctoral dissertations have been defended in the focus scientific areas.

The staff of the Institute are constantly in scientific search, making a worthy contribution to the development of fundamental science. The Institute is actively developing its scientific potential – it follows the path of expanding its own scientific schools, international contacts, exchange of leading professors and specialists. Fundamental scientific research carried out at the Institute is supported by projects of federal target programs, the Russian Science Foundation, the Russian Foundation for Basic Research, the Krasnoyarsk Science Foundation, etc. More than 500 articles published by the Institute staff over the past 5 years are included in the Web of Science database, received 53 patents.

Applied research also does not stand aside. The developments of the ICCT SB RAS are known and used in the Krasnoyarsk Territory, in Russia. The Institute actively cooperates with enterprises of the real sector of the economy, such as PJSC "MMC"Norilsk nickel", PJSC Chelyabinsk Zinc Plant, JSC "Krasmash", JSC Krastsvetmet, Federal State Unitary Enterprise "Mining and Chemical Combine", enterprises of the timber industry complex of the Krasnoyarsk Territory.

The successful development of fundamental and applied science at the Institute is facilitated by the creation at the KSC SB RAS in 2001 of the Krasnoyarsk Regional Center for Collective Use (KRCKP SB RAS) under the leadership of Doctor of Chemical Sciences, prof. Anatoly Ivanovich Rubailo. In the rating of Shared Use Centers (CSC) organized by the Federal Agency for Scientific Organizations of the Russian Federation, the KRTSKP SB RAS became one of

the leading CSCs in Russia, which made it possible to win FTP grants for the purchase of the latest devices and equipment in the amount of about 460 million rubles over the past four years. At the present time, only in our Institute there are more than 15 instruments of the first line of world instrument making, and in the CRCKP FRC KSC SB RAS – more than 50, which our scientists can use in their research.

Much attention is paid in the Institute and scientific and organizational activities: fruitful international cooperation, the development of ties with industry and university science, participation in expert councils, editorial boards of leading scientific journals. 29 employees are engaged in teaching activities, on the basis of the Institute, the basic departments of SibFU are organized. The Institute supervises in the city of Krasnoyarsk the basic school of the Russian Academy of Sciences – MAOU Lyceum №7. Scientific direction of profile classes "Environmentally friendly and resource-saving energy, effective deep processing of renewable natural raw materials to obtain a wide range of demanded chemicals". Classes for schoolchildren are conducted by young employees and graduate students of the Institute: Ph.D. Yuri Malyar, Ph.D. Dmitry Kuzmin, Ph.D. Sergey Vorobyov, Ph.D. Dmitry Zimonin under the supervision of the Director of the Institute, Doctor of Chemical Sciences, prof. RAS Oxana Pavlovna Taran.

The Institute is the organizer of significant scientific events. For many years he participated in the organization and holding of the international Congress "Non-ferrous metals and minerals" in the city of Krasnoyarsk. This year the international XIV conference "Metallurgy of non-ferrous, rare and noble metals", preceding the anniversary celebration and dedicated to the 40th anniversary of our Institute of Chemical Chemistry of the SB RAS, was organized jointly with the Institute of Non-Ferrous Metals and Materials Science of the Siberian Federal University and was held on-line from September 6 to September 9. Scientific adviser: Academician of the Russian Academy of Sciences Anatoly Ivanovich Khoklin, I.I. NS. Kurnakov RAS, Moscow, Chairmen of the Organizing



Sergey Pavlovich Gubin - Director-organizer of the Institute of Chemical Chemistry SB RAS and Oxana Taran – the present director at the anniversary of the Institute on September 10, 2021.

Committee: Doctor of Chemical Sciences, prof. Natalya Vasilievna Oleinikova and Doctor of Chemical Sciences Vladimir Ivanovich Kuzmin. More than 60 people took part in the work of the Conference, 40 reports of scientists and specialists from the Russian Federation, Kazakhstan and Uzbekistan were heard. The conference showed the importance and undoubted interest of representatives of the scientific and technological communities in solving the problems of processing mineral raw materials, scientific and technical achievements in this area. From September 29 to October 2, the Institute was host the 5th School of Young Scientists "New catalytic processes for deep processing of hydrocarbons and biomass." Scientific adviser, RAS Academician Valentin Nikolaevich Parmon, IC SB RAS, Novosibirsk,

Chairman of the Organizing Committee, Doctor of Chemical Sciences, prof. RAS Oxana Pavlovna Taran. The topic includes various fundamental and applied aspects of deep processing of oil and gas, coal, plant, microbiological raw materials and organic waste and is supported by the Russian Science Foundation.

Scientists from different cities of the country came to congratulate their colleagues at the jubilee Scientific Council. Guests from Moscow, Novosibirsk, St. Petersburg, colleagues from the Institutes of the Federal Research Center of the KSC SB RAS and universities of Krasnoyarsk in their speeches noted the value of joint interdisciplinary research and congratulated their colleagues.

Of particular interest was the report of the director-organizer of the Institute, Doctor of Chemical Sciences, Professor, Full Member of the Russian Academy of Natural Sciences Sergei Pavlovich Gubin. He told about the history of the Institute, colleagues of scientists who in the 80s of the twentieth century took an active part in translating the ideas that were born into reality, about the difficulties that had to be overcome at that time, and presented books as a souvenir. S.P. Gubin wished the staff of the Institute to continue to be constantly in scientific search, to make a worthy contribution to the development of fundamental science.

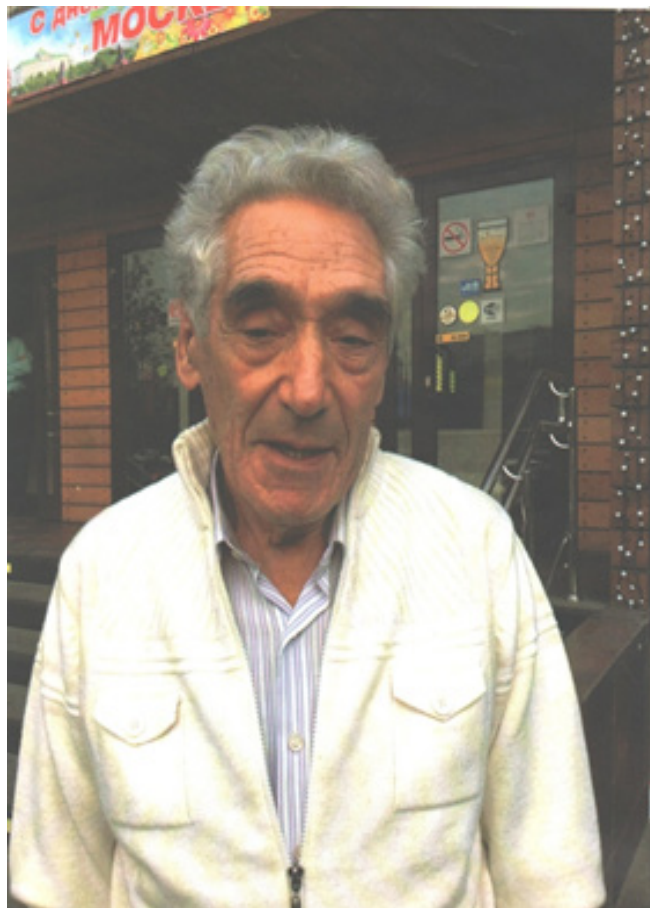
We can rightfully be proud of the pages of the Institute's biography, the names of those who stood at the origins of its creation and who ensure its authority and relevance today.



IN MEMORY OF GEORGE A. MARTYNOV

PACS: 01.60.+q

DOI: 10.17725/rensit.2021.13.533



On December 23, 2020, at the age of 94, died of coronavirus George Alexandrovich Martynov, Doctor of Physical and Mathematical Sciences, Professor, Chief Researcher of the Laboratory of Surface Forces of the A.N. Frumkin Institute of Physical Chemistry and Electrochemistry of RAS, an outstanding specialist in the field of the theory of liquid state and surface phenomena.

George Alexandrovich was born on February 23, 1927 in Moscow into the family of a famous Social Democrat, an employee of the Comintern, editor of the journal "Bolshevik" Alexander Samoilovich Martynov (1865-1935). The mother of George Alexandrovich – Anna Romanovna Martynova, was a doctor-pediatrician, sisters: Tatyana Alexandrovna (1914-1971) a physicist, and Elena Alexandrovna (1917-2019) – a chemist.

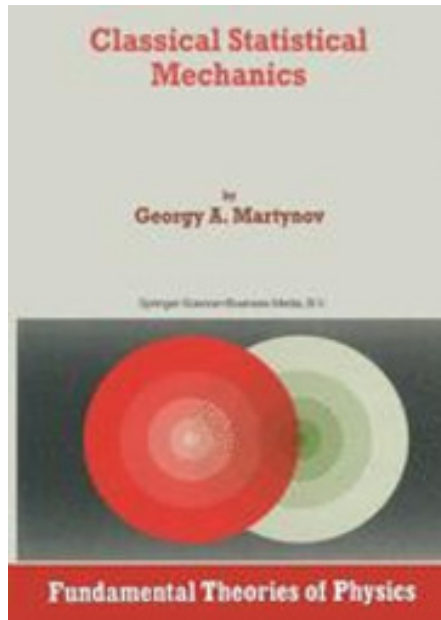
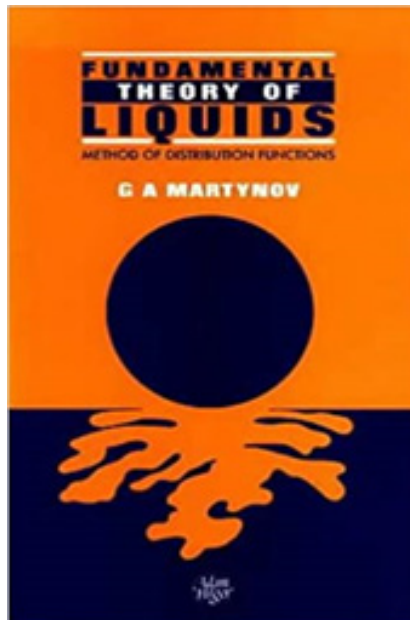
Both graduated from the M.V. Lomonosov Moscow State University.

After graduating from school, G.A. Martynov entered the Moscow Power Engineering Institute, and after the third year he moved to the Physics Faculty of the Lomonosov Moscow State University, who graduated in 1950 and was assigned to the Permafrost Institute of the Russian Academy of Sciences, where he worked as a junior researcher until 1957. From 1957 to 1959, working at the Institute of Building Physics, G.A. defended his thesis and became a candidate of technical sciences. In 1968 he defended his doctoral dissertation on the topic "Statistical theory of aqueous solutions of electrolytes" and became a doctor of physics and mathematics, and in 1980 – a professor.

From 1959 until the end of his days – Junior Researcher, Senior Researcher, Leading Researcher, Chief Researcher of the Laboratory of Surface Forces (department of Academician of the Russian Academy of Sciences B.V. Deryagin) at the A.N. Frumkin Institute of Physical Chemistry and Electrochemistry of RAS.

His research areas are the theory of surface phenomena, statistical mechanics of gases and liquids, the theory of electrolyte solutions, the theory of membrane separation of solutions, the theory of wedging pressure arising in thin layers of liquid. He proposed a universal equation of state for gases and liquids and a theory of phase transitions of the first kind. Recently, he has written works on the fluctuation theory of liquids and the fluctuation theory of critical phenomena (interest in the monograph by D.Yu. Ivanov "Critical behavior of non-idealized systems", 2003).

A wide range of interests and numerous works on the fundamental theory of the liquid state allows us to consider George Alexandrovich



Martynov one of the leading scientists in a very difficult field of science – the physics of the liquid state.

He is the author of monographs, three of which we present in this article, and more than 200 scientific publications.

Several doctoral and more than 15 candidate dissertations were defended under his supervision.

He was a permanent member of the theoretical seminar of Academician V.L. Ginzburg at the Lebedev Physical Institute of the Russian Academy of Sciences, who wrote back in 1959: "As I think, G.A. Martynov with great success can deal with a variety of problems related to molecular physics and surface phenomena".

At the meetings of the All-Russian Seminar on the Structure of Liquids and Liquid Solutions at the Kurnakov Institute of General and Inorganic Chemistry of RAS he made 16 reports. The first one was in 1964 "Statistical theory of aqueous solutions of electrolytes" and the last one – in 2019 "Statistical mechanics and the law of similarity of Bachinsky" and the fluctuation theory of liquids was formulated.

G.A. Martynov was an outstanding physicist-theorist, who did a lot in such a fundamental and difficult branch of science as the physics of the liquid state, who was able to explain the most complex questions in a simple and clear language.

We lost a person with whom we could talk and discuss fundamental scientific problems.

George Alexandrovich did not want to occupy high posts, did not aspire to be a corresponding member and academician, he lived in science and lived as he wanted...

Prof. Margarita N. Rodnikova
Prof. George G. Malenkov